

UNIVERSITY OF SÃO PAULO
SÃO CARLOS INSTITUTE OF CHEMISTRY

Paulo de Carvalho Dias Mendes

***Ab Initio* Investigation of the Adsorption of Molecules,
Involved in Carbon Dioxide and Glycerol Utilization, on
Transition-metal Substrates**

São Carlos

2020

Paulo de Carvalho Dias Mendes

***Ab Initio* Investigation of the Adsorption of Molecules,
Involved in Carbon Dioxide and Glycerol Utilization, on
Transition-metal Substrates**

Tese apresentada ao Instituto de Química de São Carlos, da Universidade de São Paulo, como parte dos requisitos para a obtenção do título de Doutor em Ciências no Programa de Pós-graduação em Química.

Área de concentração: Físico-Química

Supervisor: Prof. Dr. Juarez Lopes Ferreira da Silva

Exemplar revisado

**O exemplar original encontra-se em acervo reservado na Biblioteca
do IQSC-USP**

São Carlos

2020

*Dedicated to my mother, Gesiane Dias,
and to my first scientific adviser, Lucia H. Mascaró.*

ACKNOWLEDGEMENTS

I am grateful to several people, whose dedication and support allowed me to complete this study. I am grateful to Dr. Juarez L. F. Da Silva for his continued support, patience, sincerity and exemplary scientific guidance. I am also grateful to the researchers that supported me from the beginning of my studies and continually inspire me: Dr. Lucia H. Mascaro, Dr. Ernesto C. Pereira and Dr. Almir Sales.

I would like to thank my family for their love and support: my mother Gesiane Dias, my sisters Paula M. Mendes and Juliana M. Mendes, and my father Luiz Paulo Mendes. I am also grateful to Stella G. Justo for her companionship, for sharing good times with me and our cat, Planck, and for supporting me during my studies and other pursuits.

I want to express my sincere gratitude to all colleagues from the Quantum Theory of Nanomaterials group (QTNano - led by Dr. Juarez L. F. Da Silva) who I met during the PhD, especially Dr. Rafael Costa-Amaral for his help during my first steps with computational chemistry. I also want to thank all students who I helped when it was, later, my turn to offer guidance, as I learned much by teaching. Moreover, I want to thank all coauthors of the articles that were published or are in progress, for all of our productive interactions.

I acknowledge support from the funding agencies, CAPES (for providing my fellowship*), CNPq and FAPESP. I am grateful to the Center for Innovation on New Energies (CINE), and all related staff and institutions, for the support and meaningful interactions. I also want to express my gratitude to the São Carlos Institute of Chemistry (IQSC), University of São Paulo (USP) and to the people behind various services and programs: Comissão de Pós-Graduação (CPG), of which I was a member during one year; the General Services, Convênios, Eventos, Security and Information Technology staff of IQSC-USP; the staff from the University Restaurant, especially Campus 2; Programa de Aperfeiçoamento de Ensino (PAE - USP), due to the valuable opportunity to teach; Laboratório de Computação Científica Avançada (LCCA) and Superintendência da Tecnologia da Informação (STI), which manage high-performance computing resources for USP and provide high-quality technical support for all users; Laboratório LCCA-USP, National Laboratory for Scientific Computing, for providing HPC resources of the SDumont supercomputer; Department of Information Technology - São Carlos, and CISC-USP for hosting local computational resources.

* This study was financed in part by the Coordenação de Aperfeiçoamento de Pessoal de Nível Superior - Brasil (CAPES) - Finance Code 001.

“Not all those who wander are lost”

Gandalf

(J.R.R. Tolkien, The Fellowship of the Ring)

ABSTRACT

MENDES, P. C. D. ***Ab Initio* Investigation of the Adsorption of Molecules, Involved in Carbon Dioxide and Glycerol Utilization, on Transition-metal Substrates.** 2020. 175p. Doctoral Thesis (Physical-Chemistry) - São Carlos Institute of Chemistry, University of São Paulo, São Carlos, 2020.

This study was motivated by technologies involving the utilization of glycerol and carbon dioxide to obtain higher value products, which are economically promising and can benefit the environment. Carbon dioxide is a greenhouse gas, abundant in the atmosphere, that could be converted into monomers, fuels and other moieties, while glycerol is a polyol, accumulated as a byproduct in the production of biodiesel, that can be used to obtain other three-carbon alcohols. The aforementioned technologies could be developed by the use of transition-metal substrates as nanoparticles or extended surfaces to design catalysts with great control over properties, such as particle size, morphology and composition, which can be tuned towards optimal catalytic performance. Our study focused on adsorption, a pivotal step of the catalytic process. In this thesis, we present an extensive *ab initio* investigation, based on density functional theory, of the adsorption of carbon dioxide, glycerol and additional small model molecules on finite-sized and extended TM substrates. Concerning size effects, we found that the adsorption properties for physisorbed and chemisorbed CO₂ depended significantly on the particle size. For CO and H₂, there was alternation of the most stable adsorption site for the various substrate sizes, which resulted in small size-induced oscillations of properties, while for H₂O, the adsorption was almost independent of size effects. We also studied the adsorption of CO₂ on Pt-based nanoalloys and found that for systems containing metals with completely filled *d*-states, alloying with Pt facilitated the charge transfer to CO₂; on the other hand, for metals from groups 8, 9 and 10 of the periodic table, alloying with increasing Pt content either caused small effects on the adsorption properties or impaired charge transfer to CO₂. Moreover, we explored several stable morphologies and chemical orderings and found that CO₂ tends to bend on low-coordinated and heterogeneous adsorption sites. Concerning glycerol and other three-carbon alcohols, we systematically studied the influence of OH groups on the adsorption on model surfaces and found that increasing the number of OH groups increases the adsorption strength, while changing their relative positions leads to similar adsorption strength, but with distinctions of other properties, such as bond stretching for the molecules, such trends were discussed in terms of the reactivities of the alcohols.

Keywords: Density Functional Theory. Transition Metals. Nanoparticles. Nanoalloys. Surfaces. Adsorption. Carbon Dioxide. Glycerol. Alcohols.

RESUMO

MENDES, P. C. D. ***Ab Initio* Investigation of the Adsorption of Molecules, Involved in Carbon Dioxide and Glycerol Utilization, on Transition-metal Substrates.** 2020. 175p. Tese (Doutorado em Físico-Química) - Instituto de Química de São Carlos, Universidade de São Paulo, São Carlos, 2020.

Esse estudo foi motivado por tecnologias envolvendo a utilização de glicerol e dióxido de carbono para obter produtos de alto valor, as quais são promissoras economicamente e podem beneficiar o meio ambiente. O dióxido de carbono é um gás estufa abundante que pode ser convertido em monômeros, combustíveis e outros produtos, enquanto glicerol é um poliálcool acumulado como subproduto da indústria de biodiesel que pode ser convertido em outros álcoois de três carbonos. As tecnologias supracitadas podem ser desenvolvidas pelo uso de substratos de metais de transição, na forma de nanopartículas ou superfícies estendidas, para projetar catalisadores com grande controle de propriedades, como tamanho de partícula, morfologia e composição, visando desempenho catalítico ótimo. Nosso estudo tem foco na adsorção, passo crucial do processo catalítico. Nessa tese, apresentamos uma extensa investigação *ab initio*, baseada na teoria do funcional da densidade, da adsorção de dióxido de carbono, glicerol e outras moléculas pequenas em substratos de metais de transição de tamanho finito e estendido. Sobre efeitos de tamanho, observamos que as propriedades de adsorção para CO₂ fisissorvido e quissorvido dependem significativamente do tamanho do substrato. Para CO e H₂, houve alternância do sítio de adsorção mais estável com variação do tamanho de partícula, o que levou a pequenas oscilações nas propriedades, enquanto para H₂O a adsorção quase independe dos efeitos de tamanho. Estudamos também a adsorção de CO₂ em nanoligas baseadas em Pt e observamos que, para os sistemas contendo metais com estados *d* completamente preenchidos, as ligas com Pt facilitaram a transferência de carga para o CO₂; por outro lado, para os metais dos grupos 8, 9 e 10 da tabela periódica, o uso de ligas com cada vez mais Pt pode resultar em pequenos efeitos ou dificultar a transferência de carga. Adicionalmente, exploramos várias morfologias e distribuições de átomos e observamos que o CO₂ tende a dobrar em sítios de baixa coordenação e heterogêneos. Sobre o glicerol e outros álcoois de três carbonos, estudamos sistematicamente a influência dos grupos OH na adsorção em superfícies modelo e observamos que o aumento do número de grupos OH aumenta a intensidade de adsorção, enquanto diferentes posições relativas do grupo resultam em intensidades similares, porém com outras distinções, como nos estiramentos das ligações das moléculas; tais tendências foram discutidas em termos das reatividades dos álcoois.

Palavras-chave: Teoria do Funcional da Densidade. Metais de Transição. Nanopartículas. Nanoligas. Superfícies. Adsorção. Dióxido de Carbono. Glicerol. Álcoois.

LIST OF FIGURES

Figure 1 – Convergence, for optimization of the cell volume of face-centered cubic (fcc) Cu, of the lattice parameter, a_0 , average bond length, d_{av} , and total energy, E_{tot} , with respect to the sampling of \mathbf{k} -points, indicated by the parameter for automatic generation of the \mathbf{k} -mesh, and cutoff energy for the plane-wave basis set, indicated as multiples of the recommended cutoff (ENMAX).	62
Figure 2 – Illustrations of the unit cell for Ni(111), 3×3 slab, representing the extended surfaces, and cubic simulation box for Ni ₅₅ , located at the origin of the box, demonstrating finite systems. The distances, d , between marked atoms are indicated.	64
Figure 3 – Relative energies with respect to the fcc structure, ΔE_{TM}^{i-fcc} , for the transition-metal crystals.	68
Figure 4 – Average bond length and cohesive energy for transition metal crystals. The ranges obtained for the effective coordination numbers, ECN, are indicated for each type of structure.	69
Figure 5 – Total and local density of states (DOS, LDOS) for the most stable TM bulks; the LDOS are decomposed into s -, p -, d - and f -states. The dashed and dotted lines indicate, respectively, the Fermi level and the d -band center.	73
Figure 6 – Side and top views for 1×1 unit cells of bcc(110), fcc(111) and hcp(0001) described using the slab model. The letters A, B and C identify layers, with different letters characterizing distinct environments. The atomic radii are represented arbitrarily and not in scale.	75
Figure 7 – Relaxation of the interlayer spacing, Δd_{ij} , for the topmost atoms of slabs with 5 and 11 layers (L) for the surfaces: Fe(110), Co(0001), Ni(111), Cu(111), Ru(0001), Rh(111), Pd(111), Ag(111), Os(0001), Ir(111), Pt(111) and Au(111).	76
Figure 8 – Surface energy and work function for the surfaces: Fe(110), Co(0001), Ni(111), Cu(111), Ru(0001), Rh(111), Pd(111), Ag(111), Os(0001), Ir(111), Pt(111) and Au(111).	78
Figure 9 – Total and local density of states (DOS, LDOS) for the central (indicated as bulk) and surface layers of 11-layer slabs. The LDOS are decomposed into s -, p -, d - and f -states. The dashed and dotted lines indicate, respectively, the Fermi level and the d -band center.	80

Figure 10 – Optimized atomic structures of gas-phase molecules (CO ₂ , CO, H ₂ O and H ₂) transition-metal clusters (Co _n , Ni _n and Cu _n , for $n = 13, 55, 147$) and close-packed surfaces. The binding energies per atom, E_b , are shown below the configurations; moreover, the molecular angles and bond lengths are displayed. Between parentheses, we show the percent deviations of E_b , with respect to the bulk cohesive energies.	85
Figure 11 – Radial distribution function, $g(r)$, with respect to the geometric center of the clusters ($r = 0$) for the isolated Co _n , Ni _n and Cu _n clusters for $n = 13, 55$ and 147	87
Figure 12 – Lowest energy adsorption structures of CO ₂ , CO, H ₂ O and H ₂ adsorbed on the Co _n , Ni _n , and Cu _n ($n = 13, 55, 147$) nanoclusters and on the respective compact surfaces. Below the structures, we show the interaction energy, E_{int} (eV), with the adsorption energy, E_{ad} (eV), indicated between parenthesis energies.	88
Figure 13 – Adsorption properties versus substrate particle size for the most stable adsorption configurations. Linear regressions are indicated to guide the eyes through the data. The properties are: adsorption energy, E_{ad} , interaction energy, E_{int} , total effective charge of the adsorbed molecule, Q^{Mol} , shortest distance between an atom of the molecule and a TM, d_{Mol-TM} , percent variations of the molecular bond lengths, Δd , and percent variations of the molecular angles, $\Delta\alpha_{Mol}$	91
Figure 14 – Adsorption and interaction energy versus the average center of the occupied, up and down, d -states considering the TM atoms closer to the adsorbates. The substrate particle size is indicated next to some symbols.	93
Figure 15 – Electron density difference analysis for the most stable adsorption configurations of CO ₂ , CO, H ₂ O and H ₂ on Co _n , Ni _n and Cu _n ($n = 13, 55, 147$) nanoclusters and compact surfaces. Yellow and blue regions represent, respectively, the accumulation and depletion of electron density; the isosurface level is indicated, in $e a_0^{-3}$	96
Figure 16 – Optimized atomic structures of isolated 55-atom unary nanoclusters and Pt _n TM _{55-n} nanoalloys ($n = 13$ and 42). The configurations were denominated distorted reduced-core (DRC), hexagonal close-packed wheel-type (WHE), face-centered cubic fragments (two types, FCCf1 and FCCf2), icosahedron (ICO) and polytetrahedron (PTH). For Pt ₅₅ , the relative total energy with respect to the lowest energy, DRC, structure is indicated.	101

Figure 17 – Optimized lowest energy adsorption configurations for $\text{CO}_2^{\delta-}$ (chemisorbed molecule, bent OCO angle) and physisorbed CO_2 interacting with TM_{55} and $\text{Pt}_n\text{TM}_{55-n}$, with $n = 13$ and 42 . The adsorption energies, E_{ad} (in eV), are indicated below the configurations, while the interaction energies, E_{int} (in eV), are between parenthesis.	105
Figure 18 – Most stable optimized adsorption structures for bent and linear CO_2 interacting with various Pt_{55} clusters: distorted reduced-core (DRC), two types of face-centered cubic fragments (FCCf1 and FCCf2), hexagonal close-packed wheel-type (WHE) and icosahedron (ICO). The numbers below the structures are adsorption energies, E_{ad} (in eV), and, between parenthesis, interaction energies, E_{int} (in eV).	107
Figure 19 – Mode of CO_2 adsorption indicated by the OCO angle versus the adsorption energy for all adsorption structures studied for CO_2 adsorbed on unary and binary nanoclusters. Solid and hashed symbols represent to the most stable configurations for chemisorbed and physisorbed CO_2 , respectively.	108
Figure 20 – Adsorption properties of the most stable configurations for the chemisorption (solid symbols) and physisorption (open symbols) of CO_2 on the unary clusters and PtTM nanoalloys: adsorption energy, E_{ad} (eV), interaction energy, E_{int} (eV), effective Bader charge of adsorbed CO_2 , Q^{Mol} (e) and shortest distance between an atom of the CO_2 molecule and a TM atom, $d_{\text{Mol-TM}}$ (Å). The red solid line indicates the property for the chemisorption structure of $\text{CO}_2/\text{Pt}_{55}$ (DRC).	109
Figure 21 – Electron density difference analysis for the lowest energy adsorption configurations of chemisorbed and physisorbed CO_2 interacting with unary and binary nanoclusters. For the chemisorption systems, we employed isosurface levels of $1.5 \times 10^{-3} e a_0^{-3}$, while $3 \times 10^{-4} e a_0^{-3}$ was used for physisorbed CO_2 , which differ by a factor of 5. The accumulation and depletion of electron density are shown through yellow and blue colors, respectively. Below the structures, we indicate the total effective Bader charge of adsorbed CO_2 (e).	111
Figure 22 – Optimized isolated C_3 molecules. The atomization energies per atom, in eV, are shown below the configurations and, for the C atoms, the effective Bader charges, in e , are presented.	115

Figure 23 – Comparison of properties of the isolated stereoisomers, R-1,2-propanediol and S-1,2-propanediol. On the molecules, the effective Bader charges of C atoms are indicated, in e , followed by the atomization energy per atom, in eV, and the most important geometric properties. Moreover, the total local density of states for C, H and O atoms are presented for each enantiomer.	116
Figure 24 – Energy relative to the crystal fixed at $a_0 = 3.89 \text{ \AA}$, ΔE_{tot} , and total magnetic moment, m_{tot} , versus the lattice parameter, a_0 , for fcc Pd, PBE and PBE+D3.	119
Figure 25 – Top and side views of the most stable adsorption configurations for the C_3 molecules adsorbed on close-packed Ni, Pd and Pt surfaces. Below the configurations, we show the adsorption energy, E_{ad} in eV, and total magnetic moment, m_{tot} in μ_B	120
Figure 26 – Average total local density of states (DOS) per atom, including s -, p - and d -states, for the lowest energy configurations of isolated C_3 molecules, first and second topmost slab TM layers of clean Ni(111), Pd(111) Pt(111) surfaces, and adsorbed systems. The vertical dashed lines indicate the Fermi level of the substrates, and the highest occupied molecular orbital of the gas-phase C_3 molecules.	122
Figure 27 – Geometric properties for the adsorption of C_3 molecules on the close-packed TM surfaces. Angle between the surface normal and the line connecting the terminal C atoms ($\alpha_{CC\perp}$, in degrees) and shortest distances between C, O and H atoms and the nearest TM surface atom (d_{C-TM} , d_{O-TM} and d_{H-TM} , in \AA) for the most stable adsorption configurations.	123
Figure 28 – Electron density difference analysis the lowest energy configurations of C_3 molecules adsorbed on TM surfaces. The 3D isosurfaces, $0.0016 e/a_0^3$, show yellow and blue regions indicating, respectively, accumulation and depletion of electron density. The net variation of the electron density along the z direction, $\Delta\rho(z)$, is shown for each structure. The dashed lines indicate the positions of the surface plane (black), O (red) and H (green) atoms closer to the substrates.	125
Figure A29–Permission request process to re-use published material to elaborate Chapter 4. Permission is granted to the first author to use the complete material in this thesis and attribution was made appropriately.	153
Figure A30–Permission request process to re-use published material to elaborate Chapter 6. Permission is granted to the first author to use the complete material in this thesis and attribution was made in the respective chapter.	154

Figure A31–Explanation for re-use permission requests by the Royal Society of Chemistry showing the rules that apply to published material re-used in Chapters 4 and 6 of this thesis. Permission is granted to the first author to use the complete material in this thesis and attribution was made appropriately.	155
Figure A32–Continuation of the explanation for re-use permission requests by the Royal Society of Chemistry showing the rules that apply published material re-used in Chapters 4 and 6 of this thesis. This continuation shows how attribution must be done; both aforementioned chapters follow the rules highlighted for Physical Chemistry Chemical Physics. Permission is granted to the first author to use the complete material in this thesis and attribution was made appropriately.	156
Figure A33–Crystal structures. From the left: body-centered cubic (bcc), face-centered cubic (fcc), hexagonal close-packed (hcp) and simple cubic (sc). \mathbf{a}_i , \mathbf{b}_i and \mathbf{c}_i , with $i = \text{fcc, bcc, hcp and sc}$, indicate the translation vectors for the crystal that define the smallest unit cells.	159
Figure A34–Pictorial representation of all optimized adsorption structures of CO_2 , CO, H_2O or H_2 adsorbed on Co_{13} , Co_{55} , Co_{147} or $\text{Co}(0001)$ substrates. For each set, the structures are ordered by the energy relative to the most stable configuration, ΔE_{tot} , in meV.	164
Figure A35–Pictorial representation of all optimized adsorption structures of CO_2 , CO, H_2O or H_2 adsorbed on Ni_{13} , Ni_{55} , Ni_{147} or $\text{Ni}(111)$ substrates. For each set, the structures are ordered by the energy relative to the most stable configuration, ΔE_{tot} , in meV.	165
Figure A36–Pictorial representation of all optimized adsorption structures of CO_2 , CO, H_2O or H_2 adsorbed on Cu_{13} , Cu_{55} , Cu_{147} or $\text{Cu}(111)$ substrates. For each set, the structures are ordered by the energy relative to the most stable configuration, ΔE_{tot} , in meV.	166
Figure A37–Pictorial representation of the optimized configurations of $\text{CO}_2/\text{TM}_{55}$ and CO_2/PtTM for the $3d$ transition period. For each set, the structures are ordered by the energy relative to the most stable configuration, in eV.	168
Figure A38–Pictorial representation of the optimized configurations of $\text{CO}_2/\text{TM}_{55}$ and CO_2/PtTM for the $4d$ transition period. For each set, the structures are ordered by the energy relative to the most stable configuration, in eV.	169
Figure A39–Pictorial representation of the optimized configurations of $\text{CO}_2/\text{TM}_{55}$ and CO_2/PtTM for the $5d$ transition period, Os and Ir systems. For each set, the structures are ordered by the energy relative to the most stable configuration, in eV.	170

Figure A40–Pictorial representation of the optimized configurations of CO ₂ /TM ₅₅ and CO ₂ /PtTM for the 5 <i>d</i> transition period, Pt and Au systems. For each set, the structures are ordered by the energy relative to the most stable configuration, in eV.	171
Figure A41–Pictorial representation of the optimized adsorption structures of propane, 1-propanol and 2-propanol on Ni(111), Pd(111) and Pt(111). For each set, the structures are ordered by the energy relative to the most stable configuration. The total magnetic moment, in μ_B , is indicated between parentheses.	174
Figure A42–Pictorial representation of the optimized adsorption structures of 1,2-propanediol, 1,3-propanediol and glycerol on Ni(111), Pd(111) and Pt(111). For each set, the structures are ordered by the energy relative to the most stable configuration. The total magnetic moment, in μ_B , is indicated between parentheses.	175

LIST OF TABLES

Table 1 – List of PAW–PBE projectors, number of valence electrons (Z_{val}), default cutoff energy for the plane-wave basis set (ENMAX) and the chapter of the thesis in which the projector was employed.	59
Table 2 – Convergence test for the size of the cubic simulation box with a total energy convergence criterion of 10^{-8} eV for the frozen $\text{CO}_2/\text{Cu}_{13}$ system, which was optimized previously using a 20 \AA cubic box. We indicate the shortest distance between two periodic images, d_{im} , total electronic energy, E_{tot} , relative energy with respect to the largest box size, ΔE_{tot} , and total magnetic moment, m_{tot}	65
Table 3 – PBE equilibrium lattice parameters, a_0 and c_0 , and cohesive energy per atom, E_{coh} , compared to references ^{*,†} through percent deviations, Δa_0 , Δc_0 and ΔE_{coh}	70
Table 4 – Properties of transition-metal crystals ($3d$, $4d$, $5d$, groups 8 to 11). Equilibrium lattice parameters, a_0 and c_0 , average bond length, d_{av} , effective coordination number, ECN, cohesive energy per atom, E_{coh} , and d -band centers, $\varepsilon_{d\uparrow}$ and $\varepsilon_{d\downarrow}$	72
Table 5 – Magnetic moment per atom, m_{tot} , for Fe, Co, Ni and Pd crystals in the bcc, fcc, hcp and sc phases.	74
Table 6 – Surface energies, σ , and work functions, Φ , calculated in this study (11-layer slabs) compared to reference data from the literature, ^{*,†} indicated between brackets, through percent deviations shown between parentheses, $\Delta\sigma$ and $\Delta\Phi$	79
Table 7 – Effect of the dispersion correction (PBE compared to PBE+D3) on the properties of fcc crystals and fcc(111), 5-layer slabs, surfaces of Ni, Pd and Pt metals. Equilibrium lattice parameter, a_0 , cohesive energy per atom, E_{coh} , total magnetic moment, m_{tot} , surface energy, σ , work function, Φ , and relaxation of the interlayer spacing for the topmost layers, Δd_{12}	82
Table 8 – Characterization of Co_n , Ni_n and Cu_n ($n = 13, 55, 147$) clusters. Binding energy per atom, E_b , total magnetic moment for the unit cell, m_{tot} , effective coordination number, ECN (in number of nearest neighbors, NNN) and average bond length, d_{av}	86

Table 9 – Adsorption energy, E_{ad} , interaction energy, E_{int} , and deformation energies for the molecules and substrates, ΔE_{tot}^{Mol} and ΔE_{tot}^{sub} , respectively, for the most stable configurations of CO ₂ , CO, H ₂ O or H ₂ adsorbed on TM substrates of different size scales; namely, Co _{<i>n</i>} , Ni _{<i>n</i>} and Cu _{<i>n</i>} ($n = 13, 55, 147$) nanoclusters and with the Co ₍₀₀₀₁₎ , Ni ₍₁₁₁₎ and Cu ₍₁₁₁₎ indicating the extended surfaces.	90
Table 10 – Percent variations of molecular bond lengths ($\Delta O-C$, $\Delta H-H$ and $\Delta H-O$) and angles (ΔOCO and ΔHOH), with respect to the gas-phase molecules, for the most stable energy configurations of CO ₂ , CO, H ₂ O or H ₂ adsorbed on TM substrates of different size scales; namely, Co _{<i>n</i>} , Ni _{<i>n</i>} and Cu _{<i>n</i>} ($n = 13, 55, 147$) nanoclusters and with the Co ₍₀₀₀₁₎ , Ni ₍₁₁₁₎ and Cu ₍₁₁₁₎ indicating the extended surfaces.	94
Table 11 – Work function change, $\Delta\Phi$ (eV), due to adsorption of CO ₂ , CO, H ₂ O and H ₂ on the Co, Ni and Cu close-packed surfaces. The last row shows the work functions, Φ (eV), of the reference clean surfaces.	97
Table 12 – Characterization of the lowest energy configurations of the isolated substrates. Excess energy per atom, E_{exc} , binding energy per atom, E_b , total magnetic moment, m_{tot} , effective coordination number, ECN (in number of nearest neighbors), average bond length, d_{av} , and chemical order parameter, ζ	103
Table 13 – Face-centered cubic bulk and fcc(111) clean surface properties for Ni, Pd and Pt. For the crystals: optimized lattice parameter, a_0 , effective coordination number, ECN, in number of nearest neighbors (NNN), total magnetic moment, m_{tot} , and cohesive energy per atom, E_{coh} . For surfaces: interlayer relaxation for the topmost layers, Δ_{12} , work function, Φ , and average d -band center for the up, $\varepsilon_{d\uparrow}$, and down, $\varepsilon_{d\downarrow}$, states of the surface atoms exposed to the vacuum.	117
Table 14 – Bader charge analysis. Effective charge, Q (in e), for carbon, Q^C , the surface atom closer to the OH group, $Q^{Sur(O)}$, and average effective charges, \bar{Q} (in e), for the remaining surface atoms \bar{Q}^{Sur} , oxygen, \bar{Q}^O , hydrogen bonded to C, $\bar{Q}^{H(C)}$ and hydrogen bonded to O, $\bar{Q}^{H(O)}$. Carbon atoms are numbered according to the rules for naming alcohols (C1 is the carbon connected to the O atom closer to the substrate). Q^{Mol} (in e) is the total charge of the adsorbed molecule and $\Delta\Phi$ (in eV) is the work function change after to adsorption.	126
Table A15–Total energy, E_{tot} , and total time required to run the calculation, CPU time, for stable crystals obtained for spin-polarized (ISPIN = 2) and non spin-polarized (ISPIN = 1) calculations.	157

Table A16—Mathematical representation of the lattice translation vectors that define the smallest possible cells to construct POSCAR files for the transition-metal bulks.	160
--	-----

LIST OF ABBREVIATIONS AND ACRONYMS

1- <i>Pr</i> OH	1-propanol
1,2- <i>Pr</i> OH	1,2-propanediol
1,3- <i>Pr</i> OH	1,3-propanediol
2- <i>Pr</i> OH	2-propanol
bcc	body-centered cubic
DFT	density functional theory
DOS	density of states
DRC	distorted reduced-core
ECN	effective coordination number
fcc	face-centered cubic
FCCf	face-centered cubic fragment
GGA	generalized gradient approximation
<i>Gly</i>	glycerol
hcp	hexagonal close-packed
HK	Hohenberg–Kohn
KS	Kohn–Sham
ICO	icosahedron
LDA	local density approximation
LDOS	local density of states
NNN	number of nearest neighbors
PAW	projector augmented wave
PBE	Perdew–Burke–Ernzenhof
PTH	polytetrahedron
<i>Pr</i>	propane

Ref.	reference
sc	simple cubic
TM	transition metal
vdW	van der Waals
VASP	Vienna <i>Ab initio</i> Simulation Package
WHE	hexagonal close-packed wheel-type

CONTENTS

1	INTRODUCTION	29
1.1	Adsorption of Molecules on Transition-metal Substrates	29
1.2	Transition-metal Nanoparticles and their Interactions with Carbon Dioxide and Small Model Molecules	31
1.3	Glycerol Utilization and the Adsorption of Three-Carbon Alcohols on Transition-metal Surfaces	35
1.4	Open Problems about the Adsorption of Molecules on Transition Metal Substrates	38
1.5	Goals	38
2	METHODOLOGY	41
2.1	Many-Body Problem	41
2.2	Born–Oppenheimer Approximation	42
2.3	Density Functional Theory	44
2.3.1	Hohenberg–Kohn Existence Theorem	45
2.3.2	Hohenberg–Kohn Variational Theorem	45
2.3.3	Kohn–Sham Formalism	46
2.3.4	Exchange–Correlation Functionals	49
2.3.5	Dispersion (van der Waals) Corrections	52
2.4	Periodic Boundary Conditions and the Plane Wave Basis Set	55
2.5	Projector Augmented Wave Method	57
2.6	Projector Augmented Wave Implementation: Vienna <i>Ab initio</i> Simulation Package	59
2.6.1	Adjusting the Cutoff Energy for the Basis Set and Sampling the Brillouin Zone	60
2.6.2	Density of States, Work Function and Bader Charge Analysis	63
2.6.3	Defining the Sizes of Surface Unit Cells and Simulation Boxes	63
2.6.4	Structural and Electronic Optimizations	66
2.7	Summary	66
3	BULK AND CLEAN SURFACE PROPERTIES	67
3.1	Transition-metal Crystals	67
3.1.1	Procedures to Obtain the Atomic Structure Configurations	67
3.1.2	Relative Energy	68
3.1.3	Structural Properties	69
3.1.4	Cohesive Energy	71
3.1.5	Density of states and Magnetic Moments	74

3.2	Transition-metal Surfaces	75
3.2.1	Procedures to Obtain the Atomic Structure Configurations	75
3.2.2	Structural Relaxation	76
3.2.3	Surface Energy	77
3.2.4	Work Function and Density of States	78
3.3	Dispersion Effects on the Bulk and Surface Properties	81
3.4	Summary	82
4	THE EFFECTS OF SUBSTRATE PARTICLE SIZE ON THE ADSORPTION OF CO₂, CO, H₂O AND H₂ ON TRANSITION-METAL SUBSTRATES	83
4.1	Introduction and State of the Art	83
4.2	Isolated Molecules and Substrates	84
4.3	Procedures to Obtain Adsorption Atomic Structure Configurations	87
4.4	Adsorption of CO₂, CO, H₂O and H₂ on Co, Ni and Cu Substrates of Various Sizes	89
4.4.1	Adsorption Energy	89
4.4.2	Geometric Properties	93
4.4.3	Electron Density Difference and Distribution of Charges	95
4.5	Summary and Perspectives	97
5	THE ADSORPTION OF CO₂ ON 55-ATOM Pt-BASED NANOALLOYS	99
5.1	Introduction and State of the Art	99
5.2	Isolated Nanoparticles	101
5.3	Procedures to Obtain the Adsorption Atomic Structure Configurations	104
5.4	Lowest Energy Adsorption Configurations	105
5.5	Effects of the Occupation of <i>d</i>-states and Alloying on the Adsorption of CO₂	106
5.6	Geometric Properties of the Adsorbed Systems and Morphology Effects	108
5.7	Electron Density Analyses	110
5.8	Summary and Perspectives	112
6	EFFECTS OF THE HYDROXY GROUPS ON THE ADSORPTION OF ALCOHOLS ON TRANSITION-METAL SURFACES	113
6.1	Introduction and State of the Art	113
6.2	Isolated Molecules and Surfaces	115
6.3	Procedures to Obtain the Adsorption Atomic Structure Configurations	118
6.4	Adsorption of C₃ Alcohols on Ni(111), Pd(111) and Pt(111)	119

6.4.1	Adsorption Energy and Density of States	120
6.4.2	Geometric Properties	122
6.4.3	Electron Density Difference and Distribution of Charges	124
6.5	Summary and Perspectives	127
7	CONCLUSIONS	129
	BIBLIOGRAPHY	131
	APPENDIX	151
	APPENDIX A – PERMISSIONS TO RE-USE MATERIALS PUBLISHED IN SCIENTIFIC ARTICLES TO ELABORATE THIS THESIS	153
	APPENDIX B – DEMONSTRATION FOR SPIN-POLARIZED AND NON SPIN-POLARIZED CALCULATIONS	157
	APPENDIX C – ADDITIONAL DETAILS ON MODELING TRANSITION-METAL SOLIDS	159
	APPENDIX D – COMPLETE SET OF CONFIGURATIONS TO STUDY QUANTUM SIZE EFFECTS ON THE ADSORPTION OF CO₂, CO, H₂ AND H₂O ON TRANSITION-METAL SUBSTRATES	163
	APPENDIX E – COMPLETE SET OF CONFIGURATIONS TO STUDY THE ALLOYING EFFECTS ON THE ADSORPTION OF CO₂ ON Pt-BASED BIMETALLIC NANOALLOYS	167
	APPENDIX F – COMPLETE SET OF CONFIGURATIONS TO STUDY THE EFFECTS OF HYDROXY GROUPS IN THE ADSORPTION THREE-CARBON ALCOHOLS ON TRANSITION-METAL SURFACES	173

1 INTRODUCTION

The present thesis is based on the theoretical investigation of the adsorption of small molecules on various transition-metal (TM) substrates modeled as surfaces and nanoparticles. The leading molecules investigated were carbon dioxide and glycerol, motivated by their utilization for environmental and economic benefits, as will be discussed ahead. The adsorption process was simulated using computational chemistry based on Density Functional Theory (DFT), which is a well developed and prominent approach to study TM physical chemistry from the atomistic perspective.¹ Understanding adsorption can be critical for several phenomena that depend on the interaction of molecules with the TM materials, such as corrosion, chromatography, capture and storage of chemicals; however, the central motivation for this study was catalysis and the role of the TM substrates as catalysts. In this introductory part, we will explore the importance of adsorption in the context of catalysis, the role of transition metals, the carbon dioxide and glycerol utilization technologies and, then, the open problems about adsorption treated in this study and our goals.

1.1 Adsorption of Molecules on Transition-metal Substrates

Understanding the adsorption can help to control the catalysis of a chemical reaction, which can substantially affect the economic and technological development; one strong example of this is the worldwide impact that resulted from understanding the catalytic synthesis of ammonia, such as population growth.² In the case of CO₂, its catalytic conversions are very promising economically, considering the great abundance of this gas in the atmosphere and the environmental problems related to its accumulation.^{3,4} For glycerol, catalytic routes involved in its utilization can help improve the sustainability of the biodiesel industry.⁵ Both contexts are important environmentally and are discussed in detail ahead. Generally, The TM can participate in heterogeneous or homogeneous catalysis; in the former, the catalyst and reactants are in different phases, while in the latter, they are in the same phase. In this *ab initio* investigation, the case of TM surfaces represents the solid phase in the heterogeneous scenario, while the TM nanoparticles can be considered in the limit between heterogeneous and homogeneous catalysts, depending on their characteristics and application. Considering that no hard constraints are imposed in the atom-level for the phases involved in the interaction, atomistic insights into the interaction of molecules with nanoparticles could be useful for several technologies besides heterogeneous catalysis.

The adsorption of molecules on the catalyst changes the chemical environment and characteristics of the species involved, which can provide favorable conditions to

target processes. The purpose of a catalyst is to provide alternative reaction pathways to allow reactions to proceed through favorable activation energies that would be too high in the absence of the catalyst; as a consequence, the reaction rates can be increased. Adsorption is directly related to this big picture because the interactions between the catalyst (substrate) and the reactants, intermediates or products (adsorbates) are necessary steps. For example, the strength of interaction regulates the balance between capturing reagents and releasing products from a surface,⁶⁻⁸ which is crucial for the catalytic efficiency because of catalytic poisoning, that is, the blockage of active sites by a strongly interacting adsorbate. Furthermore, the adsorption properties of the interacting system, such as the distribution of charges, stability and variations of the molecular geometry can improve the understanding of the activation of molecules.⁹

Although adsorption is a pivotal process, the full picture of catalysis involves several factors in multiple scales, from laboratory testing to operating devices. Interest in the atomistic nature of catalysis has been increasing,^{1,10} due to the challenges of obtaining efficient practical catalysts. Therefore, paired with experimental efforts, computational chemistry can potentially reduce the costs, time and environmental impact of experimentation on candidate catalysts.¹¹ However, more than providing options for possible catalysts, theoretical studies have great potential to describe interesting effects in detail. This thesis explored some factors pertaining adsorption and the effects of substrate particle size, alloying and the presence of hydroxy (OH) groups, which will be contextualized and elaborated ahead. The main hypothesis was that such effects could be exploited to control the adsorption of model molecules on TM substrates and, consequently, affect catalytic processes.

Some of the most traditional catalysts are TM surfaces, due to the versatility of *d*-electron chemistry, including TM of the transition periods *3d* (Fe, Co, Ni and Cu), *4d* (Ru, Rh, Pd and Ag) and *5d* (Os, Ir, Pt and Au). Among them, noble metals, such as Pt and Au continue to be extensively studied models in the laboratory scale, due to their robustness and high catalytic efficiency, while *3d* TM are promising to reduce the costs of using noble metals and can promote high catalytic activity. From this variety of TM, the adsorption strength and chemical inertness of the catalyst can be balanced for optimal results. Some TM, such as Os, have limited applications because of toxicity and cost. However, it is important to study all of the aforementioned metals theoretically, either to propose their direct application or to rationalize periodic trends.¹²

Similarly to the direct application of TM surfaces as substrates, nanoparticles can compose the active phase of catalysts to facilitate chemical reactions.¹³⁻¹⁵ The TM nanoparticles studied herein were classified as nanoclusters, which are agglomerates of atoms with various morphologies and dimensions of no more than 100 nm. The substrate can be defined in several size scales, from small nanoparticles constituted of only a few

atoms (2 or more) up to the limit of infinite surfaces.¹⁶ In this thesis, various particle sizes were explored (13-, 55- and 147-atom nanoclusters and infinite surfaces). For comparable compositions, the nanoparticles have higher surface area per volume ratio than their bulk counterpart, which is desirable in catalysis;^{14,17} furthermore, unique properties can be achieved, due to quantum confinement in the nano scale.^{18,19} Currently, TM nanoparticles can be synthesized with meticulous control over their properties, such as composition, chemical ordering, morphology and size,^{15,17,20} hence, they can be tuned towards optimal catalytic performance.¹⁷

To this point, we introduced the motivation and essential concepts to understand why we chose to study adsorption in the broad context of catalysis; in this perspective, we chose two specific technologies of great environmental and, potentially, economic relevance that are based on the need to provide options for the utilization of CO₂ and glycerol. The first case concerns the adsorption and activation of CO₂ through its interaction with different TM substrates, which is important to understand the catalytic conversion of the gas into other valuable compounds to enable the utilization of this abundant greenhouse gas.^{3,4} The second topic is about the adsorption of alcohols on TM surfaces, motivated by the transformation of glycerol into other alcohols of higher economic value, which is a possible solution to alleviate the accumulation of glycerol from the transesterification process of the biodiesel industry.²¹ With those two scenarios, it was possible to evaluate cases of both weak adsorption (physisorption, typical of alcohols and CO₂ on close-packed TM surfaces) and strong adsorption (chemisorption, typical of CO₂ on nanoclusters).

The following introductory sections explore the fundamental concepts that motivated this study through a discussion about TM nanoclusters and their interaction with model molecules in the context of CO₂ utilization (Section 1.2), followed by an overview about the interaction of alcohols on TM surfaces in the context of glycerol utilization (Section 1.3). Then, in the subsequent chapters that show our findings, a short introduction elaborates further on the state-of-the-art research on each specific problem.

1.2 Transition-metal Nanoparticles and their Interactions with Carbon Dioxide and Small Model Molecules

The substrate is an essential part of an adsorption study, hence, we discuss the importance and characteristics of transition-metal nanoparticles to further understand their nature, which impacts their interaction with model molecules. After the advent of nanotechnology, rapid scientific development facilitated the experimental and theoretical study of TM nanoparticles.^{1,20} The nano scale opens unique opportunities to optimize catalysts; Au nanoclusters supported on metal oxides are a notable example, because of their high catalytic activity compared to smooth Au surfaces.¹⁶ Various properties such as size, morphology and composition can affect the catalytic performance of the nanoparticles.^{16,17}

Before studying how the adsorption of molecules occurs on TM nanoclusters, it is worthwhile to first understand some of the characteristics of nanoclusters that can explain their behavior. In this thesis, the nanoclusters composed of a single element were classified as unary, while the particular case of nanoclusters composed of two (binary) or more elements received the denomination nanoalloy. As expected, the electronic structure rapidly becomes more intricate for the nanoalloys as more elements compose the particle.²² In general, small variations in the atomistic scale, such as changing the position of one atom, can affect the properties of nanoclusters.²³

In the case of alloys and nanoalloys, synergism can improve catalysis through the creation of new characteristics that are not achieved by unary systems.²⁴ For example, the combination of Au and Pt in the surface region of nanoparticles can greatly improve the electrooxidation of methanol and carbon monoxide, due to the weaker binding of CO on Pt in the presence of Au in the surface region.²⁵ Nanoalloys containing more than two components increase the potential to optimize specific reactions, for example, it was reported that Au-Ag-Pd particles of about 4 nm diameter can catalyze the synthesis of an anti-inflammatory competitively with the traditional Pd complex catalyst,²⁶ which illustrates a behavior that could be transferable to other chemical reactions. However, considering the various permutations of atoms, morphologies and sizes, the number of possibilities is daunting.^{11,15} Then, to obtain high quality models that can help the rational design of catalysts, it is beneficial to study both unary nanoclusters and nanoalloys.

In principle, the formation of nanoclusters can be supposed stochastic, from which a continuous distribution of particle sizes would be obtained. However, certain structures are formed preferentially and correspond to mass spectrometry peaks,²⁷ such nanoclusters have specific quantities of atoms that are known as magic numbers.^{13,28} Similarly, there are preferred morphologies, such as the regular icosahedron structure, of I_h symmetry, defined by a central atom surrounded by 12 neighbors with the possibility to include additional layers of surrounding atoms to regularly grow the particle and obtain a sequence (13, 55, 147, ...) for the number of atoms.²⁹ Stable (magic) clusters generally follow similar trends and additional stable clusters can have a large variety of shapes and sizes.³⁰ However, these are not the only factors that drive stability, for example, the synthesis of nanoclusters can require the presence of adsorbed stabilizing agents to avoid agglutination, furthermore, the particles can be stabilized if supported on oxides, providing stabilization of nanoclusters with unblocked active sites,^{14,31,32} as well as synergistic effects.³³ Furthermore, clusters outside predefined magic numbers of electrons can be stable, as demonstrated by high stability of Al_nMg_m clusters, with respect to oxidation, for n and m not corresponding to magic numbers of electrons, which was attributed to geometric distortions and splitting of electronic states that affects the gap between the occupied and unoccupied states and, consequently, the reactivity.³⁴

The search for lowest energy configurations is a crucial previous step to study adsorption, because they are the species expected to be most easily found experimentally. Considering 55-atom nanoclusters, the structures of unary particles for 42 elements of alkaline and transition metals were meticulously studied previously in the atomistic level and the most stable configurations were found to be icosahedron structures (some of them distorted), with additional bulk fragments, wheel-type, polytetrahedron and distorted low-symmetry structures.³⁵ In some cases, it is possible to further minimize the energy of the structures, as demonstrated by the movement of Pt and Au, in cuboctahedron and icosahedron structures, to the surface of the nanoparticle, resulting in structures with fewer than 13 central atoms and lower energy than the regular configuration.³⁶ In the surface limit, which can be used to simulate large nanoparticles, the stability is mainly driven by the type of crystallographic plane and presence of defects.^{9,37} As expected, the stability and characteristics of the substrate affect its interaction with adsorbates.

For example, considering the adsorption of water and ethanol water on TM substrates, it was reported that, for 13-atom TM nanoclusters, the interaction occurs through the anionic O atom and it does not affect significantly the structure of the nanoclusters.³⁸ For both molecules, the same study showed that the adsorption energy increased as the *d*-states shifted towards the highest occupied molecular orbital for the different types of TM, while a small charge transfer and stretching of the O–H bonds were observed.³⁸ The same type of behavior was observed for surfaces,³⁹ although adsorption is stronger on nanoclusters, which is related to the lower coordination of the TM atoms.^{38,39} The coordination of the adsorption sites can be controlled through defects, morphology or particle size; for the interaction of CO with Pt nanoclusters, it was reported that there are different trends for the adsorption strength depending on the size range evaluated, reflecting the change between a scalable regime, that occurs for sufficiently large particles, and a non scalable regime, in which quantum size effects play a significant role.^{14,16,19,40} The same type of trend was shown for Pd nanoparticles, but with the behaviors transitioning in different size ranges.⁴¹ Moreover, adsorption can induce distortions of the nanoclusters, especially for small clusters, strongly affecting the electron density of the adsorbed system.^{42,43}

The electronic structure of the substrate is decisive for the adsorption process. From the density of states (DOS, expressing the number of electronic states available per energy level), the characteristics of the isolated substrate can be studied. For example, for metals, the valence *d*-states (named *d*-band for systems containing a large number of atoms, due to the superposition of electronic states) cross the Fermi level (highest energy occupied state). The position of the *d*-states, in relation to the Fermi level, depends on the type of metal and coordination. This characteristic was employed to devise a model, to predict the strength of the interaction between a surface and adsorbates, known as the *d*-band model.^{44,45} The idea considers the interaction between valence states of the adsorbate and

d -band of the substrate. The interaction strength is predicted considering the formation of antibonding states, which are above the d -band center, between the adsorbate and the TM. The higher the center of d -states, the higher the energy of antibonding states, resulting in stronger interaction.^{44,45} Consequently, a shift of the center of d -states towards the Fermi level suggests lower substrate stability and stronger adsorption. Originally, the model was proposed to explain the relative inertness of Ni, Pt, Cu and Au surfaces; the d -band filling increases from left to right in transition periods and is complete for Cu, Ag and Au. In this direction, there is also an increase of the nuclear charge which result in more tightly bound d -states and, for these reasons, the metals in the end of transition periods tend to be less reactive; analogously, the $5d$ TM tend to be the most noble TM.⁴⁴ The model has been employed successfully to study various TM substrates, including with discretized d -states.^{35,37} More recently, the model has been expanded to consider each spin component separately, which can improve the predictions for systems with significant spin polarization.⁴⁶ Although there are models to predict adsorption strength, as expected, each type of molecule adsorbs differently on the TM substrates.

The ideas discussed above are only a brief overview of what is possible to do, based on knowledge about adsorption, to design efficient catalysts using TM surfaces and nanoclusters.^{1,14,17} Considering such ample opportunities, this thesis explored adsorption motivated by the use of TM substrates to engender CO₂ transformations, which is currently a major multidisciplinary research challenge. It is widely discussed that the atmospheric concentration of CO₂ has been increasing from the regular use of fossil fuels to supply the worldwide energetic demand.⁴ Therefore, the use of this abundant greenhouse gas as a feedstock to obtain more valuable compounds has been a research priority, due to concerns about climate change as a consequence CO₂ accumulation.^{4,47,48} Moreover, CO₂ utilization is economically promising, because the molecule is an abundant atmospheric carbon feedstock, considering the low abundance of this element on the earth's crust.³ Some options proposed for CO₂ utilization are the electroreduction,⁴⁸ chemical reduction⁴⁹ and dry reforming of CH₄ to obtain H₂.¹² From such routes, the products could be valuable fuels, monomers or moieties. However, CO₂ is kinetically inert, in mild conditions, and its conversions require interaction with a catalyst.

The most stable structure for gas-phase CO₂ is linear; however, the OCO angle can bend if the molecule receives charge from a substrate or through electronic excitation, which can be important for activation of the molecule for its conversion.^{50,51} This thesis focused on the activation through charge transfer, due to adsorption on TM substrates, and excited states were not investigated. The TM substrates have the potential to transfer electrons and interact strongly with CO₂ (chemisorption), which can be controlled through the properties of the TM substrate and enhanced by additional effects, such as doping TM surfaces with alkaline metals.^{50,51} Alternatively, CO₂ can adsorb weakly, through physisorption, which was reported for close-packed TM planes and results in small structural perturbations

and adsorption strength independent of surface composition.⁵² It is possible to observe chemisorption in close-packed surfaces, but it is more common with the use of open planes, defects or doping; in this case, the adsorption strength depends on the type of TM and the transfer of charge from the surface to the molecule can be correlated with the adsorption strength.⁵²⁻⁵⁴ The characteristics of CO₂ adsorbed on the different surfaces can be related to the coordination of adsorption sites, since low-coordination sites can be expected to promote stronger adsorption;⁵⁵⁻⁵⁷ this has been demonstrated for the interaction between CO₂ and small 13-atom clusters containing low-coordination sites.^{43,58} Hence, it should be feasible to control CO₂ adsorption through substrate particle size, since different sizes affect the availability of adsorption sites with varied coordinations. In conjunction with such characteristics of the nanoparticles, alloying can be explored in the nanoscale to further control the adsorption. Such endeavor is supported by the observation that alloyed extended surfaces can control the adsorption strength of CO₂, which was shown using scaling relations.^{52,59}

Although CO₂ adsorption is clearly important for catalytic conversions, due to the need to activate the molecule, the phenomenon can also be relevant for technologies involving its storage and capture, since adsorption can be directly employed to capture CO₂⁶⁰ and it can also help to understand corrosion processes,^{61,62} which are important when optimizing transport and storage conditions. The reaction pathways for CO₂ conversions are beyond the scope of this thesis; they are numerous and feature several intermediates and products.^{3,48} Here, as will be elaborated in the subsequent chapters, the focus was on the adsorption of CO₂ on nanoparticles and extended surfaces.

1.3 Glycerol Utilization and the Adsorption of Three-Carbon Alcohols on Transition-metal Surfaces

Similarly to CO₂, glycerol is a molecule that has been associated with a need for utilization routes through catalysis. In this part, the main problems pertaining glycerol and its utilization are discussed to reach a key point addressed in this thesis concerning the adsorption of alcohols on TM substrates.

Glycerol, industrially known as glycerin, is non-toxic, non-corrosive and extremely useful for several applications.⁶³ The transesterification of triglycerides found in oils and fats, which is the basis of the biodiesel industry, produces glycerol in a form known as crude glycerol, which has to be carefully considered for applications due to the variation of its properties depending on the conditions of synthesis.²¹ For example, crude glycerol can contain between 38 to 96 % of glycerol and diverse additional components, such as methane, water and ashes.⁶⁴ The proportion obtained of crude glycerol to biodiesel is significant (1:10 in mass),⁶⁵ considering the incentives to grow biodiesel production in Brazil and other countries, which resulted in several thousand tons of accumulated crude

glycerol and a consequent reduction of its economic value.^{65–67} To advance the sustainability of the biodiesel production and minimize its environmental impact, it is important to evaluate options for the utilization of this accumulated glycerol.²¹ The refinement of the crude product can be performed with relative ease to allow applications that require high purity,⁶³ unfortunately however, the economic viability of this approach is questionable, due to the high cost of the procedure in comparison to the low monetary value of glycerol, due to its excess.⁶⁸

The main proposals to use glycerol are for animal nutrition,⁶⁹ as a fuel for electricity⁶⁶ and as an alternative green solvent for chemical reactions.⁷⁰ Some of the options to use refined glycerol involve heterogeneous catalysis, for example, to produce electricity in direct glycerol fuel cells,⁷¹ in the catalytic reforming process to obtain hydrogen^{72–74} and in the hydrogenolysis to form other compounds of higher value, especially three-carbon (C_3) alcohols.⁵ There is a variety of applications for glycerol in catalytic processes highlighting the importance of understanding its adsorption on TM substrates, which are used as catalysts.^{5,9,37,75} Most of these applications concern breaking glycerol molecules to obtain different compounds or convert chemical energy into electricity. The decomposition of glycerol on a TM substrate is far from trivial, because it involves a high number of intermediates and possible pathways,⁷⁶ due to the several possibilities of bond cleavage (O–H, C–C, C–O and C–H). From the theoretical DFT study of dehydrogenated intermediates, it was described that breaking the C–C bond becomes easier as the degree of dehydrogenation increases;⁷⁷ the same authors showed that Pt(111) and Pd(111) favor breaking the C–C bond, while with Ni(111) it is more favorable to cleave C–O bonds, instead of C–C, and on Cu(111) the decomposition was predicted to be slow.⁷⁷

The arrangement of surface atoms can also affect the reaction, as shown by the voltammetry profiles for the electrooxidation of glycerol on various types of Pt surfaces.⁷⁸ Through quantum chemical calculations, it was reported that glycerol adsorbs on different non-defected Pt surfaces, preferably parallel to the surface plane and with the O atoms close to top adsorption sites.^{37,75} The adsorption energies indicated that the strength of the interaction increased for the substrates in the order Pt(111), Pt(100) and Pt(110), showing that the adsorption is stronger on the less stable surfaces.³⁷ Moreover, the geometry of the molecule and the interlayer spacing of the surface layers are not altered after adsorption, but the distance between the molecule and surface decreases as the interaction strength increases, there is a reduction of the work function (which is the energy required to move one electron from the surface to the vacuum) and charge transfer from glycerol to the surfaces.^{37,75}

There is a significant gap between experiments and theoretical models, due to factors such as the presence of coadsorbed species, parallel reactions, substrate defects, temperature, pH, solvent effects, among others. Concerning defected Pt(111) substrates, it

has been shown that the adsorption strength increases in the presence of low coordinated adsorption sites with decreased Pt–O distances and greater adsorption strength, in comparison to Pt(111) without defects, which was attributed to the shift of the *d*-band towards the Fermi level, resulting from the decreased coordination.⁹ The influence of coadsorbed species and solvent effects were described for defected surfaces in a study of the simultaneous interaction among 2 glycerol, 12 water and 6 carbon monoxide molecules on Pt(111), which showed that the most stable configuration features all CO molecules strongly adsorbed on low coordinated sites, while 2 H₂O molecules adsorb similarly to Pt and glycerol interact through hydrogen interactions with the remaining molecules in a layer farther from the surface plane with O–Pt distances of at least 5.26 Å.⁷⁹

Besides Glycerol (*Gly*), the additional C₃ molecules studied in this thesis were 1,3-propanediol (1,3-*PrOH*), 1,2-propanediol (1,2-*PrOH*), 1-propanol (1-*PrOH*), 2-propanol (2-*PrOH*) and propane (*Pr*), which are possible products of glycerol hydrogenolysis, a reduction process that can use TM surfaces as a catalyst.^{5,21} The products can be selected from many potential routes according to the reaction conditions, such as the type of catalyst.⁸⁰ Several catalysts have been considered and their most common components are Co, Ni, Cu, Pt, Pd, Ir and Ag.⁸¹ The aforementioned C₃ products are valuable for several applications:⁵ the diols can be used as monomers for plastics and resins, 1,2-*PrOH* has low toxicity and is employed in detergents, foods and cosmetics, 1-*PrOH* is a prominent solvent applied, for example, in printing pigments and 2-*PrOH* is a widely commercialized solvent. The most interesting product is, arguably, 1,3-*PrOH*, because it has the highest economic value and demand.⁵ The adsorption of all of these molecules on TM surfaces is also important in additional contexts not necessarily connected to catalysis. For example, refined glycerol can be used as an additive to stabilize and control electrosynthesis,⁸² and as a corrosion inhibitor.⁸³ Although the applications are numerous, the atomistic understanding of the related phenomena is still incomplete.

The main difference between the hydroxylated products derived from glycerol are the number and position of the hydroxy groups, which should have a crucial role in the adsorption, as suggested experimentally by the strong dependence of glycerol electrooxidation with the pH⁸⁴ and the early reports about the effect of such groups in breaking the C–C bonds of C₃ alcohols.⁸⁵ Glycerol is more reactive than 1,2-*PrOH* and 1,3-*PrOH*, according to the formation of more C₁ and C₂ products during its electrooxidation, while 1-*PrOH* and 2-*PrOH* show low reactivity, suggesting the importance of the OH groups for the reaction.⁸⁶ Before this study, the literature did not have an *ab initio* systematic and comparative study of the adsorption of hydroxylated C₃ molecules; hence, here we focused on describing the role of OH groups, from the atomistic perspective, in the adsorption process considering model alcohols and TM surfaces.

1.4 Open Problems about the Adsorption of Molecules on Transition Metal Substrates

When planning this study, despite the fact that transformations of CO₂ and alcohols catalyzed by TM were rapidly attracting attention, we noted unsolved problems regarding the adsorption of relevant molecules on TM substrates. Concerning the context of CO₂, it has been known that adsorption on TM can induce bending of the OCO angle, which is a phenomenon that can be attributed to charge transfer related to the activation of the molecule towards conversions.⁵¹ Strategies have been suggested to achieve this condition, such as controlling the coordination of adsorption sites.^{55–57} Moreover, the adsorption properties have been studied for the interaction of CO₂ with various TM surfaces^{52,54} and some TM nanoclusters.^{43,58} There are contrasts between finite-size and extended substrates, for example, the low-coordinated adsorption sites on the small particles promote stronger adsorption, which could facilitate activation. This is an indication that the substrate particle size could play an important role in CO₂ adsorption and activation; however, the atomistic understanding of the dependence of substrate particle size on the adsorption of CO₂ and additional molecules, which are important in the electroreduction of CO₂ (such as CO, H₂O and H₂), was still sparse and incomplete. Previous studies^{52,54} also clarified that the type of TM strongly affect CO₂ activation and, considering that the use of alloys can greatly expand the opportunities for CO₂ transformations, the process was predicted based on scaling relations for extended alloy surfaces.^{52,59} However, the role of alloying in the nano scale in the adsorption of CO₂ on TM nanoclusters was not sufficiently explored, especially considering the great variety of possible morphologies and chemical orderings.

In the context of alcohols, various authors used DFT to investigate the adsorption of alcohols with TM surfaces considering the effects of different surface planes,³⁷ surface defects,⁹ type of metal³⁹ and size of the C chain.⁷⁵ The importance of the O atoms is evident and it was noted, but a systematic study focused on the role of OH groups on adsorption, with respect to their number and position, was still lacking. For example, adsorption is increasingly strong from methanol, to ethanol and glycerol on TM surfaces as the number of OH groups increases,⁷⁵ however, there are additional effects, such as the size of the C chain, that affect this trend. Moreover, the effects of changing the positions of the OH groups was not investigated in the atomistic level, such as the distinction between two OH groups located on adjacent or non-adjacent C atoms. Therefore, a quantitative systematic study was still lacking to complement the accumulated atomistic knowledge.

1.5 Goals

The main goal of this thesis was to study the adsorption of molecules on TM substrates through accurate *ab initio* calculations, based on DFT and using model systems, to contribute to solve the aforementioned open problems. For organization purposes, the

project was divided into three fronts with clear specific goals:

- Study the adsorption of CO₂, CO, H₂O and H₂ on TM nanoparticles of various sizes, namely, Co_{*n*}, Ni_{*n*} and Cu_{*n*} clusters (with $n = 13, 55, 147$) and Co(0001), Ni(111), Cu(111) to investigate the effects of substrate particle size on the adsorption of CO₂ and the additional small molecules that are relevant in its electroreduction;
- Study the adsorption and activation of CO₂ on stable Pt-based bimetallic nanoalloys, Pt₁₃TM₄₂ and Pt₄₂TM₁₃, including several arrangements, such as core-shell, homogeneously distributed and segregated side by side to investigate the role of alloying, in the nano scale, in the adsorption and activation of CO₂;
- Study the adsorption of glycerol and its derivative alcohols on Ni(111), Pd(111) and Pt(111) to understand the role of OH groups in the interaction between C₃ alcohols and model TM surfaces. To represent all possibilities for the number and positions of hydroxy groups, investigate the following set of adsorbates: glycerol, R- and S-1,2-propanediol, 1,3-propanediol, 1-propanol, 2-propanol and propane.

2 METHODOLOGY

This chapter summarizes the theoretical foundations of the calculations performed for the thesis based on articles cited along the text and also on several books⁸⁷⁻⁹¹ that offer complementary reading for further details on solid state physics, computational chemistry and quantum theory of the electronic structure. Here, some fundamental equations will be introduced omitting the spin variable, for simplicity, but spin polarization will be shown, and explicitly mentioned, for some selected equations, since our studies employed spin-polarized calculations; in addition, a short discussion and practical demonstrations about the effects of spin polarization on the results and computational cost were included in Appendix B. The equations will be presented in atomic units, i.e., adopting the constants $e = m_e = \hbar = (4\pi\epsilon_0)^{-1} = 1$, in which e and m_e are the elementary charge and mass of the electron, respectively, ($\hbar = h/2\pi$) is the reduced Planck constant, and ϵ_0 is the vacuum permittivity.

2.1 Many-Body Problem

To study the adsorption of molecules on surfaces and nanoclusters from the atomistic perspective, it is necessary to understand how a system of several nuclei and electrons behaves. This is related to the many-body problem, which can be treated through quantum mechanics by solving the Schrödinger equation.⁹² The non-relativistic and time-independent Schrödinger equation is expressed as $\hat{H}\Psi(\{\mathbf{r}_i\}, \{\mathbf{R}_\alpha\}) = E\Psi(\{\mathbf{r}_i\}, \{\mathbf{R}_\alpha\})$, in which E is the total energy, Ψ is the wave function associated with the system and \hat{H} is the non-relativistic Hamiltonian. For the system composed of N electrons, with coordinates $\{\mathbf{r}_i\} = (\mathbf{r}_1, \mathbf{r}_2, \dots, \mathbf{r}_N)$, and M nuclei, with coordinates $\{\mathbf{R}_\alpha\} = (\mathbf{R}_1, \mathbf{R}_2, \dots, \mathbf{R}_M)$, the \hat{H} operator has the form

$$\hat{H} = \hat{T}_n + \hat{T}_e + \hat{V}_{nn} + \hat{V}_{ne} + \hat{V}_{ee} , \quad (2.1)$$

which includes all known interactions among the particles of the system. \hat{T}_n and \hat{T}_e are the kinetic energy operators, respectively, for the nuclei and electrons; \hat{V}_{nn} , \hat{V}_{ne} and \hat{V}_{ee} are the operators for the potential energy corresponding to the Coulomb interactions, namely, nucleus–nucleus, nucleus–electron and electron–electron, respectively.

The kinetic energy operators are

$$\hat{T}_n = \sum_{\alpha=1}^M -\frac{1}{2M_\alpha} \nabla_{\mathbf{R}_\alpha}^2 , \quad \hat{T}_e = -\frac{1}{2} \sum_{i=1}^N \nabla_{\mathbf{r}_i}^2 , \quad (2.2)$$

in which $\nabla_{\mathbf{r}_i}^2$ and $\nabla_{\mathbf{R}_\alpha}^2$ are Laplacian operators with respect to the coordinates of the electron i at the position \mathbf{r}_i and of the nucleus α at the position \mathbf{R}_α . The terms for the

Coulomb potential interactions are

$$\hat{V}_{nn} = \frac{1}{2} \sum_{\alpha=1}^M \sum_{\substack{\beta=1 \\ (\beta \neq \alpha)}}^M \frac{Z_{\alpha} Z_{\beta}}{|\mathbf{R}_{\alpha} - \mathbf{R}_{\beta}|}, \quad \hat{V}_{ee} = \frac{1}{2} \sum_{i=1}^N \sum_{\substack{j=1 \\ (j \neq i)}}^N \frac{1}{|\mathbf{r}_i - \mathbf{r}_j|}, \quad \hat{V}_{ne} = - \sum_{\alpha=1}^M \sum_{i=1}^N \frac{Z_{\alpha}}{|\mathbf{R}_{\alpha} - \mathbf{r}_i|}, \quad (2.3)$$

in which Z_{α} and Z_{β} are the atomic numbers (equal to the charges) of the nuclei α and β , respectively, while the denominators compute the distance between the interacting particles.

Despite the definition of \hat{H} , the analytic solution of the Schrödinger equation, which is the determination of wave functions and energy eigenvalues, is only tractable for hydrogenic atoms and simple models, such as one particle confined in a box, which is far from the situation of the many-body problem. Besides the usually large number of particles, the many-body Hamiltonian includes the term \hat{V}_{ne} , which couples electronic and nuclear coordinates, hindering the separation of variables in the Schrödinger equation. Finding a solution for the problem is not a simple task and approximations are required; Born, M. and Oppenheimer, J. R. proposed one of the most successful approaches to enable the treatment of this problem.⁹³

2.2 Born–Oppenheimer Approximation

The Born–Oppenheimer approximation provides an effective way to approach the many-body problem; it is based on the idea that the speed of an electron should be much higher than the speed of a nucleus, which is supported by the natural discrepancy between the masses of these particles. The mass of a single proton is about 1836 times greater than the mass of an electron, which makes the factor $1/M_{\alpha}$ in the nuclear kinetic energy much smaller than $1/m_e = 1$ (atomic units). In this condition, the electrons answer immediately to any change of nuclear motion; in other words, from the electronic reference, the rates at which the nuclei and electrons change positions can be considered in different scales. The approximation, within its validity, implies that the nuclear and electronic states are weakly coupled mathematically, which allows the descriptions for the movements of electrons and nuclei to be isolated in equations that can be treated separately.

In terms of the many-body Hamiltonian, the Born–Oppenheimer approximation consists in neglecting the term \hat{T}_n , with respect to the remaining terms, and considering the term \hat{V}_{nn} constant. Therefore, the wave function $\Psi_k(\{\mathbf{r}_i\}, \{\mathbf{R}_{\alpha}\})$, with k representing all possible solutions of the Schrödinger equation, can be rewritten in a separable form as

$$\Psi_k(\{\mathbf{r}_i\}, \{\mathbf{R}_{\alpha}\}) = \psi_k(\{\mathbf{r}_i\}, \{\mathbf{R}'_{\alpha}\}) \chi(\{\mathbf{R}_{\alpha}\}), \quad (2.4)$$

in which the complete wave function has an electronic part, ψ , and a nuclear part, χ . The line in $\{\mathbf{R}'_{\alpha}\}$ indicates that the functions depend parametrically on the coordinates of the nuclei; this means that a different electronic solution exists for each set of nuclear

positions. This separation of movements results in one Hamiltonian for the energy related to the nuclei, \hat{H}_n , and another for the electrons, \hat{H}_e , each with its respective eigenvalue, E_n and E_e , as parts of the total Hamiltonian, $\hat{H} = \hat{H}_n + \hat{H}_e$. Now, the complete Schrödinger equation, written with \hat{H} and $\Psi_k(\{\mathbf{r}_i\}, \{\mathbf{R}_\alpha\})$, can be separated in the following pair of equations.

$$\hat{H}_e \psi_k(\{\mathbf{r}_i\}, \{\mathbf{R}'_\alpha\}) = E_e \psi_k(\{\mathbf{r}_i\}, \{\mathbf{R}'_\alpha\}) , \quad (2.5a)$$

$$\hat{H}_n \chi(\{\mathbf{R}_\alpha\}) = E_n \chi(\{\mathbf{R}_\alpha\}) . \quad (2.5b)$$

Then, Equation 2.5a can be solved for the electronic movement separately from the equation for the nuclei. The complete electronic equation is

$$[(\hat{T}_e + \hat{V}_{ee}(\{\mathbf{r}_i\}) + \hat{V}_{ne}(\{\mathbf{r}_i\}, \{\mathbf{R}'_\alpha\}))\psi_k(\{\mathbf{r}_i\}, \{\mathbf{R}'_\alpha\}) = E_e(\{\mathbf{R}'_\alpha\})\psi_k(\{\mathbf{r}_i\}, \{\mathbf{R}'_\alpha\}) , \quad (2.6)$$

in which $E_e(\{\mathbf{R}'_\alpha\})$ is the total electronic energy for fixed nuclear positions and the term for the nuclear attraction energy, which is parameterized, is denominated external potential (V_{ext}), because the calculation focuses only on the electrons, while the nuclei are treated as external fixed particles. The nuclear equation is not the focus of the calculations performed in this thesis; however, it can be treated after solving the electronic part by considering the total electronic energy as a background potential, so that the nuclear movement is subjected to an average field created by the electrons. This involves a separated treatment for the nuclear degrees of freedom (rotations, vibrations and translations), which will not be discussed in this text. Finally, the total energy of the system containing N electrons and M fixed nuclei is $E = E_e(\{\mathbf{R}'_\alpha\}) + E_{nn} + T_n \approx E_e(\{\mathbf{R}'_\alpha\}) + E_{nn}$, in which T_n is the kinetic energy of the nuclei and E_{nn} is the energetic term considering the repulsion among nuclei.

As presented here, the Born–Oppenheimer approximation allows a reasonable route to approach the many-body problem; however, it is important to note that the approximation could be invalid if its assumptions were not sensible, for example, in cases with strong vibronic coupling. In such cases, separating the Schrödinger equation would be unreasonable, because the assumptions that led to neglecting \hat{T}_n and considering \hat{V}_{nn} constant could be false. For the systems studied herein and within the adopted formalism that will be discussed ahead, there is no reason to suggest that the approximation could fail.

To treat the many-body problem, within the Born–Oppenheimer approximation, is to solve the aforementioned electronic part to describe the electronic structure of the system. This can be considered in a domain of nuclear coordinates, each with the respective electronic ground state parameterized by the nuclear positions, to obtain the mathematical description known as the potential energy surface, which is often multidimensional and usually requires calculation of several electronic ground states for a satisfactory description.

Calculating the electronic structure for a single atomic configuration is not a simple task, because of the nature of interelectronic interactions and the large number of variables (three spatial coordinates and the spin variable for each electron). Some methods, such as Hartree and Hartree–Fock,^{94,95} search for a multi electronic wave function to solve the Schrödinger equation and determine observable quantities, such as the electronic energy. There are various methods to describe the electronic structure;⁹⁶ the specific formalism employed in this thesis is based on the Kohn–Sham approach to Density Functional Theory (DFT), which has been successful in electronic structure theory because of its affordable computational cost, high versatility and accuracy, if used appropriately.⁹⁷ The fundamentals pertaining DFT and the Kohn–Sham formalism are discussed in the following sections.

2.3 Density Functional Theory

The electron density, $\rho(\mathbf{r})$, is the central quantity used in DFT to describe the many-body system. Unlike the wave function, the electron density can be expressed using only 3 spatial coordinates plus the spin coordinate, regardless of the number of electrons; furthermore, it can be measured experimentally (X-ray crystallography) and, thus, can be assigned an operator. The electron density can be defined from the probability density ($|\Psi|^2$ for a system of one electron). Naturally, the electron density is constrained by the total number of electrons, N , through $\int \rho(\mathbf{r})d\mathbf{r} = N$, has units of charge per volume and it is expected to vanish at infinity, $\rho(\mathbf{r} \rightarrow \infty) = 0$. Moreover, the electron density presents cusps at the positions of the nuclei, which avoid singularities due to the characteristics of the Hamiltonian⁹⁸ and is a preliminary indication that it should be possible to obtain the nuclear positions and, thus, the Hamiltonian from the electron density.

Historically, the use of $\rho(\mathbf{r})$ to calculate the electronic energy initiated with the Thomas–Fermi model,^{99,100} in which the kinetic energy is approximated as a functional of $\rho(\mathbf{r})$ using the model of a non-interacting uniform electron gas (a fictitious system known as jellium). The term functional means that the quantity, such as energy, is mapped using a function, $\rho(\mathbf{r})$. The Thomas–Fermi formalism was a noteworthy endeavor in the history of DFT, but it did not consider exchange and correlation terms; the former is connected to the antisymmetric nature necessary for an eigenfunction that captures the fermionic nature of the electrons, while the latter computes the effects of interelectronic interactions in the electronic movement. The lack of such terms led to severe failings in the description of non homogeneous electron densities, which is the case of most realistic systems, such as atoms and molecules. Moreover, no variational principle had been established within the formalism and, without a complete and reliable description of the electronic energy, the model found little popularity in chemistry.

A complete and rigorous description of the total electronic energy in terms of

$\rho(\mathbf{r})$ was engendered by the Hohenberg–Kohn (HK) theorems.¹⁰¹ These developments established DFT as a trustworthy quantum mechanical formulation to determine the electronic structure and paved the way for research that is pursued to this date; the theorems will be explained ahead.

2.3.1 Hohenberg–Kohn Existence Theorem

The first theorem connects the electron density with the attraction of electrons to the nuclei, namely, the external potential, V_{ext} .

Theorem I. *The external potential is determined uniquely, apart from a trivial additive constant, by the non degenerate ground-state electron density $\rho(\mathbf{r})$.*

The corollary is that, for a known N and V_{ext} , the complete electronic Hamiltonian can be written to define a Schrödinger equation; theoretically, this allows one to obtain the exact wave function, a mathematical representation that describes the system completely and exactly. The HK Theorem I is sometimes called HK existence theorem because it determines the existence of a map between the non degenerate ground-state $\rho(\mathbf{r})$ and the exact wave function, $\Psi[\rho(\mathbf{r})]$; this established the search for $\rho(\mathbf{r})$ as a valid method to calculate observable properties.

Notice that the Hamiltonian determines the wave functions for all excited states through the Schrödinger equation, not only the ground state. Then, it should be possible to study excited states through DFT, although this is still a topic of ongoing research. In this thesis, we focused on the ground-state electron density and did not explore excited states. Despite the certainty in the description of the ground-state electronic energy and mapping the density to the exact wave function, guaranteed by the HK existence theorem, up to this moment there was no mention of a method to search for the best $\rho(\mathbf{r})$. This is elaborated through the second theorem.

2.3.2 Hohenberg–Kohn Variational Theorem

To apply DFT, it is desirable to use $\rho(\mathbf{r})$ to obtain the total electronic energy of the system. The second HK theorem provides the means to do so.

Theorem II. *The ground-state energy can be calculated through a variational principle using the electron density.*

Considering the HK existence theorem, the total electronic energy can be expressed as a functional of the electron density through

$$\begin{aligned} E_{el}[\rho(\mathbf{r})] &= T_e[\rho(\mathbf{r})] + E_{ext}[\rho(\mathbf{r})] + E_{ee}[\rho(\mathbf{r})] \\ &= \int \rho(\mathbf{r})V_{ext}(\mathbf{r})d\mathbf{r} + F_{HK} , \end{aligned} \tag{2.7}$$

in which $T_e[\rho(\mathbf{r})]$ is the kinetic energy of the electrons, $E_{ext}[\rho(\mathbf{r})]$ is the interaction energy of the electrons with the nuclei defined through the external potential, $E_{ee}[\rho(\mathbf{r})]$ is the interelectronic interaction energy. Moreover, $F_{HK}[\rho(\mathbf{r})] = T_e[\rho(\mathbf{r})] + E_{ee}[\rho(\mathbf{r})]$ is emphasized as a universal HK functional that does not depend on the external potential and has the same form for any N and V_{ext} .

Consider a candidate electron density, ρ_c , that appropriately integrates to the total number of electrons, and the guarantee from the first HK theorem that there is only a single ρ_c for a given V_{ext} and, hence, a single associated candidate wave function Ψ_c . Then, the variational HK theorem guarantees that the expectation value for the total electronic energy is always greater than the energy of the ground state, E_0 , for any expression of ρ_c that is not the exact ground-state electron density ρ_0 .

$$\begin{aligned} \langle \Psi_c | \hat{H} | \Psi_c \rangle &= \int \rho_c(\mathbf{r}) V_{ext}(\mathbf{r}) d\mathbf{r} + F_{HK}[\rho_c(\mathbf{r})] \\ &= E[\rho_c(\mathbf{r})] \geq E[\rho_0(\mathbf{r})] = E_0, \end{aligned} \tag{2.8}$$

hence, theoretically the variational principle can be employed by updating ρ_c and minimizing the corresponding energy to search for the one and only ρ that describes the system exactly, with $\rho_c = \rho_0 \rightarrow E_c = E_0$. In practice, various forms of the ρ_c functions could be tested and the one providing the lowest energy would be the best option from the set. However, the practical application of DFT stayed out of reach for years, because there was no idea on how to find the best possible ρ_c rationally. Moreover, the formalism needed to overcome two major deterrents. First, the mathematical form of F_{HK} was not explicitly known, especially the kinetic energy term, which would severely impair accuracy if based on the pioneer Thomas–Fermi model. Moreover, Ψ and ρ were naturally mingled in the theory, but the application of DFT should focus entirely on the electron density and not touch the wave function, since there were other well established procedures based on the wave function. The development of methods entirely based on ρ is still a topic of active research. This thesis was based on one of the most successful approaches that solved the aforementioned problems and is known today as Kohn–Sham Density Functional Theory.

2.3.3 Kohn–Sham Formalism

Considering the major problem of the unknown form of the electronic Hamiltonian, the Kohn–Sham (KS) method was proposed, in 1965, considering the use of a fictitious auxiliary system of non-interacting electrons that is represented by the same ground-state electron density as the real interacting system.¹⁰² Then, the complicated interacting system is replaced by the simpler auxiliary system and, deftly, the problem becomes solving the many-body Hamiltonian for independent particles, but with an interacting density. Importantly, and based on the first HK theorem, the densities of the real and of the non-interacting system are necessarily the same. This idea was invaluable to advance DFT,

because the total electronic energy of the non-interacting system is simply the summation of eigenvalues for each electron. Hence, the method allows the energy terms, including the kinetic energy, to be calculated through the use of a non-interacting system. To elaborate, consider the total electronic energy as

$$E_{el}[\rho(\mathbf{r})] = T_{ni}[\rho(\mathbf{r})] + E_{ext}[\rho(\mathbf{r})] + E_H[\rho(\mathbf{r})] + E_{xc}[\rho(\mathbf{r})] , \quad (2.9)$$

in which $T_{ni}[\rho(\mathbf{r})]$ is the kinetic energy of the auxiliary non-interacting electronic system, $E_{ext}[\rho(\mathbf{r})]$ is the functional for the Coulomb electron–nuclei interactions, $E_H[\rho(\mathbf{r})]$ is the functional for the Coulomb electron–electron interactions, known as Hartree interactions, and $E_{xc}[\rho(\mathbf{r})]$ is the exchange–correlation energy functional. As emphasized, all terms are functionals of the same electron density, ρ . The KS method treats the electronic problem introducing monoelectronic orthonormal functions, $\phi_i(\mathbf{r}_i)$, denominated Kohn–Sham orbitals. The electron density is related to the KS orbitals by

$$\rho(\mathbf{r}) = \sum_i^N |\phi_i(\mathbf{r})|^2 , \quad (2.10)$$

considering ϕ_i as the occupied orbitals defined by Fermi–Dirac statistics and the condition $N = \int \rho(\mathbf{r}) d\mathbf{r}$. Using the KS orbitals, Equation 2.9 can be rewritten as

$$\begin{aligned} E_{el}[\rho(\mathbf{r})] = & \sum_i^N \left(\langle \phi_i(\mathbf{r}_i) | -\frac{1}{2} \nabla_{\mathbf{r}_i}^2 | \phi_i(\mathbf{r}_i) \rangle - \langle \phi_i(\mathbf{r}_i) | \sum_{\alpha}^M \frac{Z_{\alpha}}{|\mathbf{r}_i - \mathbf{R}_{\alpha}|} | \phi_i(\mathbf{r}_i) \rangle \right) \\ & + \sum_i^N \langle \phi_i(\mathbf{r}_i) | \frac{1}{2} \int \frac{\rho(\mathbf{r}')}{|\mathbf{r}_i - \mathbf{r}'|} d\mathbf{r}' | \phi_i(\mathbf{r}_i) \rangle + E_{xc}[\rho(\mathbf{r})] , \end{aligned} \quad (2.11)$$

in which the first and second terms correspond, respectively, to the kinetic energy of the non-interacting electrons, T_{ni} , and the electron–nuclei attraction energy, E_{ext} . The third term, E_H , corresponds to the classical electron–electron repulsion, which includes the non-realistic and classical self-interaction effect (in the Hartree–Fock method, this effect cancels with part of the exchange term, but in DFT it is corrected as will be mentioned next). Finally, the last term, E_{xc} represents the exchange and correlation energy contributions, which consider the fermionic nature of the electrons, through the exchange part, and the dependence of the movement of one electron on its interaction with the remaining electrons, through the correlation part. The KS formalism shifts all unknown quantities that should be computed for an exact solution into the exchange–correlation term, namely, a correction for the use of a classical expression for the interelectronic interaction, including the classical self-interaction, and a correction for the difference that exists between the kinetic energy of the non-interacting system and the real system. Then, if it could be defined exactly, E_{xc} could complete the description of the electronic structure for an exact solution.

At this point, considering the expression for the total electronic energy defined in Equation 2.9, one can follow the idea of the second HK theorem and minimize the energy

functional through the variational method. This is done using the Lagrange multipliers strategy, minimizing the derivative of a function with respect to the KS orbitals and considering orthonormality for ϕ_i and the constraint that the integration of the electron density yields N . Then, the following critical result is obtained:

$$\left[-\frac{1}{2}\nabla_{\mathbf{r}}^2 + V_{ef}(\mathbf{r}) \right] \phi_i(\mathbf{r}_i) = \varepsilon_i \phi_i(\mathbf{r}_i) , \quad (2.12)$$

in which $V_{ef}(\mathbf{r})$ is the effective potential, which includes the external potential, dependent on parameterized nuclear positions, Hartree potential and the exchange-correlation potential as shown below.

$$V_{ef}(\mathbf{r}) = V_{ext}(\mathbf{r}) + V_H(\mathbf{r}) + V_{xc}(\mathbf{r}) , \quad V_{xc} = \frac{\delta E_{xc}[\rho(\mathbf{r})]}{\delta \rho(\mathbf{r})} . \quad (2.13)$$

Equation 2.12 is known as the Kohn–Sham equation; it depends solely on $\rho(\mathbf{r})$ that, in turn, depends on the KS orbitals that one wishes to determine. For this reason, solving the equation requires an iterative process denominated self-consistent field. For this, a candidate density, $\rho^1(\mathbf{r})$, which obeys $\int \rho(\mathbf{r}) d\mathbf{r} = N$, is suggested using a basis set of functions and the effective potential, V_{ef}^1 , is defined to obtain the KS equation. Then, the equation is solved through an electronic minimization algorithm, normally involving iterative matrix-diagonalization algorithms, to obtain a new density $\rho^2(\mathbf{r})$. In this point, $\rho^1(\mathbf{r})$ and $\rho^2(\mathbf{r})$ are compared, generally based on the corresponding total electronic energies for each density. Then, if this comparison shows that the new density is not sufficiently similar to the tentative density, the densities are combined and the cycle repeats using this new combined density until the input and output densities are comparable within a desired convergence criterion. There are several ways to combine the densities for continuation of the cycle and the process is known as electron density mixing. The converged $\rho(\mathbf{r})$ is known as a self-consistent or fixed-point solution. The more rigorous the convergence criterion, the higher the accuracy of the calculation and the difficulty to reach self-consistency; the effectiveness of the process greatly depends on the quality of its initialization, algorithms chosen to solve the KS equation and to mix the electron densities.

After obtaining the best electron density possible, the total electronic energy can be calculated as

$$E_{el}[\rho(\mathbf{r})] = \sum_{i=1}^N \varepsilon_i - \int \rho(\mathbf{r}) V_{ext}(\mathbf{r}) d\mathbf{r} - \frac{1}{2} \int \int d\mathbf{r} d\mathbf{r}' \frac{\rho(\mathbf{r})\rho(\mathbf{r}')}{|\mathbf{r} - \mathbf{r}'|} + E_{xc}[\rho(\mathbf{r})] , \quad (2.14)$$

where the energy eigenvalues are summed for occupied states; if required, the total energy can be obtained by summing E_{el} with the repulsive energy among the nuclei.

To employ the KS method within a spin-polarized approach, the electron density is defined with its spin components for occupied states as

$$\rho_{\sigma}(\mathbf{r}) = \{\rho^{\uparrow}(\mathbf{r}), \rho^{\downarrow}(\mathbf{r})\} = \sum_{\sigma=\uparrow,\downarrow} \sum_{i,occ}^N |\phi_{\sigma i}(\mathbf{r})|^2 , \quad (2.15)$$

in which σ indicates the spin channel and the curly brackets indicate the set considering two spin components, \uparrow and \downarrow (sometimes alternatively noted as *up* and *down*, α and β or $+$ and $-$), used to express the electron density. Each KS orbital, $\phi_{\sigma i}(\mathbf{r}_i)$, can be multiplied by a factor modulating the spin components. The set of single-electron KS equations can be written in the form

$$\left[-\frac{1}{2}\nabla_{\mathbf{r}_i}^2 + V_{ef}^\sigma[\rho^\uparrow(\mathbf{r}), \rho^\downarrow(\mathbf{r})] \right] \phi_{\sigma i} = \varepsilon_{\sigma, i} \phi_{\sigma i} , \quad (2.16)$$

in which the particles are counted for each spin component. The spin-polarized form of the KS equation shows that the use of the spin-polarized electron density results in energy eigenvalues dependent on spin polarization; thus, the effective potential becomes

$$V_{ef}^\sigma[\rho^\uparrow(\mathbf{r}), \rho^\downarrow(\mathbf{r})] = V_{ext}^\sigma[\rho^\uparrow(\mathbf{r}), \rho^\downarrow(\mathbf{r})] + \int \frac{\rho(\mathbf{r}')}{|\mathbf{r} - \mathbf{r}'|} d\mathbf{r}' + V_{xc}^\sigma[\rho^\uparrow(\mathbf{r}), \rho^\downarrow(\mathbf{r})] , \quad (2.17)$$

with

$$V_{xc}^\sigma[\rho^\uparrow(\mathbf{r}), \rho^\downarrow(\mathbf{r})] = \frac{\delta E_{xc}[\rho^\uparrow(\mathbf{r}), \rho^\downarrow(\mathbf{r})]}{\delta \rho_\sigma(\mathbf{r})} , \quad (2.18)$$

hence, the expressions can have different values for each spin component. The formalism tends to the non spin-polarized case when $\rho^\uparrow(\mathbf{r}) = \rho^\downarrow(\mathbf{r})$. Due to the use of two channels to consider the spin coordinate, the spin-polarized approach substantially increases the computational cost, compared to the use of a non spin-polarized $\rho(\mathbf{r})$, however, spin polarization is mandatory for a realistic description of several materials (tests and more details are available in Appendix B). From this point, the notation ρ_σ will be used to indicate the dependence on both spin channels.

The KS method, besides presenting a great way to calculate the electronic energy, is a prescription on how to search for the best electron density. However, it is still not possible to solve the electronic structure exactly. Unfortunately, the exact mathematical expression of the exchange-correlation functional is undetermined and, therefore, approximations are needed. They will be discussed in the following part.

2.3.4 Exchange-Correlation Functionals

In the previous sections, we discussed that the DFT determination of the total electronic energy involves adopting an approximation for the exchange-correlation functional, hence, the accuracy of DFT can be improved by finding a more suitable approximation for the target system. The exchange-correlation functional, $E_{xc}[\rho_\sigma(\mathbf{r})]$, can be written as

$$E_{xc}[\rho_\sigma(\mathbf{r})] = \int \rho_\sigma(\mathbf{r}) \varepsilon_{xc}[\rho_\sigma(\mathbf{r})] d\mathbf{r} , \quad (2.19)$$

in which $\varepsilon_{xc}[\rho_\sigma(\mathbf{r})]$ is the exchange-correlation energy per particle. This equation can be separated in two parts as

$$E_{xc}[\rho_\sigma(\mathbf{r})] = E_x[\rho_\sigma(\mathbf{r})] + E_c[\rho_\sigma(\mathbf{r})] = \int \rho_\sigma(\mathbf{r}) \varepsilon_x([\rho_\sigma(\mathbf{r}), \mathbf{r}]) d\mathbf{r} + \int \rho_\sigma(\mathbf{r}) \varepsilon_c([\rho_\sigma(\mathbf{r}), \mathbf{r}]) d\mathbf{r} , \quad (2.20)$$

in which $E_x[\rho_\sigma(\mathbf{r})]$ is the exchange energy functional and $E_c[\rho_\sigma(\mathbf{r})]$ is the correlation energy functional that express the respective energies from the quantities ε_x and ε_c , which are the exchange and correlation energies per particle, respectively. As noted previously, the complete exact form of $E_{xc}[\rho_\sigma(\mathbf{r})]$ is unknown, hence, several approximations have been suggested.

The exchange energy is related to the fermionic nature of the electrons and exists because of the mathematical requirement of antisymmetric wave functions, with respect to swapping spatial and spin coordinates, to describe fermions, due to the Pauli exclusion principle. The exchange energy of the uniform electron gas, ε_x^{unif} , can be expressed exactly through the Slater formulation¹⁰³ as

$$\varepsilon_x^{unif}[\rho_\sigma(\mathbf{r})] = -\frac{3}{4} \left(\frac{3\rho_\sigma(\mathbf{r})}{\pi} \right)^{\frac{1}{3}}, \quad (2.21)$$

for a spherically symmetric electron density centered in one referential electron. This density is constant from the center to the Wigner–Seitz radius, $r_s = \left(\frac{3}{4\pi\rho_\sigma(\mathbf{r})} \right)^{\frac{1}{3}}$, and is null outside the sphere.

On the other hand, the analytical determination of the correlation energy per particle is still not available, even for the simple case of the uniform electron gas. Estimates for specific cases have been proposed, such as for the limits of infinite density.¹⁰⁴ More broadly, using quantum Monte Carlo methods, the E_{xc} of various uniform electron gases of different densities were computed with high numerical accuracy and, by subtracting the E_x term for each gas, it was possible to estimate E_c .¹⁰⁵

One of the first methods to approximate the exchange–correlation functional was provided by Kohn and Sham themselves¹⁰² dividing the real system in infinitesimal parts so that, locally, the electron density is considered uniform in each part, and can be approximated by a homogeneous electron gas, a type of approach denominated local density approximation (LDA). Functionals of this type were the first choice to apply DFT during some years, because they provided good accuracy, since the errors of the exchange and correlation terms can cancel each other and these early approximations can provide good accuracy for some systems.¹⁰⁶ However, the binding energies are generally overestimated and the surface energies of metallic surfaces are generally underestimated; more serious errors can occur, such as the wrongful prediction of instability for certain anions.¹⁰⁷

The electron density of realistic molecular systems is not normally uniform in space, which justifies the limitations of the LDA. In time, this type of approximation lost the spotlight to other approximations. One of the most successful proposals to improve the exchange–correlation functionals regarded the manner by which ρ changes locally by means of its gradient, $\nabla\rho$, which tends to improve the description of inhomogeneous electron densities.¹⁰⁸

The generalized gradient approximation (GGA) functionals are known as semi-local, due to the consideration of both ρ and $\nabla\rho$ by

$$E_{xc}^{\text{GGA}}[\rho_\sigma(\mathbf{r})] = \int f(\rho_\sigma(\mathbf{r}), |\nabla\rho_\sigma(\mathbf{r})|) d\mathbf{r} , \quad (2.22)$$

and the exchange-correlation potential is

$$V_{xc}^{\sigma,\text{GGA}}(\mathbf{r}) = \frac{\partial E_{xc}^{\text{GGA}}}{\partial \rho_\sigma(\mathbf{r})} = \frac{\partial f}{\partial \rho_\sigma(\mathbf{r})} - \nabla \cdot \left(\frac{\partial f}{\partial \nabla \rho_\sigma(\mathbf{r})} \right) , \quad (2.23)$$

in which $f = f(\rho, |\nabla\rho|)$ is defined differently for each formulation. Several functionals have been proposed throughout the years, some with excellent performance for specific systems, others with broader appeal.¹⁰⁹ For this thesis, the PBE functional was selected, thus named because of its developers: Perdew, J. P., Burke, K. and Ernzerhof, M.¹⁰⁸ This functional provides good accuracy for several systems, which justifies its use for a study of diverse materials; PBE was developed from PW91, a GGA functional proposed previously by Perdew, J. P. and Wang, Y.¹¹⁰ PBE is less dependent on fitting parameters, which can cause oscillations of the potential for extremities of the dimensionless density gradient, and, although it is a simplification of PW91, PBE does not lose in terms of computational efficiency.¹⁰⁸

For the PBE functional, the exchange part is

$$E_x^{\text{PBE}}[\rho_\sigma(\mathbf{r})] = \int \rho_\sigma(\mathbf{r}) \varepsilon_x^{\text{unif}}[\rho_\sigma(\mathbf{r})] F_x^{\text{PBE}}(s) d\mathbf{r} , \quad (2.24)$$

with the function $F_x^{\text{PBE}}(s)$ given by

$$F_x^{\text{PBE}}(s) = 1 + \kappa - \frac{\kappa}{1 + \frac{\mu s^2}{\kappa}} , \quad s(\mathbf{r}) = \frac{|\nabla\rho_\sigma(\mathbf{r})|}{2k_F\rho_\sigma(\mathbf{r})} , \quad \mu = \frac{\beta\pi^2}{3} , \quad (2.25)$$

in which, $\beta = 0.066725$ and $\kappa = 0.804$; the function $s(\mathbf{r})$ relates the electron density gradient with the radius of the Fermi sphere, which is the Fermi wavevector, $k_F = [3\pi^2\rho(\mathbf{r})]^{1/3}$. Thus, if $\nabla\rho \rightarrow 0$, the function $F_x^{\text{PBE}} \rightarrow (1 + \kappa - \kappa) = 1$ and the PBE exchange energy tends to the LDA formulation.

The correlation part of the PBE functional has the form

$$E_c^{\text{PBE}}[\rho_\sigma(\mathbf{r})] = \int \rho_\sigma(\mathbf{r}) (\varepsilon_c^{\text{unif}}[\rho_\sigma(\mathbf{r})] + H_c^{\text{PBE}}(r_s, \xi, t)) d\mathbf{r} , \quad (2.26)$$

in which the function H_c employs the conventional normalized spin polarization, $\xi(\mathbf{r}) = \frac{\rho^\uparrow(\mathbf{r}) - \rho^\downarrow(\mathbf{r})}{\rho_\sigma(\mathbf{r})}$. For the PBE functional, the function $H_c^{\text{PBE}}(r_s, \xi, t)$ was defined for limiting cases: for high densities, $t \rightarrow 0$ and $H_c \rightarrow \beta\phi^3 t^2$; for low densities, $t \rightarrow \infty$, the correlation contribution tends to zero and $H \rightarrow -\varepsilon_c^{\text{unif}}$. In normal conditions, up to the limiting cases, $H \rightarrow \gamma\phi^3 \ln t^2$. The function H_c has the general form

$$H_c^{\text{PBE}}(r_s, \xi, t) = \gamma \ln \left[1 + \frac{\beta}{\gamma} t^2 \left(\frac{1 + At^2}{1 + At^2 + A^2 t^4} \right) \right] , \quad (2.27)$$

with

$$\gamma = \frac{1 - \ln 2}{\pi^2}, \quad A = \frac{\beta}{\gamma} [\exp(-\varepsilon_c^{unif} / \gamma \phi^3) - 1]^{-1}, \quad t(\mathbf{r}) = \frac{|\nabla \rho(\mathbf{r})|}{2\phi k_s \rho(\mathbf{r})}, \quad k_s = \sqrt{4k_F/\pi}, \quad (2.28)$$

in which $t(\mathbf{r})$ is a dimensionless representation for the electron density gradient and k_s is the Thomas–Fermi screening wavenumber. Here, spin is considered through a spin-scaling factor, ϕ , which is related to the normalized spin polarization, ξ , by $\phi = [(1+\xi)^{2/3} + (1-\xi)^{2/3}]/2$. To disregard spin polarization, $\rho^\uparrow = \rho^\downarrow$ and $\phi = 1$. Notably, the PBE functional recovers the LDA form in the case of $t = 0$ or $|\nabla \rho| = 0$.

The same authors that proposed the PBE functional performed calculations¹⁰⁸ for reference systems and showed that PBE estimates the atomization energies of various molecules with greater accuracy than LDA and similarly to PW91, but with the advantage of being easier to understand and apply. However, there are other options of functionals with different characteristics besides GGA or LDA. It is possible to mix the aforementioned functionals with part of the exact exchange functional from the Hartree–Fock method, resulting in formulations known as hybrid functionals that can present excellent accuracy for some systems.¹¹¹ The options discussed herein can be, written in order of increasing accuracy as LDA < GGA < hybrid (roughly, since exceptions are possible within chemical accuracy); unfortunately, the computational cost usually increases in the same order and one needs to consider a reasonable balance for each study.¹¹² For this thesis, PBE provides sufficient accuracy, at a feasible computational cost, to study physical chemical trends for the systems investigated,^{35,39,58,113,114} which is referred to as chemical accuracy.

The formalism discussed thus far has been extremely valuable in physical chemistry. To further improve the description of some systems, several types of corrections have been developed for DFT, for example, to consider relativistic effects (spin-orbit coupling), the strong Coulomb interaction of localized d - of f -states (DFT+U) and dispersion interactions. There are several ways to correct such effects, for example, they can be included in the construction of the exchange-correlation functional or considered after the DFT calculation. For the present study, the most important factor that needs to be considered is the contribution of long range interactions for the total electronic energy; the effects and implementation chosen are discussed ahead.

2.3.5 Dispersion (van der Waals) Corrections

For the DFT community, van der Waals interactions mostly refer to the London dispersion effects that are omnipresent, since they emerge from electronic correlation, which does not require the presence of a permanent dipole, in contrast to dipole–induced dipole and dipole–dipole interactions. The dispersion effects were first described to explain the attraction between noble gas atoms,^{115,116} it is a non-bonded long range interaction

that occurs due to spontaneous fluctuations of the electron density. In this thesis, the terms van der Waals (vdW) interactions refer to this dispersion effect.

The vdW interactions can be described by a first-order term, which has an attractive nature and an inverse dependence on R^6 (R representing the distance between two interacting parts), factored by a C_6 coefficient; this description can be expanded to additional orders (R_n, C_n). Such interactions are weaker than chemical bonds, but are crucial for the behavior and functionality of several physical and chemical systems, including molecules adsorbed on TM substrates,^{39,117–119} the target system of this thesis. Although dispersion effects are normally attractive, the intermolecular interactions can have a repulsive nature, depending on the distances between interacting dipoles, as well as their charges and orientation. Although the two aforementioned intermolecular interactions (dipole–dipole, dipole–induced dipole) can be described effectively through the Coulomb part of the DFT functionals, the dispersion effects have a quantum mechanical origin, since the electron density fluctuations are due to the electronic correlation; this is not promptly described by most exchange–correlation functionals at affordable computational costs.¹²⁰ The LDA and GGA approximations consider the electron density, as well as its gradient in the case of GGA, locally and normally fail to describe the asymptotic behavior of the long range vdW term and its R^6 dependence.

For this thesis, the method chosen to describe vdW interactions in DFT was the addition of a dispersion term, E_{disp} , to the total electronic energy according to

$$E_{\text{DFT+D}} = E_{\text{DFT}} + E_{disp} , \quad (2.29)$$

in which $E_{\text{DFT+D}}$ is the corrected total electronic energy, E_{DFT} is the self-consistent total electronic energy calculated from the exchange–correlation functional adopted and E_{disp} is the dispersion correction, which can be simply denominated D.

The first attempts to consider dispersion in DFT were based on fitting parameters from empirical data; among them are the methods developed by Grimme, S., DFT+D¹²¹ and DFT+D2,¹²² which consider pairwise interactions between two atoms A and B. The correction has the form

$$E_{disp} = -s_6 \sum_{A=1}^{N_{at}-1} \sum_{B=i+1}^{N_{at}} \frac{C_6^{AB}}{R_6^{AB}} f_{dmp}(R_{AB}) , \quad (2.30)$$

in which N_{at} is the number of atoms in the system, R_{AB} is the interatomic distance, s_6 is a global scaling factor that changes according to the exchange–correlation functional employed, C_6^{AB} is a dispersion coefficient for the atomic pair AB , which is adjusted according to the version of the correction, for example, in the DFT+D2 method it has the form $C_6^{AB} = (C_6^A C_6^B)^{1/2}$, which yields accurate results; $f_{dmp}(R_{AB})$ is a damping function that can be used to control the reach of the correction to avoid problems that occur for the limit of small R_{AB} , obtain negligible dispersion for atoms at typical distances in which

bonding is expected to be dominant, or to avoid double-counting of dispersion effects, due to the overlap of the correction with the standard description of the exchange-correlation functional. The dispersion corrections can employ different damping functions, such as

$$f_{dmp}(R_{AB}) = \frac{1}{1 + \exp\left[-d\left(\frac{R_{AB}}{R_r} - 1\right)\right]}, \quad (2.31)$$

in which d is scaling factor and R_r is the sum of atomic vdW radii that effectively control the reach of the damping function. This form shows that the f_{dmp} decreases as does the interatomic distance, with respect to the vdW radii, which can help to describe the repulsion that occurs for small interatomic distances.

Through the DFT+D method, it was possible to accurately describe the structure and binding energy of a great variety of weakly bound molecular complexes.¹²¹ Compared to DFT+D, the DFT+D2 method was an improvement, especially due to the improved treatment of the double-counting situation and better adjustment of the parameters to estimate long-reach interactions.¹²² For this thesis, a third option named DFT+D3¹²³ was chosen, because it features the aforementioned improvements, is less dependent experimental data, includes a three-body term and provides similar results compared to other more costly corrections.¹²⁴ The D3 correction is a sum of two- and three-body terms, $E_{disp} = E^{(2)} + E^{(3)}$. The two-body term is the most important and has the form

$$E^{(2)} = \sum_{AB} \sum_{n=6,8,10,\dots} s_n \frac{C_n^{AB}}{r_{AB}^n} f_{d,n}(r_{AB}), \quad (2.32)$$

in which the first summation considers all possible AB atomic pairs and C_n^{AB} are dispersion coefficients of order n for each AB that are based on *ab initio* calculations of reference molecular systems, which is one distinction of the D3 correction compared to other implementations. The quantity r_{AB}^n is the distance between the nuclei A and B , $f_{d,n}$ is the damping function and s_n are global scaling factors adjusted for $n > 6$ that depend on the exchange-correlation functional. The developers recommend truncating $E^{(2)}$ at $n = 8$, due to instabilities observed for greater values.¹²³ The three-body term is

$$E^{(3)} = \sum_{ABC} f_{d,(3)}(\bar{r}_{ABC}) E^{ABC}, \quad (2.33)$$

in which \bar{r}_{ABC} is the average of the AB , BC and CA distances, $f_{d,(3)}$ is a damping function for the three-body term and E^{ABC} is a non-additive term for the dispersion written as

$$E^{ABC} = \frac{C_9^{ABC} [3\cos(\theta_a)\cos(\theta_b)\cos(\theta_c) + 1]}{(r_{AB}r_{BC}r_{CA})^3}, \quad (2.34)$$

in which θ_a , θ_b and θ_c are the angles of the triangle defined by A , B and C , C_9^{ABC} is a triple-dipole constant that is defined by the pairwise C_6 coefficients as $C_9^{ABC} = -\sqrt{C_6^{AB}C_6^{AC}C_6^{BC}}$ and the denominator contains the distances between the atoms, r_{AB} , r_{BC} and r_{CA} . For computational reasons, the three-body term is switched off by default, because it is not

essential for the pairwise correction and could add a negligible contribution to the energy for some systems.¹²³

As commented before, in the D3 method, the C_6 dispersion coefficients are not obtained from empirically derived interpolation, but they are computed *ab initio* by time-dependent DFT. For this, the Casimir–Polder formula¹²⁵ is employed,

$$C_6^{AB} = \frac{3}{\pi} \int_0^\infty \alpha^A(i\omega) \alpha^B(i\omega) d\omega, \quad (2.35)$$

in which $\alpha(i\omega)$ is the averaged dipole polarizability at imaginary frequency ω . From C_6^{AB} , the higher order C_n^{AB} can be calculated recursively. Further details are available in the original publication of the D3 correction.¹²³ Here, we employed a damping function of the D3 method in the form

$$f_{d,n}(r_{AB}) = \frac{1}{1 + 6 [R_{AB}/(s_{r,n} R_0^{AB})]^{-\alpha_n}}, \quad (2.36)$$

in which $s_{r,n}$ is a scaling factor dependent on the order ($n = 6, 8, 10, \dots$) for the pairwise cutoff radius R_0^{AB} ; α_n is a steepness parameter adjusted for each order, n .¹²³

The D3 correction has several advantages: it is simply additive and, hence, can be used with any exchange-correlation functional, it does not increase the computational cost drastically, uses dispersion coefficients obtained from accurate *ab initio* calculations, it does not require any information about atom connectivity and it can be applied to several elements of the periodic table and structures, such as molecules and solids. The main caveat is that it does not consider the electronic information in any way and, hence, it does not affect the electronic structure directly.¹²³

Up to this point, the methodology to accurately compute the total electronic energy has been discussed. However, there is still the subject of basis function to discuss, because of the requirement to express the KS orbitals within a basis set of functions, $\{\phi\}$; the adopted approach is discussed ahead.

2.4 Periodic Boundary Conditions and the Plane Wave Basis Set

Solving the KS equation requires basis functions to express the KS orbitals. There is a great variety of possible functions, such as Gaussian- or Slater-type orbitals and the choice can be based on the type of system. This study included both finite (molecules, atoms and nanoparticles) and infinite periodic systems (crystals and surfaces), hence, the software VASP (Vienna *Ab initio* Simulation Package), version 5.4.4, was chosen, which uses plane waves as the basis set in a very efficient framework for periodic phases that can be easily adapted to study the finite systems.

The fundamental long-range periodic system is a crystal, which is defined as the combination of a periodic lattice and a base, which are repeating units (in this case,

atomic positions). The lattice defines a coordinate system through the lattice translation vectors, $\mathbf{a}_1, \mathbf{a}_2, \mathbf{a}_3$ and the crystal is invariant upon application of a translation vector $\mathbf{T} = n_1\mathbf{a}_1 + n_2\mathbf{a}_2 + n_3\mathbf{a}_3$, for integer n_i . The lattice vectors define a volume through their triple product and, using this model and symmetry, allow modeling an infinite system using a small primitive cell containing only a few atoms in the space defined by the translation vectors. To simulate surfaces or finite systems, the atoms can be separated by a vacuum region appropriately defined and subjected to the same periodicity rules.

The symmetry of the periodic systems can be used to greatly simplify the DFT calculations; this is based on Bloch's theorem:¹²⁶

Bloch's Theorem. *If the Hamiltonian is invariant with respect to translations, \mathbf{T} , the solution of Schrödinger's equation has the form $\psi_{\mathbf{k}}(\mathbf{r}) = u_{\mathbf{k}}(\mathbf{r})e^{i\mathbf{k}\cdot\mathbf{r}}$, in which \mathbf{k} is the crystal momentum vector and $u_{\mathbf{k}}(\mathbf{r})$ are functions with the same periodicity of the Hamiltonian.*

It is appropriate to describe a periodic system using the reciprocal space, in which the same concepts presented above for the Bravais lattice are applicable for a reciprocal lattice, which completely describes the system for an appropriate range of crystal momentum vectors, \mathbf{k} , confined to the first Brillouin Zone, which is taken as the primitive reciprocal lattice. To relate real and reciprocal spaces, the Fourier transform can be employed with the following set of plane waves

$$u_i(\mathbf{r}) = \frac{1}{\sqrt{\Omega}} \sum_{\mathbf{G}} c_i(\mathbf{G}) e^{i\mathbf{G}\cdot\mathbf{r}}, \quad (2.37)$$

in which Ω is the volume of the cell, \mathbf{G} is the wave vector in reciprocal space and $c_i(\mathbf{G})$ are the expansion coefficients. Because $u_i(\mathbf{r})$ is invariant with \mathbf{T} , the associated physical properties are as well. The \mathbf{G} vector can be written as $\mathbf{G} = m_1\mathbf{b}_1 + m_2\mathbf{b}_2 + m_3\mathbf{b}_3$, for integer m_i . The real and reciprocal vectors, \mathbf{a}_i and \mathbf{b}_i , respectively, are related through

$$\mathbf{b}_1 = 2\pi \frac{\mathbf{a}_2 \times \mathbf{a}_3}{|\mathbf{a}_1 \cdot (\mathbf{a}_2 \times \mathbf{a}_3)|} = 2\pi \frac{\mathbf{a}_2 \times \mathbf{a}_3}{\Omega}, \quad (2.38)$$

and all cyclical permutations, with Ω the volume defined by the lattice translation vectors.

A set containing an infinite number of plane waves would be the best set to expand the KS orbitals; however, in practice the set is truncated at a user-defined cutoff kinetic energy, $\frac{1}{2}|\mathbf{k} + \mathbf{G}|^2 \leq E_c$. Thus, the KS orbitals are expanded as

$$\phi_i^{\text{KS}}(\mathbf{r}, \mathbf{k}) = \frac{1}{\sqrt{\Omega}} \sum_{\mathbf{G}}^{\frac{1}{2}|\mathbf{k}+\mathbf{G}|^2 \leq E_c} c_i(\mathbf{k} + \mathbf{G}) e^{i(\mathbf{k}+\mathbf{G})\cdot\mathbf{r}}. \quad (2.39)$$

With this definition, the efficacy of the basis set can be improved simply by tuning the cutoff kinetic energy for the plane waves, E_c , which significantly affects the number of

plane waves in the set. In a self-consistent calculation, one searches for the set of coefficients, $c_i(\mathbf{G}, \mathbf{k})$, that minimize the total energy, with E_c affecting the accuracy. Moreover, for computational reasons, integrations on the Brillouin zone need to be approximated by a summation over a finite set of \mathbf{k} -points and, thus, sampling the Brillouin zone appropriately is also critical for accurate calculations.

The plane waves form a complete and orthonormal set of functions, however, they are not efficient to describe core states, which present eigenvectors that oscillate strongly in space. This oscillating behavior would require a large number of plane waves, implying high computational cost, for correct representation. For this reason, the use of plane waves can be coupled with the pseudopotential approximation, in which an effective ionic potential replaces the strong Coulomb potential of the nuclei, as well as all effects of the core electrons, while the valence electrons are treated in the KS self-consistency field.¹²⁷ Fortunately, the valence electrons are the most decisive for the majority of chemical phenomena.

The construction of pseudopotentials is intricate and involves the *ab initio* (not parameterized with experimental data) calculation of a free reference atom considering all electrons and interactions, with replacement of the wave functions by a smooth pseudo function to calculate the pseudopotential; there is freedom to choose a cutoff separating core and valence electrons as desired. The pseudopotentials are not only studied due to their application in KS DFT, but they are an active topic of research to develop theories to treat the many-body problem. Nevertheless, they are powerful tools for KS DFT; most pseudopotentials are norm-conserving (which refers to the matching, outside the core, of the all electron and pseudo wave functions), accurate and transferable, hence, although they are constructed in one specific condition (usually atomic), they can be employed for condensed matter and molecules. Moreover, relativistic effects can be considered in the reference all electron calculation to generate the pseudopotential incorporating effects, such as spin-orbit interactions and scalar relativistic effects, that are transferred to the condensed phase calculations. To greatly improve the computational efficiency, the use of plane waves and pseudopotentials can be combined in the projector augmented wave method, which is discussed next.

2.5 Projector Augmented Wave Method

To solve the KS equation, we employed a technique denominated Projector Augmented Wave (PAW),^{128,129} which greatly improves the computational efficiency of DFT calculations. Here, a short summary of the main ideas of this method is provided.⁹¹

In the last section, it was mentioned that the use of plane waves can be assisted by pseudopotentials. Additionally, the Augmented Plane Waves method can be adopted for the same purpose of improving the usability of this basis set; such method consists in

dividing the space in augmentation and interstitial regions.¹³⁰ The augmentation region is constructed from parts spherically centered on the atoms and is collectively named augmentation spheres, which are represented by the product of atomic functions and spherical harmonics. The interstitial region is outside the augmentation spheres and it is represented by a set of envelope functions that appropriately describe chemical bonds. In the intersecting part of the two regions, the functions are combined.

The PAW technique combines advantages of the pseudopotential and augmented plane wave methods.¹²⁸ In this method, auxiliary functions are employed to describe correctly both the oscillatory nature of core electrons and the valence. Hence, the whole electronic system is computed and the approach is classified as all electron. The space is divided, as mentioned before, in one part of spheres centered on the atoms and one interstitial part, while their combination is done using projectors. The all electron wave function of the PAW method, $|\psi_n\rangle$, is obtained from a linear transformation, $\hat{\mathcal{T}}$, applied on the auxiliary smooth function, $|\tilde{\psi}_n\rangle$, as

$$|\psi_n\rangle = \hat{\mathcal{T}}|\tilde{\psi}_n\rangle, \quad |\tilde{\psi}_n\rangle = |\tilde{\psi}_n\rangle + \sum_a \sum_i (|\phi_i^a\rangle - |\tilde{\phi}_i^a\rangle) \langle \tilde{p}_i^a | \tilde{\psi}_n \rangle, \quad (2.40)$$

in which a is an index to identify the atoms and define one projector for each type of atom; $|\psi_i^a\rangle$ are all electron partial waves, orthogonal to the core states and solutions to the radial Schrödinger equation for the free atoms; each $\tilde{\phi}_i^a$ is a partial pseudo wave that coincides with the respective all electron partial wave function outside the augmentation spheres for each partial wave; $\langle \tilde{p}_i^a | \tilde{\psi}_n \rangle$ is a projector function for each pseudo wave inside the augmentation sphere that satisfies two conditions: (i) $\langle \tilde{p}_i^a | \tilde{\psi}_j^a \rangle = \delta_{i,j}$, which means that the pseudo functions and partial waves are orthonormal, (ii) $|\mathbf{r} - \mathbf{R}^a| < r_c^a$, which controls the region in which the $\hat{\mathcal{T}}$ operator acts through the cutoff radius, r_c^a , chosen such as there is no superposition of augmentation spheres. This operator has the form

$$\hat{\mathcal{T}} = 1 + \sum_i (|\phi_i^a\rangle - |\tilde{\phi}_i^a\rangle) \langle \tilde{p}_i^a |. \quad (2.41)$$

The PAW method employs the frozen core approximation, in which the core states occupy the region inside the augmentation spheres and are not affected by environmental change, such as the formation of chemical bonds. Such core electrons, indicated by c , are represented by

$$|\psi_i^c\rangle = |\tilde{\psi}_i^c\rangle + |\phi_i^c\rangle - |\tilde{\phi}_i^c\rangle, \quad (2.42)$$

with i indicating the different core states. Unlike the valence states, the core states do not require projectors in the frozen core approximation and do not vary significantly in response to the chemical environment. In this manner, the PAW method has been essential to provide excellent computational performance for DFT codes, such as VASP.

Table 1 – List of PAW–PBE projectors, number of valence electrons (Z_{val}), default cutoff energy for the plane-wave basis set (ENMAX) and the chapter of the thesis in which the projector was employed.

Element	POTCAR	Z_{val}	ENMAX	Chapters
Fe	Fe_GW 31Mar2010	8	321	Chapters 3 and 5
Co	Co_GW 31Mar2010	9	323	Chapters 3, 4 and 5
Ni	Ni_GW 31Mar2010	10	357	Chapters 3, 4, 5 and 6
Cu	Cu_GW 19May2006	11	417	Chapters 3, 4, 5
Ru	Ru_sv_GW 05Dec2013	16	348	Chapters 5 and
Ru	Ru 04Feb2005	8	213	Chapter 3
Rh	Rh_GW 06Mar2008	9	247	Chapters 3, 5 and
Pd	Pd_GW 06Mar2008	10	251	Chapters 3, 5 and 6
Ag	Ag_GW 06Mar2008	11	250	Chapters 3 and 5
Os	Os_sv_GW 23Mar2010	16	320	Chapter 5
Os	Os 17Jan2003	8	228	Chapter 3
Ir	Ir_sv_GW 23Mar2010	17	320	Chapter 5
Ir	Ir 06Sep2000	9	211	Chapter 3
Pt	Pt_GW 10Mar2009	10	249	Chapters 3, 5 and 6
Au	Au_GW 23Mar2010	11	248	Chapters 3 and 5
C	C_GW_new 19Mar2012	4	414	Chapters 4, 5 and 6
H	H_GW 21Apr2008	1	300	Chapters 4 and 6
O	O_GW 19Mar2012	6	434	Chapters 4, 5 and 6

Source: Own study.

2.6 Projector Augmented Wave Implementation: Vienna *Ab initio* Simulation Package

In this section, we present some comments about using the VASP software and the most important computational parameters that were controlled to guarantee convergence and consistency. Our calculations were based on the methodology discussed in the previous sections and employed the implementation of the PAW method available in the VASP,^{131,132} using the PAW projectors provided in the VASP library, shown in Table 1 for each element.

There are several computer programs available to perform *ab initio* calculations based on DFT. The VASP software was chosen for this study due to its streamlined features for the user and good computational efficiency to work with all systems studied herein: bulks, surfaces and nanoparticles. VASP employs pseudopotentials and the PAW method using plane waves as basis functions and taking full advantage of periodic boundary conditions. To start a VASP DFT calculation, the user must provide four input files: POTCAR, POSCAR, KPOINTS and INCAR. The POTCAR file shows all data required to describe the pseudopotentials and information about each type of atom involved in the calculation, such as the definition of valence and core electrons, as well as a suggested

cutoff energy for the plane wave basis set. The POTCAR files can be constructed or updated by the user, however, for this study they were employed as provided and yielded the desired accuracy. The POSCAR file defines the structure of the system through a unit cell (or simulation box) defined from the lattice translation vectors, the number and types of atoms, as well as the respective atomic positions. The KPOINTS file provides the \mathbf{k} -point coordinates and weights, or conditions for automatic generation of a \mathbf{k} -point mesh for integration of the Brillouin zone. In this study, the Γ point was employed for finite systems, such as molecules, atoms and nanoparticles, while \mathbf{k} -point meshes were generated automatically using schemes implemented in VASP to generate equally spaced \mathbf{k} -points from appropriate subdivisions on the reciprocal space; this will be further explained ahead.

The INCAR file establishes several computational parameters that control the calculations; it is there that the user sets the convergence criteria (EDIFFG and EDIFF) and algorithms for electron density mixing, (IMIX, AMIX, BMIX, AMIX_MAG, BMIX_MAG), electronic minimization (ALGO), ionic optimization (IBRION, ISIF, NSW), electronic smearing (SIGMA), as well as specifications about the type of calculation (ISPIN, PREC) and corrections (IVDW, IDIPOL). Some computational parameters do not affect the results of the calculation, but they affect the efficiency for reaching the results. Normally, examples of parameters that have such characteristics are the ones that control the algorithms for electronic minimization, density mixing and structural optimization. However, other conditions strongly affect the accuracy of the results and have to be selected carefully, for convergence reasons, such as EDIFF and the KPOINTS sampling, or to properly represent the physical system (for example, electronic smearing: ISMEAR, SIGMA). Our choices of computational parameters were thoroughly tested, as shown in this section, and also based on the literature cited in each chapter of the thesis.

It is important to mention, for any reader intending to use VASP or other codes to run *ab initio* calculations, that it is essential to study the high performance computing (hpc) systems attentively in order to run the calculations efficiently, without wasting valuable computational resources. The details entailing hpc and its relation to VASP are outside the scope of this thesis, however, basic knowledge on the subject is undoubtedly crucial to conduct a project efficiently.

2.6.1 Adjusting the Cutoff Energy for the Basis Set and Sampling the Brillouin Zone

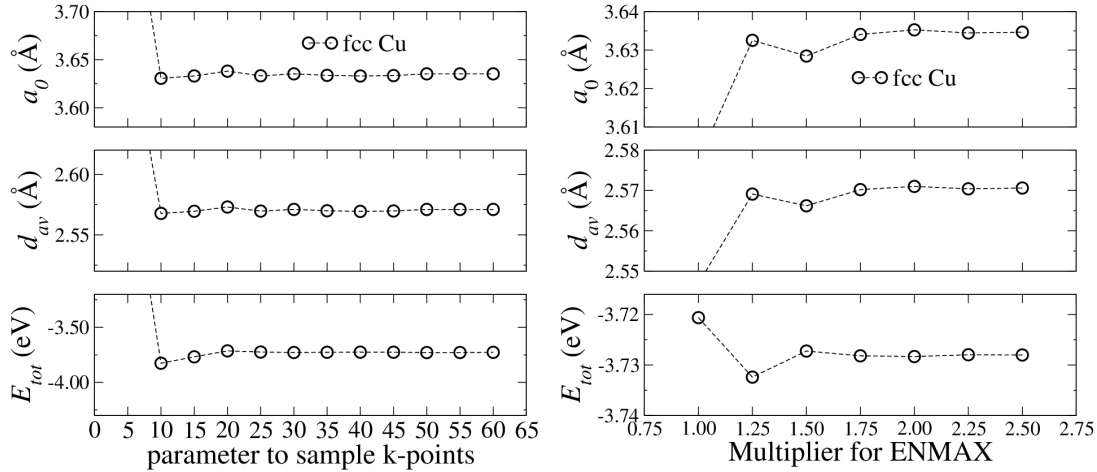
The basis set must be sufficient to obtain accurate results considering all types of atoms that compose the many-body system. For this, we employed a cutoff energy for the plane wave basis set of 489 eV (compare with Table 1) for all isolated and adsorbed systems studied in Chapters 4, 5 and 6. This value is 12.5% higher than the default recommended value for the O atom, the most demanding in terms of number of plane waves, which is related to its *s* and *p* states. The cutoff energies were different than 489 eV

in the following exceptions: (i) to optimize crystal lattice parameters, through calculation of the stress tensors and minimization of the forces on each atom changing the volume of the unit cell, a higher multiplier was applied for the recommended cutoff (2 times the default value, instead of 1.125 times, for each metal), due to the slower convergence of the stress tensor with respect to the basis set, which was tested in a previous study done by other authors;¹³³ (ii) to calculate the clean surface properties discussed in Chapter 6 the cutoff was adjusted to be 12.5 % higher than the required cutoff for each metal (for example, 402, 282 and 280 eV were employed, respectively, to calculate the clean Ni(111), Pd(111) and Pt(111) surface properties), since there is no need to comply with a higher cutoff in a self-contained investigation of the clean surface properties; (iii) the results shown in Chapter 3 employed a cutoff energy 12.5 % higher than the recommended cutoff, ENMAX, for each metal, since the O atom was not studied in the referred chapter.

The choice of the 12.5 % multiplier is based on several previous studies of the properties of transition-metal bulks, surfaces and nanoclusters reported extensively in the literature^{35,37,133–137} This allowed the quick selection of well-converged computational parameters for the present study. Here, we selected some model systems to demonstrate the convergence of the properties with respect to the most important computational parameters. For face-centered cubic Cu, the convergence with respect to the cutoff energy for the plane wave basis set and the sampling of \mathbf{k} -points, which will be further elaborated in the next section, is demonstrated in Figure 1. For this demonstrative test, one of the parameters (cutoff or \mathbf{k} -point sampling) was fixed, while the other varied. For the fixed parameter, a known well-converged value, with respect to the calculation of stress tensors and minimization of forces on the atoms, was chosen to isolate the effect of the parameter that was changed. To test the sampling of \mathbf{k} -points, the cutoff energy was fixed at 2.0 times the recommended value, on the other hand, to test the cutoff energy, the parameter for automatic generation of the grid of \mathbf{k} -points was fixed at 30. The convergence test was performed only for this crystal because of the vast accumulated experience of the research group with TM bulks (demonstrated in the references above). However, for anyone studying systems without knowledge of the convergence, it is imperative to perform more convergence tests. Based on this demonstrative test and on the previous experience of the research group, the optimization of volume, a_0^3 , of crystals was performed using a cutoff energy of 2.0 times the recommended value (ENMAX) and a grid of \mathbf{k} -points generated using a length of 50 for the subdivisions; this sampling of \mathbf{k} -points is more rigorous than what is required for fcc Cu, but it allows good convergence for properties (such as the lattice parameter and total energy) for all bulks in our set, as verified in previous studies.^{35,136} Differently from the optimization of the cell volume, for total energy calculations not involving stress tensor calculations, a multiplier of 1.125 was employed for ENMAX, as it is sufficient to obtain well converged results.

For different non-crystalline systems, the \mathbf{k} -points were sampled accordingly. Con-

Figure 1 – Convergence, for optimization of the cell volume of face-centered cubic (fcc) Cu, of the lattice parameter, a_0 , average bond length, d_{av} , and total energy, E_{tot} , with respect to the sampling of \mathbf{k} -points, indicated by the parameter for automatic generation of the \mathbf{k} -mesh, and cutoff energy for the plane-wave basis set, indicated as multiples of the recommended cutoff (ENMAX).



Source: Own study.

veniently, the subdivisions to sample the \mathbf{k} -points can be set differently along each lattice vector for unit cells of various shapes. In this study, this was convenient for the surfaces, which were modeled using the slab model (explained further in Chapter 3) and a \mathbf{k} -mesh generated from $n \times n \times 1$ subdivisions, where n was chosen based on convergence and 1 corresponds to the z dimension, which is a substantially larger than the x and y dimensions of the unit cell in real space and, thus, requires fewer \mathbf{k} -points. For 1×1 surface unit cells (1 atom per layer), n can be a large number, such as 30 or 60; however, for larger unit cells (such as 3×3 or 4×4) the sampling has to be chosen sparingly, due to the rapid increase in the computational cost as the number of atoms increases.

To integrate the Brillouin zone, the Γ point was sufficient for the finite systems (nanoparticles, molecules and atoms), because there is no dispersion of electronic states. For the bulks, as mentioned above, an automatically generated and equally spaced \mathbf{k} -point mesh was employed using a length parameter of 50 for to generate the mesh through subdivisions. For the surface slabs, the \mathbf{k} -mesh was adjusted setting subdivisions for automatic generation proportionally to the size of the unit cells: for Chapter 6, the \mathbf{k} -point meshes were generated with the parameters $30 \times 30 \times 1$ (for 1×1 unit cells, 5 layers, 1 atom per layer) and $3 \times 3 \times 1$ (for 4×4 unit cells, 5 layers, 16 atoms per layer) for the separate discussions about the clean surfaces properties and to study adsorption, respectively. For the surfaces studied in Chapter 4, the \mathbf{k} -point mesh was generated with the setting $4 \times 4 \times 1$ (for 3×3 unit cells, 9 atoms per layer), which a finer sampling because the unit cells are smaller laterally compared to the other aforementioned surfaces. These choices are based on a large number of previous studies.^{9,37,133,134,136,137} Notice that for the 1×1 slabs

using large \mathbf{k} -point meshes does not cause problems with the computational cost, since the system contains only a few atoms, this was applied for the study of the clean surfaces, Chapter 3.

2.6.2 Density of States, Work Function and Bader Charge Analysis

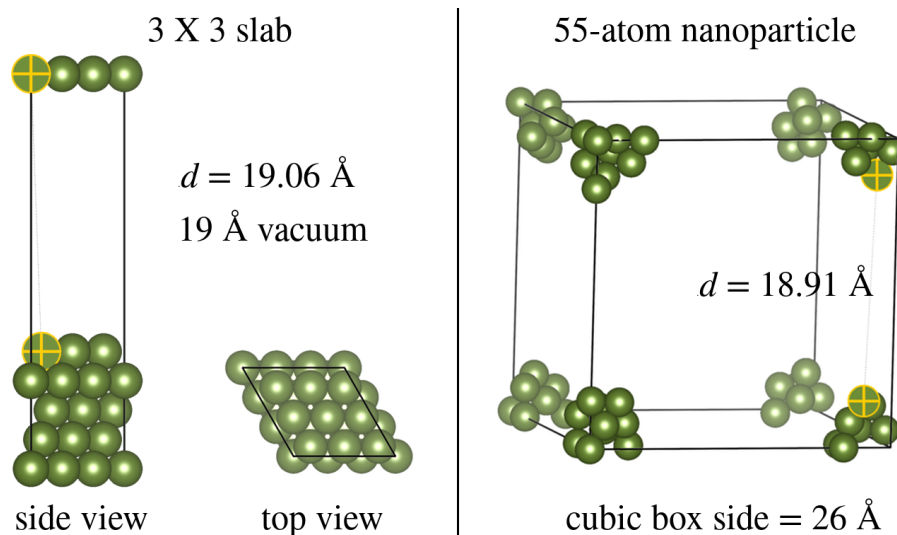
To calculate the density of states and work function, the \mathbf{k} -mesh was doubled for the surfaces, except for the z -direction of the slabs and for the finite systems; for crystals, the \mathbf{k} -mesh parameter was increased to 75. To calculate the work function of the molecule/surface systems, the dipole correction¹³⁸ was applied to compensate the decay of the electrostatic potential along the z -axis that results from the consideration of the adsorbate on only one side of the slab.

There are several methods to calculate the charges on atoms; in this thesis, we employed the Bader charge analysis.¹³⁹ This approach is based on dividing the real space into volumes setting the limits for each atoms in the regions where the charge density tends to zero, which are defined through the zero flux condition $\nabla\rho(\mathbf{r})\cdot\hat{\mathbf{n}}(\mathbf{r})=0$, in which $\hat{\mathbf{n}}$ is the normal to the surface that encloses the volume containing the atom, V .¹⁴⁰ Then, for each volume, the charge is simply, $Q^{\text{Bader}} = \int_V \rho(\mathbf{r})dV$. To calculate the Bader charges,¹⁴¹ a fine FFT-mesh (Fast Fourier Transform, which relates real and reciprocal space) was employed by increasing the default NGXF, NGYF and NGZF flags in the VASP software from the recommended values, which are mainly based on the size of the unit cell (or box) and the plane-wave basis set. For this, we considered the NGX(YZ)F recommended by VASP and multiplied each by a factor of 3 (or 2 for the study shown in Chapter 4, due to the large box sizes of the TM_{147} systems), thus, obtaining sufficiently converged results. Further increases of the mesh would incur severe computational costs. Moreover, we disabled the VASP supporting grid (ADDGRID) and employed the all-electron charge by summing core and valence charges.¹⁴¹ This procedure was done as a single-point calculation (fixed atomic positions) using previously optimized atomic configurations to avoid prohibitive computational costs.

2.6.3 Defining the Sizes of Surface Unit Cells and Simulation Boxes

For the surfaces, we employed the slab model, which is explained further in Chapter 3. Here, Figure 2 illustrates the surface slabs employed to study adsorption and a simulation box for a nanoparticle. The size of the surface unit cells can be adjusted according to the number of layers, size of the plane defined by the \mathbf{a} and \mathbf{b} lattice vectors (noted here as xy plane), as well as the vacuum region. To calculate the clean surface properties shown in Chapter 3, we employed 1×1 slabs with 5 or 11 layers, which helps to evaluate the convergence of the surface properties with the number of layers. The convergence of the surface properties improves as the number of layers, L , increases,^{142,143} however, for adsorption studies, a small and sufficient L (we chose 5 layers) has to be selected to avoid

Figure 2 – Illustrations of the unit cell for Ni(111), 3×3 slab, representing the extended surfaces, and cubic simulation box for Ni₅₅, located at the origin of the box, demonstrating finite systems. The distances, d , between marked atoms are indicated.



Source: Own study.

prohibitive computational costs. To study adsorption, the lateral sizes of the unit cells (xy plane) were adjusted depending on the size of the adsorbates (4×4 for Chapter 6 or 3×3 for Chapter 4) to obtain sufficiently small interactions among periodic images with manageable computational costs and, as mentioned above, the \mathbf{k} -point sampling was adjusted accordingly. Concerning the vacuum, the surface unit cells were constructed with a vacuum thickness chosen to keep a distance of at least 12 \AA , between the periodic images along the z -axis, to obtain negligible and consistent interactions between such parts.^{37,75} Considering the aforementioned requirement, a vacuum of 21 \AA was employed for the surfaces studied in Chapter 6, while a vacuum region of 19 \AA was employed for the surfaces studied in Chapter 4, which were selected based on the different sizes of the molecules.

This requirement for negligible interactions among periodic images is also important for the finite systems, such as nanoclusters, atoms and molecules.^{35,144} For the free atoms, an orthorhombic box of $20 \times 21 \times 22$ was employed. For the isolated CO_2 , CO , H_2O and H_2 molecules, a cubic box with sides of 20 \AA was employed; however, for the molecules studied in Chapter 6, $20 \times 21 \times 22$ boxes were employed, although we found negligible differences in the total energies of these molecules calculated with orthorhombic or cubic boxes. The 13-, 55- and 147-atom TM nanoparticles and their respective adsorbed systems were modeled using cubic boxes with sides of 20, 26 and 31 \AA , respectively; these considerable differences were due to the sizes of the clusters and also to consider systems with linear CO_2 distant from the substrate. For Chapter 5, the nanoclusters and nanoalloys were modeled in cubic

Table 2 – Convergence test for the size of the cubic simulation box with a total energy convergence criterion of 10^{-8} eV for the frozen $\text{CO}_2/\text{Cu}_{13}$ system, which was optimized previously using a 20 Å cubic box. We indicate the shortest distance between two periodic images, d_{im} , total electronic energy, E_{tot} , relative energy with respect to the largest box size, ΔE_{tot} , and total magnetic moment, m_{tot} .

PBE					PBE+D3		
Box (Å)	d_{im} (Å)	E_{tot} (eV)	ΔE_{tot} (meV)	m_{tot} (μ_{B})	E_{tot} (eV)	ΔE_{tot} (meV)	m_{tot} (μ_{B})
9	3.06	-58.622 638 59	-942.66	1.00	-57.199 866 93	-425.87	1.00
10	3.91	-58.093 420 83	-413.44	1.00	-56.952 374 79	-178.37	1.00
11	4.75	-57.857 692 86	-177.71	0.99	-56.842 991 64	-68.99	0.99
12	5.65	-57.752 466 35	-72.49	1.00	-56.792 368 05	-18.37	1.00
13	6.57	-57.723 494 60	-43.52	1.00	-56.788 102 70	-14.10	1.00
14	7.51	-57.693 038 31	-13.06	1.00	-56.769 977 48	4.02	1.00
15	8.47	-57.687 974 92	-8.00	1.00	-56.771 576 07	2.43	1.00
16	9.43	-56.768 848 57	5.15	1.00	-57.681 417 06	-1.44	1.00
17	10.40	-56.770 149 94	3.85	0.99	-57.680 408 40	-0.43	0.99
18	11.38	-56.775 938 39	-1.94	1.00	-57.684 752 46	-4.77	1.00
19	12.36	-56.769 011 14	4.99	1.00	-57.676 893 09	3.09	1.00
20	13.34	-56.779 303 85	-5.30	1.00	-57.686 563 25	-6.59	1.00
21	14.33	-56.768 340 56	5.66	1.00	-57.675 171 64	4.81	1.00
22	15.32	-56.776 949 72	-2.95	1.00	-57.683 481 41	-3.50	1.00
23	16.31	-56.776 707 76	-2.71	1.00	-57.683 026 91	-3.05	1.00
24	17.30	-56.766 751 15	7.25	1.00	-57.672 918 63	7.06	1.00
25	18.29	-56.772 401 24	1.60	0.99	-57.678 458 90	1.52	0.99
26	19.28	-56.774 001 84	0.00	1.00	-57.679 978 10	0.00	1.00

Source: Own study reproduced with permission for the thesis.¹⁴⁵ Reproduced by permission of the PCCP Owner Societies.

boxes with different sides, depending on the elements present, because of the different atomic radii (26 Å for systems containing Ag, 25 Å for Ru and Rh and 24 Å for all other TM) and to obtain similar negligible interactions among the periodic images.

Simulation boxes of different sizes result in different distances between periodic images, due to the varying volume of the vacuum region. To demonstrate the convergence of the total energy, with respect to this subject, we present a convergence test in Table 2, changing the box size to calculate the total energy through single-point calculations. The results show that the total energy is well converged, at least within 7 meV, in the range from 12.36 to 19.28 Å for the distance between periodic images. In conclusion, to obtain consistent and well-converged calculations, it is desirable to have approximately constant and sufficiently large distances between the images. This test improves our understanding of this effect on the convergence of the total energy, and further tests are available in publications from other authors.^{35,37}

2.6.4 Structural and Electronic Optimizations

A brief section in each chapter shows the procedure to obtain starting atomic structure configurations employed to model the systems. All geometries of isolated systems were fully relaxed before adsorption, then, the adsorption configurations were fully optimized before any analysis. As an exception, for adsorption on surfaces, the bottom layer of the slab was fixed in the positions optimized for the clean surfaces, while all other atomic positions were optimized. The structural optimizations employed the conjugate gradient algorithm until the forces were at least smaller than $0.025 \text{ eV}/\text{\AA}$ for the studies shown in Chapters 6 and 4, while this was changed to $0.05 \text{ eV}/\text{\AA}$ for the systems in Chapter 5. The total energy convergence criterion was of 10^{-6} eV for the studies shown in Chapters 6 and 4, while this was changed to 10^{-5} eV for the systems in Chapter 5. The different convergence criteria for Chapter 5 were made to manage the computational cost, because of the large number of adsorption configurations optimized and only a small impact is expected for the results, according to convergence tests and the literature, such as previous studies with TM nanoclusters.^{35,146} Regarding spin polarization and the local magnetic moments, the electronic optimizations were not constrained and the self-consistent lowest energy solution was employed for each system.

2.7 Summary

In this section we presented some fundamental concepts to understand the calculations and results discussed in this study. We discussed the need to approach the many-body problem through quantum mechanics and the main approximations required for this. Then, we discussed the electron density as a fundamental quantity for a quantum-mechanical description of the many-body systems and discussed the Kohn–Sham formalism within DFT. Furthermore, we showed the approximations (exchange-correlation) and corrections (dispersion) employed in this study and discussed the periodic approach of the VASP software within the PAW method. Finally, we discussed the most important computational parameters employed and the reasoning behind our choices.

3 BULK AND CLEAN SURFACE PROPERTIES

In this chapter, we discuss a preliminary investigation of bulk and clean surface properties. These model systems can help to understand the characteristics of the TM substrates that will be explored along this thesis. The study was carefully performed, before starting any investigation about adsorption, to comprehend both the physical chemistry of the materials and how to approach the systems from the *ab initio* methodology in a way that reproduces realistic trends observed in nature. Therefore, the results discussed in this chapter can help the reader to further understand other results of the thesis. As an exception of the thesis, the calculations shown in this chapter employed the PBE functional without the dispersion (D3) correction; the dispersion effects on the bulk and clean surface properties are discussed in separate subsections of this chapter explicitly stating the use of the D3 correction.

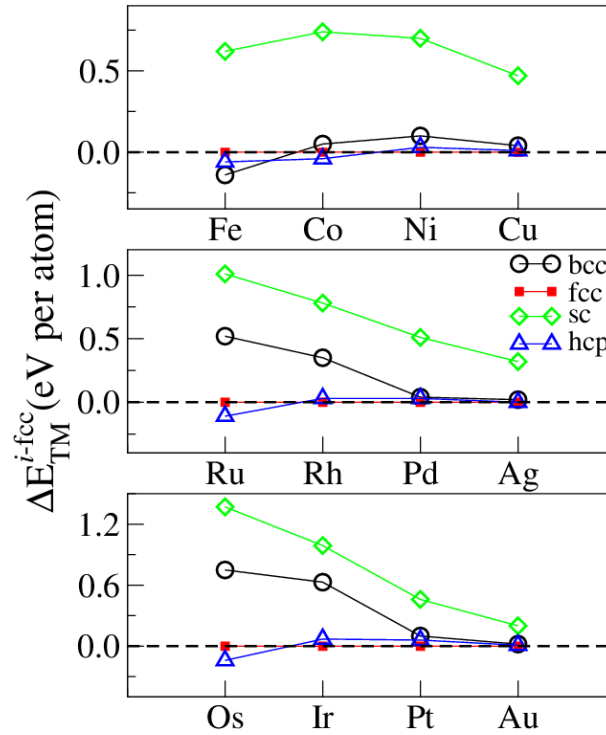
3.1 Transition-metal Crystals

The crystals can be referred to as the bulk phase, which is the infinite arrangement, with long-range ordering, of TM atoms. This theoretical model can represent large bulk materials, defined in the macroscopic size scale, disregarding the presence of interfaces with other phases, such as the air or vacuum. Here, we discuss some bulk properties for Fe, Co, Ni, Cu, Ru, Rh, Pd, Ag, Os, Ir, Pt and Au (*3d*, *4d* and *5d* periods, groups 8 to 11 of the periodic table) in the following phases: hexagonal close-packed (hcp), face-centered cubic (fcc), body-centered cubic (bcc) and simple cubic (sc). These phases are only some of the possibilities for regular (non-defected) bulk materials, but they are common models.⁸⁷

3.1.1 Procedures to Obtain the Atomic Structure Configurations

Different cells can be used to represent a given crystal structure.¹⁴⁷ The conventional cells allow the easy visualization of the lattice parameters (a_0 and c_0), however, it is ideal to use the smallest possible cells to reduce the computational cost of the calculations, since they reproduce exactly the same system. Some examples and additional details about how such models can be defined from the lattice parameters are available in Appendix C. The starting configurations employed cells with lattice parameter 20% higher than our reference lattice parameters,⁸⁷ which come from an extensive database.¹⁴⁸ For each element, the same starting a_0 for the most stable phase was employed to define all four phases studied (fcc, bcc, hcp, sc), the starting value of c_0 was taken similarly for cases where hcp was the most stable bulk phase. Alternatively, the value of c_0 was estimated to generate a reasonable distancing, without overlapping or large interstitial space, between

Figure 3 – Relative energies with respect to the fcc structure, $\Delta E_{\text{TM}}^{i\text{-fcc}}$, for the transition-metal crystals.



Source: Own study.

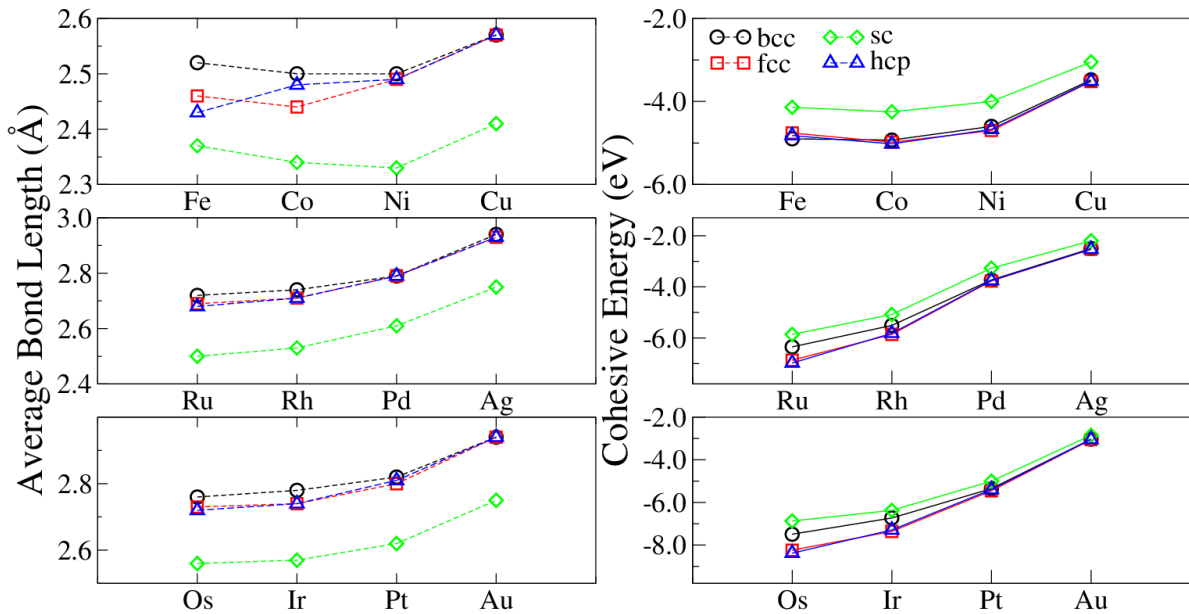
the atoms. All structures were fully optimized (unit cell volume and atomic positions) before any analysis.

3.1.2 Relative Energy

The total energy of the crystals was evaluated in Figure 3 adopting the fcc structure, for each element, as a reference because it is the most stable configuration for most metals.⁸⁷ This comparison was done according to $\Delta E_{\text{TM}}^{i\text{-fcc}} = E_{\text{TM}}^i - E_{\text{TM}}^{\text{fcc}}$, in which $\Delta E_{\text{TM}}^{i\text{-fcc}}$ is the energetic comparative measure with respect to the fcc phase of the metal, E_{TM}^i is the total energy per atom of crystal i (with $i = \text{bcc}, \text{fcc}, \text{hcp}$ and sc), and $E_{\text{TM}}^{\text{fcc}}$ is the total energy per atom of the fcc crystal. Our calculations confirm the experimental observation that sc structures are rarely found in nature, since they have higher energy compared to the other phases.⁸⁷ The $\Delta E_{\text{TM}}^{i\text{-fcc}}$ tends to decrease for sc structures as the atomic number increases and the same behavior is observed for the bcc structures of periods 4d and 5d. This suggests that, as the d -band is filled along the transition periods, the directionality of the metallic bonds increases and the total energy is less dependent on the type of phase. For the 3d period, this trend is not clear, since the magnetic moments can cause some deviation of this behavior, as will be shown ahead.

The hcp structure is the most stable configuration for elements of group 8, while elements from groups 9, 10 and 11 preferably adopt the fcc structure, except Fe and

Figure 4 – Average bond length and cohesive energy for transition metal crystals. The ranges obtained for the effective coordination numbers, ECN, are indicated for each type of structure.



Source: Own study.

Co which are more stable in the bcc and hcp phases, respectively. Several crystals have similar energies, especially hcp and fcc which are very similar geometrically (see details in Appendix C). In nature, such similar energies allow the metals to assume various structures and undergo phase transformations with variations of temperature and pressure, or even to coexist in different structures. For example, Co can coexist as hcp and fcc structures at room temperature and, when pulverized or kept at 400 K, it can adopt the fcc structure preferably.¹⁴⁹ Additionally, Fe is found as the bcc phase at mild conditions, but at high pressures it assumes the hcp structure and, at high temperatures, fcc.¹⁵⁰

To further understand the crystals, some properties were calculated for all structures. The next subsections show analyses focused on the most stable structures (according to Figure 3) for each metal. However, the properties of all, low and high energy, crystals are summarized in Table 4 and will be mentioned along the discussions.

3.1.3 Structural Properties

In Figure 4, the most stable crystals are compared with respect to the average bond length, d_{av} , while Table 3 shows the equilibrium lattice parameters. The definition of the effective coordination concept, employed to calculate d_{av} and effective coordination numbers, ECN (in number of nearest neighbors, NNN), is available elsewhere.¹⁵¹ The profiles illustrate the periodic trend, connected to the occupation of d -states, that will be discussed ahead.

Table 3 – PBE equilibrium lattice parameters, a_0 and c_0 , and cohesive energy per atom, E_{coh} , compared to references^{*,†} through percent deviations, Δa_0 , Δc_0 and ΔE_{coh} .

Crystal	Reference	a_0 (Å)	Δa_0 (%)	c_0 (Å)	Δc_0 (%)	Reference	E_{coh} (eV)	ΔE_{coh} (%)
bcc Fe	This study	2.83	-	-	-	This study	-4.90	-
	Ref. 87	2.87	-1.39	-	-	Ref. 152	-4.28	14.49
	Ref. 39	2.84	-0.35	-	-	Ref. 113	-4.87	0.62
hcp Co	This study	2.49	-	4.02	-	This study	-5.02	-
	Ref. 87	2.51	-0.80	4.07	-1.23	Ref. 152	-4.43	13.32
	Ref. 39	2.50	-0.40	4.03	-0.25	Ref. 113	-5.27	-4.74
fcc Ni	This study	3.52	-	-	-	This study	-4.70	-
	Ref. 87	3.52	0.00	-	-	Ref. 152	-4.44	5.86
	Ref. 39	3.52	0.00	-	-	Ref. 113	-4.87	-3.49
fcc Cu	This study	3.63	-	-	-	This study	-3.52	-
	Ref. 87	3.61	0.55	-	-	Ref. 152	-3.48	1.15
	Ref. 39	3.63	0.00	-	-	Ref. 113	-3.48	1.15
hcp Ru	This study	2.71	-	4.28	-	This study	-6.98	-
	Ref. 87	2.71	0.00	4.28	0.00	Ref. 152	-6.74	3.56
	Ref. 39	2.73	-0.73	4.31	-0.70	Ref. 113	-6.67	4.65
fcc Rh	This study	3.83	-	-	-	This study	-5.86	-
	Ref. 87	3.80	0.79	-	-	Ref. 152	-5.72	2.45
	Ref. 39	3.85	-0.52	-	-	Ref. 113	-5.62	4.27
fcc Pd	This study	3.94	-	-	-	This study	-3.77	-
	Ref. 87	3.89	1.29	-	-	Ref. 152	-3.90	-3.33
	Ref. 39	3.96	-0.51	-	-	Ref. 113	-3.71	1.62
fcc Ag	This study	4.15	-	-	-	This study	-2.53	-
	Ref. 87	4.09	1.47	-	-	Ref. 152	-2.94	-13.95
	Ref. 39	4.16	-0.24	-	-	Ref. 113	-2.49	1.61
hcp Os	This study	2.75	-	4.35	-	This study	-8.38	-
	Ref. 87	2.74	0.36	4.32	0.69	Ref. 152	-8.17	2.57
	Ref. 39	2.76	-0.36	4.35	0.00	Ref. 113	-8.29	1.09
fcc Ir	This study	3.87	-	-	-	This study	-7.36	-
	Ref. 87	3.84	0.78	-	-	Ref. 152	-6.92	6.36
	Ref. 39	3.88	-0.26	-	-	Ref. 113	-7.32	0.55
fcc Pt	This study	3.97	-	-	-	This study	-5.45	-
	Ref. 87	3.92	1.28	-	-	Ref. 152	-5.85	-6.84
	Ref. 39	3.98	-0.25	-	-	Ref. 113	-5.50	-0.91
fcc Au	This study	4.15	-	-	-	This study	-3.05	-
	Ref. 87	4.08	1.72	-	-	Ref. 152	-3.81	-19.95
	Ref. 39	4.16	-0.24	-	-	Ref. 113	-2.99	2.01

* Reference a_0 and c_0 , measured at room temperature, obtained from Kittel, C.⁸⁷ and calculated by Tereshchuk, P. et al.³⁹ using PAW-PBE.

† Reference E_{coh} data from Young, D. A.¹⁵² (experimental, handbook) and theoretical reference E_{coh} data calculated by Janthon, P., et al.¹¹³ using PAW-PBE.

Source: Own study. This table displays cited reference data.^{39,87,113,152}

For each transition period, the magnitude of d_{av} (and of the lattice parameters) tends to increase with the atomic number, suggesting that the distancing increases to

compensate the interactions among an increasing number of electrons. In the vertical downwards direction of the periodic table, from period $3d$ to $4d$, d_{av} shows a small increase; moreover, for a given group and from periods $4d$ to $5d$, the increase of d_{av} is almost negligible. This can be rationalized considering the presence of filled f -states for the $5d$ elements; shielding effects from f -orbitals are weaker, and this results in a strong attraction of the electrons by the nuclei, impacting the trend for increased d_{av} along the transition groups. The ECN of bcc, fcc and sc crystals were, respectively, of 11.63, 12.02 and 6.04 nearest neighbors for all TM; however, for hcp, the values varied in the range from 11.87 to 12.02 for different TM, due to the independent relaxation of the two lattice parameters, a_0 and c_0 . The expected coordination number (CN) for the crystals are 8, 6, 12 and 12, respectively for bcc, sc, fcc and hcp; the ECN differs from those values due to the formalism involved in its calculation: while the CN counts all neighbors bonded to a given atom with equal importance, the ECN attributes weights to each neighbor, depending on the its proximity to the atom evaluated. Therefore, the ECN is able to capture more details about the structure, which helps to describe distorted structures;¹⁵¹ this will be useful in the next chapters, where we use the ECN to characterize various nanoparticles.

To validate our description of the structures of the crystals, Table 3 shows a comparison between the lattice parameters obtained in this study with the literature cited in the table.^{39,87} The calculated values are close to the experimental literature,⁸⁷ with a deviation of at most 1.72% for fcc Au. The deviations with respect to another theoretical study³⁹ are very small, at most -0.73% . The good performance of the PBE functional is well-known, with extensive studies available in the literature.^{113,153} However, PBE tends to overestimate the lattice parameter of some crystals; in fact, any functional will have some error that needs to be considered collectively for all systems in the target set of configurations.¹⁵⁴ For the hcp phase, the c_0/a_0 ratio can be evaluated considering the ideal condition, in which $c_0/a_0 = 1.6333$, a value rarely found in metals.¹⁵⁵ This ratio is affected by the errors in estimating the lattice parameters, however, they were smaller than 2%. Hence, our results showed c_0/a_0 very close to the ideal value for all cases in which the hcp structure is the most stable phase; namely, Co, Ru and Os with c_0/a_0 of 1.60, 1.58 and 1.59, respectively. The experimental reference⁸⁷ shows the same trend, with c_0/a_0 of 1.62, 1.58 and 1.58 for Co, Ru and Os, respectively. For the remaining TM, the ratio was between 1.16 and 1.22, except Fe, which showed a c_0/a_0 of 1.35, which is a little closer to the ideal, a result that could be related to the stability of hcp Fe in certain high-pressure conditions.¹⁵⁰

3.1.4 Cohesive Energy

The cohesive energy, E_{coh} , measures the binding strength of solids as

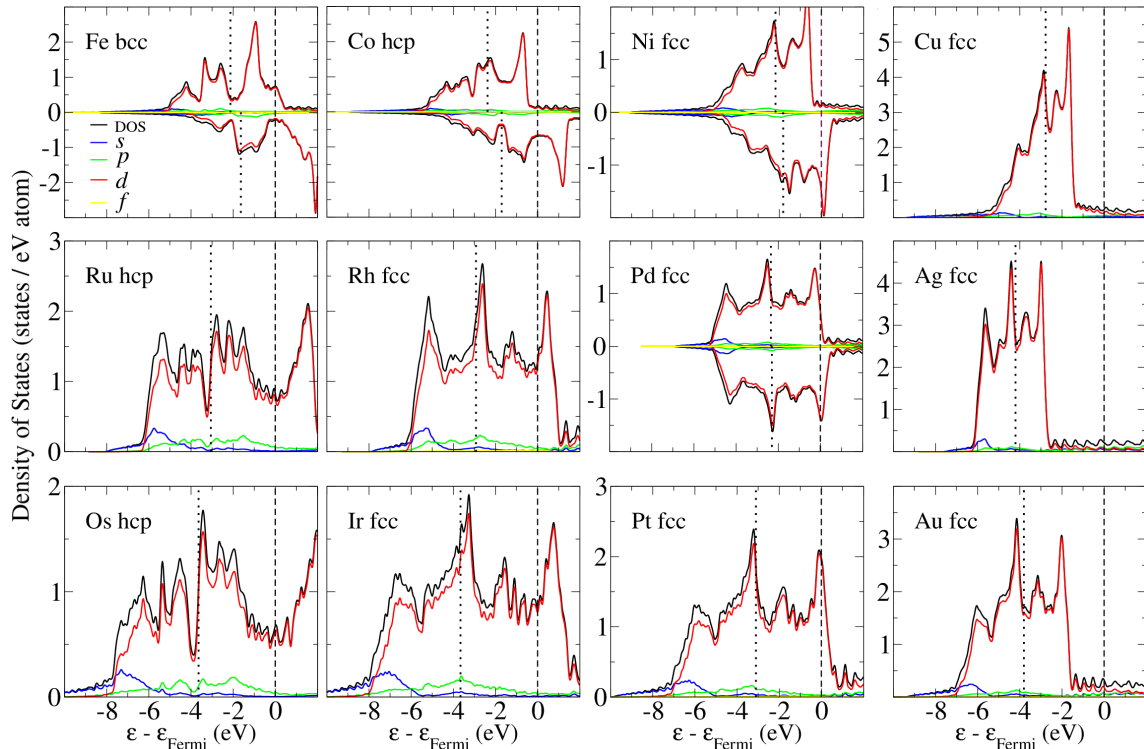
$$E_{coh} = E_{tot}^{crystal} - E_{tot}^{free\ atom}, \quad (3.1)$$

Table 4 – Properties of transition-metal crystals (3d, 4d, 5d, groups 8 to 11). Equilibrium lattice parameters, a_0 and c_0 , average bond length, d_{av} , effective coordination number, ECN, cohesive energy per atom, E_{coh} , and d -band centers, $\varepsilon_{d\uparrow}$ and $\varepsilon_{d\downarrow}$.

Crystal	a_0 (Å)	c_0 (Å)	d_{av} (Å)	ECN (NNN)	E_{coh} (eV)	$\varepsilon_{d\uparrow}$ (eV)	$\varepsilon_{d\downarrow}$ (eV)
Fe bcc	2.83	-	2.52	11.63	-4.90	-2.13	-1.63
Fe fcc	3.48	-	2.46	12.02	-4.76	-2.25	-2.01
Fe sc	2.36	-	2.37	6.04	-4.14	-2.23	-1.50
Fe hcp	2.46	3.88	2.43	11.97	-4.82	-2.22	-2.22
Co bcc	2.81	-	2.50	11.63	-4.93	-2.78	-2.01
Co fcc	3.45	-	2.44	12.02	-4.98	-2.09	-2.09
Co sc	2.34	-	2.34	6.04	-4.25	-2.61	-1.73
Co hcp	2.49	4.02	2.48	12.01	-5.02	-2.37	-1.70
Ni bcc	2.80	-	2.50	11.63	-4.60	-1.91	-1.57
Ni fcc	3.52	-	2.49	12.02	-4.70	-2.18	-1.81
Ni sc	2.33	-	2.33	6.04	-4.00	-1.90	-1.57
Ni hcp	2.48	4.08	2.49	12.02	-4.67	-2.18	-1.80
Cu bcc	2.89	-	2.57	11.63	-3.48	-2.72	-
Cu fcc	3.63	-	2.57	12.02	-3.52	-2.78	-
Cu sc	2.41	-	2.41	6.04	-3.05	-2.37	-
Cu hcp	2.57	4.20	2.57	12.02	-3.51	-2.71	-
Ru bcc	3.05	-	2.72	11.63	-6.35	-2.92	-
Ru fcc	3.80	-	2.69	12.02	-6.87	-2.92	-
Ru sc	2.50	-	2.50	6.04	-5.86	-2.87	-
Ru hcp	2.71	4.28	2.68	11.97	-6.98	-3.06	-
Rh bcc	3.07	-	2.74	11.63	-5.51	-2.46	-
Rh fcc	3.83	-	2.71	12.02	-5.86	-2.93	-
Rh sc	2.53	-	2.53	6.04	-5.08	-2.56	-
Rh hcp	2.72	4.39	2.71	12.01	-5.82	-2.98	-
Pd bcc	3.13	-	2.79	11.63	-3.73	-2.25	-2.25
Pd fcc	3.94	-	2.79	12.02	-3.77	-2.35	-2.30
Pd sc	2.61	-	2.61	6.04	-3.27	-2.19	-2.19
Pd hcp	2.77	4.61	2.79	12.00	-3.75	-2.33	-2.27
Ag bcc	3.30	-	2.94	11.63	-2.50	-4.20	-
Ag fcc	4.15	-	2.93	12.02	-2.53	-4.21	-
Ag sc	2.75	-	2.75	6.04	-2.20	-3.98	-
Ag hcp	2.93	4.80	2.93	12.02	-2.53	-4.23	-
Os bcc	3.09	-	2.76	11.63	-7.49	-3.51	-
Os fcc	3.86	-	2.73	12.02	-8.24	-3.45	-
Os sc	2.56	-	2.56	6.04	-6.87	-3.20	-
Os hcp	2.75	4.35	2.72	11.97	-8.38	-3.64	-
Ir bcc	3.11	-	2.78	11.63	-6.73	-3.05	-
Ir fcc	3.87	-	2.74	12.02	-7.36	-3.66	-
Ir sc	2.57	-	2.57	6.04	-6.37	-2.97	-
Ir hcp	2.75	4.46	2.74	12.02	-7.29	-3.75	-
Pt bcc	3.16	-	2.82	11.63	-5.35	-2.83	-
Pt fcc	3.97	-	2.80	12.02	-5.45	-3.11	-
Pt sc	2.62	-	2.62	6.04	-5.00	-2.80	-
Pt hcp	2.76	4.77	2.81	11.87	-5.39	-3.04	-
Au bcc	3.30	-	2.94	11.63	-3.03	-3.82	-
Au fcc	4.15	-	2.94	12.02	-3.05	-3.81	-
Au sc	2.75	-	2.75	6.04	-2.85	-3.22	-
Au hcp	2.92	4.88	2.94	11.99	-3.04	-3.77	-

Source: Own study.

Figure 5 – Total and local density of states (DOS, LDOS) for the most stable TM bulks; the LDOS are decomposed into s -, p -, d - and f -states. The dashed and dotted lines indicate, respectively, the Fermi level and the d -band center.



Source: Own study.

in which $E_{tot}^{crystal}$ is the total energy per atom for the crystal and $E_{tot}^{free\ atom}$ is the total energy of the TM atom isolated in the vacuum. Profiles of E_{coh} versus the type of metal are shown in Figure 4, while the data is displayed and compared to the literature^{113,152} in Table 3.

The E_{coh} is negative for all cases, indicating that it is energetically favorable to form these crystals with respect to isolated atoms. There is a parabolic trend for E_{coh} related to the electronic nature of the TM.¹⁵⁶ This will be discussed ahead with the electronic properties, considering that the properties of the materials are correlated; for example, the d_{av} also shows a parabolic profile along each entire transition period, which is connected to the electronic properties. As expected, estimating the cohesive energy is more difficult than the lattice parameters,^{113,157} which can be attributed to the differences between the ideal theoretical models and the real experimental systems. There are corrections that can be employed to consider such differences,¹⁵⁷ but in this study we did not apply any of them. Comparing our calculations with the experimental data shown in Table 3,¹⁵² we can observe that most of our results are overestimated, especially for Fe and Co, although some were underestimated, such as Ag and Au. However, the deviations of our results from other theoretical calculations are below 5%. In practice, for a study including various systems, a sensible approach is to select a functional that provides appropriate balance

Table 5 – Magnetic moment per atom, m_{tot} , for Fe, Co, Ni and Pd crystals in the bcc, fcc, hcp and sc phases.

TM	m_{tot} (μ_B/atom)			
	bcc	fcc	hcp	sc
Fe	2.16	1.02	0.00	2.40
Co	1.75	1.61	1.58	1.89
Ni	0.56	0.63	0.64	0.55
Pd	0.00	0.40	0.40	0.00

Source: Own study.

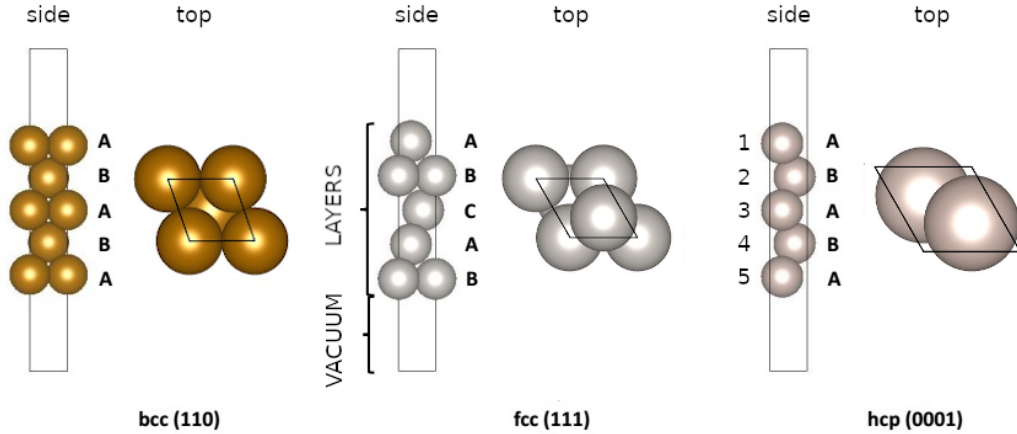
between the overall computational cost and accuracy for several systems.

3.1.5 Density of states and Magnetic Moments

To better understand the properties of the crystals, Figure 5 depicts the total and local density of states (DOS, LDOS) of the bulk systems, with the local density of states decomposed into local s , p , d and f states. As expected, the d -band is the major component of the DOS. The graphs show that the Fermi level shifts to the right (more energetic) along the transition periods, especially for cases where the d -band is not completely filled ($4d$ and $5d$); for the $3d$ period, this effect is not clearly visible because of spin polarization. For completely filled d -bands (group 11 metals), the Fermi level is located beyond the d -band. Following the pattern, one can assume that the Fermi level should be close to the d -band center, ε_d , for the metals of the center of the transition periods. Additional factors can affect the ε_d , such as coordination, as demonstrated in the data shown in Table 4, which emphasize that, for a fixed metal, the ε_d shifts to the right towards the Fermi level as the ECN decreases for different crystalline phases. The fcc and hcp structures have very similar values of ε_d , the bcc crystals show a subtle shift, while the sc structures show a pronounced shift. Furthermore, the aforementioned shift of the d -band center, with respect to the filling of the d -band, holds true for fixed phases, regardless of their relative stability, since the trends derive mainly from the electronic nature of the atoms that compose the material.

The integrated DOS, with respect to the energy, up to the limit of the Fermi level yields the number of electrons of occupied states. Then, the magnetic moment can be defined as the difference between integrated spin components of the DOS. The VASP software provides the local magnetic moments from integrated DOS inside the augmentation spheres, as well as the total magnetic moment for the entire unit cell, m_{tot} . Table 5 shows how m_{tot} varies for Fe, Co, Ni and Pd crystals. The m_{tot} is high for bcc and sc Fe, followed by Co and Ni, which do not vary much depending on the structure. Notably, hcp Fe has a null value of m_{tot} , which is possible due to the cancellation of contributions within the unit cell.¹⁵⁰ The magnetic moment is affected by the distance between the

Figure 6 – Side and top views for 1×1 unit cells of bcc(110), fcc(111) and hcp(0001) described using the slab model. The letters A, B and C identify layers, with different letters characterizing distinct environments. The atomic radii are represented arbitrarily and not in scale.



Source: Own study.

atoms and the distribution of electrons, hence, it can change depending on lattice strain; this means that structural optimization affects this property. The Pd metal presents low magnetic moment for the bcc and sc structures, while $m_{tot} = 0$ in the atomic limit, due to the closed electronic shell ($4d^{10}5s^0$). Pd and Ni are similar metals, both have 10 valence electrons and adopt the fcc structure, however, their m_{tot} are not the same; for fcc Pd, it is equal to zero in experimental equilibrium conditions, but a small expansion of the lattice results in a non-zero magnetic moment.¹⁵⁸ Considering that PBE overestimates a_0 , a small m_{tot} can be expected for fcc Pd. This situation, as well as the dispersion effects on this trend, will be reviewed¹⁵⁹ and demonstrated further in Chapter 6.

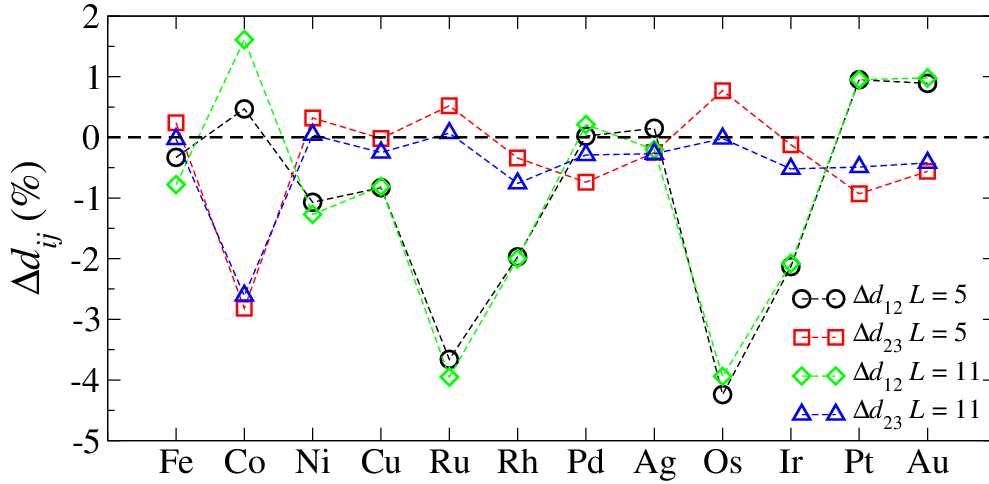
3.2 Transition-metal Surfaces

From the most stable TM crystals, the compact (close-packed) surfaces, fcc(111), bcc(110) and hcp(0001) were studied as models, due to their high stability compared to other more open surface planes.³⁷ Specifically, the surfaces are: Fe(110), Co(0001), Ni(111), Cu(111), Ru(0001), Rh(111), Pd(111), Ag(111), Os(0001), Ir(111), Pt(111) and Au(111). Here, we will discuss some periodic trends and understand how to model TM surfaces.

3.2.1 Procedures to Obtain the Atomic Structure Configurations

The surfaces were constructed using the slab model, demonstrated in Figure 6 from the optimized lattice parameters. The surfaces can be rationalized considering well-defined planes applied to the crystal structure, with replacement of the infinite arrangement of atoms in one of the sides of the plane by a vacuum region of appropriate size, to obtain the metal–vacuum interface. In the slab model, the dimensions of the surface plane are

Figure 7 – Relaxation of the interlayer spacing, Δd_{ij} , for the topmost atoms of slabs with 5 and 11 layers (L) for the surfaces: Fe(110), Co(0001), Ni(111), Cu(111), Ru(0001), Rh(111), Pd(111), Ag(111), Os(0001), Ir(111), Pt(111) and Au(111).



Source: Own study

defined by two numbers, n and m , resulting in a classification for the unit cell of $n \times m$, while L indicates the number of layers. The top view of the 1×1 (1 atom per layer) surfaces is shown in Figure 6. The application of this concept on different crystals results in various crystallographic facets. For the bcc(110) and hcp(0001) surfaces, two types of layers repeat an AB pattern, while the pattern ABC occurs for the fcc(111) surface. The surfaces bcc(110), fcc(111) and hcp(0001) present the D_{2h} , C_{3v} and D_{3h} symmetries, respectively.

3.2.2 Structural Relaxation

The organization of topmost surface atoms exposed to the vacuum affects the properties of the material. When a surface is formed, the structure relaxes, compared to the bulk positions, to compensate for the variations of charge and coordination. This effect was measured by the relaxation of the interlayer spacing as

$$\Delta d_{ij} = \left(\frac{d_{ij} - d_0}{d_0} \right) \times 100 \% , \quad (3.2)$$

in which i and j are counters for the layers, as exemplified from 1 to 5 in Figure 6, Δd_{ij} is the relaxation of the spacing between the layers, d_{ij} is the distance between the layers and d_0 is the equilibrium distance between the layers in the bulk phase.

The Δd_{ij} is a percent variation that represents expansion (if positive) or contraction (if negative) of the interlayer spacing; the results are shown in Figure 7. Most surfaces present a contraction of the first atomic layers; moreover, the relaxation of more internal layers (Δd_{23} , red and blue symbols) is less than 1 %, indicating a gradual approach to the bulk geometry that is expected for the bulk layers, that is, the atoms far from the vacuum

region. For our surfaces, the top and bottom sides of the slab showed symmetric relaxations and, hence, all other properties, such as the local magnetic moments and charges, were symmetric with respect to the center layer. The behaviors are very similar for slabs of 5 and 11 layers, suggesting that 5 layers can be reasonable to observe well-converged trends.

3.2.3 Surface Energy

To characterize the surfaces, the surface energy, σ , was calculated, for 1×1 unit cells, as

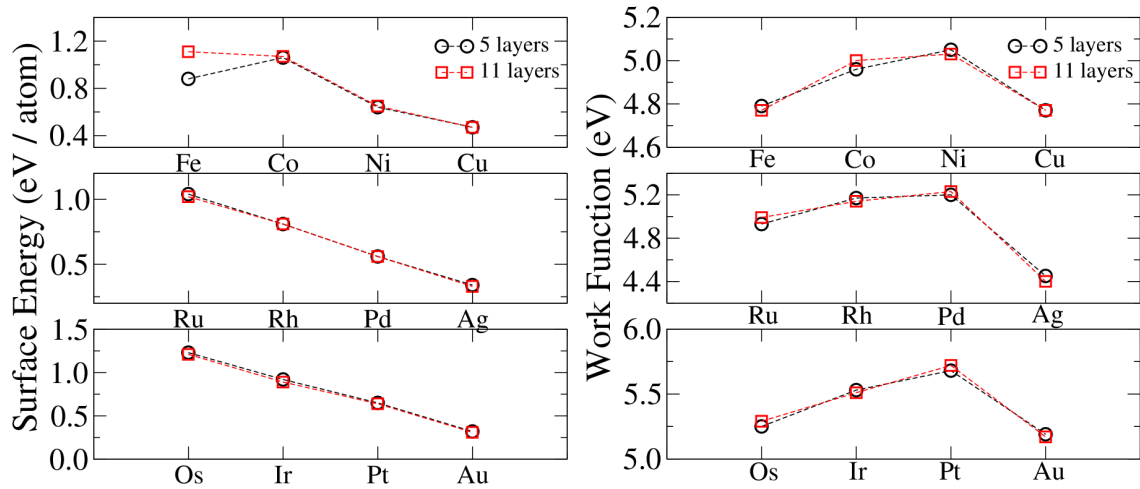
$$\sigma = \frac{1}{2}(E_{tot}^{\text{slab}} - LE_{tot}^{\text{crystal}}), \quad (3.3)$$

in which E_{tot}^{slab} is the total energy of the slab per unit cell (1×1), L is the number of layers and E_{tot}^{crystal} is the total energy per atom for the crystal. The factor 1/2 is included to consider that there are two metal–vacuum interfaces. The calculation of this property is important, considering that its experimental determination is difficult, due to impurities and surface defects that are present in experimental conditions. The results are presented in Figure 8 and Table 6.

The surface energy decreases along the transition periods, from group 8 of the periodic table, due to the d -band filling, with a slightly distinct profile for the $3d$ period. In fact, there is a parabolic profile for σ , such as from Y to Ag,¹⁶⁰ which occurs because the binding is expected to be the strongest when half of the d -band is filled, while it becomes weaker as the d -band is emptied or completely filled. Weak binding facilitates the process of forming the surface, which depends on the number of broken bonds from the crystal; hence, σ follows the same parabolic trend of the binding strength. Notice that the results for this study show only part of the parabolic behavior (from group 8 to 11 of the periodic table). For $3d$ metals, our results show a distinct profile for σ compared to the other periods of the periodic table. First, it is important to notice that the convergence of σ depends on the number of layers. For bcc(100), bcc(110) and bcc(111) Fe surfaces, other authors suggested that slabs of at least 9 layers are required to obtain well-converged results,¹⁶¹ which can explain the difference observed in our results for Fe(110) with 11 and 5 layers. Furthermore, the profile of σ for the $3d$ metals has some natural deviations that were addressed in the literature,¹⁶² and attributed to magnetism.¹⁶³

The results obtained here for σ were compared to reference data from the literature,^{136,143,160,162–164,166} shown in Table 6. Although the profiles obtained for the surface energy versus the type of metal are correct, the deviations with respect to experimental data are significant, such deviations can be attributed to the clear distinction between the theoretical slab model and a real surface subjected to experimental conditions, as commented before. Furthermore, the experimental reference data do not depend on the surface plane, since the experimental surface energies were obtained from liquid metals. Considering other theoretical studies, the deviations could be related to the different

Figure 8 – Surface energy and work function for the surfaces: Fe(110), Co(0001), Ni(111), Cu(111), Ru(0001), Rh(111), Pd(111), Ag(111), Os(0001), Ir(111), Pt(111) and Au(111).



Source: Own study

methodologies employed to calculate the property and technical details, such as the choice of computational parameters, slab construction and different vacuum regions; however, such deviations do not change the aforementioned periodic trends for the TM surfaces. Moreover, comparing our results for σ with the values from a previous study in our group,¹³⁶ which also employed PAW-PBE, we found excellent agreement, within 0.01 eV, except for Fe and Co surfaces, due to deviations from the magnetic moments.

3.2.4 Work Function and Density of States

The work function, Φ , corresponds to the energy required to remove one electron from the surface and put it into the vacuum region. From the Fermi energy, $\varepsilon_{\text{Fermi}}$, and the electrostatic potential in a region far from the surface, $\varepsilon_{\text{vacuum}}^{\text{electron}}$, the work function can be calculated as $\Phi = \varepsilon_{\text{vacuum}}^{\text{electron}} - \varepsilon_{\text{Fermi}}$.^{142,143} The work function is important to study adsorption, because the property depends on the reorganization of atoms and affects the redistribution of the electron density. Hence, the work function change due to adsorption is an interesting property, which will be studied in the next chapters. The profiles of Φ versus the transition periods are shown in Figure 8, while the comparison with reference data is in Table 6.

For various surfaces, the work function can be expected to follow a trend related to the electronic structure of corresponding free atoms, with Φ increasing as the electronic occupation increases. However, for transition metals, the trend is more intricate.¹⁶⁵ Our results indicate that Φ increases with the atomic number, from the group of Fe on each transition period, however, the work function decreases for metals from group 10 to 11. This behavior was observed by other authors in smooth profiles;^{160,162} at the beginning of

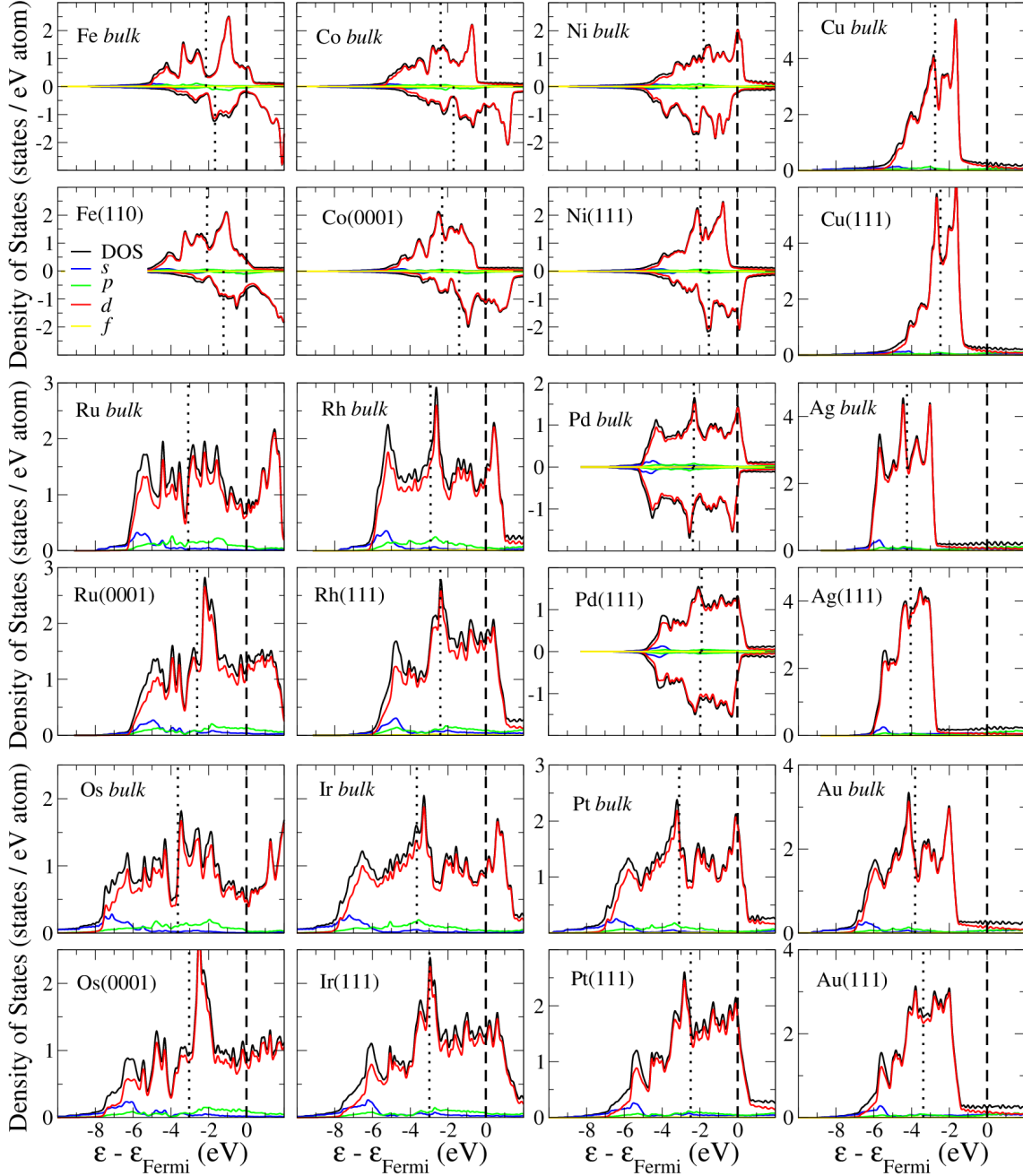
Table 6 – Surface energies, σ , and work functions, Φ , calculated in this study (11-layer slabs) compared to reference data from the literature,^{*,†} indicated between brackets, through percent deviations shown between parentheses, $\Delta\sigma$ and $\Delta\Phi$.

Data ^{*,†}	σ (eV)	σ (J/m ²)	Φ (eV)	
Fe(110), this study	1.11	3.15	4.77	
Literature	0.96 [163] (15.61)	2.48 [164] (27.01)	4.82 [39] (-1.04)	4.50 [165] (6.00)
Co(0001), this study	1.07	3.19	5.00	
Literature	0.94 [163] (13.84)	2.55 [164] (25.24)	4.93 [39] (1.42)	5.00 [165] (0.00)
Ni(111), this study	0.65	1.94	5.03	
Literature	0.90 [163] (-28.07)	2.45 [164] (-20.95)	5.02 [39] (0.20)	5.35 [165] (-5.98)
Cu(111), this study	0.47	1.33	4.77	
Literature	0.50 [143] (-5.26)	1.83 [164] (-27.37)	4.76 [39] (0.21)	4.98 [165] (-4.22)
Ru(0001), this study	1.02	2.56	4.99	
Literature	1.28 [162] (-20.35)	3.05 [164] (-16.09)	5.00 [39] (-0.20)	4.71 [165] (5.94)
Rh(111), this study	0.81	2.06	5.14	
Literature	0.99 [160] (-17.76)	2.70 [164] (-23.76)	5.11 [39] (0.59)	4.98 [165] (3.21)
Pd(111), this study	0.56	1.34	5.23	
Literature	0.56 [166] (0.69)	2.05 [164] (-34.41)	5.25 [39] (-0.38)	5.60 [165] (-6.61)
Ag(111), this study	0.33	0.72	4.40	
Literature	0.55 [160] (-39.39)	1.25 [164] (-42.59)	4.45 [39] (-1.12)	4.74 [165] (-7.17)
Os(0001), this study	1.21	2.94	5.29	
Literature	1.60 [162] (-24.56)	3.45 [164] (-14.67)	5.37 [39] (-1.49)	4.83 [165] (9.52)
Ir(111), this study	0.89	2.21	5.51	
Literature	1.36 [162] (-34.19)	3.00 [164] (-26.39)	5.42 [39] (1.66)	5.76 [165] (-4.34)
Pt(111), this study	0.64	1.51	5.72	
Literature	0.71 [143] (-9.70)	2.48 [164] (-39.18)	5.73 [39] (-0.17)	5.70 [165] (0.35)
Au(111), this study	0.31	0.67	5.17	
Literature	0.35 [166] (-10.60)	1.50 [164] (-55.27)	-5.13 [39] (0.78)	5.31 [165] (-2.64)

* Experimental σ reference obtained from the surface tension of liquids.¹⁶⁴ Theoretical σ references employing diverse methods;^{143, 160, 162–164, 166} σ deviations from previous PAW-PBE calculations in our group¹³⁶ are around 2%, except for Fe and Co.

† Experimental Φ reference,¹⁶⁵ where values for Fe, Co, Ru, Rh and Os were obtained for polycrystalline samples. Theoretical Φ reference (PAW-PBE) reported by other authors.³⁹ Source: Own study. This table displays cited reference data.^{39, 136, 143, 160, 162–166}

Figure 9 – Total and local density of states (DOS, LDOS) for the central (indicated as bulk) and surface layers of 11-layer slabs. The LDOS are decomposed into s -, p -, d - and f -states. The dashed and dotted lines indicate, respectively, the Fermi level and the d -band center.



Source: Own study.

the transition period, Φ increases accompanying the trend for the first ionization potential of the free atoms, due to the reduction of the Fermi energy with the increasing nuclear charges.¹⁶⁰ After complete occupation of the d -band, the more energetic sp states increase the $\varepsilon_{\text{Fermi}}$, hence, decreasing the magnitude of Φ . Our results for Φ deviated by less than 10% from reference data for polycrystalline solids,¹⁶⁵ moreover, our results show higher

values than this reference,¹⁶⁵ which can be related to the high atomic density of our model close-packed planes compared to polycrystalline samples. For increasingly compact surfaces, σ decreases and Φ increases, due to the cleavage of fewer bonds to form the surface, as well as the higher relative stability of the compact facets.¹⁶²

Finally, to demonstrate the effect of coordination in the shift of the d -states, Figure 9 shows the density of states (DOS) for the clean surfaces showing the central atom of the slab (bulk regime) and the topmost atom (surface) for 11-layer slabs. In the center of the slab, the atoms tend to the bulk regime and the DOS profiles are very similar to the DOS of the crystals (Figure 5). The DOS for the surface atom has a different profile, and the main difference is a shift of the d -band towards the Fermi level, due to the reduced coordination of the surface atoms compared to atoms in the center of the slab. For Fe, Co, Ni and Pd, two DOS (up, \uparrow , and down, \downarrow) are shown, due to spin polarization. Considering the surface atoms, for Pd, the up and down centers of the d -states are only 0.06 eV apart, while for Fe, Co and Ni the differences $\varepsilon_{d\uparrow} - \varepsilon_{d\downarrow}$ are of 0.88, 0.90 and 0.44, respectively. In fact, the higher the magnetic moment, the greater the distinction of the DOS for each spin component.⁴⁶ For the atoms at the center of the slabs, this splitting of the d -band centers was smaller, of 0.48, 0.68, 0.37 and 0.04 for Fe, Co, Ni and Pd, respectively, suggesting that spin polarization is greater for low-coordinated atoms compared to the bulk regime.

3.3 Dispersion Effects on the Bulk and Surface Properties

To discuss dispersion effects on the properties of model TM materials, we calculated the PBE+D3 properties for the examples of Ni, Pd and Pt fcc crystals and close-packed surfaces using the same conditions applied to calculate the PBE properties shown in this chapter. Here, we discuss the data for the 5-layer slabs, since this is the same number of layers that will be employed to study adsorption in the next chapters. The results are shown in Table 7.

The dispersion has an attractive nature, hence, there is a small reduction of 0.04, 0.06 and 0.05 Å of the lattice parameters of fcc Ni, Pd and Pt, respectively. Furthermore, the cohesive energies become more negative, indicating greater binding; for example, the cohesive energy was 0.77 eV more negative for fcc Pd with PBE+D3 compared to PBE. Due to the change of a_0 , there is a small reduction of the magnetic moment; for fcc Ni, m_{tot} varied by only 0.01 μ_B , while for fcc Pd the reduction was of 0.07 μ_B . Since the dispersion correction results in more cohesive systems, the surface energy is affected; the σ can be observed as the energy required to create the surface, hence, the creation of a surface from more cohesive crystals tends to require more energy, resulting in greater σ with PBE+D3. The effects of the dispersion interactions on the work function are very small, which was also observed by other authors.³⁹ This occurs because the dispersion correction only affects the electronic properties indirectly, due to the structural changes,

Table 7 – Effect of the dispersion correction (PBE compared to PBE+D3) on the properties of fcc crystals and fcc(111), 5-layer slabs, surfaces of Ni, Pd and Pt metals. Equilibrium lattice parameter, a_0 , cohesive energy per atom, E_{coh} , total magnetic moment, m_{tot} , surface energy, σ , work function, Φ , and relaxation of the interlayer spacing for the topmost layers, Δd_{12} .

		Ni		Pd		Pt	
		PBE	PBE+D3	PBE	PBE+D3	PBE	PBE+D3
fcc	a_0 (Å)	3.52	3.48	3.94	3.88	3.97	3.92
	E_{coh} (eV)	-4.70	-5.10	-3.77	-4.35	-5.45	-6.22
	m_{tot} (μ_B)	0.63	0.62	0.40	0.33	0.00	0.00
fcc(111)	σ (eV)	0.64	0.88	0.56	0.87	0.65	1.04
	Φ (eV)	5.05	5.08	5.20	5.21	5.68	5.68
	Δd_{12} (%)	-1.07	0.00	0.02	1.25	0.95	1.93

as observed for the different a_0 and Δd_{12} . Regarding the DOS, other authors^{9,37} verified that the dispersion correction does not affect significantly the DOS of clean surfaces; there is a small broadening effect for the d -band, but the profile is virtually unchanged. The PBE+D3 framework was employed in all subsequent chapters of this thesis.

3.4 Summary

The results discussed in this chapter allowed us to better understand the nature of TM model materials through a discussion of their properties along the transition periods. We discussed that the bulk cohesive energy increases towards the center of the periodic table, from the right, while the average bond lengths tend to, consequently, decrease. Moreover, we reproduced the properties and periodic trends for surface energy and work function of close-packed TM surfaces. We also discussed the effects of the dispersion correction for the aforementioned properties. Our results reproduce natural, well-known, trends for the metals, thus, validating our methodology. Moreover, this preliminary study brought us closer to our goals through the demonstration of the dependence of several properties on the electronic nature of the TM, which will be important to discuss the results, concerning adsorption, presented in the next chapters.

For the subsequent chapters of this thesis and articles published while developing this thesis,^{145,146,159} all relevant bulk and clean surface properties were recalculated using the conditions established for each self-contained study; for example, using the D3 correction and respecting the specific POTCAR files, cutoff energies and convergence criteria defined for each chapter. Hence, small differences in the properties are possible, but all variations are within expected errors from DFT calculations (order of meV), considering that the computational parameters satisfy the convergence of the properties. All details concerning this subject for the thesis were explained in Chapter 2.

4 THE EFFECTS OF SUBSTRATE PARTICLE SIZE ON THE ADSORPTION OF CO₂, CO, H₂O AND H₂ ON TRANSITION-METAL SUBSTRATES

This chapter is an adaptation for the thesis, with permission, of a published article.¹⁴⁵ Reproduced by permission of the PCCP Owner Societies from Paulo C. D. Mendes, Vivianne K. Ocampo-Restrepo, Juarez L. F. Da Silva, *Ab Initio* Investigation of Quantum Size Effects on the Adsorption of CO₂, CO, H₂O, and H₂ on Transition-metal Particles. *Physical Chemistry Chemical Physics*, v. 22, n. 16, p. 8998-9008 (2020) <<https://doi.org/10.1039/D0CP00880J>>.

Further details about the permissions are in Appendix A. Additional analyses and resources were published in the referred article and its Supporting Information.¹⁴⁵

4.1 Introduction and State of the Art

The study discussed herein is based on the influence of substrate particle size on the adsorption of model molecules, which is motivated by the use of TM nanoparticles as catalysts.^{14,17,167,168} The focus of this investigation was CO₂, considering its central role in the critical environmental and economic subject of CO₂ capture and utilization. Through the use of catalysts, CO₂ can be converted into methanol, solid carbonaceous materials, hydrocarbons, formic acid, among other products that can be employed as monomers, fuels or other moieties.³ For example, the valuable syngas (a mixture of H₂ and CO) is one of the possible target products that can open a great variety of further routes.¹⁶⁹ The reduction of CO₂ can involve several different molecules that can spectate, react, poison the catalyst or be obtained as products. Concerning the type of metal, some 3d metals (Co, Ni and Cu) were chosen for the present study, because they are considered as good components to improve the catalytic activity and mitigate the cost of using noble metals, although other problems, such as deactivation, are still challenges to overcome before reaching the optimal material.¹² The focus of this study was the adsorption of CO₂, but additional important model molecules involved in the reduction process were studied comparatively: CO, H₂O and H₂.⁴⁸ This introduction focuses on CO₂, while relevant literature concerning the adsorption of the additional model molecules is mentioned opportunely along the discussion of results.

The adsorption of CO₂ can occur through two clear modes of interaction (physisorption and chemisorption). First, considering surfaces, the molecule can bind weakly, through physisorption, at about 3.0 Å from TM surfaces, with negligible geometric distortions and constant adsorption energies, of approximately -0.30 eV, for several types of TM.^{52,170} In the case of stronger interaction (chemisorption), CO₂ approaches the TM atom, removes charge from the TM substrate and, as a consequence, the molecular angle bends as π -type

orbitals are occupied and stabilized.^{50,51} For chemisorption, the charge transferred can be related to the adsorption energies, which are not constant for different types of TM. For some TM, such as Cu, Au and Ag, physisorption is consistently observed as the energetically preferable condition.^{52,54}

Considering particle size, it is expected that small clusters promote stronger adsorption than compact surfaces, because of the lower coordination of the atoms,^{58,171} which shift the d -states in the direction of the Fermi level. Moreover, surface modifications can be exploited for similar effects on the coordination and d -states. One of the most important examples is Cu. Small Cu clusters promote stronger CO₂ adsorption than compact surfaces,¹⁷¹ but they do not stabilize the chemisorbed structure;^{58,171} the same trend is observed for small Cu clusters supported on close-packed Cu surfaces.¹⁷² However, CO₂ can chemisorb and dissociate on stepped Cu surfaces^{55,57} and small nanoparticles.⁵⁶ These varied outcomes show that the particle size be strategic to control CO₂ adsorption, moreover, there are experimental efforts connected to the optimization of catalytic activities through substrate particle size effects.^{173–175} The interest to study such effects on the adsorption is not only due to the area per volume ratio and presence of low-coordinated atoms, compared to condensed phases, but also due to thermodynamic, electromagnetic and quantum effects that influence the properties of nanoparticles in the atomistic level.^{19,176}

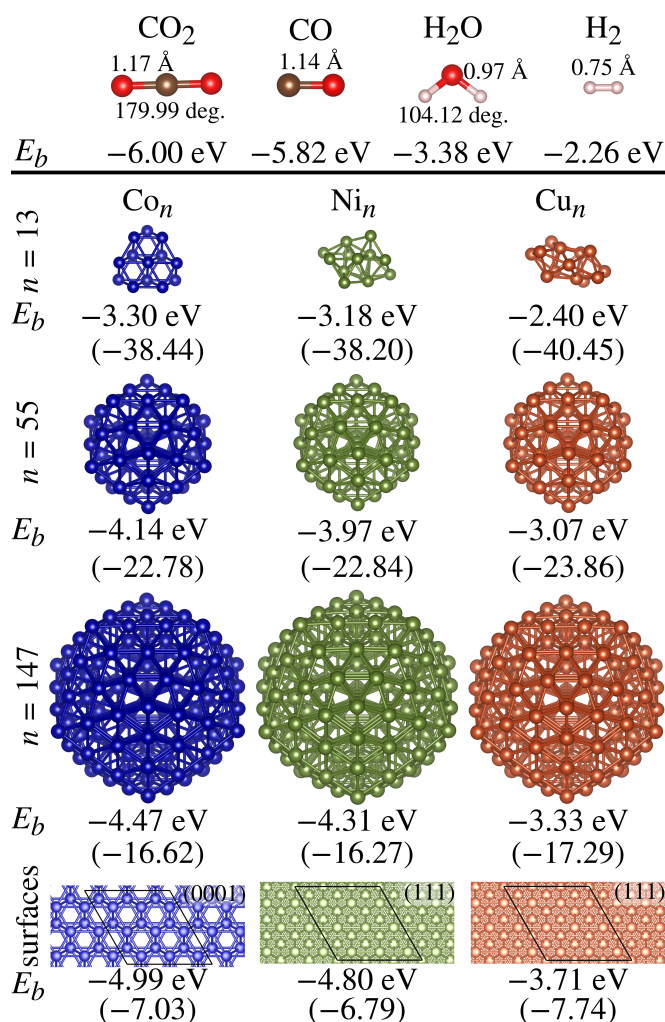
The ability to control the type of CO₂ interaction would be valuable, especially for the aforementioned TM that do not stabilize chemisorbed CO₂ easily. However, the physisorbed state does not imply that the substrate is not a viable catalyst, since the reaction could involve steps in which linear CO₂ could interact with other adsorbed species.¹⁷⁷ Furthermore, coverage, coadsorption, temperature and solvation effects affect the experimental observations. It is evident that the substrate size is important for the CO₂ conversions; however, the effects of substrate particle size on the adsorption of CO₂, and other adsorbates involved in CO₂ reduction (CO, H₂O and H₂), on TM particles is still a topic of active research. Here, to contribute to build this knowledge, a systematic investigation was performed to study the adsorption properties for the interaction of CO₂, CO, H₂O and H₂ with TM_{*n*} nanoparticles, namely, Co_{*n*}, Ni_{*n*} and Cu_{*n*} ($n = 13, 55, 147$) nanoclusters and model close-packed surfaces, which model large particles, namely, Co(0001), Ni(111) and Cu(111).

4.2 Isolated Molecules and Substrates

The most stable optimized configurations of isolated molecules and substrates are depicted in Figure 10 along with some properties, while additional characteristics of the TM_{*n*} clusters are shown in Table 8. Complementary bulk and surface properties were discussed in Chapter 3.

The binding energies per atom were calculated as $E_b = (E_{tot}^{system} - \sum_i E_{tot}^{free\ atom})/N$,

Figure 10 – Optimized atomic structures of gas-phase molecules (CO_2 , CO , H_2O and H_2) transition-metal clusters (Co_n , Ni_n and Cu_n , for $n = 13, 55, 147$) and close-packed surfaces. The binding energies per atom, E_b , are shown below the configurations; moreover, the molecular angles and bond lengths are displayed. Between parentheses, we show the percent deviations of E_b , with respect to the bulk cohesive energies.



Source: Own study reproduced with permission for the thesis.¹⁴⁵ Reproduced from Ref. 145 with permission from the PCCP Owner Societies.

in which N is the number of atoms, E_{tot}^{system} and $E_{tot}^{\text{free atom}}$ are, respectively, the total electronic energies of the bound system and of the isolated atom in the vacuum, summed over all atoms of the system. For the isolated molecules, the deviations from previous calculations^{58,108} and spectroscopic data¹⁷⁸ were smaller than 1.55 and 7.92% for the geometric properties and binding energies, respectively. Moreover, the E_b increases from H_2 to H_2O , due to the greater ionic character for H_2O , as well as and from CO to CO_2 , due to the more stable oxidation state of carbon for CO_2 .

Considering the TM substrates, the model TM_n particles ($n = 13, 55, 147$) were the most stable compact structures for each TM size. The icosahedron structure was

Table 8 – Characterization of Co_n , Ni_n and Cu_n ($n = 13, 55, 147$) clusters. Binding energy per atom, E_b , total magnetic moment for the unit cell, m_{tot} , effective coordination number, ECN (in number of nearest neighbors, NNN) and average bond length, d_{av} .

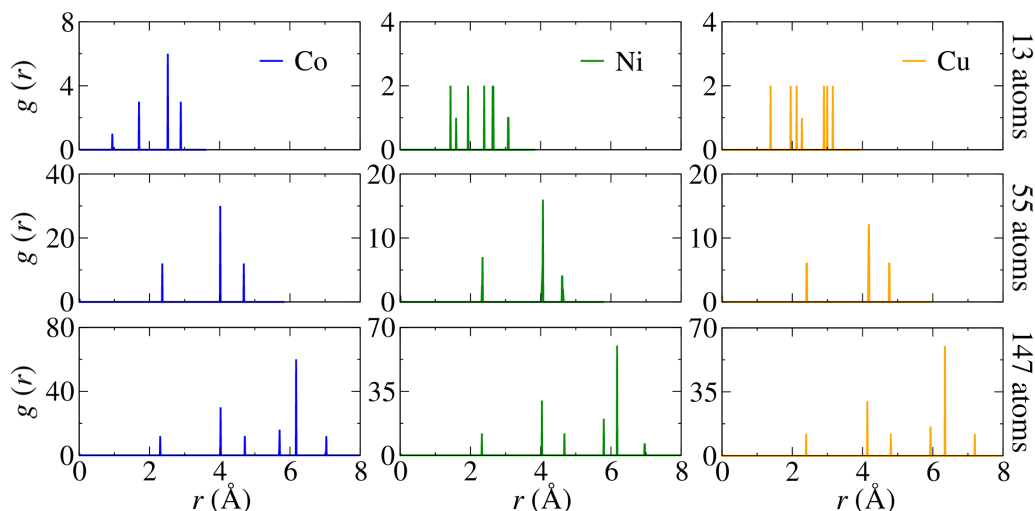
Cluster	E_b (eV)	m_{tot} (μ_B)	ECN (NNN)	d_{av} (\AA)
Co_{13}	-3.30	27	5.45	2.33
Ni_{13}	-3.18	10	5.67	2.36
Cu_{13}	-2.40	1	5.69	2.45
Co_{55}	-4.14	105	8.37	2.43
Ni_{55}	-3.97	40	8.39	2.43
Cu_{55}	-3.07	3	8.39	2.50
Co_{147}	-4.47	259	9.36	2.44
Ni_{147}	-4.31	100	9.35	2.44
Cu_{147}	-3.33	1	9.38	2.51

Source: Own study reproduced with permission for the thesis.¹⁴⁵ Reproduced from Ref. 145 with permission from the PCCP Owner Societies.

adopted for the TM_{55} and TM_{147} clusters of Cu, Ni and Co, which is stable for these metals.^{35,179,180} However, for Co_{13} , Ni_{13} and Cu_{13} different geometries were employed, based on previous studies that obtained structures of higher stability.^{135,181} Nevertheless, all configurations are close-packed, although TM_{13} are not icosahedron particles, such as Co_{13} , which is composed of two stacked atomic planes. To characterize the structures, we show the radial distribution function in Figure 11 and properties in Table 8. The function shows the atomic positions represented by a small number of peaks, which is characteristic of a regular geometry, indicating that the geometric distortions of the optimized TM_n are small. The infinite limit for large particles was simulated using stable $\text{Co}(0001)$, $\text{Ni}(111)$, and $\text{Cu}(111)$ models, which were constructed from the optimized lattice parameters of the most stable corresponding crystal phases (Co hcp, Ni fcc and Cu fcc).

For the TM substrates, the E_b increases with the substrate size, approaching the bulk characteristic cohesive energy, as demonstrated by the smaller deviations of E_b from the bulk regime for increasing particle size (Figure 10). This behavior is well defined because the clusters are not defected and the average effective coordination¹⁵¹ increases with substrate size; namely, 5.60, 8.38, 9.36, and 10.81 nearest neighbors for TM_{13} , TM_{55} , TM_{147} and TM slabs, respectively, on average considering all atoms. Moreover, along the transition periods, the results agree with the expected increased d_{av} and decreased E_b , as discussed in Chapter 4 for the crystals.^{44,182} The magnetic moments, m_{tot} of the lowest energy nanoclusters are in agreement with reports from other authors:^{35,183} the Co and Ni substrates present significant spin polarization and the m_{tot} decreases with increasing substrate size, due to the broadening of the DOS as coordination increases.¹⁸⁴

Figure 11 – Radial distribution function, $g(r)$, with respect to the geometric center of the clusters ($r = 0$) for the isolated Co_n , Ni_n and Cu_n clusters for $n = 13, 55$ and 147 .



Source: Own study reproduced with permission for the thesis.¹⁴⁵ Reproduced from Ref. 145 with permission from the PCCP Owner Societies.

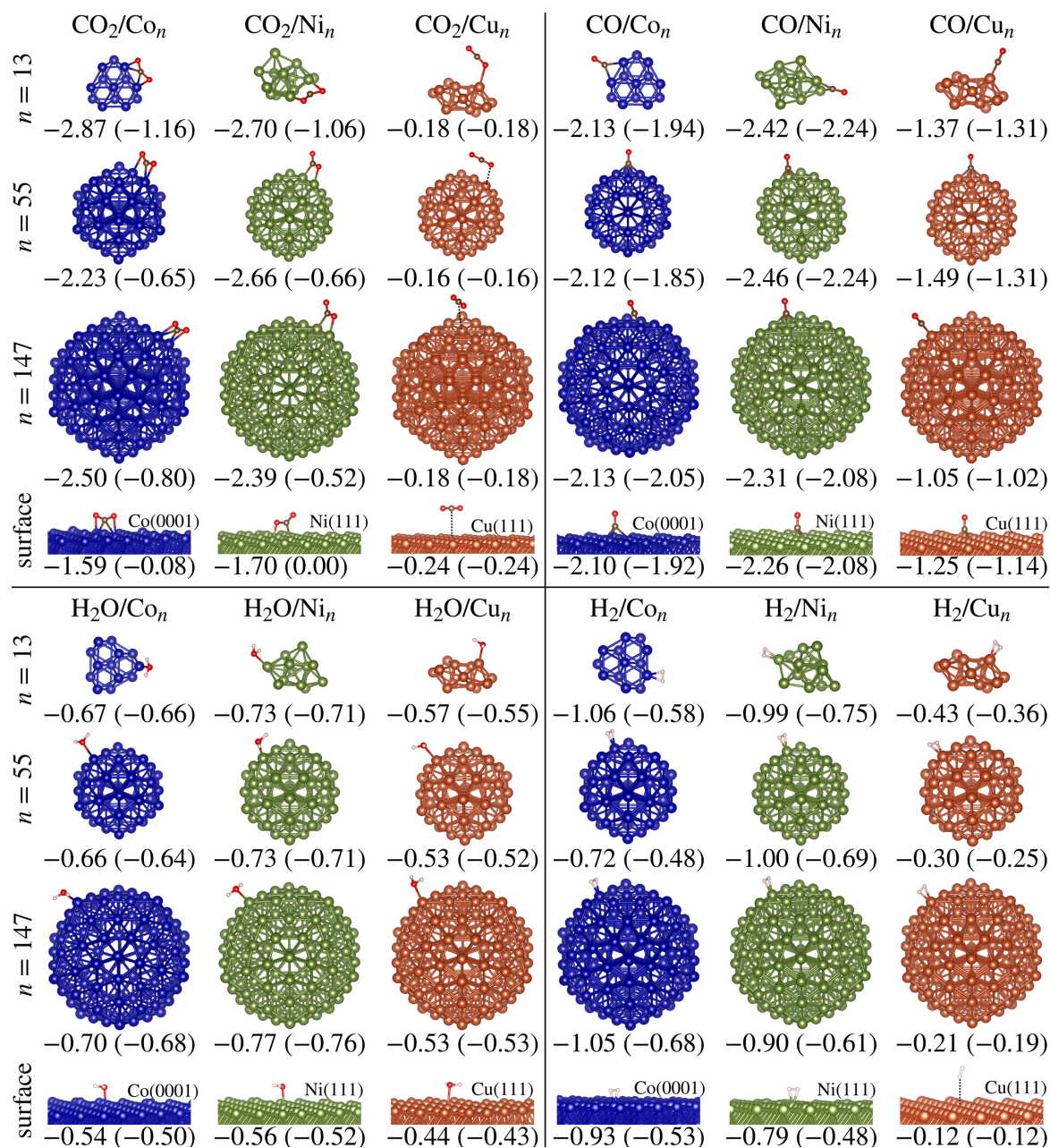
For the limit of large particles, the models were validated by comparing the clean surface properties with the bulk phases and the literature.^{39,113,153,154} These surfaces were studied previously in great detail,³⁹ and were discussed in Chapter 3. In summary, the results show well-converged trends; the D3 correction yields reduced lattice parameters, increased binding and slightly reduced magnetic moments, due to the attractive character of the correction, while the clean surfaces correctly reproduce the experimental properties.

4.3 Procedures to Obtain Adsorption Atomic Structure Configurations

For the adsorbed systems, a set of atomic configurations that allows effective exploration of the potential energy surface is necessary, thus, it is important to understand the variety of adsorption sites available for each substrate size. The TM_{13} clusters do not have well-defined planes, therefore, the adsorption sites can be distinguished through the coordination of the TM atoms.^{58,185} For TM_{55} and TM_{147} , the icosahedron configuration features high-symmetry 1-fold (top), 2-fold (bridge) and 3-fold (hcp or fcc hollow) sites, which are further distinguished by the type of region on the particle, such as vertices, edges or (111) facets; various regions are symmetrically equivalent.^{186,187} Analogously, the extended surfaces feature hollow, bridge and top high-symmetry sites.¹⁸⁸

To obtain the starting sets of adsorption structures, all of the aforementioned high-symmetry sites were considered on facet, edge, and vertex regions considering the adsorbates at about 2.0 \AA from the TM atoms. Furthermore, for CO_2 , linear and bent OCO angles (about 130°) were considered, to avoid bias towards a specific local minimum configuration. As an exception, for $\text{Mol}/\text{TM}_{13}$, the starting structures were the non

Figure 12 – Lowest energy adsorption structures of CO₂, CO, H₂O and H₂ adsorbed on the Co_n, Ni_n, and Cu_n ($n = 13, 55, 147$) nanoclusters and on the respective compact surfaces. Below the structures, we show the interaction energy, E_{int} (eV), with the adsorption energy, E_{ad} (eV), indicated between parenthesis energies.



Source: Own study reproduced with permission for the thesis.¹⁴⁵ Reproduced from Ref. 145 with permission from the PCCP Owner Societies.

degenerate configurations obtained from a previous investigation focused on the adsorption on the TM₁₃ nanoclusters.⁵⁸ Moreover, for Mol/TM₁₄₇, to obtain configurations sufficient to study the size effects at affordable computational costs, a limited number of starting adsorption structures was constructed (at least two) based on the lowest energy structures obtained for the other particle sizes, this is not expected to impair the results of the study,

considering some expanded sets illustrated in Appendix D, which showed small energetic changes for different adsorption sites on TM₁₄₇. All structures were relaxed before any analyses.

4.4 Adsorption of CO₂, CO, H₂O and H₂ on Co, Ni and Cu Substrates of Various Sizes

The optimized lowest energy adsorption configurations for the interaction of CO₂, CO, H₂O and H₂ on Co, Ni and Cu nanoparticles of various sizes are shown in Figure 12, while the complete sets of configurations studied for each Mol/TM system (with Mol indicating the molecule) are illustrated in Appendix D.

For CO₂/Co, the molecule bends and adsorbs via the C atom on the edges of the clusters and bridge sites. A similar trend occurs for CO₂/Ni₁₃, however, as the substrate size increases, CO₂ rotates and aligns one of the C–O bonds away from the nanocluster, which is accompanied by a small decrease of the molecular angle. Despite the geometric differences of the two aforementioned structures, their energy difference is of only about 1 meV in the case of CO₂/Ni₅₅. Considering CO₂/Cu, although the adsorbate maintains a linear OCO angle as the substrate size changes, it reorients from tilted to an almost parallel orientation, in relation to the substrate. Furthermore, bent CO₂ adsorbed on Cu was only found for the smaller particles and at high energy configurations: 109 (Cu₁₃, bridge site) and 198 meV (Cu₅₅, bridge site, edge region) higher than each respective most stable configuration.

As expected, CO binds through the carbon atom for all systems;^{185,189,190} however, there are clear changes of the most stable adsorption site for different substrate sizes. Particularly, for CO/Cu, there is alternation of the preference for hollow and top adsorption sites in the following sequence: top (Cu₁₃), fcc hollow (Cu₅₅), top (Cu₁₄₇) and fcc hollow (Cu(111)). Similarly, this is apparent for Co between bridge and hollow sites; in contrast, for Ni, the hollow site is energetically favored for all substrate sizes, except for Ni₁₃ that showed a bridge site preference, due to the unique morphology of Ni₁₃. For H₂O and H₂, top sites are the most favorable for all particle sizes, but H₂ binds to vertex and edge regions depending on the TM and substrate size. It is noteworthy that H₂ adsorption can change significantly with coverage;¹⁹¹ moreover, for Cu(111), H₂ is tilted in relation to substrate, as was observed by other researchers.¹⁹²

4.4.1 Adsorption Energy

The adsorption strength was investigated through the adsorption energy,

$$E_{ad} = E_{tot}^{Mol/sub} - E_{tot}^{Mol} - E_{tot}^{sub}, \quad (4.1)$$

in which $E_{tot}^{Mol/sub}$ is the total electronic energy of the adsorbed system, while E_{tot}^{Mol} and E_{tot}^{sub} are the total electronic energies of the isolated molecule and substrate, respectively.

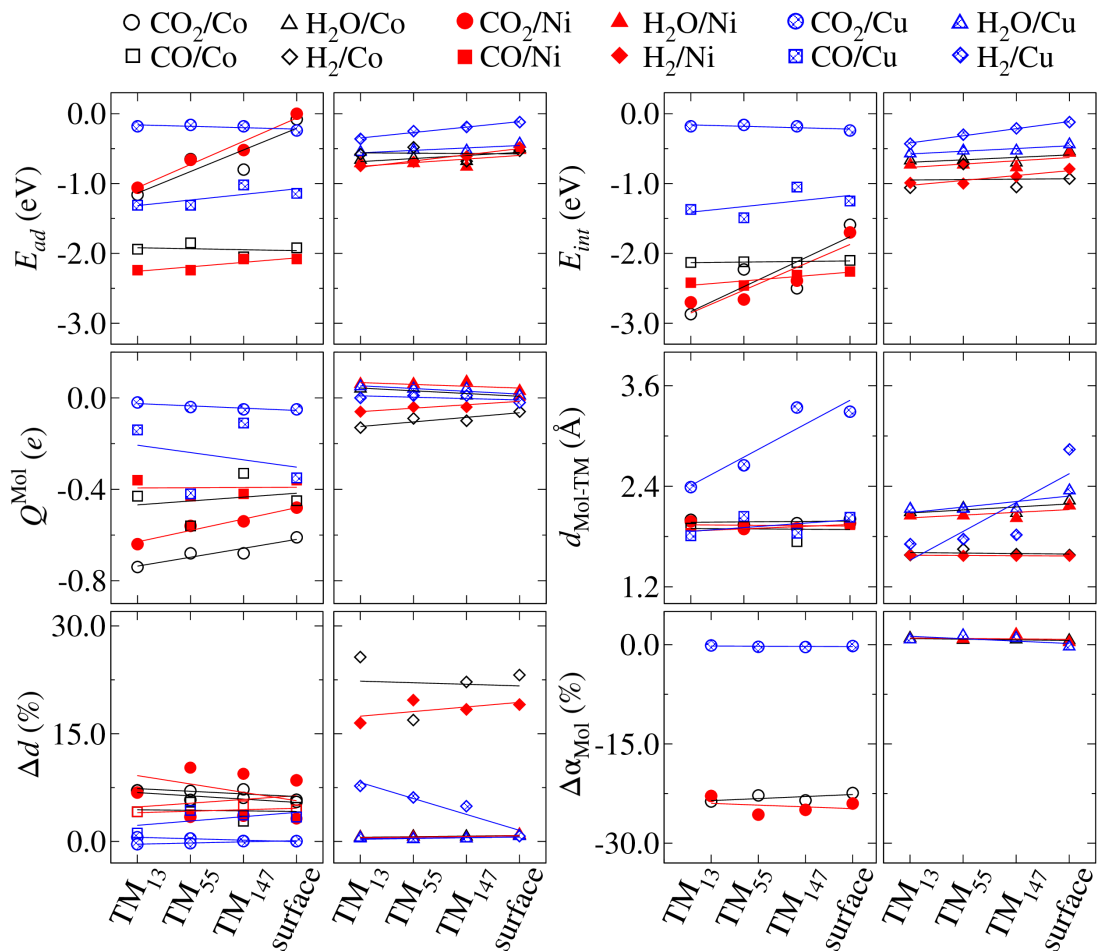
Table 9 – Adsorption energy, E_{ad} , interaction energy, E_{int} , and deformation energies for the molecules and substrates, ΔE_{tot}^{Mol} and ΔE_{tot}^{sub} , respectively, for the most stable configurations of CO₂, CO, H₂O or H₂ adsorbed on TM substrates of different size scales; namely, Co_{*n*}, Ni_{*n*} and Cu_{*n*} ($n = 13, 55, 147$) nanoclusters and with the Co₍₀₀₀₁₎, Ni₍₁₁₁₎ and Cu₍₁₁₁₎ indicating the extended surfaces.

Structure	E_{ad} (eV)	E_{int} (eV)	ΔE_{tot}^{Mol} (eV)	ΔE_{tot}^{sub} (eV)	Structure	E_{ad} (eV)	E_{int} (eV)	ΔE_{tot}^{Mol} (eV)	ΔE_{tot}^{sub} (eV)
CO ₂ /Co ₁₃	-1.16	-2.87	1.67	0.04	H ₂ O/Co ₁₃	-0.66	-0.67	0.00	0.01
CO ₂ /Co ₅₅	-0.65	-2.23	1.51	0.07	H ₂ O/Co ₅₅	-0.64	-0.66	0.00	0.01
CO ₂ /Co ₁₄₇	-0.80	-2.50	1.61	0.09	H ₂ O/Co ₁₄₇	-0.68	-0.70	0.00	0.01
CO ₂ /Co ₍₀₀₀₁₎	-0.08	-1.59	1.40	0.11	H ₂ O/Co ₍₀₀₀₁₎	-0.50	-0.54	-0.01	0.04
CO ₂ /Ni ₁₃	-1.06	-2.70	1.55	0.08	H ₂ O/Ni ₁₃	-0.71	-0.73	0.00	0.02
CO ₂ /Ni ₅₅	-0.66	-2.66	1.93	0.06	H ₂ O/Ni ₅₅	-0.71	-0.73	0.00	0.01
CO ₂ /Ni ₁₄₇	-0.52	-2.39	1.79	0.08	H ₂ O/Ni ₁₄₇	-0.76	-0.77	0.00	0.01
CO ₂ /Ni ₍₁₁₁₎	0.00	-1.70	1.62	0.08	H ₂ O/Ni ₍₁₁₁₎	-0.52	-0.56	-0.01	0.05
CO ₂ /Cu ₁₃	-0.18	-0.18	0.00	0.00	H ₂ O/Cu ₁₃	-0.55	-0.57	0.00	0.02
CO ₂ /Cu ₅₅	-0.16	-0.16	0.00	0.00	H ₂ O/Cu ₅₅	-0.52	-0.53	0.00	0.01
CO ₂ /Cu ₁₄₇	-0.18	-0.18	0.00	-0.01	H ₂ O/Cu ₁₄₇	-0.53	-0.53	0.00	0.00
CO ₂ /Cu ₍₁₁₁₎	-0.24	-0.24	0.00	0.00	H ₂ O/Cu ₍₁₁₁₎	-0.43	-0.44	-0.01	0.02
CO/Co ₁₃	-1.94	-2.13	0.11	0.08	H ₂ /Co ₁₃	-0.58	-1.06	0.44	0.04
CO/Co ₅₅	-1.85	-2.12	0.21	0.06	H ₂ /Co ₅₅	-0.48	-0.72	0.21	0.03
CO/Co ₁₄₇	-2.05	-2.13	0.05	0.03	H ₂ /Co ₁₄₇	-0.68	-1.05	0.34	0.02
CO/Co ₍₀₀₀₁₎	-1.92	-2.10	0.15	0.04	H ₂ /Co ₍₀₀₀₁₎	-0.53	-0.93	0.37	0.03
CO/Ni ₁₃	-2.24	-2.42	0.11	0.06	H ₂ /Ni ₁₃	-0.75	-0.99	0.20	0.03
CO/Ni ₅₅	-2.24	-2.46	0.16	0.06	H ₂ /Ni ₅₅	-0.69	-1.00	0.28	0.03
CO/Ni ₁₄₇	-2.08	-2.31	0.16	0.07	H ₂ /Ni ₁₄₇	-0.61	-0.90	0.25	0.03
CO/Ni ₍₁₁₁₎	-2.08	-2.26	0.13	0.05	H ₂ /Ni ₍₁₁₁₎	-0.48	-0.79	0.26	0.04
CO/Cu ₁₃	-1.31	-1.37	0.01	0.06	H ₂ /Cu ₁₃	-0.36	-0.43	0.05	0.02
CO/Cu ₅₅	-1.31	-1.49	0.11	0.07	H ₂ /Cu ₅₅	-0.25	-0.30	0.03	0.02
CO/Cu ₁₄₇	-1.02	-1.05	0.01	0.02	H ₂ /Cu ₁₄₇	-0.19	-0.21	0.02	0.00
CO/Cu ₍₁₁₁₎	-1.14	-1.25	0.08	0.03	H ₂ /Cu ₍₁₁₁₎	-0.12	-0.12	0.00	0.00

Source: Own study reproduced with permission for the thesis.¹⁴⁵ Reproduced from Ref. 145 with permission from the PCCP Owner Societies.

Moreover, the interaction energy, E_{int} , was expressed considering the energies of the isolated systems calculated for the fixed simulation box and atomic positions defined by each respective optimized adsorption structure. Therefore, E_{int} can be related to E_{ad} through $E_{int} = E_{ad} - \Delta E_{tot}^{Mol} - \Delta E_{tot}^{sub}$, where ΔE_{tot}^{Mol} and ΔE_{tot}^{sub} are the deformation energies for the molecule and cluster, respectively, which indicate the energy difference between the most stable optimized system and the same species with geometry fixed after deformations due to adsorption. The results are shown in Figures 12, 13 and 14. Furthermore, in Table 9 we show the data for adsorption, interaction and deformation

Figure 13 – Adsorption properties versus substrate particle size for the most stable adsorption configurations. Linear regressions are indicated to guide the eyes through the data. The properties are: adsorption energy, E_{ad} , interaction energy, E_{int} , total effective charge of the adsorbed molecule, Q^{Mol} , shortest distance between an atom of the molecule and a TM, d_{Mol-TM} , percent variations of the molecular bond lengths, Δd , and percent variations of the molecular angles, $\Delta\alpha_{Mol}$.



Source: Own study reproduced with permission for the thesis.¹⁴⁵ Reproduced from Ref. 145 with permission from the PCCP Owner Societies.

energies.

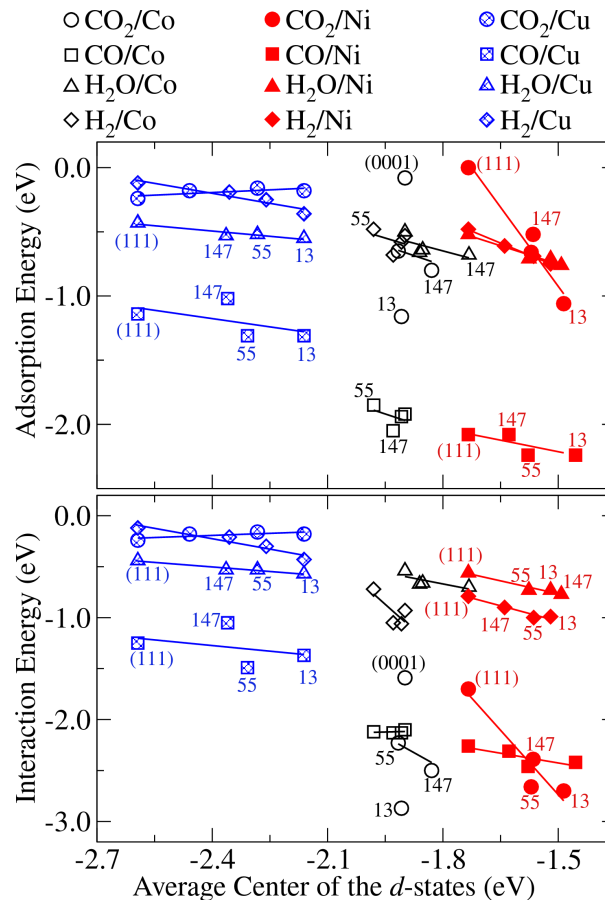
For physisorbed systems, the deformation energies are very small, around 10^{-2} eV, moreover, the deformation energy for the molecule was almost always greater than the term for the TM substrate, which shows that the substrates are stable, while the molecules are more flexible geometrically. The deformation energies of the molecule can be significant, especially for CO₂ which is affected by the simultaneous perturbations of its C–O bonds and OCO angle. In such cases, it is crucial to evaluate the adsorption strength through both E_{ad} and E_{int} . For example, CO₂/Ni(111) shows $E_{ad} = 0.00$ eV, suggesting that the systems do not bind strongly. However, this seems conflicting since the OCO angle is bent, which is typical of chemisorption; after considering the deformation energies, one finds

$E_{int} = -1.70$ eV, which suggests strong interaction. In such case, the small adsorption energy can be related to a large deformation energy of CO_2 , $\Delta E_{tot}^{\text{Mol}} = 1.62$ eV and, although the binding is strong, it is not stable. Similarly, E_{ad} is less negative than expected for $\text{CO}_2/\text{Co}(0001)$. Here, CO_2 is the most susceptible adsorbate to such E_{ad} variations, but this effect occurs for any molecule and substrate. For CO and H_2 the effect is not negligible, because of the bond stretching, while for H_2O adsorption the effect is negligible and the geometric structural perturbations of the H_2O molecule are small.

Particle size strongly affects the adsorption strength for CO_2 , while it has almost no effect for H_2O and causes small oscillations for CO and H_2 , due to the distinct adsorption sites for different substrate sizes. At first, the adsorption strength could be expected to increase categorically with decreasing particle size, due to the lower coordination of the TM atoms, which could promote stronger binding in the smaller particles. Our results shows such behavior for some systems (for example, CO_2/Ni and H_2/Cu) and almost always comparing TM_{13} with the surfaces, which are the extremes of our size range. However, this trend can be deviated due to oscillations of the adsorption properties, as presented in Figure 13, which is expected for a non scalable regime. In fact, more specific trends or oscillations can be expected for more detailed size ranges around each of the TM_n particle sizes investigated herein. Other authors^{40,41} reported that the adsorption strength for CO on Pt and Pd decrease abruptly with increasing size for small cluster sizes (up to 30 atoms), there is an intermediate trend as the particle size increases before the behavior slowly approaches the extended surface limit.^{40,41} Considering the type of TM, Co and Ni show a trend for stronger interaction with all molecules, while the interactions are weaker with Cu. The adsorption strength is affected by many factors, such as the type of TM, its capacity to donate or receive charge and its coordination, particle size, the type of adsorption site and its environment (edge, vertex, surface of the nanoparticle), particle morphology, among others. All of these factors affect the electronic structure of the TM atoms closer to the adsorbate, hence, the d -states can be used to investigate the adsorption strength.¹⁹³

For periodic systems, the d -band model considers the position of the d -states with respect to the Fermi level to predict the adsorption strength.^{44,182} Motivated by this model, we considered a similar approach for the nanoclusters. For this, the center of occupied d -states was calculated as the center of the distribution of d -states, with each sampled ε weighted by the density of d -states for the TM close to the molecule, which is an expectation value of ε averaged by the number of d -electrons. The results are shown in Figure 14. As the substrate size decreases, so can the coordination of surface atoms and the center of d -states can move in the direction of the Fermi level, which promotes increased adsorption strength. Natural deviations from the model can occur because hybridization is not the only factor driving adsorption.³⁹ For all adsorbates on Cu and Ni, the profiles are almost linear, with exceptions for CO and CO_2 , suggesting that additional effects,

Figure 14 – Adsorption and interaction energy versus the average center of the occupied, up and down, d -states considering the TM atoms closer to the adsorbates. The substrate particle size is indicated next to some symbols.



Source: Own study reproduced with permission for the thesis.¹⁴⁵ Reproduced from Ref. 145 with permission from the PCCP Owner Societies.

such as the formation of dipoles and charge transfer, impact the adsorption. For Co, the model did not show linear profiles, which could be related to the high spin polarization.⁴⁶ The conclusions are similar for E_{ad} and E_{int} versus the center of the d -states, with small variations due to the deformation energies.

4.4.2 Geometric Properties

The geometries of the adsorbed systems are important to understand how different TM particle sizes affect the molecules. To investigate the proximity between the two interacting parts, the shortest distances between an atom of the adsorbate and a TM, d_{Mol-TM} , are shown in Figure 13. For CO_2 , the d_{Mol-TM} varies only slightly for different particle sizes, except within the Cu set for Cu_{55} and Cu_{13} , due to the different orientations of the adsorbate. There is a trend for small d_{Mol-TM} for TM_{13} , followed by small oscillations and an increase of the property as the particle size increases, which agrees with the trend for the adsorption strength. The oscillations can be related to alternating adsorption sites,

Table 10 – Percent variations of molecular bond lengths ($\Delta\text{O-C}$, $\Delta\text{H-H}$ and $\Delta\text{H-O}$) and angles (ΔOCO and ΔHOH), with respect to the gas-phase molecules, for the most stable energy configurations of CO_2 , CO , H_2O or H_2 adsorbed on TM substrates of different size scales; namely, Co_n , Ni_n and Cu_n ($n = 13, 55, 147$) nanoclusters and with the $\text{Co}_{(0001)}$, $\text{Ni}_{(111)}$ and $\text{Cu}_{(111)}$ indicating the extended surfaces.

Structure	$\Delta\text{O1-C}$ (%)	$\Delta\text{O2-C}$ (%)	ΔOCO (%)	Structure	$\Delta\text{H1-H2}$ (%)	$\Delta\text{H1-O}$ (%)	$\Delta\text{H2-O}$ (%)	ΔHOH (%)
$\text{CO}_2/\text{Co}_{13}$	7.12	7.11	-23.70	$\text{H}_2\text{O}/\text{Co}_{13}$	-	0.58	0.61	1.00
$\text{CO}_2/\text{Co}_{55}$	5.79	7.04	-22.78	$\text{H}_2\text{O}/\text{Co}_{55}$	-	0.54	0.66	0.71
$\text{CO}_2/\text{Co}_{147}$	6.07	7.26	-23.53	$\text{H}_2\text{O}/\text{Co}_{147}$	-	0.69	0.66	0.77
$\text{CO}_2/\text{Co}_{(0001)}$	5.51	5.81	-22.42	$\text{H}_2\text{O}/\text{Co}_{(0001)}$	-	0.86	0.84	0.65
$\text{CO}_2/\text{Ni}_{13}$	6.81	6.79	-22.87	$\text{H}_2\text{O}/\text{Ni}_{13}$	-	0.53	0.63	0.82
$\text{CO}_2/\text{Ni}_{55}$	3.44	10.28	-25.69	$\text{H}_2\text{O}/\text{Ni}_{55}$	-	0.68	0.58	0.87
$\text{CO}_2/\text{Ni}_{147}$	3.59	9.42	-24.96	$\text{H}_2\text{O}/\text{Ni}_{147}$	-	0.42	0.49	1.55
$\text{CO}_2/\text{Ni}_{(111)}$	8.51	3.19	-24.01	$\text{H}_2\text{O}/\text{Ni}_{(111)}$	-	0.97	0.94	0.37
$\text{CO}_2/\text{Cu}_{13}$	0.59	-0.39	-0.12	$\text{H}_2\text{O}/\text{Cu}_{13}$	-	0.41	0.50	0.79
$\text{CO}_2/\text{Cu}_{55}$	0.42	-0.25	-0.32	$\text{H}_2\text{O}/\text{Cu}_{55}$	-	0.30	0.35	1.40
$\text{CO}_2/\text{Cu}_{147}$	0.07	0.05	-0.35	$\text{H}_2\text{O}/\text{Cu}_{147}$	-	0.42	0.41	1.00
$\text{CO}_2/\text{Cu}_{(111)}$	0.04	0.05	-0.21	$\text{H}_2\text{O}/\text{Cu}_{(111)}$	-	0.74	0.74	-0.29
CO/Co_{13}	4.13	-	-	$\text{H}_2/\text{Co}_{13}$	25.67	-	-	-
CO/Co_{55}	5.75	-	-	$\text{H}_2/\text{Co}_{55}$	16.90	-	-	-
$\text{CO}/\text{Co}_{147}$	2.82	-	-	$\text{H}_2/\text{Co}_{147}$	22.21	-	-	-
$\text{CO}/\text{Co}_{(0001)}$	4.76	-	-	$\text{H}_2/\text{Co}_{(0001)}$	23.17	-	-	-
CO/Ni_{13}	4.14	-	-	$\text{H}_2/\text{Ni}_{13}$	16.49	-	-	-
CO/Ni_{55}	4.96	-	-	$\text{H}_2/\text{Ni}_{55}$	19.68	-	-	-
$\text{CO}/\text{Ni}_{147}$	4.98	-	-	$\text{H}_2/\text{Ni}_{147}$	18.39	-	-	-
$\text{CO}/\text{Ni}_{(111)}$	4.41	-	-	$\text{H}_2/\text{Ni}_{(111)}$	19.06	-	-	-
CO/Cu_{13}	1.17	-	-	$\text{H}_2/\text{Cu}_{13}$	7.73	-	-	-
CO/Cu_{55}	4.13	-	-	$\text{H}_2/\text{Cu}_{55}$	6.13	-	-	-
$\text{CO}/\text{Cu}_{147}$	0.89	-	-	$\text{H}_2/\text{Cu}_{147}$	4.91	-	-	-
$\text{CO}/\text{Cu}_{(111)}$	3.40	-	-	$\text{H}_2/\text{Cu}_{(111)}$	0.74	-	-	-

Source: Own study reproduced with permission for the thesis.¹⁴⁵ Reproduced from Ref. 145 with permission from the PCCP Owner Societies.

as observed for CO adsorption (bridge and hollow sites). For H_2O and H_2 , the distances showed much smaller oscillations, due to the greater similarity of the adsorption sites.

The adsorption process can distort the molecular geometries; such perturbations were studied through the percent variations of molecular angles and bond lengths, with respect to the isolated molecules, shown in Figure 13 and Table 10. The geometries of the substrates were almost unaffected by adsorption, except for the TM atoms close to the molecules, which tend to approach the adsorbates causing a small local distortion. The

molecular angles are only affected by substrate size in the case of chemisorbed CO_2 . For physisorbed CO_2 and H_2O , the molecular geometric perturbations are negligible; however, for most molecules, all bonds stretch (weaken) and smaller substrates tend to promote greater stretching. The bonds are more weakened for systems featuring the molecules closer to the substrate and greater adsorption strength; for example, the C–O bonds are more weakened and closer to the substrates for CO_2 chemisorption on Co and Ni compared to CO_2 physisorption on Cu. The molecules that are most susceptible to distortions are H_2 and CO_2 , since H_2 has a weak E_b and CO_2 has the flexible angular degree of freedom, which can be accompanied by bond stretching for a stable superposition of the atomic orbitals.⁵⁰ For chemisorbed CO_2 , the molecular orientation on the edge adsorption sites dictated whether the two C–O bonds stretched equally or differently. For example, both C–O bonds show the same stretching for $\text{CO}_2/\text{Ni}_{13}$, because of the symmetric orientation of the adsorbate, with respect to the adsorption site; however, for larger nanoparticles the C–O bond almost parallel to the substrate is more stretched than the C–O bond that points away from the particle. This behavior could be critical to control bond cleavage, which could be exploited to promote target dissociation pathways.

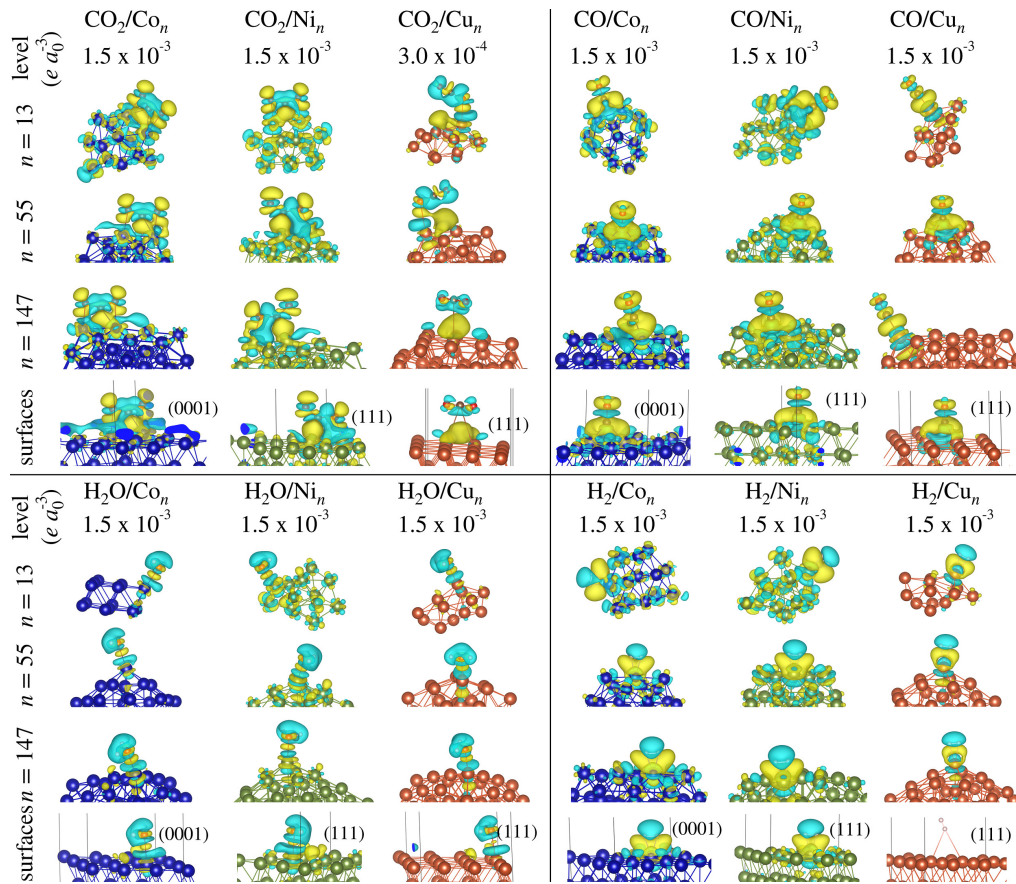
4.4.3 Electron Density Difference and Distribution of Charges

After adsorption, the electron density changes, resulting in a redistribution of charge. A qualitative description of this rearrangement was made through the electron density difference, which is calculated as $\Delta\rho(\mathbf{r}) = \rho^{\text{Mol/sub}}(\mathbf{r}) - \rho^{\text{Mol}}(\mathbf{r}) - \rho^{\text{sub}}(\mathbf{r})$, in which $\rho^{\text{Mol/sub}}$ is the electron density of the adsorbed system, while ρ^{Mol} and ρ^{sub} represent the electron densities of the isolated molecule and clean substrate, respectively, calculated for the atomic coordinates fixed in the adsorption positions. The isosurfaces are shown in Figure 15.

For the TM atoms, the perturbations of the electron density are associated with the redistribution of charge and also with the small changes of local magnetic moments. For the TM_{13} particles, the perturbations reach the entire particle, but for larger particles the perturbations are more localized around the TM closer to the adsorbates, analogously to the behavior for the first layers of the extended surfaces. For CO_2 , the profiles corresponding to chemisorption on Co and Ni are similar; however, there are perturbations around the C–O bonds that can be related to the bond weakening effect, which depends on the orientation of CO_2 . For Cu nanoparticles, the isosurface profiles change with substrate size, which can be related to the possibilities of parallel (Cu_{147} and $\text{Cu}(111)$) and tilted (Cu_{13} and Cu_{55}) orientations discussed above.

The region between the C atoms and the TM showed accumulation of charge, regardless of the type of adsorption, due to polarization to form a C–TM bond. Moreover, we observed a depletion of charge along the edge of some nanoclusters (e.g., Co_{55} , Co_{147} ,

Figure 15 – Electron density difference analysis for the most stable adsorption configurations of CO₂, CO, H₂O and H₂ on Co_n, Ni_n and Cu_n ($n = 13, 55, 147$) nanoclusters and compact surfaces. Yellow and blue regions represent, respectively, the accumulation and depletion of electron density; the isosurface level is indicated, in $e a_0^{-3}$.



Source: Own study reproduced with permission for the thesis.¹⁴⁵ Reproduced from Ref. 145 with permission from the PCCP Owner Societies.

Ni₁₄₇), which could be related to the preference for edge adsorption sites for molecules that remove charge from the nanoparticles. For CO₂, the depletion of electron density on the C atom and its accumulation around O atoms are suggestive of the expected occupation of π -type orbitals of the bent molecule.^{50,51} For CO, H₂O and H₂, the particle size does not affect the isosurfaces significantly and the differences can be attributed to the different adsorption sites.

The distribution of charge on each adsorption configuration was investigated through the effective Bader charge calculated as $Q_{ef} = Z_{val} - Q_{Bader}$, in which Z_{val} is the valence charge and Q_{Bader} is the Bader charge.¹⁴¹ The total charge of the adsorbed molecules are presented in Figure 13. As expected, physisorbed CO₂ and H₂ show negligible charge transfer, chemisorbed CO₂ and CO remove charge from the substrates, while H₂O loses a small quantity of charge. The charge on CO oscillates with substrate size, due to the change of adsorption sites; this can be observed in the CO/Cu systems, in which

Table 11 – Work function change, $\Delta\Phi$ (eV), due to adsorption of CO_2 , CO , H_2O and H_2 on the Co, Ni and Cu close-packed surfaces. The last row shows the work functions, Φ (eV), of the reference clean surfaces.

	Co(0001)	Ni(111)	Cu(111)
CO_2	0.57	0.97	-0.10
CO	0.63	0.64	0.29
H_2O	-0.74	-0.79	-0.48
H_2	-0.41	-0.44	-0.10
Φ	4.96	5.08	4.80

Source: Own study reproduced with permission for the thesis.¹⁴⁵ Reproduced from Ref. 145 with permission from the PCCP Owner Societies.

the TM atoms of hollow sites (CO on Cu_{55} and $\text{Cu}(111)$) transfer more charge to the molecule than the single TM atom of top sites (CO on Cu_{13} and Cu_{147}). Moreover, the charge transfer increases on smaller substrate sizes, which can be exemplified by CO_2 chemisorption with fixed adsorption sites and different particle sizes. The charges on the atoms could be important to rationalize probable reaction mechanisms; after adsorption, less positive charges are observed for the carbon atoms, compared to the gas phase, while there are small differences for the oxygen atoms; the H atoms (for H_2O) also become more positive, which should facilitate their detachment.

For the extended surfaces, the work function has been related to the adsorption of CO_2 and charge transfer.¹⁹⁴ Here, the work function change was calculated for the extended surfaces as $\Delta\Phi = \Phi^{\text{Mol/sub}} - \Phi^{\text{sub}}$, where Φ^{sub} is the work function of the clean surface and $\Phi^{\text{Mol/sub}}$ is the property for the adsorbed system. The results are shown in Table 11, while details about the work function and its calculation were discussed in Chapter 3 and can be found in the literature.^{142,143} For CO_2 and CO adsorption, $\Delta\Phi > 0$ (except for physisorption on Cu), while $\Delta\Phi < 0$ for H_2O and H_2 . Therefore, the Φ reduced for adsorbates that donated charge to the surface and increased for adsorbates that removed charge from the surfaces. The exceptions are cases with negligible charge transfer. This trend can be rationalized in parallel with the adsorption of atomic species: atoms with higher electronegativity than the surface atoms tend to increase Φ , as a consequence of the accumulation of charge around the adsorbate, which results in a dipole, while the opposite relationship can be expected for atoms of lower electronegativity than the surface atoms.^{195,196}

4.5 Summary and Perspectives

In the present chapter, we discussed the adsorption properties for the interaction of CO_2 , CO , H_2O and H_2 with model Co, Ni and Cu substrates simulating nanoparticles

of various particle sizes. As hypothesized in the introductory section of the thesis, for all systems, the particle size affected most of the adsorption properties; CO₂ adsorption showed the most significant size dependence, while for H₂O this dependence was almost negligible in the atomistic level. The small clusters promoted stronger adsorption, small oscillations were observed for intermediate sizes and the surface limit promoted weaker adsorption, as expected from the higher coordination of atoms for increasing substrate sizes. This behavior was also affected by the orientation of the adsorbed molecule and the adsorption site preference. In summary, we effectively investigated the quantum size effects on adsorption and discussed how several size dependent factors affect the process and cause oscillations of the adsorption properties. Future theoretical studies could benefit applied technologies by exploring the size effects in the thermodynamic limit. For example, although the adsorption properties for H₂O/TM did not show significant size dependence from the atomistic level, the collective macroscopic response could still be affected by substrate size. Moreover, coadsorption and bond cleavage could be explored for some configurations selected from our study.

After closing the investigation of size effects for the present thesis, it was clear that the type of TM is one of the most important factors for adsorption, since it changed the size dependence of some properties and directed the relative stability of the different types of adsorption configurations. For example, Cu substrates favored the physisorption of CO₂ regardless of particle size; for small Cu nanoparticles, CO₂ chemisorption was still observed, but as higher energy configurations. On the other hand, chemisorbed CO₂ was favored by the other TM studied. Then, to further investigate this characteristic of the different types of TM and contribute to the context of CO₂ utilization with additional atomistic insights, the next chapter of this thesis focused on expanding the set of TM investigated and exploring how mixing TM to obtain nanoalloys affects the adsorption of CO₂.

5 THE ADSORPTION OF CO₂ ON 55-ATOM Pt-BASED NANOALLOYS

This chapter is an adaptation for the thesis of a study that is currently (around the time of writing this thesis) being reviewed to be published as a scientific article in the near future. The authors that contributed to the study, up to the present moment, are: Paulo C. D. Mendes, Lucas G. Verga, Juarez L. F. Da Silva and the publication is expected for the year 2020. Permissions to re-use and adapt the material for the thesis will be requested and are normally granted for the purpose of the thesis. Additional analyses and resources will be published in the referred article and its Supporting Information.

5.1 Introduction and State of the Art

As commented in Chapters 1 and 4, the capture and conversion of CO₂ has been attracting attention, due to the possible positive environmental and economic impacts.^{197,198} In principle, the conversion of CO₂ can take place through homogeneous or heterogeneous catalysis;^{3,51} either way the catalyst has a pivotal role in the conversion, since CO₂ is kinetically inert. The molecule can be activated for reactions through the interaction with a TM substrate; however, the knowledge of the factors that drive this activation in the atomistic level and, consequently, promote reactivity is still not consolidated.¹⁹⁹ The activation has been connected to the formation of the negatively charged and bent molecule (CO₂^{δ-}), which is one of the key intermediates of CO₂ transformations.^{197,199} This anionic species can be formed through the chemisorption of CO₂ on TM substrates^{43,51,58,145} and its stabilization is related to a strong interaction with the substrate and donation of charge to CO₂.^{51,199}

In the previous chapter, it was demonstrated that the type of TM is very important to stabilize the bent CO₂ configuration on nanoparticles and extended surfaces; based on this crucial role of the type of TM on CO₂ adsorption, there are great opportunities to tune the substrates towards target adsorption properties through alloying. Hence, in this chapter, we focus on the adsorption of CO₂ on bimetallic nanoalloys composed of Pt and another TM; moreover, we expand the TM₅₅ sets that were studied in the previous chapter including the 3*d*, 4*d* and 5*d* metals from groups 8 to 11 of the periodic table. Instead of extended alloy surfaces, we selected 55-atom nanoclusters for this study, which involve the alloying effects and also the nano scale effects, discussed previously, that can be promising to design catalysts due to the great versatility of nanoparticles to optimize catalytic properties.^{14,17,32,200} Some features that can be interesting for the adsorption and stabilization of CO₂^{δ-} are the sizes and morphologies of the nanoparticles, which can affect the proportions of uncoordinated and coordinated sites that can be exploited to control the adsorption strength.^{43,58,145} Furthermore, tuning the composition of nanoalloys

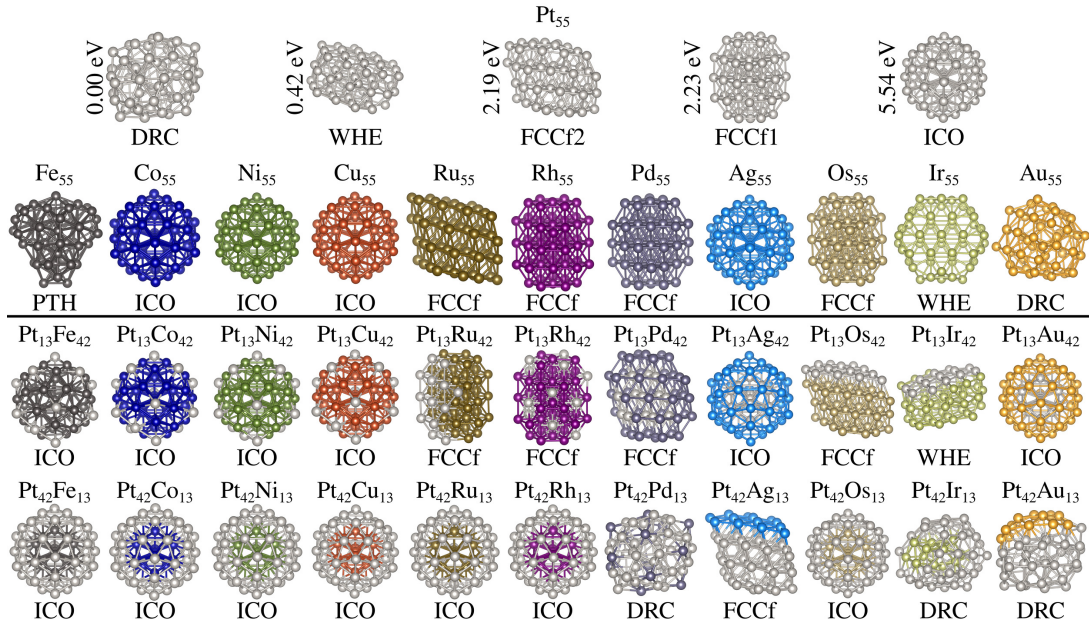
greatly increases the possibilities to design catalysts, due to the diversity of compositions, chemical orderings and synergistic effects.^{15, 18, 201}

From the staggering variety of choices to study model nanoalloys, Pt-based systems are interesting for catalytic applications, because Pt is a versatile, relatively inert, model catalyst that can provide a good balance of the catalytic activity, resistance to catalytic poisoning and substrate degradation.^{12, 202–204} For 4-atom clusters based on Cu or Pt, it was reported that bimetallic systems affect the OCO angle of adsorbed CO₂ differently than the unary nanoclusters and extended surfaces.^{205–207} For Pt nanoparticles, alloying with Co atoms to form Pt₃Co octapods can promote CO₂ activation and improve the catalytic activity in comparison to unary Pt systems.²⁰⁸ Besides the type of TM, the proportion of each component of the nanoalloy is critical to design better catalysts; for example, the composition of PdAg alloys can be tuned to weaken the binding of CO with respect to other intermediates during the electroreduction of CO₂.²⁰⁹ Similarly, it was possible to change the selectivity of CuSn catalysts through composition by increasing the quantities of positively charged Sn sites.²¹⁰ Unfortunately, despite the fact that various alloys can be suggested to greatly improve the electroreduction of CO₂, the materials can be unstable and prone to segregation or degradation.²¹¹ Hence, it is not sufficient to control the binding of intermediates, but it is also important to explore materials that are highly stable to withstand operation conditions. It can be noted that nanoalloys containing different types of metals can be involved in the applications; for the present theoretical investigation, a wide range of Pt-based systems were used as models to investigate alloying effects, which could also occur for other types of metals interesting for various applications.

For CO₂ reduction, the activation energies for the dissociation of CO₂ were predicted for close-packed binary TM surfaces from calculations for unary surfaces by other authors.⁵² It has been discussed that alloying can be an effective strategy to overcome linear scaling relations^{59, 212, 213} for the binding of intermediates, thus, controlling the catalytic activity and selectivity of CO₂ reduction.^{209, 214} For example, the inclusion of Ni, Pt or Rh as a subsurface layer on Au surfaces favor the formation of hydrocarbons instead of CO during CO₂ reduction.²¹⁵ The alloying effects can be noted from doping, as shown for Cu(211) surfaces doped with different TM atoms.²¹⁶ The effect produced through doping can either favor or impair CO₂ activation depending on the type of dopant,²¹⁶ hence, this can also be expected for other types of alloys. For the practical applications, this type of theoretical insight can provide criteria to guide the experiments towards a rational design of catalysts.

Most studies about CO₂ adsorption and activation focused on unary substrates or alloyed extended surfaces and the atomistic knowledge about the role of nano scale alloying to control the activation of CO₂ is still incomplete. Here, aiming to expand this knowledge, we studied the adsorption of CO₂ on various stable bimetallic 55-atom nanoclusters composed of Pt and a TM from the 3*d*, 4*d* and 5*d* periods, groups 8 to 11 of the periodic

Figure 16 – Optimized atomic structures of isolated 55-atom unary nanoclusters and $\text{Pt}_n\text{TM}_{55-n}$ nanoalloys ($n = 13$ and 42). The configurations were denominated distorted reduced-core (DRC), hexagonal close-packed wheel-type (WHE), face-centered cubic fragments (two types, FCCf1 and FCCf2), icosahedron (ICO) and polytetrahedron (PTH). For Pt_{55} , the relative total energy with respect to the lowest energy, DRC, structure is indicated.



Source: Own study in preparation to be submitted for publication. Permission to use will be requested.

table ($\text{Pt}_n\text{TM}_{55-n}$, with $n = 13$ and 42). Furthermore, we explored the adsorption of CO_2 on all corresponding unary substrates and, as will be elaborated ahead, our study involved several types of stable nanoclusters, including core-shell, homogeneously distributed and segregated side by side. To fully explore the behavior of CO_2 , both physisorbed (linear) and chemisorbed (bent) CO_2 were explored.

5.2 Isolated Nanoparticles

For this study, we aimed to obtain a set of high-quality configurations that are well documented and stable. First, the choice the 55-atom size was based on the fact that such nanoparticles are clearly distinguishable from periodic surfaces at a manageable computational cost, as we found in Chapter 4. Hence, for the unary systems, we employed the lowest energy 55-atom configurations obtained after a detailed investigation, of several different morphologies for each metal, done in a previous study by other authors.³⁵ For such systems, dispersion corrections, spin-orbit coupling, and corrections for localized electronic states are not expected to greatly change the results.^{35,217} For the nanoalloys, the number of possible configurations increase dramatically, then, our group performed a systematic study to investigate the formation of several types of $\text{Pt}_{13}\text{TM}_{42}$ and $\text{Pt}_{42}\text{TM}_{13}$

nanoalloys, including core-shell, homogeneously distributed and segregated side by side.¹⁴⁶ The aforementioned investigation initiated with a Master degree study that explored some trends driving the formation of core-shell arrangements.¹³⁶ The study was published later, after a meticulous review, normalization of the calculations to improve the consistency of computational parameters, further exploration of the possible local magnetic moments for each nanoparticle, evaluation of all properties and additional analyses of the correlations between such properties and the stability of the nanoalloys; in total, 330 nanoalloys were investigated.¹⁴⁶ Here, we employed the lowest energy configuration, from the referred previous study,¹⁴⁶ for each PtTM system to study CO₂ adsorption. Additionally, all cluster morphologies observed for the nanoalloys were also studied for Pt₅₅ to demonstrate the influence of particle morphology on the adsorption.

The optimized configurations for the isolated unary Pt₅₅, TM₅₅ nanoclusters, and for the bimetallic Pt_{*n*}TM_{55-*n*} nanoalloys, with $n = 13$ and 42, are shown in Figure 16, while some of their properties are shown in Table 12. The most stable morphology for the nanoalloy is not necessarily the same that is observed for the unary cluster of the predominant component of the binary system.¹⁴⁶ As expected, our calculations for the present study reproduce the trends reported previously for the isolated systems,¹⁴⁶ but with stronger binding and shorter d_{av} , due to the inclusion of the D3 dispersion correction for the present study, while the previous report employed only the PBE functional.¹⁴⁶ Compared to the unary systems, significant structural changes can occur after alloying, as observed between low-symmetry structures and regular configurations, such as from Au₅₅ (low-symmetry) to Pt₁₃Au₄₂ (icosahedron structure). The different effective coordination numbers (ECN),¹⁵¹ Table 12, indicates the variety of nanoalloys in our set. Considering Pt₁₃TM₄₂, core-shell arrangements with Pt on the core were the most stable condition only for Pt₁₃Ag₄₂ and Pt₁₃Au₄₂; a Pt core was also observed for Pt₁₃Pd₄₂, but three Pt atoms were in the surface region. Seven Pt₄₂TM₁₃ nanoalloys present ICO core-shell arrangements as the lowest energy structure.¹⁴⁶

The stability of the nanoparticles was measured through the binding energies per atom, E_b and excess energies, E_{exc} . In summary, the first measures the stability of the particle in relation to atomization, while the latter compares the energy of the nanoalloys with the energies of the most stable corresponding unary nanoclusters; the mathematical definitions and further details are available in the article published previously.¹⁴⁶ The binding energies of the unary nanoclusters were weaker than the respective lowest energy bulk phases,¹¹³ due to the finite nature of the nanoclusters; furthermore, E_b exhibits a trend analogous to the parabolic behavior of the bulk E_{coh} along the transition periods,¹⁴⁶ as discussed in Chapter 3 considering the characteristics of the d -band.^{156,181} Consequently, the average bond lengths¹⁵¹ increase as the binding weakens. For most nanoalloys, the E_b is intermediate in relation to the respective unary clusters; for PtPd, PtAg, PtAu, and the nanoalloys with a 3d TM, the binding is stronger than for the respective TM₅₅, coinciding

Table 12 – Characterization of the lowest energy configurations of the isolated substrates. Excess energy per atom, E_{exc} , binding energy per atom, E_b , total magnetic moment, m_{tot} , effective coordination number, ECN (in number of nearest neighbors), average bond length, d_{av} , and chemical order parameter, ς .

System	E_{exc} (eV)	E_b (eV)	m_{tot} (μ_B)	ECN (NNN)	d_{av} (\AA)	ς
Fe ₅₅	-	-3.97	154	8.24	2.49	1.00
Co ₅₅	-	-4.13	105	8.37	2.43	1.00
Ni ₅₅	-	-3.97	40	8.39	2.43	1.00
Cu ₅₅	-	-3.06	3	8.39	2.50	1.00
Ru ₅₅	-	-5.64	6	7.60	2.57	1.00
Rh ₅₅	-	-4.79	29	7.96	2.62	1.00
Pd ₅₅	-	-3.17	22	7.93	2.70	1.00
Ag ₅₅	-	-2.27	3	8.42	2.88	1.00
Os ₅₅	-	-6.80	2	7.85	2.61	1.00
Ir ₅₅	-	-6.19	1	6.28	2.58	1.00
Pt ₅₅	-	-4.83	0	6.83	2.66	1.00
Au ₅₅	-	-2.84	1	6.44	2.78	1.00
Pt ₁₃ Fe ₄₂	-0.22	-4.39	124	8.17	2.53	0.38
Pt ₁₃ Co ₄₂	-0.17	-4.46	88	8.37	2.48	0.35
Pt ₁₃ Ni ₄₂	-0.13	-4.31	40	8.45	2.49	0.35
Pt ₁₃ Cu ₄₂	-0.13	-3.61	2	8.46	2.54	0.35
Pt ₁₃ Ru ₄₂	-0.05	-5.50	10	7.89	2.61	0.65
Pt ₁₃ Rh ₄₂	-0.02	-4.82	20	7.93	2.63	0.20
Pt ₁₃ Pd ₄₂	-0.03	-3.59	10	7.88	2.71	0.30
Pt ₁₃ Ag ₄₂	-0.09	-2.96	0	8.42	2.85	0.38
Pt ₁₃ Os ₄₂	-0.07	-6.41	2	7.70	2.63	0.68
Pt ₁₃ Ir ₄₂	0.00	-5.87	4	6.26	2.59	0.57
Pt ₁₃ Au ₄₂	-0.03	-3.34	2	8.44	2.84	0.38
Pt ₄₂ Fe ₁₃	-0.28	-4.91	38	8.38	2.63	0.38
Pt ₄₂ Co ₁₃	-0.22	-4.89	35	8.30	2.62	0.38
Pt ₄₂ Ni ₁₃	-0.16	-4.79	22	8.29	2.62	0.38
Pt ₄₂ Cu ₁₃	-0.14	-4.56	9	8.38	2.63	0.38
Pt ₄₂ Ru ₁₃	-0.21	-5.24	6	8.39	2.69	0.38
Pt ₄₂ Rh ₁₃	-0.07	-4.89	19	8.38	2.69	0.38
Pt ₄₂ Pd ₁₃	-0.01	-4.45	2	6.94	2.67	0.21
Pt ₄₂ Ag ₁₃	0.02	-4.20	1	7.49	2.73	0.68
Pt ₄₂ Os ₁₃	-0.30	-5.60	4	8.39	2.70	0.38
Pt ₄₂ Ir ₁₃	-0.08	-5.23	1	6.81	2.65	0.39
Pt ₄₂ Au ₁₃	0.02	-4.34	1	6.83	2.70	0.60

Source: Own study in preparation to be submitted for publication. Permission to use will be requested.

with the fact that the binding for TM₅₅ is weaker than for Pt₅₅ in these cases.¹⁴⁶ The remaining nanoalloys have the opposite behavior, which reproduces our previous results.¹⁴⁶ Considering the excess energy, E_{exc} , shown in Table 12, most binary systems present

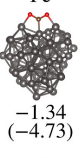
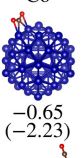
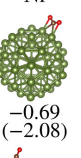
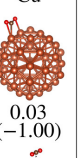
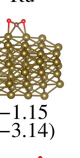
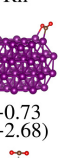
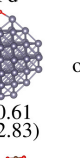
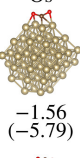
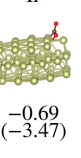
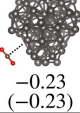
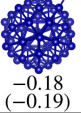
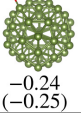
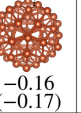
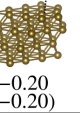
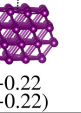
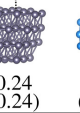
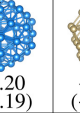
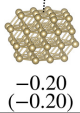
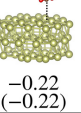
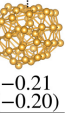
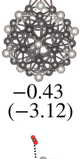
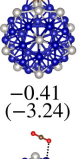
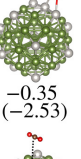
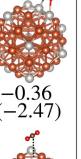
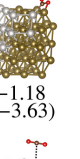
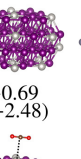
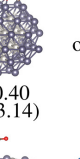
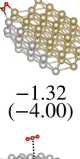
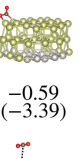
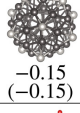
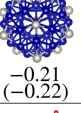
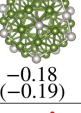
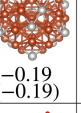
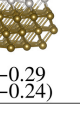
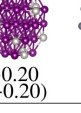
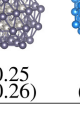
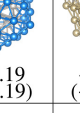
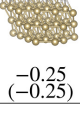
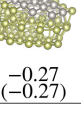
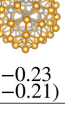
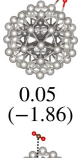
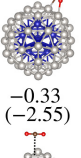
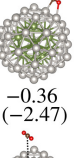
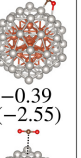
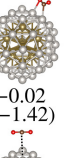
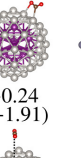
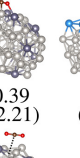
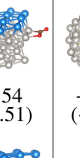
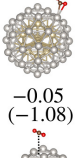
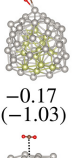
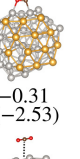
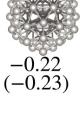
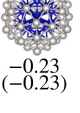
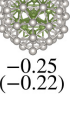
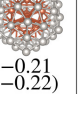
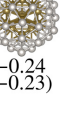
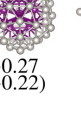
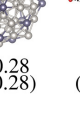
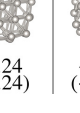
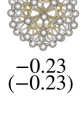
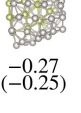
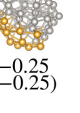
negative E_{exc} , indicating greater stability in comparison to the respective unary clusters, except $\text{Pt}_{42}\text{Ag}_{13}$ and $\text{Pt}_{42}\text{Au}_{13}$, which have a small positive E_{exc} . As mentioned above, the model nanoalloys selected for this study minimize the excess energy through variations of morphology and chemical ordering,¹⁴⁶ which is important before studying CO_2 adsorption, since it could reduce the risk of proposing nanoalloys that are excellent to activate CO_2 , but unstable or irrelevant because of fluxionality. For Pt_{55} , the most important and stable configuration is the distorted reduced-core cluster, while the additional morphologies studied are unstable, as indicated by the relative energies shown in Figure 16.

As published previously,¹⁴⁶ the formation of Pt-based nanoalloys can be predicted through a simple model based on atomic radii and surface energies, which could be transferable for different compositions. In conjunction with the results presented herein about the adsorption of CO_2 , these studies offer theoretical insights that could benefit practical technologies for CO_2 conversions. The model 55-atom nanoparticles are extremely rich sources of features that could be exploited to control CO_2 adsorption. The stable unary nanoclusters present an assortment of adsorption sites, due to their several morphologies, and the model nanoalloys expand these characteristics even further, due to the several arrangements of Pt and TM atoms. For further details about the isolated systems studied herein and several additional configurations, we direct the reader to the articles published previously.^{35,146}

5.3 Procedures to Obtain the Adsorption Atomic Structure Configurations

After defining a high-quality set of model nanoparticles, to obtain the starting adsorption configurations, we employed a procedure similar to the steps discussed in Chapter 4 to obtain initial adsorption structures, that is, a careful exploration of all high-symmetry adsorption sites. Based on cluster symmetry, we manually generated starting adsorption configurations to explore homogeneous (Pt–Pt and TM–TM) and heterogeneous (Pt–TM) regions with CO_2 at approximately 2 \AA from the substrate, starting from bent and linear CO_2 configurations to avoid bias. Following this procedure, we explored from 10 to 15 structures for each substrate. For the low-symmetry clusters (DRC), due to the diversity of sites that would be difficult to accurately select by visual means, we generated about 20 million random adsorption configurations, with CO_2 at about 2 \AA from the substrates, from which we selected 10 configurations, based on a modified Euclidean similarity distance^{38,218,219} and further inspection to ensure that various heterogeneous adsorption sites were explored for the nanoalloys. All structures were optimized. To cross-check our results, additional configurations were studied, specifically, to search for optimized structures featuring linear or bent CO_2 ; for example, for Fe_{55} cluster, we only observed bent CO_2 after following the aforementioned procedure, then, we added a few structures containing linear CO_2 at about 3 \AA from the substrate to obtain a physisorption

Figure 17 – Optimized lowest energy adsorption configurations for $\text{CO}_2^{\delta-}$ (chemisorbed molecule, bent OCO angle) and physisorbed CO_2 interacting with TM_{55} and $\text{Pt}_n\text{TM}_{55-n}$, with $n = 13$ and 42 . The adsorption energies, E_{ad} (in eV), are indicated below the configurations, while the interaction energies, E_{int} (in eV), are between parenthesis.

	Fe	Co	Ni	Cu	Ru	Rh	Pd	Ag	Os	Ir	Au
$\text{CO}_2^{\delta-}/\text{TM}_{55}$	 -1.34 (-4.73)	 -0.65 (-2.23)	 -0.69 (-2.08)	 0.03 (-1.00)	 -1.15 (-3.14)	 -0.73 (-2.68)	 -0.61 (-2.83)	not observed	 -1.56 (-5.79)	 -0.69 (-3.47)	not observed
$\text{CO}_2/\text{TM}_{55}$	 -0.23 (-0.23)	 -0.18 (-0.19)	 -0.24 (-0.25)	 -0.16 (-0.17)	 -0.20 (-0.20)	 -0.22 (-0.22)	 -0.24 (-0.24)	 -0.20 (-0.19)	 -0.20 (-0.20)	 -0.22 (-0.22)	 -0.21 (-0.20)
$\text{CO}_2^{\delta-}/\text{Pt}_{13}\text{TM}_{42}$	 -0.43 (-3.12)	 -0.41 (-3.24)	 -0.35 (-2.53)	 -0.36 (-2.47)	 -1.18 (-3.63)	 -0.69 (-2.48)	 -0.40 (-3.14)	not observed	 -1.32 (-4.00)	 -0.59 (-3.39)	not observed
$\text{CO}_2/\text{Pt}_{13}\text{TM}_{42}$	 -0.15 (-0.15)	 -0.21 (-0.22)	 -0.18 (-0.19)	 -0.19 (-0.19)	 -0.29 (-0.24)	 -0.20 (-0.20)	 -0.25 (-0.26)	 -0.19 (-0.19)	 -0.25 (-0.25)	 -0.27 (-0.27)	 -0.23 (-0.21)
$\text{CO}_2^{\delta-}/\text{Pt}_{42}\text{TM}_{13}$	 0.05 (-1.86)	 -0.33 (-2.55)	 -0.36 (-2.47)	 -0.39 (-2.55)	 -0.02 (-1.42)	 -0.24 (-1.91)	 -0.39 (-2.21)	 -0.54 (-2.51)	 -0.05 (-1.08)	 -0.17 (-1.03)	 -0.31 (-2.53)
$\text{CO}_2/\text{Pt}_{42}\text{TM}_{13}$	 -0.22 (-0.23)	 -0.23 (-0.23)	 -0.25 (-0.22)	 -0.21 (-0.22)	 -0.24 (-0.23)	 -0.27 (-0.22)	 -0.28 (-0.28)	 -0.24 (-0.24)	 -0.23 (-0.23)	 -0.27 (-0.25)	 -0.25 (-0.25)

Source: Own study in preparation to be submitted for publication. Permission to use will be requested.

configuration. Similarly, we added more structures searching for chemisorbed CO_2 for substrates that only presented physisorbed CO_2 . All structures were optimized before any analysis and the complete sets of configurations are illustrated in Appendix E.

5.4 Lowest Energy Adsorption Configurations

After optimizing all adsorption configurations, we selected the most stable adsorption structures of each system for chemisorbed $\text{CO}_2^{\delta-}$ (bent) and physisorbed CO_2 (linear). These selected structures are shown in Figure 17 for TM and PtTM, while Pt_{55} will be discussed ahead and is shown in Figure 18. The stability of the adsorbed systems was measured through the relative energies within each set and, analogously to the analyses done in the previous chapter, we studied the adsorption energy and interaction energy in conjunction to consider the adsorption strength and the effects of geometric deformations. The results show that alloying can affect the adsorption site preference, adsorption properties

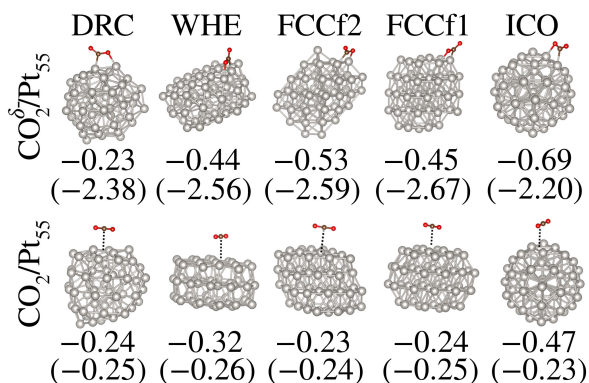
and the relative stability of linear and bent CO_2 . We found a preference for chemisorption on low-coordinated adsorption sites (homogeneous or heterogeneous regions), which could be due to the promotion of increased adsorption strength. The chemisorbed $\text{CO}_2^{\delta-}$ was also observed on various heterogeneous regions (Pt-TM), which could be facilitated due to the separation of charges on the TM and Pt, as indicated by Bader charge analysis: the CO_2 adsorbs with the C atom close to the anionic Pt atom, while the O atoms approach cationic (or less negatively charged) TM atoms, resulting in a stabilizing Coulomb effect. In contrast, physisorption was observed on various close-packed planar regions and several homogeneous sites (Pt-Pt and TM-TM).

5.5 Effects of the Occupation of d -states and Alloying on the Adsorption of CO_2

For the unary substrates of $3d$, $4d$, and $5d$ TM, as expected, for the TM from groups 8 to 10 of the periodic table, the CO_2 chemisorption is favored over its physisorption, while for the TM with completely filled d -states (group 11: Cu, Ag and Au) the opposite is observed.^{43, 58, 145} As the occupation of d -states increases, the adsorption and interaction energies tend to weaken for the chemisorption structures, with few exceptions, such as E_{int} from Rh_{55} to Pd_{55} systems. For Ag_{55} and Au_{55} , all optimized configurations resulted in linear CO_2 , even after searching for several additional configurations starting from bent CO_2 , suggesting that it is difficult to stabilize the $\text{CO}_2^{\delta-}$ species in such cases. The Pt_{55} DRC cluster distinctly showed degenerate physisorption and chemisorption structures, suggesting equal stability for both types of adsorption on Pt_{55} , although the E_{int} differs on both cases (Figure 18), as expected by definition. Alloying Pt causes different effects depending on the periodic group of the added TM and also on the fraction of Pt atoms on the nanoalloy. For low Pt content ($\text{Pt}_{13}\text{TM}_{42}$), alloying weakens the E_{ad} for chemisorbed CO_2 compared to the unary nanoclusters for almost all TM from groups 8 to 10; this is most expressive for $\text{Pt}_{13}\text{Fe}_{42}$, while $\text{Pt}_{13}\text{Ru}_{42}$ shows almost the same E_{ad} as Ru_{55} . For $\text{Pt}_{13}\text{Cu}_{42}$, alloying with Pt results in the opposite trend and the E_{ad} for chemisorbed CO_2 is enhanced in comparison to the unary Cu_{55} nanocluster. For $\text{Pt}_{42}\text{TM}_{13}$ systems, the same type of dependence on the periodic group of the alloyed TM is observed, but with even greater effect, for most systems. Hence, alloying affects the adsorption strength differently, depending on the occupation of d -states for the TM_{55} .

The adsorption properties are closely related to the adsorption strength, especially the OCO angle, which effectively characterizes the type of adsorption, because it is connected to the accumulation of charge on the CO_2 molecule.^{51, 52, 58} Thus, Figure 19 shows the OCO angle versus adsorption energy for all systems. The results confirm that the most stable adsorption mode on the unary nanoclusters is physisorption for Cu, Ag and Au, while chemisorption is the most stable mode for the other TM towards the left in the periodic groups. The OCO angle and, consequently, the charge of adsorbed CO_2 can

Figure 18 – Most stable optimized adsorption structures for bent and linear CO_2 interacting with various Pt_{55} clusters: distorted reduced-core (DRC), two types of face-centered cubic fragments (FCCf1 and FCCf2), hexagonal close-packed wheel-type (WHE) and icosahedron (ICO). The numbers below the structures are adsorption energies, E_{ad} (in eV), and, between parenthesis, interaction energies, E_{int} (in eV).

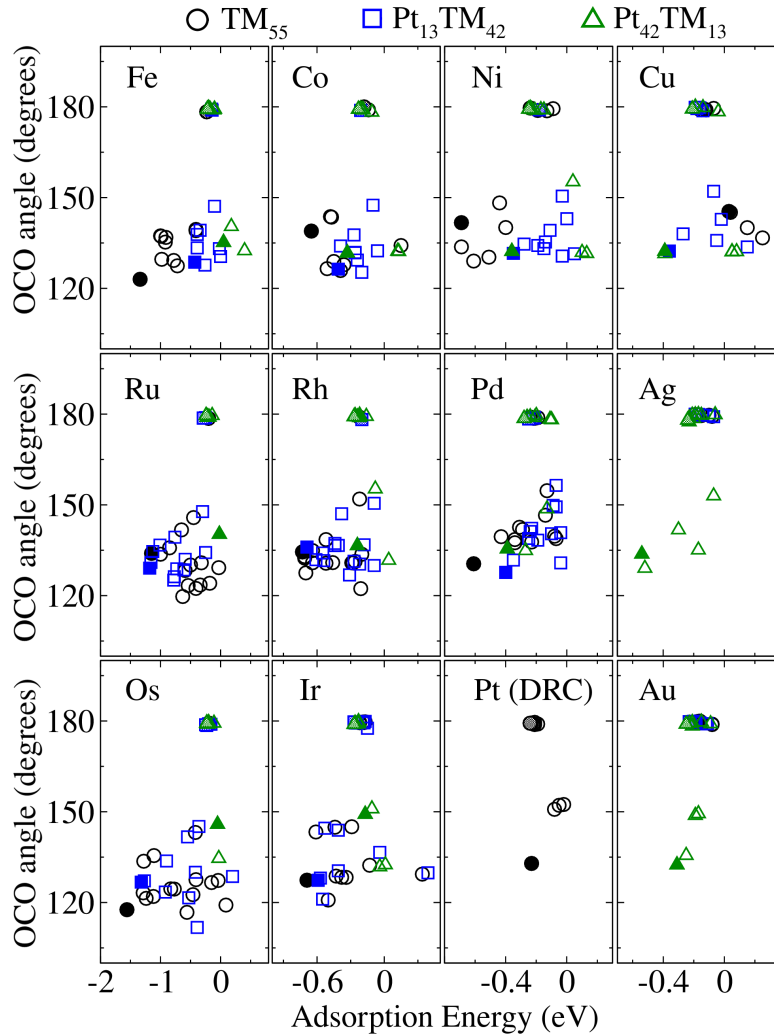


Source: Own study in preparation to be submitted for publication. Permission to use will be requested.

be controlled through alloying; for example, there is an increasing stability of chemisorbed $\text{CO}_2^{\delta-}$ in comparison to physisorbed CO_2 in the order Cu, $\text{Pt}_{13}\text{Cu}_{42}$ and $\text{Pt}_{42}\text{Cu}_{13}$; in contrast, the opposite occurs for the TM of group 8 of the periodic table, although for such TM chemisorption can still be more stable than physisorption depending on the Pt content. Notably after optimization of Ag and Au systems, $\text{CO}_2^{\delta-}$ was only observed for the systems with highest Pt content, which could be connected to the complete filling of d -states for the TM from group 11. As expected, for physisorption, the OCO angles and other properties, such as the adsorption energies, are very similar among the different substrates, due to the weak interaction, which is also observed for TM surfaces.⁵²

There are additional factors that impact the adsorption energies and drive the stabilization of either linear or bent CO_2 , such as the coordination and heterogeneity of the adsorption site and substrate morphology. For example, the adsorption strength of chemisorbed CO_2 on Fe systems decreases significantly with increasing Pt content, because both the adsorption site and morphology change with alloying, the former increases in coordination while the latter goes from a poly-tetrahedron to icosahedron structure, which contribute to weaken the adsorption when only 13 Pt compose the nanoalloy. In contrast, for Ru and Os the adsorption strength does not change as drastically as for Fe when comparing the TM_{55} to $\text{Pt}_{13}\text{TM}_{42}$, because the morphologies of such particles are much less affected by alloying with Pt. However, for $\text{Pt}_{42}\text{Ru}_{13}$ and $\text{Pt}_{42}\text{Os}_{13}$, the E_{ad} sharply decreases because of the significant change to core-shell configurations. The effect of different morphologies on the adsorption of CO_2 are exemplified by the results for CO_2 adsorbed on different Pt_{55} clusters, Figure 18, which show that the different

Figure 19 – Mode of CO₂ adsorption indicated by the OCO angle versus the adsorption energy for all adsorption structures studied for CO₂ adsorbed on unary and binary nanoclusters. Solid and hashed symbols represent to the most stable configurations for chemisorbed and physisorbed CO₂, respectively.



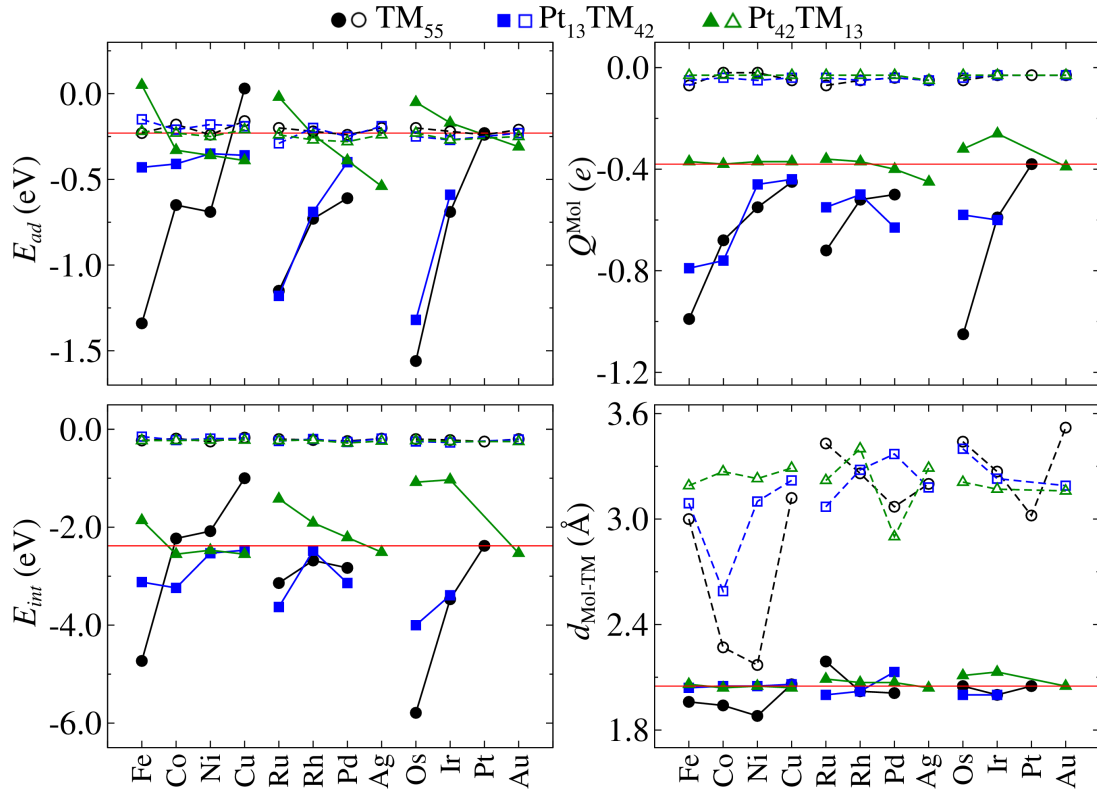
Source: Own study in preparation to be submitted for publication. Permission to use will be requested.

morphologies play a role in the adsorption strength, especially due to the availability of different adsorption sites. Moreover, there are distinctions of geometric properties for different morphologies, which will be elaborated ahead.

5.6 Geometric Properties of the Adsorbed Systems and Morphology Effects

Characteristic geometric properties for CO₂ adsorption, as discussed in the previous chapter, were observed: all C–O bonds are weakened (stretched) and their stretching was greater when accompanied by a decrease of the molecular angle (chemisorption). Furthermore, the orientation of CO₂ in relation to the substrate defined if the O–C bonds stretched equally or not, as shown in Chapter 4 and reported previously.¹⁴⁵ The shortest

Figure 20 – Adsorption properties of the most stable configurations for the chemisorption (solid symbols) and physisorption (open symbols) of CO_2 on the unary clusters and PtTM nanoalloys: adsorption energy, E_{ad} (eV), interaction energy, E_{int} (eV), effective Bader charge of adsorbed CO_2 , Q^{Mol} (e) and shortest distance between an atom of the CO_2 molecule and a TM atom, $d_{\text{Mol-TM}}$ (\AA). The red solid line indicates the property for the chemisorption structure of $\text{CO}_2/\text{Pt}_{55}$ (DRC).



Source: Own study in preparation to be submitted for publication. Permission to use will be requested.

distance between one atom of the molecule to a TM atom, shown in Figure 20, positively correlates with the adsorption strength for $\text{Pt}_{42}\text{TM}_{13}$, because the structures are similar. However, this is not observed for TM_{55} and $\text{Pt}_{13}\text{TM}_{42}$ due to the simultaneous influence of several effects, such as different morphologies, adsorption sites and orientations of the adsorbed CO_2 .

As discussed above, the molecular angle is a key property to characterize the type of CO_2 adsorption, therefore, the OCO angle was plotted versus the E_{ad} for the entire set of configurations (Figure 19). We observed different ranges of angles and corresponding E_{ad} depending on the type of TM; the spreading of such ranges could be related to the variety of adsorption structures, due to the assortment of adsorption sites and particle morphologies of each group of substrates. In the case of core-shell substrates, the adsorption was affected by the type of atom in the shell region, which is close to the adsorbate; this is similar to what occurs in extended surfaces, in which the layers closer to the adsorbate normally

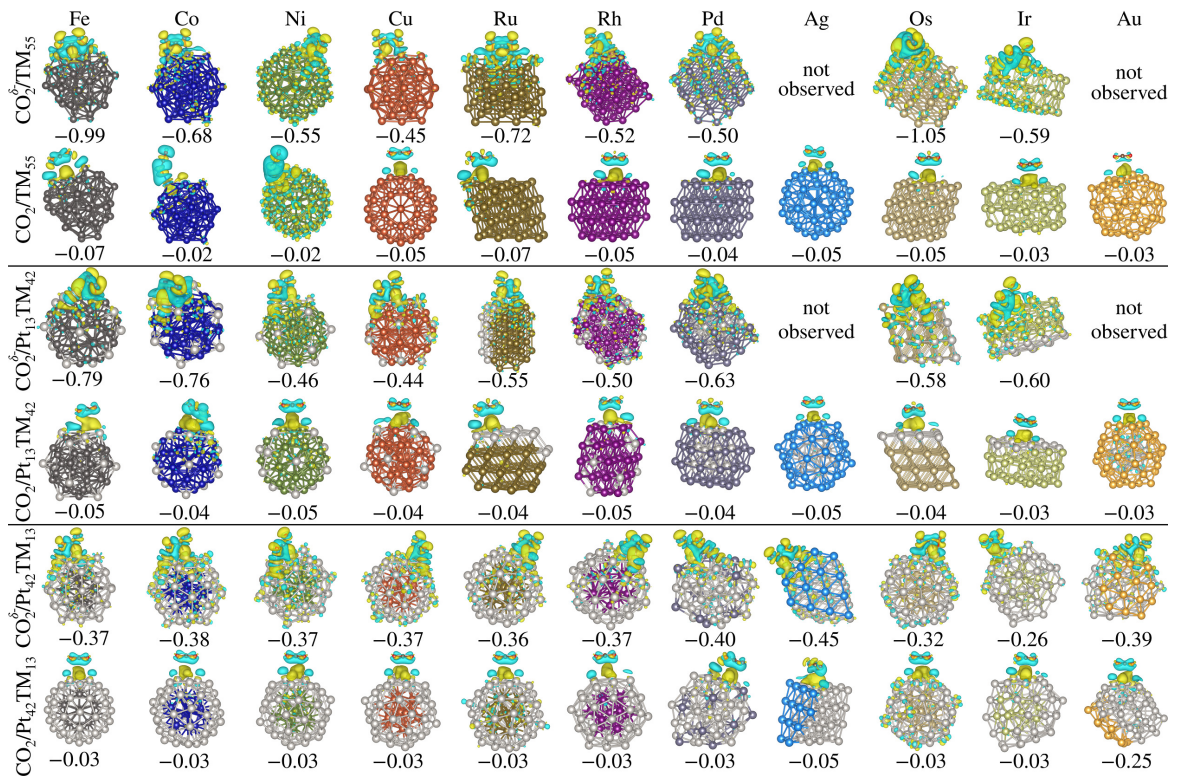
affect adsorption more significantly than the innermost layers.^{39,75} This effect could be interesting to explore experimentally, because it suggests that it could be possible to change the core region of nanoalloys keeping the atomistic characteristics of the adsorption. However, the core-shell structures are susceptible to strain effects¹⁴⁶ that can shift the center of the *d*-states for the atoms close to the molecule, as observed by other authors;¹³⁴ this effect could explain the different interaction and adsorption energies for core-shell systems varying the TM core. A small strain could result in slightly different Pt–Pt distances in the shell region, which affects coordination and adsorption strength, inducing different deformations of CO₂. Such strain effects are subtle for our model systems, but they could become even more important as coverage increases.

Regarding the effects of geometric distortions on the energetic properties of the systems, we observed that the interaction and adsorption energies show similar dependence with the type of substrate, as shown in Figure 20. Moreover, we found the same behavior discussed in the previous chapter: the effects of the geometric distortions of the clusters were small compared to the effects for CO₂. This can be attributed to the high stability of the model nanoparticles, considering that the most significant exceptions occurred for the different, less stable, morphologies of Pt₅₅ shown in Figure 18. Comparing the CO₂/Pt₅₅ for ICO systems to the other Pt₅₅ clusters, the ICO system presents the strongest adsorption energies for chemisorption and physisorption, which could be related to the significant energetic stabilization of the cluster resulting from its geometric distortions. For physisorption and for chemisorption on Pt₅₅ ICO, we measured a deformation energies of -0.24 eV and -0.14 eV, respectively. Moreover, we found one chemisorption configuration (illustrated in Appendix E) where the ICO frame was restructured after CO₂ chemisorption ($E_{ad} = -0.94$ eV, $E_{int} = -3.44$ eV), with a deformation energy of -0.31 eV for the cluster. Hence, from these deformation energies, the strength of adsorption does not seem correlated with the stabilization of the cluster, since the stronger adsorption did not always show greater stabilization resulting from cluster deformations. Besides the deformation effects, the exemplified CO₂/Pt₅₅ systems suggest that changing cluster morphology does not cause dramatic changes of adsorption strength from the atomistic level, but the clusters can feature distinct adsorption sites (such as low-coordinated regions) that can affect the adsorption properties.

5.7 Electron Density Analyses

To reinforce the conclusions drawn through the OCO angle and adsorption energies about CO₂ activation, we calculated the effective Bader charges¹⁴¹ of adsorbed CO₂ and the electron density difference for the adsorbed systems; the results are in Figures 20 and 21. As expected, the charges closely follow the trends of the adsorption strength, it tends to decrease from the periodic groups 8 to 11, except for Pt₄₂TM₁₃ for which the

Figure 21 – Electron density difference analysis for the lowest energy adsorption configurations of chemisorbed and physisorbed CO_2 interacting with unary and binary nanoclusters. For the chemisorption systems, we employed isosurface levels of $1.5 \times 10^{-3} e a_0^{-3}$, while $3 \times 10^{-4} e a_0^{-3}$ was used for physisorbed CO_2 , which differ by a factor of 5. The accumulation and depletion of electron density are shown through yellow and blue colors, respectively. Below the structures, we indicate the total effective Bader charge of adsorbed CO_2 (e).



Source: Own study in preparation to be submitted for publication. Permission to use will be requested.

charges are almost constant, because adsorption is mostly driven by the interaction with Pt atoms close to the adsorbate (shell region). The distribution of charges on the isolated nanoalloys exhibit a varied and intricate behavior affected by several factors, such as the spilling of charge to the vacuum, electronegativity differences and coordination.¹⁴⁶ For physisorbed systems, the charges are almost unchanged, due to adsorption; in contrast, for chemisorption, the metal atoms closer to CO_2 are positively charged, since $\text{CO}_2^{\delta-}$ removes charge from the nearest TM. Moreover, as mentioned before, the local separation of charges play a role to stabilize $\text{CO}_2^{\delta-}$. As expected, the redistribution of charges around the substrates could not be simplified as a single behavior for all substrates, due to the unique characteristics of each system, which suggests an interesting opportunity to design catalysts focusing on the stabilization of electron-deficient nanoparticles produced after the formation of $\text{CO}_2^{\delta-}$.

To qualitatively evaluate the redistribution of charges of the adsorbed systems, we

calculated the electron density difference isosurfaces pictured in Figure 21. As expected, the perturbations were greater for chemisorption compared to physisorption and the isosurfaces show characteristic profiles for CO₂ adsorption, discussed in Chapter 4 and reported in previous studies.^{58,145} In summary, the perturbations around CO₂ are affected by its orientation, in relation to the nanoclusters, and the type of adsorption. For the substrates, we found small perturbations on some TM atoms, resulting from two effects: the redistribution of charges and rearrangements of local magnetic moments, due to the geometric perturbations after adsorption.

5.8 Summary and Perspectives

The results discussed in this chapter show the effects of alloying a TM with Pt on the adsorption of CO₂, indicating the importance of the Pt content to control the type of adsorption differently for each TM. From alloying, we observed the possibility to change the most favorable type of adsorption, defined by the TM that is alloyed with Pt; nanoalloys constructed with a TM from the periodic groups 8 to 10 and Pt effectively formed CO₂^{δ-}, although increasing Pt content could reduce the adsorption strength; moreover, the presence of Pt facilitated the chemisorption for metals with completely filled *d*-states (group 11). This could be interesting in conjunction with synergistic effects on the properties of the substrates as Pt content changes. Hence, future studies could focus on the dependence of interesting properties of the catalysts on the quantity of Pt. Other types of TM could also be considered to investigate specific nanoalloys, and the present results could be useful to orient the expectations for the adsorption process. Moreover, specific systems could be selected for studies, in conjunction to experimental efforts, considering several properties and processes, such as resistance to catalytic poisoning, dissociation pathways and reaction barriers.

This chapter closes the investigation of the adsorption properties for CO₂ interacting with TM substrates. As mentioned above, from this point, there is still a vast chemical space to explore about small molecules connected to CO₂ utilization, as well as considering processes beyond adsorption. However, the next chapter was dedicated to study small alcohols, more specifically, to investigate how its functional group affects the adsorption process on TM surfaces.

6 EFFECTS OF THE HYDROXY GROUPS ON THE ADSORPTION OF ALCOHOLS ON TRANSITION-METAL SURFACES

This chapter is an adaptation for the thesis, with permission, of a published article.¹⁵⁹ Reproduced by permission of the PCCP Owner Societies from Paulo C. D. Mendes, Rafael Costa-Amaral, Janaina F. Gomes, Juarez L. F. Da Silva, The Influence of Hydroxy Groups on the Adsorption of Three-carbon Alcohols on Ni(111), Pd(111) and Pt(111) Surfaces: a Density Functional Theory Study within the D3 Dispersion Correction. *Physical Chemistry Chemical Physics*, v. 21, n. 16, p. 8434-8444 (2019) <<https://doi.org/10.1039/C9CP00752K>>.

Further details about the permissions are in Appendix A. Additional analyses and resources were published in the referred article and its Supporting Information.¹⁵⁹

6.1 Introduction and State of the Art

This chapter focuses on the adsorption of alcohols on TM surfaces. Such molecules can be used as solvents, fuels or industrial precursors. As will become clear throughout this introduction, this study employed three-carbon (C_3) alcohols, due to the interest to understand the impacts of hydroxy functional groups on the adsorption, which brings glycerol into focus. Similarly to the need to find routes for CO_2 utilization, discussed separately in the previous chapters of this thesis, glycerol has also been mobilizing researchers to find options for its utilization, because of the expressive accumulation of this compound as a byproduct of biodiesel production.⁶⁷ This motivation and several applications proposed for glycerol were explained in the Chapter 1. Hydrogenolysis is one of the technologies most closely related to the present study, because it involves the formation of all C_3 molecules studied in this chapter: propane, 1-propanol, 2-propanol, 1,2-propanediol, 1,3-propanediol and glycerol. Understanding the adsorption of alcohols on TM substrates is important, since such materials can be employed as catalysts for the hydrogenolysis process;^{5,220,221} moreover, the TM are ubiquitous in the conversion of alcohols into H_2 and other technologies,^{71,74,222} because the TM can activate H_2 molecules⁵ and promote bond cleavage for glycerol conversions.²²² Practical catalysts can contain several parts, such as supported particles and layered substrates;^{73,74,80,221} however, theoretical insights can be obtained using model systems, such as TM surfaces.^{9,37,77}

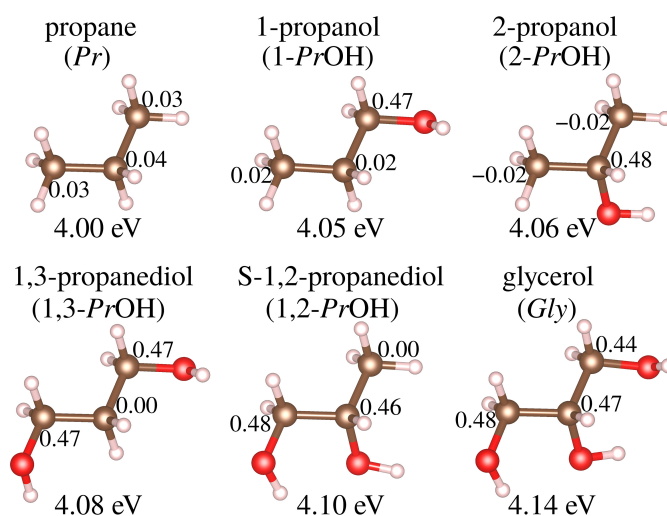
The adsorption of alcohols, including glycerol, on TM substrates has been explored in great detail previously.^{37,38,75,77,79,133,223} The alcohols normally bind to the substrate through the O atom close to top adsorption sites, while the remaining regions of the molecule maximize the interaction with the nearest TM atoms.^{75,223} For this, the C–C bonds can rotate and the OH groups can reorient to adjust the molecule towards the

substrate; however, the sp^3 geometry is stable.^{37,220} After adsorption, the alcohols usually donate a small quantity of charge to the substrates, as suggested by the overall positive charge on the adsorbate although, locally, the electronegative O atom removes charge from the nearest TM atom.^{39,75} Hence, the adsorption has a strong Coulombic character, which has been related to the strengthened adsorption in the presence of cationic sites.^{75,224,225} For small 13-atom clusters, the aforementioned trends are observed, but there is a substantial increase in the adsorption strength of alcohols attributed to the low coordination of the atoms interacting with the molecules.³⁸ Despite the prevalence of the aforementioned characteristics in the adsorption of alcohols, the process can be expected to change for different types of alcohols. For example, the adsorption strength increases with the size of the C chain from methanol to ethanol and glycerol.⁷⁵ Glycerol presents a much stronger adsorption than the other alcohols, which is related to the presence of more OH groups in glycerol,^{75,226} hence, it is clear that the OH groups are pivotal to the adsorption and reactivity of alcohols.

The adsorption strength of glycerol adsorbed on model Pt surfaces can be controlled through the type of surface plane³⁷ and the presence of defects,^{9,137} due to the promotion of stronger adsorption by low-coordinated Pt atoms, which have the d -band positioned closer to the Fermi level in comparison to more coordinated atoms. Considering that this is an effect of the substrate, controlling adsorption through reactivity should also be possible for other alcohols.^{38,134} Alcohols, such as glycerol, are also prone to additional effects related to hydrogen interactions; for example, the presence of one H₂O molecule coadsorbed with glycerol forms intermolecular hydrogen interactions that stabilize the adsorption structures of glycerol adsorbed on Pd(111).²²⁷ For glycerol, and also for its dehydrogenated intermediates, the OH groups reorient after adsorption to optimize intramolecular hydrogen interactions.²²⁸ Dehydrogenation can facilitate breaking C–C and C–O bonds;⁷⁷ thus, the lability of the H atoms, which is related to inductive effects, impacts the reactivity of alcohols.⁸⁵ Different types of TM can favor specific dissociation paths; for the example of compact (111) planes, Pt, Pd and Rh favor breaking C–C bonds, while Ni promotes C–O scission and Cu is predicted to form the dissociated species at a high energetic cost.⁷⁷

Experimentally, it is clear that the number and positions of hydroxy groups affect molecular inductive effects and the reactivity.⁸⁵ This is demonstrated by the different trends observed for the products formed from the steam reforming of 1,2-propanediol, 1-propanol and glycerol.⁷⁴ Various electrochemical studies^{85,86,229,230} discussed alcohol reactivity based on molecular steric²²⁹ and inductive effects;⁸⁵ however, it is challenging to relate all experimental observations to the atomistic level, because applied conditions often carry several factors that can affect the reactions in parallel to the effects related to the OH groups. For example, depending on surface treatment, the catalyst could easily have low coordinated and highly reactive adsorption sites,^{9,79} cations in solution can form water complexes of different sizes that can inhibit the processes²³¹ and the pH can drastically

Figure 22 – Optimized isolated C_3 molecules. The atomization energies per atom, in eV, are shown below the configurations and, for the C atoms, the effective Bader charges, in e , are presented.



Source: Own study reproduced with permission for the thesis.¹⁵⁹ Reproduced from Ref. 159 with permission from the PCCP Owner Societies.

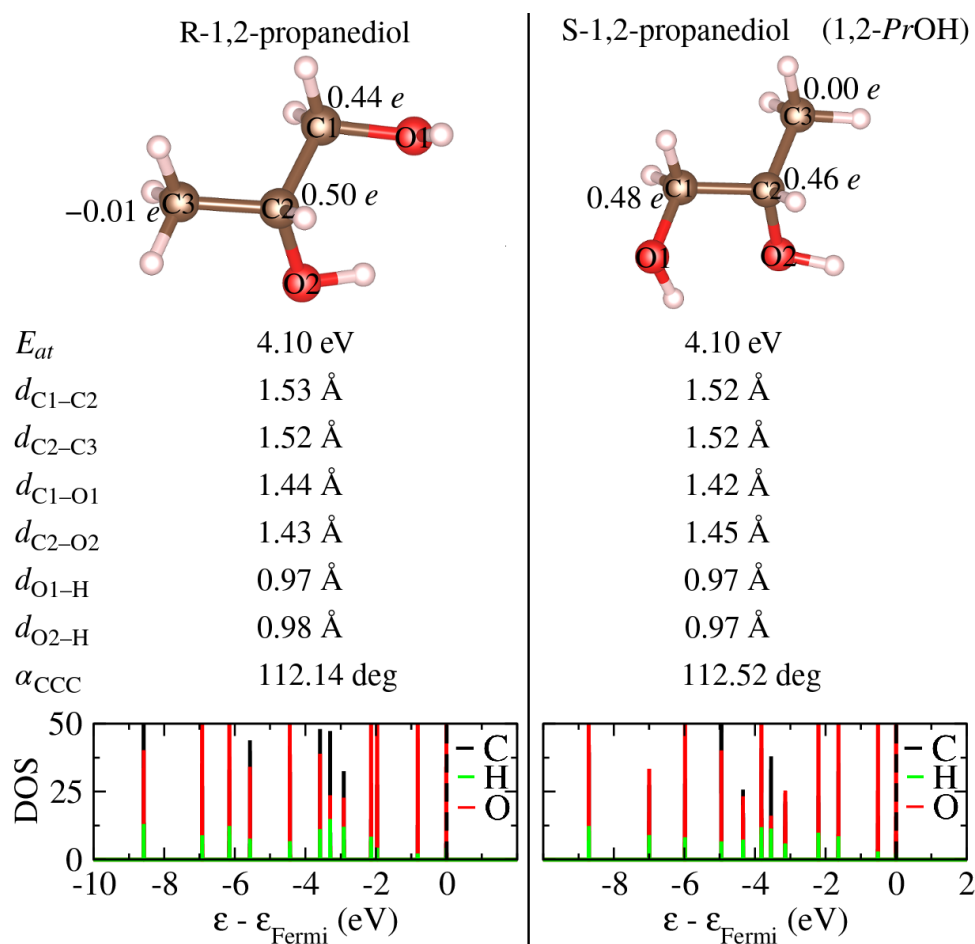
affect the selectivity and activity.^{84,232} The relevance of the O atoms in the adsorption process has been recognized in various studies.^{37,75,223} However, before starting the present study, the atomistic details of how changing the number and positions of OH groups affects the adsorption properties for alcohols interacting with TM substrates had not been described systematically in the literature.

Here, focusing on the effect of the hydroxy groups on the adsorption of alcohols on TM surfaces, we selected the model Ni(111), Pd(111) and Pt(111) surfaces to investigate the adsorption of C_3 molecules considering all structural possibilities with respect to the OH groups: propane (*Pr*), 1-propanol (1-*PrOH*), 2-propanol (2-*PrOH*), 1,3-propanediol (1,3-*PrOH*), 1,2-propanediol (1,2-*PrOH*) and glycerol (*Gly*). With the combination of these molecule–TM systems, it was possible to focus on the OH groups, which was the goal of the study, while considering different types of TM modeled as compact surfaces.

6.2 Isolated Molecules and Surfaces

Compared to the molecules studied in the previous chapters, the C_3 molecules have more degrees of freedom and more intricate potential energy surfaces. There are several possible isomers for polyol configurations, such as 1,2-propanediol,²³³ 1,3-propanediol²³⁴ and glycerol.²³⁵ Most isomers are simply conformers, which differ mainly by the orientation of the OH groups; moreover, 1,2-propanediol exists as two enantiomers, since the central carbon is a stereogenic center.²³⁶ Overall, the number of isomers for the alcohols increases with the number of hydroxy groups, due to the higher number of possibilities for O–H rotations and also to intramolecular H interactions.²³⁵ Therefore, the starting atomic

Figure 23 – Comparison of properties of the isolated stereoisomers, R-1,2-propanediol and S-1,2-propanediol. On the molecules, the effective Bader charges of C atoms are indicated, in e , followed by the atomization energy per atom, in eV, and the most important geometric properties. Moreover, the total local density of states for C, H and O atoms are presented for each enantiomer.



Source: Own study reproduced with permission for the thesis.¹⁵⁹ Reproduced from Ref. 159 with permission from the PCCP Owner Societies.

configurations were selected carefully; for gas-phase glycerol, we employed the most stable configuration obtained from previous studies,^{9,37} followed by optimization, while the other isolated molecules were constructed from the optimized glycerol molecule by substituting a selected hydroxy group by one H atom, followed by structural optimization.

The optimized configurations of the gas-phase C_3 adsorbates are shown in Figure 22 with the respective atomization energies per atom, $E_{at} = \frac{1}{N}(\sum E_{tot}^{atom\ i} - E_{tot}^{C_3})$, in which $E_{tot}^{atom\ i}$ is the total electronic energy of the free atom, i , and $E_{tot}^{C_3}$ is the total electronic energy of the C_3 adsorbate. Notice that the binding energy per atom, E_b , discussed in the previous chapters has a similar meaning to E_{at} , but the properties have opposite signs; the first represents the cohesiveness (binding), which is normally a negative energetic change, while the latter represents atomization (breaking the system into atoms), which

Table 13 – Face-centered cubic bulk and fcc(111) clean surface properties for Ni, Pd and Pt. For the crystals: optimized lattice parameter, a_0 , effective coordination number, ECN, in number of nearest neighbors (NNN), total magnetic moment, m_{tot} , and cohesive energy per atom, E_{coh} . For surfaces: interlayer relaxation for the topmost layers, Δ_{12} , work function, Φ , and average d -band center for the up, $\varepsilon_{d\uparrow}$, and down, $\varepsilon_{d\downarrow}$, states of the surface atoms exposed to the vacuum.

Bulk	a_0 (Å)	ECN (NNN)	m_{tot} (μ_B)	E_{coh} (eV)
fcc Ni	3.48	12.0	0.62	-5.10
fcc Pd	3.88	12.0	0.33	-4.35
fcc Pt	3.92	12.0	0.00	-6.22
Surface	Δ_{12} (%)	Φ (eV)	$\varepsilon_{d\uparrow}$ (eV)	$\varepsilon_{d\downarrow}$ (eV)
Ni(111)	0.00	5.08	-1.96	-1.54
Pd(111)	1.25	5.21	-2.08	-2.03
Pt(111)	1.93	5.68	-2.64	-2.64

Source: Own study reproduced with permission for the thesis.¹⁵⁹ Reproduced from Ref. 159 with permission from the PCCP Owner Societies.

is normally a positive energy variation. The different C_3 molecules showed very small differences of bond lengths and angles; the largest variations were of 0.02 Å for C–O and of 0.01 Å for C–C and C–H. The CCC angles were within the very short range from 112.14° (1,2-propanediol) to 112.92° (glycerol). Hence, the number and positions of hydroxy groups do not disturb the geometry of the C_3 chain, due to the stable hybridization. The E_{at} changes by 0.14 eV comparing propane and glycerol, which is related to the greater ionic character of C–O and O–H bonds, compared to C–H bonds, as well as to intramolecular H interactions involving the hydroxy groups. The adjacency of OH groups is slightly more favorable energetically than the non-vicinal positioning of such groups, which can be related to the intramolecular hydrogen interactions and is demonstrated by 1,2-propanediol and 1,3-propanediol; moreover, 2-propanol is slightly more stable than 1-propanol, due to the degree of substitution of the C atom bonded to the OH group. The effective Bader charges¹⁴¹ of the C atoms are related to the presence of the O atoms, while the charges of the H and O atoms were, on average for all species, of 0.01 e (H bonded to C atoms) 0.58 e (H bonded to O atoms) and -1.08 e (O atoms).

For any adsorption study, it is essential to be aware of isomerisms. As mentioned before, 1,2-propanediol has a stereogenic center on the C atom, since the atom is connected to four different ligands: -H, -OH, -CH₃ and -CH₂OH. This means that two different molecules (stereoisomers) exist,²³⁶ depending on the relative position of these ligands, namely, S-1,2-propanediol (S = *sinister*) and R-1,2-propanediol (R = *rectus*). In this study, we compared some properties of these isolated molecules, Figure 23, and concluded that

the differences in the atomization energy, bond lengths, angles and density of states of these molecules are negligible for this investigation to understand the effect of the OH groups on adsorption.

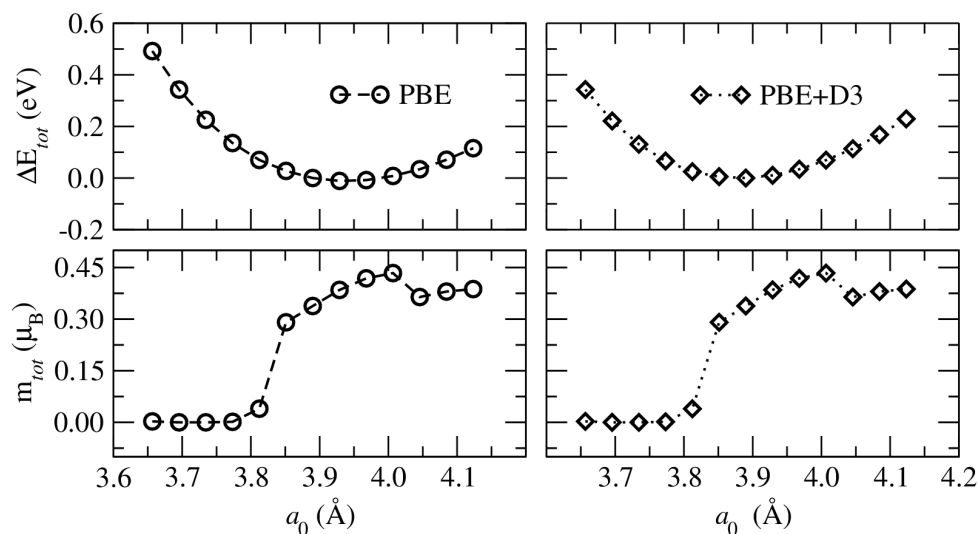
The Ni, Pd and Pt substrates studied in this chapter were fcc(111) surfaces, which were discussed in Chapter 3, but here, we focus on the PBE+D3 results and provide a closer look at the trends specific for this periodic group in Table 13. First, considering the bulk phases, descending on the periodic group, a_0 increases following the increased atomic radius in this direction. Our results for a_0 show slightly smaller values than the reference data,⁸⁷ by 1.26, 0.21 and 0.11 %, respectively, for fcc Ni, Pd and Pt, which can be related to the attractive character of the dispersion and usual overestimation of a_0 by PBE.¹⁵⁴ The bulk cohesive energies deviated from experimental results^{113,152} by 14.93, 11.60 and 6.27 %, respectively, for fcc Ni, Pd and Pt. Concerning the magnetic moment per atom, fcc Ni presented a result close to the experimental value of $0.60 \mu_B$.²³⁷ Considering fcc Pd, a small magnetic moment was obtained after optimization; as mentioned in Chapter 3, this behavior was reported by other authors¹⁵⁸ for fcc Pd and it is related to the increased the magnetic moment resulting from small variations of the lattice. To reproduce this characteristic, we calculated the total energy and the magnetic moments of fcc Pd varying the volume of the unit cell a_0^3 , as shown in Figure 24 for PBE and PBE+D3. The profiles show that the lowest energy conditions present a small magnetic moment, indicating that spin-polarized calculations are important for this system.

Considering the clean TM(111) surfaces, the work functions are smaller than experimental results by 5.04, 6.90 and 0.34 %, respectively, for Ni, Pd and Pt.¹⁶⁵ The interlayer relaxations agree with experimental evidences that there is no relaxation or only a slight contraction for Ni(111),²³⁸ while for Pd(111)²³⁹ and Pt(111),²⁴⁰ the interlayer spacing expands ($\Delta_{12} > 0$) by less than 2 %. The d -band centers of the surface atoms follow the periodic trends discussed in Chapter 3 and will be related to the adsorption strength and density of states in the discussions ahead.

6.3 Procedures to Obtain the Adsorption Atomic Structure Configurations

The starting adsorption configurations were obtained from the most important configurations for glycerol adsorbed on Pt(111) reported previously by other authors.^{9,37} To this set, we included various additional configurations. Then, after geometric optimization of the aforementioned structures, the geometrically and energetically unique structures were selected as initial configurations to obtain starting structures for glycerol adsorbed on Ni(111) and Pd(111). Then, similarly to what was done to construct the gas-phase molecules, the configurations for 1,2-propanediol and 1,3-propanediol interacting with the TM surfaces were constructed from the optimized structures for glycerol adsorbed on each respective surface by substituting one hydroxy group by H. From this, the procedure was

Figure 24 – Energy relative to the crystal fixed at $a_0 = 3.89 \text{ \AA}$, ΔE_{tot} , and total magnetic moment, m_{tot} , versus the lattice parameter, a_0 , for fcc Pd, PBE and PBE+D3.



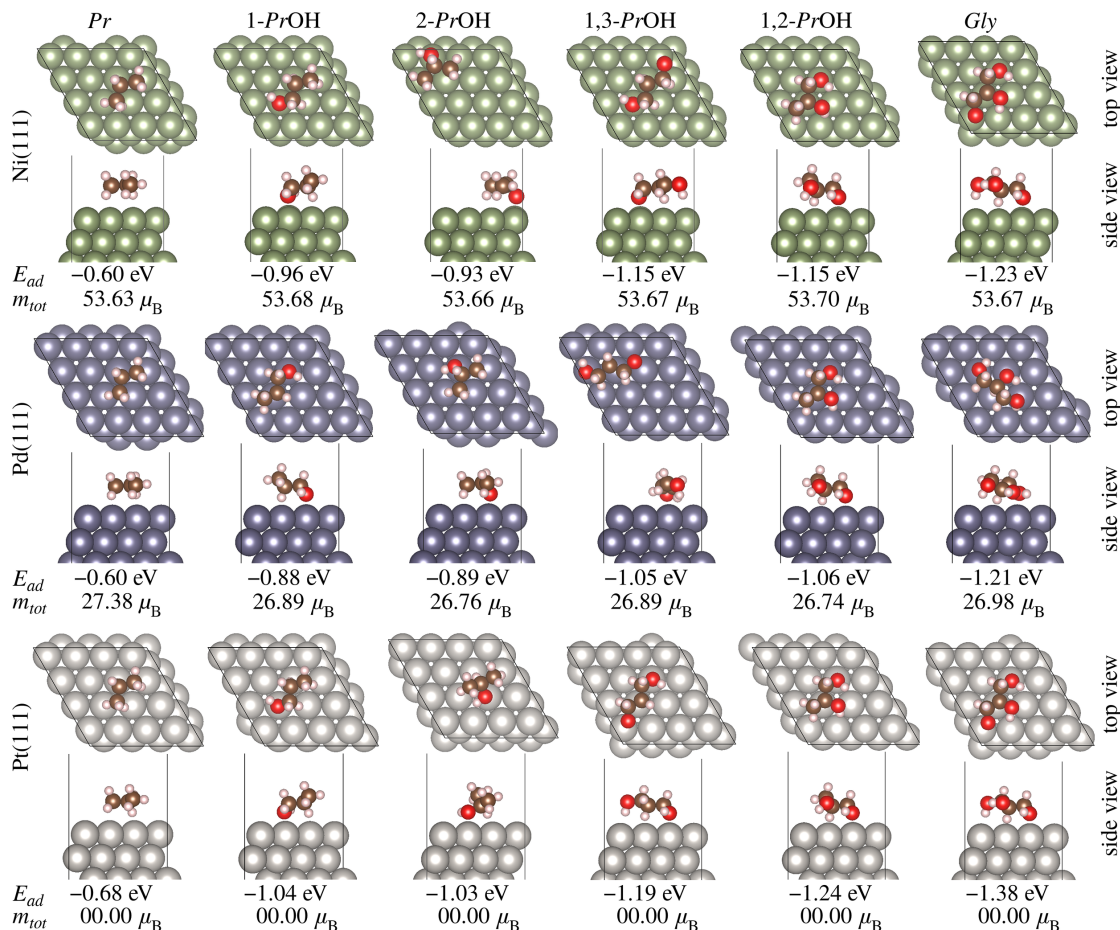
Source: Own study reproduced with permission for the thesis.¹⁵⁹ Reproduced from Ref. 159 with permission from the PCCP Owner Societies.

repeated to obtain adsorption configurations involving 2-propanol, 1-propanol and propane. This method was computationally feasible and allowed the investigation of a several relevant configurations. Due to the method for generating our starting adsorption structures, our adsorption configurations contain one of the stereoisomers of 1,2-propanediol, while the enantiomer was explored in different adsorption positions; considering the comparison presented in the previous section, this fact does not affect the conclusions about the effect of the hydroxy groups on adsorption. The enantiomers were identified in all of our adsorption configurations.¹⁵⁹ All structures were fully optimized before any analysis.

6.4 Adsorption of C₃ Alcohols on Ni(111), Pd(111) and Pt(111)

The most stable adsorption configurations are shown in Figure 25 and the complete sets of configurations are illustrated in Appendix F. As expected, the alcohols adsorb through the O atoms close to top sites and the C chain is almost parallel to the substrate maximizing the interaction. Considering propane, in which there are no hydroxy groups, one H atoms bonded to the central C approaches the top site of the surface and the C chain remains parallel to the surface. For the OH groups that bind closer to the surface, the O–H bond is almost parallel to the surface; overall, the H atoms of the hydroxy groups reorient to interact with the surface and also to stabilize the systems through intramolecular H interactions; examples of each behavior can be observed in each OH group of the glycerol adsorbate. Other types of orientation of the molecules led to higher energy structures, such as the vertical orientation of the C chain or cases with the OH groups pointing towards the vacuum instead of the surfaces. Interestingly, the adsorption

Figure 25 – Top and side views of the most stable adsorption configurations for the C_3 molecules adsorbed on close-packed Ni, Pd and Pt surfaces. Below the configurations, we show the adsorption energy, E_{ad} in eV, and total magnetic moment, m_{tot} in μ_B .



Source: Own study reproduced with permission for the thesis.¹⁵⁹ Reproduced from Ref. 159 with permission from the PCCP Owner Societies.

configurations for propane spanned a shorter range of relative energies compared to the hydroxylated molecules, which could be related to a more corrugated potential energy surface for the molecules containing more OH groups.

6.4.1 Adsorption Energy and Density of States

As in the previous chapters, the adsorption energy, E_{ad} , was calculated to measure the intensity of the interaction between the adsorbate and the surfaces as $E_{ad} = E_{tot}^{C_3/sub} - E_{tot}^{C_3} - E_{tot}^{sub}$, in which $E_{tot}^{C_3/sub}$ is the total electronic energy of the adsorbed system, while $E_{tot}^{C_3}$ and E_{tot}^{sub} are the total electronic energies of the isolated C_3 molecule and clean surfaces, respectively. The results are shown in Figure 25. For this chapter, the interaction energies were not calculated, because the contributions of the deformation energies for the molecules and surfaces are not expected to be significant. There is a contribution related to the variations of the dihedral angles, which result in less stable adsorbed conformers,

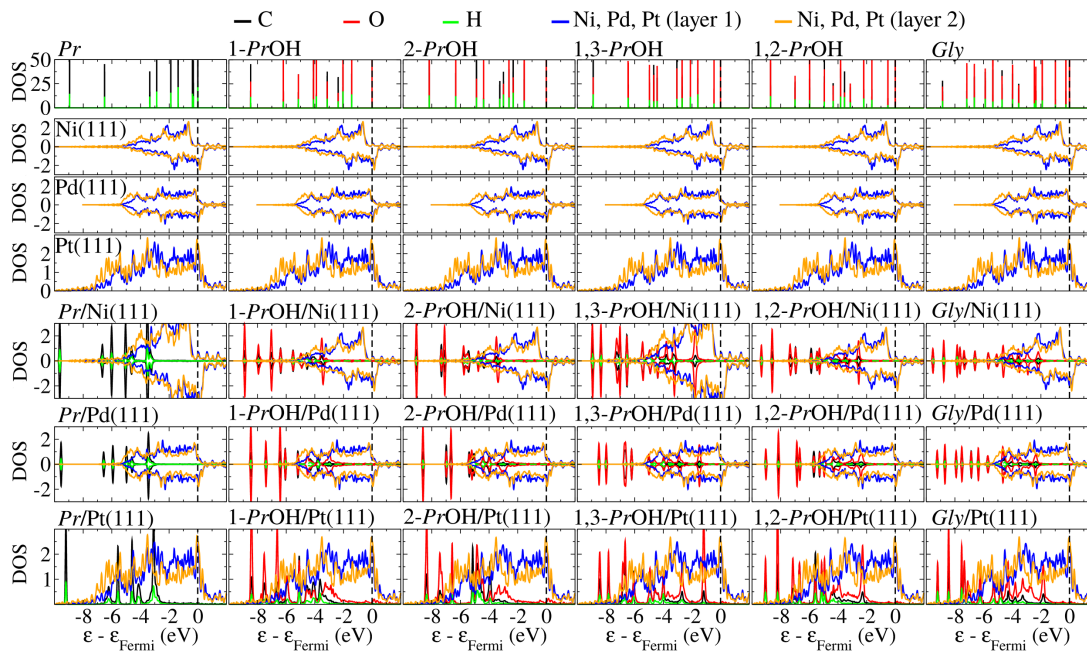
however, the geometric deformations of bond lengths and angles were small compared to the molecules discussed in the previous chapters, as will be discussed ahead. In such case, by definition, the adsorption and interaction energies can be expected to have approximately the same value.

For all surfaces, the adsorption strength becomes more negative (stronger adsorption) as the number of OH groups increases from propane to glycerol. For most cases, the pairs of regioisomers show similar values of E_{ad} , since they bind to similar adsorption sites, which leads to similar perturbations of the electron density that will be discussed ahead, Figure 28. This consistent E_{ad} between the regioisomers can also be related to the capacity of the small C_3 adsorbates to reorient towards the surface, unhindered by steric effects, which allows all O atoms to approach the substrates. Considering that such O atoms are the most important to increase the adsorption strength,^{37,75} small variations on the geometries of the molecules were not sufficient to distinguish the adsorption energies of the regioisomers.

Considering the type of TM, according to ε_d from Table 13, the interaction strength would be expected to follow the descending order on the periodic group: Ni(111) > Pd(111) > Pt(111). However, our results show that the adsorption strength followed the order Pt > Ni > Pd for most adsorbates on the close-packed surfaces, hence, the TM atom that has the ε_d closer to the Fermi level does not show the strongest adsorption, which does not agree with the expectation from the d -band model.^{44,182} This type of deviation from the model can occur because the adsorption of alcohols is relatively weak on TM surfaces and not entirely driven by the hybridization; there are additional factors, such as charge transfer accompanied by the formation of dipoles that can lead to a strong Coulombic character for the interaction. Similar situations were faced by other researchers studying the adsorption of glycerol^{9,37} and ethanol³⁹ on TM surfaces.

To further understand the interactions among electronic states due to adsorption, the DOS was calculated for the lowest energy adsorption configurations. The total local DOS, which is the summation of the local s , p and d states are shown in Figure 26. The molecules present the characteristic sharp peaks with contributions from the s - and p states of the C, O and H atoms. For the TM atoms, the ε_d of the topmost slab layer shifts towards the Fermi level compared to the innermost atoms, due to the lower coordination of the atoms exposed to the vacuum, as we demonstrated in Chapter 3. The changes observed for the DOS after adsorption of the C_3 molecules, compared to the isolated systems, reproduce the behavior that was described previously in the literature.^{9,37} The DOS for the surface TM atoms are virtually unchanged by adsorption and the DOS of the molecules broaden and shift away from the Fermi level, because of the different referential for the most energetic occupied electronic state. Since the DOS of the surfaces is almost unchanged, small variations are also observed for the total magnetic moments after adsorption; for

Figure 26 – Average total local density of states (DOS) per atom, including s -, p - and d -states, for the lowest energy configurations of isolated C_3 molecules, first and second topmost slab TM layers of clean Ni(111), Pd(111) Pt(111) surfaces, and adsorbed systems. The vertical dashed lines indicate the Fermi level of the substrates, and the highest occupied molecular orbital of the gas-phase C_3 molecules.



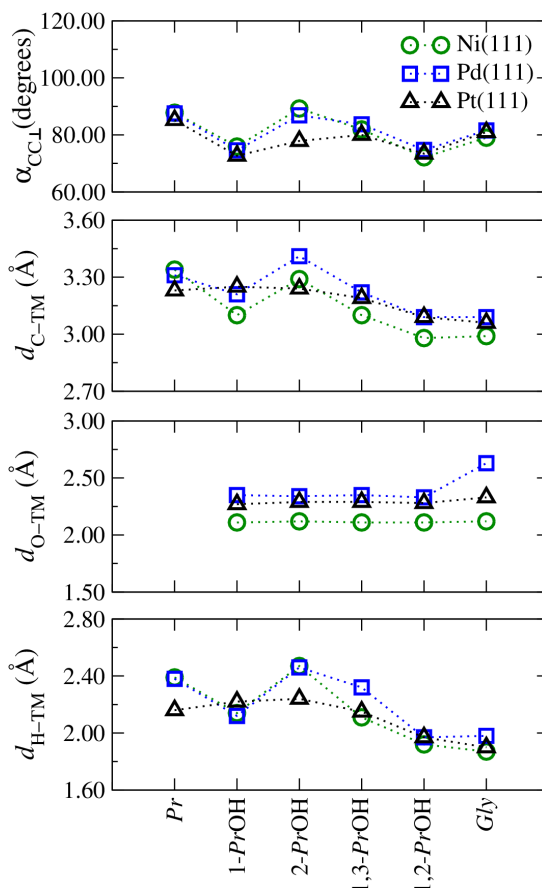
Source: Own study reproduced with permission for the thesis.¹⁵⁹ Reproduced from Ref. 159 with permission from the PCCP Owner Societies.

Pd(111) and Ni(111) adsorption structures, the total magnetic moment for the unit cell, m_{tot} , closely followed the value for the clean surfaces, $27.43 \mu_B$ for Pd(111) and $53.63 \mu_B$ for Ni(111), with negligible contributions from the molecules. For Pt(111), up and down occupations are the same and $m_{tot} = 0 \mu_B$ regardless of molecular orientation.

6.4.2 Geometric Properties

The geometric properties that characterize the adsorption of the C_3 molecules on the TM surfaces are presented in Figure 27. The angle between the normal vector, with respect to the surface plane, and the straight line connecting the terminal C atoms, $\alpha_{CC\perp}$, is in the range from 72.16° , for 1,2-propanediol/Ni(111), to 89.25° , for 2-propanol/Ni(111). Since $\alpha_{CC\perp} = 90^\circ$ means a parallel orientation of the C chain, our results confirm the almost parallel orientation of the C_3 molecules in relation to the surface. The different orientations evidenced by the aforementioned range can be attributed to the attractive interaction between the O and TM atoms and to steric effects. The shortest distances between C, O and H atoms to a surface TM atom (d_{C-TM} , d_{O-TM} and d_{H-TM}) showed that the O and H atoms are closer to the surface than the C atoms, which is characteristic of stable adsorption configurations for alcohols. The d_{O-TM} values are in the range from 2.11 \AA to

Figure 27 – Geometric properties for the adsorption of C_3 molecules on the close-packed TM surfaces. Angle between the surface normal and the line connecting the terminal C atoms ($\alpha_{CC\perp}$, in degrees) and shortest distances between C, O and H atoms and the nearest TM surface atom (d_{C-TM} , d_{O-TM} and d_{H-TM} , in Å) for the most stable adsorption configurations.



Source: Own study reproduced with permission for the thesis.¹⁵⁹ Reproduced from Ref. 159 with permission from the PCCP Owner Societies.

2.63 Å, d_{C-TM} are in the range from 2.98 to 3.41 Å, while d_{H-TM} span the range from 1.87 to 2.47 Å. Considering the different TM, d_{O-TM} and d_{H-TM} accompany the atomic radii of the TM, which are in the following order: Ni < Pd \approx Pt. The slight variations observed for different alcohols are consistent with the orientation of the molecules relative to the surface plane (Figure 25). It can be expected that shorter distances from the molecule to the surface are related to stronger adsorption and greater perturbations of the bond lengths and electron density. Notably, Pt(111) shows shorter d_{O-TM} than Pd(111), which agrees with the stronger adsorption strength observed for Pt(111).

One of the core principles of catalysis is that, after adsorption, the molecular geometry (bonds and angles) can change, which affects the lability of atoms and fragments of the molecules. To verify such effects in our systems, we calculated the percent variations of the bond lengths and CCC angle, comparing the atomic positions of the adsorbed

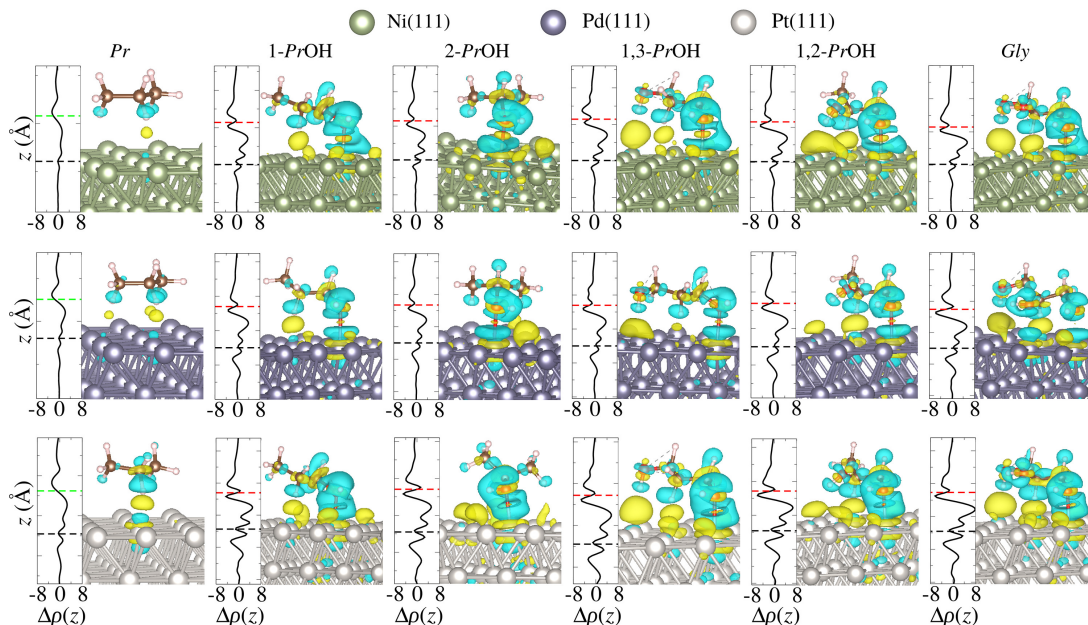
molecules with the most stable isolated molecules.¹⁵⁹ Differently from the small molecules discussed in the previous chapters, the C_3 molecules have a greater variety of regions within the molecular structure that can behave differently; to summarize the results here and standardize the analysis, the C atoms are denominated using the same numbering employed to name the alcohols, following standard nomenclature and considering the C atom bonded to the O atom closer to the substrate as C1. The CCC angle presented very small changes upon adsorption, at most of 3.58% for glycerol/Pt(111), due to the stability of the sp^3 geometry; this is one of the main reasons why the deformation energy is small for the C_3 molecules. The C–C bonds showed a small contraction (strengthening), except for glycerol and 1,3-propanediol, in which the C2–C3 bond was slightly stretched (weakened). The C–O bonds adjacent to the hydroxy group closer to the substrates stretched by approximately 2%, while the other C–O bonds contracted slightly. All O–H bonds and the C–H bonds for the H atoms close to the surfaces stretched, as observed for similar systems in the literature.⁷⁵ The most weakened C–H bonds involved the central C2 atom, for example, the C2–H bond stretched by 1.17% for 2-propanol/Pt(111). The proximity to the surface can be crucial to detach the H atoms from the molecules; this is demonstrated by the adsorption of 2-propanol on Pd(111) and Ni(111), in which the C2–H bonds contracted by -0.29% and -0.43% , respectively, due to the significant distances between such atoms and the substrates (visible in Figure 25).

6.4.3 Electron Density Difference and Distribution of Charges

For a qualitative description of the changes in the electron density after the adsorption, the electron density difference was calculated, analogously to the procedure explained in the previous chapters, as $\Delta\rho(\mathbf{r}) = \rho^{C_3/sub}(\mathbf{r}) - \rho^{C_3}(\mathbf{r}) - \rho^{sub}(\mathbf{r})$, where $\rho^{C_3/sub}$, ρ^{C_3} and ρ^{sub} indicate the electron densities of the adsorbed system, isolated C_3 molecule and substrate, respectively. The isosurfaces and the net variation of $\Delta\rho$ in the z direction are presented in Figure 28. The isosurfaces show expressive perturbations around the hydroxy groups and small perturbations for propane. We observed accumulation of charge close to the O atoms, although the region around the hydroxy groups presents a depletion of charge that extends towards the surfaces. The importance of the distance between the molecule and the surface is also evident in the isosurfaces, for example, the perturbations are significant for species close to the surface, such as OH. Some perturbations occur around the chemical bonds, which could be connected to the percent variations of the bond lengths, as suggested by the depletion of electron density in stretched O–H and C2–H bonds. However, exceptions occur, since this electron density difference analysis is qualitative; for example, the contracted C–C bonds in all 2-propanol structures presented a depletion of charge along the respective bond axis.

For the surfaces, the perturbations are only significant for the two outermost layers of the slab, more specifically, for the TM atoms close to the O and H atoms. Around

Figure 28 – Electron density difference analysis the lowest energy configurations of C_3 molecules adsorbed on TM surfaces. The 3D isosurfaces, $0.0016 e/a_0^3$, show yellow and blue regions indicating, respectively, accumulation and depletion of electron density. The net variation of the electron density along the z direction, $\Delta\rho(z)$, is shown for each structure. The dashed lines indicate the positions of the surface plane (black), O (red) and H (green) atoms closer to the substrates.



Source: Own study reproduced with permission for the thesis.¹⁵⁹ Reproduced from Ref. 159 with permission from the PCCP Owner Societies.

the TM atoms, there is a depletion of charge perpendicular to the surface plane, the same direction of d_{z^2} orbitals, while charge accumulates around this direction forming a shape that could be related to the d_{yz} and d_{xz} orbitals. This profile can be related to the formation of a O–TM bond that can be illustrated, similarly, for the region around the C2 atom in propane/Pt(111). In this case, the interaction involves one H atom close to the substrate, charge accumulates around the C2 atom, while the region along the C–H bond is depleted of charge. For all systems, there is accumulation of charge in the space between the adsorbates and the substrates, which is greater the closer the molecules are to the substrates. The net variation of the electron density on the z axis, $\Delta\rho(z)$, shows that the perturbations are greater for Pt(111), which is also the substrate that promotes the strongest adsorption, compared to Ni(111) and Pd(111). Furthermore, the perturbations are negligible for the innermost slab layers, further confirming that the most important adsorption effects on the electron density are for the local surface region.

As explained in the introductory section of this chapter, it has been described that alcohols usually transfer a small quantity of charge to TM surfaces;^{37,75} then, to further understand how the number and positions of OH groups of the C_3 molecules affect this behavior, we calculated the effective Bader charges;¹⁴¹ the results are shown

Table 14 – Bader charge analysis. Effective charge, Q (in e), for carbon, Q^C , the surface atom closer to the OH group, $Q^{\text{Sur(O)}}$, and average effective charges, \bar{Q} (in e), for the remaining surface atoms \bar{Q}^{Sur} , oxygen, \bar{Q}^{O} , hydrogen bonded to C, $\bar{Q}^{\text{H(C)}}$ and hydrogen bonded to O, $\bar{Q}^{\text{H(O)}}$. Carbon atoms are numbered according to the rules for naming alcohols (C1 is the carbon connected to the O atom closer to the substrate). Q^{Mol} (in e) is the total charge of the adsorbed molecule and $\Delta\Phi$ (in eV) is the work function change after to adsorption.

Mol/TM(111)	Q^{C1}	Q^{C2}	Q^{C3}	$Q^{\text{Sur(O)}}$	\bar{Q}^{Sur}	\bar{Q}^{O}	$\bar{Q}^{\text{H(C)}}$	$\bar{Q}^{\text{H(O)}}$	Q^{Mol}	$\Delta\Phi$
<i>Pr</i> (gas)	0.03	0.04	0.03	-	-	-	-0.01	-	0.00	-
<i>Pr</i> /Ni	-0.03	0.01	-0.03	-	-0.03	-	0.00	-	-0.03	-0.36
<i>Pr</i> /Pd	-0.04	0.03	-0.01	-	-0.03	-	0.00	-	0.00	-0.34
<i>Pr</i> /Pt	-0.01	0.02	-0.03	-	-0.05	-	0.01	-	0.04	-0.40
1- <i>Pr</i> OH (gas)	0.47	0.02	0.02	-	-	-1.08	0.00	0.57	0.00	-
1- <i>Pr</i> OH/Ni	0.40	0.00	0.01	0.15	-0.04	-1.09	0.01	0.60	0.02	-1.10
1- <i>Pr</i> OH/Pd	0.41	0.00	0.01	0.09	-0.04	-1.07	0.02	0.60	0.07	-0.84
1- <i>Pr</i> OH/Pt	0.41	0.00	-0.03	0.10	-0.06	-1.03	0.03	0.61	0.14	-0.98
2- <i>Pr</i> OH (gas)	-0.02	0.48	-0.02	-	-	-1.08	0.01	0.57	0.00	-
2- <i>Pr</i> OH/Ni	-0.04	0.41	-0.05	0.15	-0.04	-1.08	0.03	0.60	0.02	-1.15
2- <i>Pr</i> OH/Pd	-0.06	0.44	-0.03	0.09	-0.04	-1.06	0.03	0.59	0.06	-0.86
2- <i>Pr</i> OH/Pt	-0.04	0.40	-0.05	0.10	-0.06	-1.02	0.04	0.60	0.14	-0.93
1,3- <i>Pr</i> OH (gas)	0.47	0.00	0.47	-	-	-1.08	0.01	0.57	0.00	-
1,3- <i>Pr</i> OH/Ni	0.39	-0.01	0.47	0.15	-0.04	-1.08	0.02	0.58	-0.01	-0.62
1,3- <i>Pr</i> OH/Pd	0.41	-0.04	0.48	0.09	-0.04	-1.07	0.03	0.58	0.02	-0.47
1,3- <i>Pr</i> OH/Pt	0.37	-0.01	0.48	0.10	-0.06	-1.06	0.04	0.59	0.12	-0.61
1,2- <i>Pr</i> OH (gas)	0.48	0.46	0.00	-	-	-1.09	0.01	0.59	0.00	-
1,2- <i>Pr</i> OH/Ni	0.40	0.47	-0.02	0.16	-0.04	-1.10	0.04	0.60	0.01	-0.64
1,2- <i>Pr</i> OH/Pd	0.41	0.47	-0.02	0.10	-0.04	-1.09	0.03	0.61	0.08	-0.54
1,2- <i>Pr</i> OH/Pt	0.39	0.47	-0.02	0.10	-0.07	-1.07	0.04	0.61	0.17	-0.75
<i>Gly</i> (gas)	0.48	0.47	0.44	-	-	-1.09	0.03	0.59	0.00	-
<i>Gly</i> /Ni	0.39	0.48	0.45	0.15	-0.04	-1.10	0.04	0.60	0.02	-0.58
<i>Gly</i> /Pd	0.43	0.45	0.46	0.04	-0.04	-1.08	0.05	0.60	0.07	-0.75
<i>Gly</i> /Pt	0.39	0.50	0.47	0.09	-0.07	-1.08	0.05	0.61	0.19	-0.72

Source: Own study reproduced with permission for the thesis.¹⁵⁹ Reproduced from Ref. 159 with permission from the PCCP Owner Societies.

in Table 14. The total effective charges of the adsorbed C_3 molecules, Q^{C_3} , confirmed a small charge transfer from the C_3 adsorbates to the surface for most systems; the cases of 1,3-propanediol and propane adsorbed on Ni(111) resulted in $Q^{\text{C}_3} \approx 0$. Considering specific atoms, most surface atoms remain anionic after adsorption, as is characteristic of the clean surfaces, but the atoms below the nearest OH groups are positively charged, due to the proximity to the electronegative O atom. Comparing the charges of the adsorbed and isolated molecules, we found that, on average, the adsorbed molecules presented more

positive H atoms, less positive C atoms and slightly less negative O atoms, suggesting that adsorption can enhance inductive effects already present in the molecules, which increases the reactivity of the alcohols and supports their ubiquitous use in heterogeneous catalysis.

To further investigate the adsorption of the C_3 molecules on TM surfaces, the work function change due to adsorption was calculated as $\Delta\Phi = \Phi^{C_3/\text{sub}} - \Phi^{\text{sub}}$, where $\Phi^{C_3/\text{sub}}$ and Φ^{sub} are the work functions^{142,143} for the adsorbed system and clean surface, respectively. The results are shown in Table 14. Adsorption of all C_3 molecules resulted in a decrease of the work function ($\Delta\Phi < 0$), which is typical of systems that donate charge to the substrate, as discussed in Chapter D. The orientation of the C_3 molecules strongly affects $\Delta\Phi$. In general, the magnitude of the reduction is different depending on the adsorbate; for molecules containing only one OH group (2-propanol and 1-propanol), there is a significant decrease of Φ compared to propane. However, the adsorbates with multiple OH groups promoted smaller decreases of Φ , which is contrasting with higher dipole moments due to the presence of more OH groups, because greater dipole moments could be expected to induce greater the work function changes. The same behavior that we observed was reported in other studies about the adsorption of glycerol, methanol and ethanol on Pt(111) and Ni(111).⁷⁵ This can be explained by the fact that the contribution of the dipole moments to the $\Delta\Phi$ is shown as a net variation, which results from the summation of all components of the dipole with various directions induced in the surface.

6.5 Summary and Perspectives

In this chapter, we discussed the adsorption properties of propane, 1-propanol, 2-propanol, 1,2-propanediol, 1,3-propanediol and glycerol on close-packed Ni, Pd and Pt surfaces. The results showed that adsorption becomes stronger as the number of hydroxy groups increases and that it is more dependent on the number than on the positions of the OH groups, due to the similar adsorption strength of regioisomers. Normally, the C_3 alcohols transfer a small quantity of charge to the surface, which results in polarization and a net reduction of the work function. The interaction with the surfaces emphasizes the charges of the alcohols enhancing molecular inductive effects that can be related to the reactivity; moreover, the proximity of atomic species to the surfaces was directly related to the variations in the electron density, bond lengths and charges. Moreover, we identified some of the regions of the molecule that could more susceptible to break after adsorption, such as the C–H bonds involving the alpha carbon to the hydroxy group closest to the substrate.

The results discussed in this chapter effectively improved our understanding of the influence of OH groups on the adsorption of alcohols, from the systematic investigation of the adsorption properties of model molecules including all possible variations of the positions and number of OH groups for C_3 molecules. Although the adsorption properties

seem to vary only slightly for some alcohols, such as the pairs of regioisomers, the reactivity of the alcohols can differ experimentally, due to some features of the experimental scale; we discussed some of these factors in the literature.¹⁵⁹ There are several phenomena that can motivate future studies, for example, specific reaction mechanisms could be explored, considering cleaving first the bonds that were shown to be most weakened by our calculations; this could be connected to electrooxidation mechanisms. Furthermore, different levels of theory, for example, molecular dynamics, could be employed to explore effects in the thermodynamic limit, such as temperature and solvation effects.

7 CONCLUSIONS

This document summarizes the research performed to understand the interaction between molecules, involved in the utilization of carbon dioxide and glycerol, and model TM substrates. We started our investigation studying TM crystals and clean extended (periodic) surfaces, which are theoretical model materials, in Chapter 3. In this preliminary study, we discussed the physical-chemical nature of model solid state materials, such as the effects of the d -band occupation on the cohesive energy and structure of the crystals. This type of behavior was related, in subsequent chapters, to the results observed for the adsorption studies involving surfaces and nanoclusters. The bulk and surface properties reproduced the well-known behavior of the materials, thus, validating our methodology; moreover, this preliminary study was a valuable experience in preparation to study the adsorption of molecules on model TM substrates in the next chapters.

Concerning adsorption, in Chapter 4, we presented in our exploration of transition-metal (Co, Ni and Cu) substrate particle size effects on the adsorption of CO₂, CO, H₂O and H₂. We effectively modeled the different sizes using stable TM₁₃, TM₅₅, TM₁₄₇ nanoclusters and extended close-packed surfaces to model large particles. The adsorption of H₂O was almost independent on the substrate size, however, CO and H₂ showed small oscillations of several adsorption properties, which we related to the alternation of the adsorption site energetic preference. For CO₂, the different particle sizes resulted in significant effects in the adsorption properties, which were related to the degrees of freedom of the adsorbate, such as the possibility of bending the OCO angle, due to charge transfer to the molecule, which is not commonly observed in the contrasting example of the HOH angle of the H₂O molecule. After exploring the size-dependence of various adsorption properties, we emphasized the role of the type of TM through the fact that, although CO₂ adsorption showed size-dependent properties on all substrates studied, the Co and Ni particles featured the bent OCO angle, while the bent OCO angle was more difficult to observe for Cu substrates, which we attributed to the nature of the d -states, adsorption strength and distances between the molecule and the substrates.

Considering that the type of TM greatly affects the type of adsorption (physisorption or chemisorption) for CO₂, we selected the CO₂ molecule and explored, in Chapter 5, its adsorption on a wider range of TM nanoclusters (groups 8 to 11, periods 3d, 4d and 5d of the periodic table) and on Pt-based bimetallic nanoalloys. For the unary nanoclusters, we confirmed the trends expected according to the nature of d -states. In summary, we found that nanoclusters composed of TM from periodic groups 8 to 10 can transfer charge to the CO₂ molecule and stabilize chemisorption structures (bent OCO angle), in contrast, the metals from group 11, which have completely filled d -states, tend to stabilize physisorbed

CO₂ (linear OCO angle) instead of the chemisorbed structure. For bimetallic Pt-based nanoalloys, we found that the chemisorbed CO₂ can be formed effectively on substrates containing Pt alloyed with a TM from groups 8 to 10 of the periodic table, although increasing Pt content could decrease the adsorption strength for TM that adsorb CO₂ strongly on their own unary systems, for example, Fe and Os. Additionally, the presence of Pt facilitated the chemisorption process for the metals with completely filled *d*-states (Cu, Ag, Au). Hence, we emphasized the possibility to change, through the quantity of Pt, the most favorable type of adsorption defined by the TM that will be alloyed with Pt.

After the detailed studies centered on CO₂ and model molecules involved in its utilization, we contributed to better understand the adsorption of alcohols focusing on the influence of hydroxy functional groups on the adsorption process. For this, we selected the close-packed Ni(111), Pd(111) and Pt(111) as substrates to explore the adsorption of three-carbon molecules featuring all variations of the positions and number of hydroxy groups. We found a strong dependence of the adsorption strength with the number of hydroxy groups, which was expected, but the adsorption strength was not significantly changed for different relative positions of the functional groups. In contrast, other adsorption properties, such as the structural perturbations of the molecular geometries and electron density, were affected by both the number and positions of the hydroxy groups. From the adsorption properties, we were able to suggest the most weakened bonds, for example, the C–H bond on the alpha carbon to the O atom closer to the substrate. These findings could be important to additional studies of bond scission. Furthermore, we were able to relate the charges on the molecules and the adsorption strength to the reactivity expected for the alcohols.

Overall, this study resulted in extensive contributions to the literature about the adsorption of model molecules on transition-metal substrates. Further interesting research topics abound and some of them were mentioned as perspectives along the thesis. Great worldwide scientific efforts have been focused on finding solutions for CO₂ and glycerol utilization from several perspectives, and we expect a bright future for this field.

BIBLIOGRAPHY

- 1 CRAMER, C. J.; TRUHLAR, D. G. Density functional theory for transition metals and transition metal chemistry. **Physical Chemistry Chemical Physics**, v. 11, n. 46, 2009.
- 2 ERISMAN, J. W.; SUTTON, M. A.; GALLOWAY, J.; KLIMONT, Z.; WINIWARTER, W. How a century of ammonia synthesis changed the world. **Nature Geoscience**, v. 1, n. 10, p. 636–639, 2008.
- 3 COKOJA, M.; BRUCKMEIER, C.; RIEGER, B.; HERRMANN, W. A.; KÜHN, F. E. Transformation of carbon dioxide with homogeneous transition-metal catalysts: A molecular solution to a global challenge? **Angewandte Chemie International Edition**, v. 50, n. 37, p. 8510–8537, 2011.
- 4 CUÉLLAR-FRANCA, R. M.; AZAPAGIC, A. Carbon capture, storage and utilisation technologies: A critical analysis and comparison of their life cycle environmental impacts. **Journal of CO₂ Utilization**, v. 9, p. 82–102, 2015.
- 5 NAKAGAWA, Y.; TOMISHIGE, K. Heterogeneous catalysis of the glycerol hydrogenolysis. **Catalysis Science & Technology**, v. 1, n. 2, p. 179–190, 2011.
- 6 SABATIER, P. Hydrogénations et déshydrogénations par catalyse. **Berichte der Deutschen Chemischen Gesellschaft**, v. 44, n. 3, p. 1984–2001, 1911.
- 7 SKÚLASON, E.; TRIPKOVIC, V.; BJOORKETUN, M. E.; GUDMUNDSDÓTTIR, S.; KARLBERG, G.; ROSSMEISL, J.; BLIGAARD, T.; JONSSON, H.; NØRSKOV, J. K. Modeling the electrochemical hydrogen oxidation and evolution reactions on the basis of density functional theory calculations. **The Journal of Physical Chemistry C**, v. 114, n. 42, 2010.
- 8 FALIVENE, L.; KOZLOV, S. M.; CAVALLO, L. Constructing bridges between computational tools in heterogeneous and homogeneous catalysis. **ACS Catalysis**, v. 8, n. 6, p. 5637–5656, 2018.
- 9 AMARAL, R. C.; TERESHCHUK, P.; SEMINOVSKI, Y.; DA SILVA, J. L. F. The role of low-coordinated sites on the adsorption of glycerol on defected Pt_n/Pt(111) substrates: A density functional investigation within the D3 van der Waals correction. **The Journal of Physical Chemistry C**, v. 121, n. 6, p. 3445–3454, 2017.
- 10 CALLE-VALLEJO, F.; KOPER, M. T. M.; BANDARENKA, A. S. Tailoring the catalytic activity of electrodes with monolayer amounts of foreign metals. **Chemical Society Reviews**, v. 42, n. 12, p. 5210–5230, 2013.
- 11 NØRSKOV, J. K.; BLIGAARD, T.; ROSSMEISL, J.; CHRISTENSEN, C. H. Towards the computational design of solid catalysts. **Nature Chemistry**, v. 1, n. 1, p. 37–46, 2009.
- 12 BIAN, Z.; DAS, S.; WAI, M. H.; HONGMANOROM, P.; KAWI, S. A review on bimetallic nickel-based catalysts for CO₂ reforming of methane. **ChemPhysChem**, v. 18, n. 22, p. 3117–3134, 2017.

- 13 AIKEN III, J. D.; FINKE, R. G. A review of modern transition-metal nanoclusters: Their synthesis, characterization, and applications in catalysis. **Journal of Molecular Catalysis A: Chemical**, v. 145, n. 1–2, p. 1 – 44, 1999.
- 14 VIÑES, F.; GOMES, J. R. B.; ILLAS, F. Understanding the reactivity of metallic nanoparticles: Beyond the extended surface model for catalysis. **Chemical Society Reviews**, v. 43, n. 14, p. 4922–4939, 2014.
- 15 FERRANDO, R.; JELLINEK, J.; JOHNSTON, R. L. Nanoalloys: From theory to applications of alloy clusters and nanoparticles. **Chemical Reviews**, v. 108, n. 3, p. 845–910, 2008.
- 16 TAKETOSHI, A.; HARUTA, M. Size- and structure-specificity in catalysis by gold clusters. **Chemistry Letters**, v. 43, n. 4, 2014.
- 17 RODRIGUES, T. S.; SILVA, A. G. M. da; CAMARGO, P. H. C. Nanocatalysis by noble metal nanoparticles: Controlled synthesis for the optimization and understanding of activities. **Journal of Materials Chemistry A**, v. 7, n. 11, p. 5857–5874, 2019.
- 18 RODNER, E. Size matters: why nanomaterials are different. **Chemical Society Reviews**, v. 35, n. 7, p. 583–592, 2006.
- 19 JORTNER, J. Cluster size effects. **Zeitschrift für Physik D Atoms, Molecules and Clusters**, v. 24, n. 3, p. 247–275, 1992.
- 20 LUO, Z.; CASTLEMAN, A. W.; KHANNA, S. N. Reactivity of metal clusters. **Chemical Reviews**, v. 116, n. 23, p. 14456–14492, 2016.
- 21 LEONETI, A. B.; ARAGÃO-LEONETI, V.; OLIVEIRA, S. V. W. B. de. Glycerol as a by-product of biodiesel production in brazil: Alternatives for the use of unrefined glycerol. **Renewable Energy**, v. 45, p. 138–145, 2012.
- 22 TROGLER, W. C. Electronic structures and reactivities of metal cluster complexes. **Accounts of Chemical Research**, v. 23, n. 8, p. 239–246, 1990.
- 23 BALETTO, F.; FERRANDO, R. Structural properties of nanoclusters: Energetic, thermodynamic, and kinetic effects. **Reviews of Modern Physics**, v. 77, n. 1, p. 371–423, 2005.
- 24 TOSHIMA, N.; YONEZAWA, T. Bimetallic nanoparticles—novel materials for chemical and physical applications. **New Journal of Chemistry**, v. 22, n. 11, p. 1179–1201, 1998.
- 25 SUNTIVICH, J.; XU, Z.; CARLTON, C. E.; KIM, J.; HAN, B.; LEE, S. W.; BONNET, N.; MARZARI, N.; ALLARD, L. F.; GASTEIGER, H. A.; HAMAD-SCHIFFERLI, K.; SHAO-HORN, Y. Surface composition tuning of Au–Pt bimetallic nanoparticles for enhanced carbon monoxide and methanol electro-oxidation. **Journal of the American Chemical Society**, v. 135, n. 21, p. 7985–7991, 2013.
- 26 TSAI, S.-H.; LIU, Y.-H.; WU, P.-L.; YEH, C.-S. Preparation of Au–Ag–Pd trimetallic nanoparticles and their application as catalysts. **Journal of Materials Chemistry**, v. 13, n. 5, p. 978–980, 2003.

-
- 27 POLYMEROPOULOS, E. E.; BRICKMANN, J. On the origin of the occurrence of “magic numbers” in cluster size distributions of xenon in the compressed gas phase. **Chemical Physics Letters**, v. 96, n. 3, p. 273–275, 1983.
- 28 HARBOLA, M. K. Magic numbers for metallic clusters and the principle of maximum hardness. **Proceedings of the National Academy of Sciences**, v. 89, n. 3, p. 1036–1039, 1992.
- 29 MACKAY, A. L. A dense non-crystallographic packing of equal spheres. **Acta Crystallographica**, v. 15, n. 9, p. 916–918, 1962.
- 30 MORI, T.; HEGMANN, T. Determining the composition of gold nanoparticles: a compilation of shapes, sizes, and calculations using geometric considerations. **Journal of Nanoparticle Research**, v. 18, n. 10, p. 295, 2016.
- 31 GATES, B. C. Supported metal clusters: Synthesis, structure, and catalysis. **Chemical Reviews**, v. 95, n. 3, p. 511–522, 1995.
- 32 LU, Y.; CHEN, W. Sub-nanometre sized metal clusters: From synthetic challenges to the unique property discoveries. **Chemical Society Reviews**, v. 41, n. 9, p. 3594–3623, 2012.
- 33 SHRESTHA, S.; LIU Y. AND MUSTAIN, W. E. Electrocatalytic activity and stability of Pt clusters on state-of-the-art supports: A review. **Catalysis Reviews**, v. 53, n. 3, p. 256–336, 2011.
- 34 LUO, Z.; GROVER, C. J.; REBER, A. C.; KHANNA, S. N.; CASTLEMAN, A. W. J. Probing the magic numbers of aluminum–magnesium cluster anions and their reactivity toward oxygen. **Journal of the American Chemical Society**, v. 135, n. 11, p. 4307–4313, 2013.
- 35 PIOTROWSKI, M. J.; UNGUREANU, C. G.; TERESHCHUK, P.; BATISTA, K. E. A.; CHAVES, A. S.; GUEDES-SOBRINHO, D.; DA SILVA, J. L. F. Theoretical study of the structural, energetic, and electronic properties of 55-atom metal nanoclusters: A DFT investigation within van der Waals corrections, spin-orbit coupling, and PBE + U of 42 metal systems. **The Journal of Physical Chemistry C**, v. 120, n. 50, p. 28844–28856, 2016.
- 36 DA SILVA, J. L. F.; KIM, H. G.; PIOTROWSKI, M. J.; PRIETO, M. J.; TREMILIOSI-FILHO, G. Reconstruction of core and surface nanoparticles: The example of Pt₅₅ and Au₅₅. **Physical Review B**, v. 82, n. 20, p. 205424, 2010.
- 37 TERESHCHUK, P.; CHAVES, A. S.; DA SILVA, J. L. F. Glycerol adsorption on platinum surfaces: A density functional theory investigation with van der Waals corrections. **The Journal of Physical Chemistry C**, v. 118, n. 28, p. 15251–15259, 2014.
- 38 ZIBORDI-BESSE, L.; TERESHCHUK, P.; CHAVES, A. S.; DA SILVA, J. L. F. Ethanol and water adsorption on transition-metal 13-atom clusters: A density functional theory investigation within van der Waals corrections. **The Journal of Physical Chemistry A**, v. 120, n. 24, p. 4231–4240, 2016.

- 39 TERESHCHUK, P.; DA SILVA, J. L. F. Ethanol and water adsorption on close-packed 3d, 4d, and 5d transition-metal surfaces: A density functional theory investigation with van der Waals correction. **The Journal of Physical Chemistry C**, v. 116, n. 46, p. 24695–24705, 2012.
- 40 LALETINA, S. S.; MAMATKULOV, M.; SHOR, E. A.; KAICHEV, V. V.; GENEST, A.; YUDANOV, I. V.; RÖSCH, N. Size-dependence of the adsorption energy of CO on Pt nanoparticles: Tracing two intersecting trends by DFT calculations. **The Journal of Physical Chemistry C**, v. 121, n. 32, p. 17371–17377, 2017.
- 41 YUDANOV, I. V.; GENEST, A.; SCHAUERMANN, S.; FREUND, H.-J.; RÖSCH, N. Size dependence of the adsorption energy of CO on metal nanoparticles: A DFT search for the minimum value. **Nano Letters**, v. 12, n. 4, p. 2134–2139, 2012.
- 42 PIOTROWSKI, M. J.; PIQUINI, P.; ZENG, Z.; DA SILVA, J. L. F. Adsorption of NO on the Rh₁₃, Pd₁₃, Ir₁₃, and Pt₁₃ clusters: A density functional theory investigation. **The Journal of Physical Chemistry C**, v. 116, n. 38, p. 20540–20549, 2012.
- 43 BATISTA, K. E. A.; OCAMPO-RESTREPO, V. K.; SOARES, M. D.; QUILES, M. G.; PIOTROWSKI, M. J.; DA SILVA, J. L. F. *Ab Initio* investigation of CO₂ adsorption on 13-atom 4d clusters. **Journal of Chemical Information and Modeling**, v. 60, n. 2, p. 537–545, 2020.
- 44 HAMMER, B.; NØRSKOV, J. K. Why gold is the noblest of all the metals. **Nature**, v. 376, n. 6537, p. 238–240, 1995.
- 45 NØRSKOV, J. K.; ABILD-PEDERSEN, F.; STUDT, F.; BLIGAARD, T. Density functional theory in surface chemistry and catalysis. **Proceedings of the National Academy of Sciences**, v. 108, n. 3, p. 937–943, 2011.
- 46 BHATTACHARJEE, S.; WAGHMARE, U. V.; LEE, S.-C. An improved d-band model of the catalytic activity of magnetic transition metal surfaces. **Scientific Reports**, v. 6, n. 1, p. 35916(1)–35916(9), 2016.
- 47 SAEIDI, S.; AMIN, N. A. S.; RAHIMPOUR, M. R. Hydrogenation of CO₂ to value-added products—a review and potential future developments. **Journal of CO₂ Utilization**, v. 5, p. 66–81, 2014.
- 48 ZHANG, W.; HU, Y.; MA, L.; ZHU, G.; WANG, Y.; XUE, X.; CHEN, R.; YANG, S.; JIN, Z. Progress and perspective of electrocatalytic CO₂ reduction for renewable carbonaceous fuels and chemicals. **Advanced Science**, v. 5, n. 1, p. 1700275(1)–1700275(24), 2017.
- 49 YANG, H.; ZHANG, C.; GAO, P.; WANG, H.; LI, X.; ZHONG, L.; WEI, W.; SUN, Y. A review of the catalytic hydrogenation of carbon dioxide into value-added hydrocarbons. **Catalysis Science & Technology**, v. 7, n. 20, p. 4580–4598, 2017.
- 50 FREUND, H.-J.; ROBERTS, M. Surface chemistry of carbon dioxide. **Surface Science Reports**, v. 25, n. 8, p. 225–273, 1996.
- 51 TAIFAN, W.; BOILY, J.-F.; BALTRUSAITIS, J. Surface chemistry of carbon dioxide revisited. **Surface Science Reports**, v. 71, n. 4, p. 595–671, 2016.

- 52 KO, J.; KIM, B.-K.; HAN, J. W. Density functional theory study for catalytic activation and dissociation of CO₂ on bimetallic alloy surfaces. **The Journal of Physical Chemistry C**, v. 120, n. 6, p. 3438–3447, 2016.
- 53 LIU, C.; CUNDARI, T. R.; WILSON, A. K. CO₂ reduction on transition metal (Fe, Co, Ni, and Cu) surfaces: In comparison with homogeneous catalysis. **The Journal of Physical Chemistry C**, v. 116, n. 9, p. 5681–5688, 2012.
- 54 LIU, X.; SUN, L.; DENG, W.-Q. Theoretical investigation of CO₂ adsorption and dissociation on low index surfaces of transition metals. **The Journal of Physical Chemistry C**, v. 122, n. 15, p. 8306–8314, 2018.
- 55 BÖNICKE, I. A.; KIRSTEIN, W.; THIEME, F. A study on CO₂ dissociation on a stepped (332) copper surface. **Surface Science**, v. 307-309, p. 177–181, 1994.
- 56 GAUTAM, S.; DHARAMVIR, K.; GOEL, N. CO₂ adsorption and activation over medium sized Cu_{*n*} (*n* = 7, 13 and 19) clusters: A density functional study. **Computational and Theoretical Chemistry**, v. 1009, p. 8–16, 2013.
- 57 HAGMAN, B.; POSADA-BORBÓN, A.; SCHAEFER, A.; SHIPILIN, M.; ZHANG, C.; MERTE, L. R.; HELLMAN, A.; LUNDGREN, E.; GRÖNBECK, H.; GUSTAFSON, J. Steps control the dissociation of CO₂ on Cu(100). **Journal of the American Chemical Society**, v. 140, n. 40, p. 12974–12979, 2018.
- 58 OCAMPO-RESTREPO, V. K.; ZIBORDI-BESSE, L.; DA SILVA, J. L. F. *Ab Initio* investigation of the atomistic descriptors in the activation of small molecules on 3*d* transition-metal 13-atom clusters: The example of H₂, CO, H₂O, and CO₂. **Journal of Chemical Physics**, v. 151, n. 21, p. 214301, 2019.
- 59 PETERSON, A. A.; NØRSKOV, J. K. Activity descriptors for CO₂ electroreduction to methane on transition-metal catalysts. **The Journal of Physical Chemistry Letters**, v. 3, n. 2, p. 251–258, 2012.
- 60 BEN-MANSOUR, R.; HABIB, M.; BAMIDELE, O.; BASHA, M.; QASEM, N.; PEEDIKAKKAL, A.; LAOUI, T.; ALI, M. Carbon capture by physical adsorption: Materials, experimental investigations and numerical modeling and simulations – a review. **Applied Energy**, v. 161, p. 225–255, 2016.
- 61 GLEZAKOU, V.-A.; DANG, L. X.; MCGRAIL, B. P. Spontaneous activation of CO₂ and possible corrosion pathways on the low-index iron surface Fe(100). **The Journal of Physical Chemistry C**, v. 113, n. 9, p. 3691–3696, 2009.
- 62 BARKER, R.; HUA, Y.; NEVILLE, A. Internal corrosion of carbon steel pipelines for dense-phase CO₂ transport in carbon capture and storage (CCS) – a review. **International Materials Reviews**, v. 62, n. 1, p. 1–31, 2016.
- 63 TAN, H.; AZIZ, A. A.; AROUA, M. Glycerol production and its applications as a raw material: A review. **Renewable and Sustainable Energy Reviews**, v. 27, p. 118–127, 2013.
- 64 HANSEN, C. F.; HERNANDEZ, A.; MULLAN, B. P.; MOORE, K.; TREZONA-MURRAY, M.; KING, R. H.; PLUSKE, J. R. A chemical analysis of samples of crude glycerol from the production of biodiesel in australia, and the effects of feeding crude

glycerol to growing-finishing pigs on performance, plasma metabolites and meat quality at slaughter. **Animal Production Science**, v. 49, n. 2, p. 154–161, 2009.

65 AYOUB, M.; ABDULLAH, A. Z. Critical review on the current scenario and significance of crude glycerol resulting from biodiesel industry towards more sustainable renewable energy industry. **Renewable and Sustainable Energy Reviews**, v. 16, n. 5, p. 2671–2686, 2012.

66 ALBARELLI, J. Q.; SANTOS, D. T.; HOLANDA, M. R. Energetic and economic evaluation of waste glycerol cogeneration in brazil. **Brazilian Journal of Chemical Engineering**, v. 28, n. 4, p. 691–698, 2011.

67 SAMUDRALA, S. P.; KANDASAMY, S.; BHATTACHARYA, S. Turning biodiesel waste glycerol into 1,3-propanediol: Catalytic performance of sulphuric acid-activated montmorillonite supported platinum catalysts in glycerol hydrogenolysis. **Scientific Reports**, v. 8, n. 7484, p. 1–12, 2018.

68 SLINN, M.; KENDALL, K.; MALLON, C.; ANDREWS, J. Steam reforming of biodiesel by-product to make renewable hydrogen. **Bioresource Technology**, v. 99, n. 13, p. 5851–5858, 2008.

69 YANG, F.; HANNA, M. A.; SUN, R. Value-added uses for crude glycerol—a byproduct of biodiesel production. **Biotechnology for Biofuels**, v. 5, n. 1, p. 13, 2012.

70 WOLFSON, A.; LITVAK, G.; DLUGY, C.; SHOTLAND, Y.; TAVOR, D. Employing crude glycerol from biodiesel production as an alternative green reaction medium. **Industrial Crops and Products**, v. 30, n. 1, p. 78–81, 2009.

71 BENIPAL, N.; QI, J.; GENTILE, J. C.; LI, W. Direct glycerol fuel cell with polytetrafluoroethylene (PTFE) thin film separator. **Renewable Energy**, v. 105, p. 647–655, 2017.

72 WEN, G.; XU, Y.; MA, H.; XU, Z.; TIAN, Z. Production of hydrogen by aqueous-phase reforming of glycerol. **International Journal of Hydrogen Energy**, v. 33, n. 22, p. 6657–6666, 2008.

73 NICHELE, V.; SIGNORETTO, M.; MENEGAZZO, F.; GALLO, A.; SANTO, V. D.; CRUCIANI, G.; CERRATO, G. Glycerol steam reforming for hydrogen production: Design of Ni supported catalysts. **Applied Catalysis B: Environmental**, v. 111–112, p. 225–232, 2012.

74 GODINA, L. I.; TOKAREV, A. V.; SIMAKOVA, I. L.; MÄKI-ARVELA, P.; KORTESMÄKI, E.; GLÄSEL, J.; KRONBERG, L.; ETZOLD, B.; MURZIN, D. Y. Aqueous-phase reforming of alcohols with three carbon atoms on carbon-supported Pt. **Catalysis Today**, v. 301, p. 78–89, 2018.

75 COSTA-AMARAL, R.; DA SILVA, J. L. F. The adsorption of alcohols on strained Pt₃Ni(111) substrates: A density functional investigation within the D3 van der Waals correction. **Physical Chemistry Chemical Physics**, v. 20, n. 37, p. 24210–24221, 2018.

76 OLIVEIRA, C. P.; LUSSARI, N. V.; SITTA, E.; VARELA, H. Oscillatory electro-oxidation of glycerol on platinum. **Electrochimica Acta**, v. 85, p. 674–679, 2012.

- 77 LIU, B.; GREELEY, J. A density functional theory analysis of trends in glycerol decomposition on close-packed transition metal surfaces. **Physical Chemistry Chemical Physics**, v. 15, n. 17, p. 6475–6485, 2013.
- 78 FERNÁNDEZ, P. S.; MARTINS, C. A.; ANGELUCCI, C. A.; GOMES, J. F.; CAMARA, G. A.; MARTINS, M. E.; TREMILIOSI-FILHO, G. Evidence for independent glycerol electrooxidation behavior on different ordered domains of polycrystalline platinum. **ChemElectroChem**, v. 2, n. 2, p. 263–268, 2014.
- 79 FERNÁNDEZ, P. S.; TERESHCHUK, P.; ANGELUCCI, C. A.; GOMES, J. F.; GARCIA, A. C.; MARTINS, C. A.; CAMARA, G. A.; MARTINS, M. E.; DA SILVA, J. L. F.; TREMILIOSI-FILHO, G. How do random superficial defects influence the electro-oxidation of glycerol on Pt(111) surfaces? **Physical Chemistry Chemical Physics**, v. 18, n. 36, p. 25582–25591, 2016.
- 80 DELGADO, S. N.; YAP, D.; VIVIER, L.; ESPECEL, C. Influence of the nature of the support on the catalytic properties of pt-based catalysts for hydrogenolysis of glycerol. **Journal of Molecular Catalysis A: Chemical**, v. 367, p. 89–98, 2013.
- 81 WANG, Y.; ZHOU, J.; GUO, X. Catalytic hydrogenolysis of glycerol to propanediols: a review. **RSC Advances**, v. 5, n. 91, p. 74611–74628, 2015.
- 82 LUCAS, F. W. de S.; LIMA, A. R. F.; MASCARO, L. H. Glycerol as additive in copper indium gallium diselenide electrodeposition: morphological, structural and electronic effects. **RSC Advances**, v. 5, n. 24, p. 18295–18300, 2015.
- 83 CHI-UCÁN, S. L.; CASTILLO-ATOCHE, A.; BORGES, P. C.; MANZANILLACANO, J. A.; GONZÁLEZ-GARCÍA, G.; PATIÑO, R.; DÍAZ-BALLOTE, L. Inhibition effect of glycerol on the corrosion of copper in NaCl solutions at different pH values. **Journal of Chemistry**, v. 2014, p. 1–10, 2014.
- 84 GOMES, J. F.; TREMILIOSI-FILHO, G. Spectroscopic studies of the glycerol electro-oxidation on polycrystalline Au and Pt surfaces in acidic and alkaline media. **Electrocatalysis**, v. 2, n. 2, p. 96–105, 2011.
- 85 SUMODJO, P.; SILVA, E. da; RABOCKAI, T. Electrosorption of hydroxylated compounds: a comparative study of molecules with three carbon atoms. **Journal of Electroanalytical Chemistry and Interfacial Electrochemistry**, v. 271, n. 1-2, p. 305–317, 1989.
- 86 DE SOUZA, N. E.; GOMES, J. F.; TREMILIOSI-FILHO, G. Reactivity of 3-carbon-atom chain alcohols on gold electrode: A comparison to understand the glycerol electro-oxidation. **Journal of Electroanalytical Chemistry**, v. 800, p. 106–113, 2017.
- 87 KITTEL, C. **Introduction to solid state physics**. [S.l.: s.n.], 1976. ISBN 0471490245.
- 88 SZABO, A.; OSTLUND, N. S. **Modern quantum chemistry**. [S.l.: s.n.], 1996. ISBN 0486691861.
- 89 LEVINE, I. N. **Quantum chemistry**. 5th. ed. [S.l.: s.n.], 1999. ISBN 0136855121.
- 90 CRAMER, C. J. **Essentials of computational chemistry: theories and models**. [S.l.: s.n.], 2004. Chap. 8. ISBN 0470091819.

- 91 MARTIN, R. M. **Electronic structure**. [S.l.: s.n.], 2008. ISBN 978-0-521-53440-6.
- 92 SCHRÖDINGER, E. An undulatory theory of the mechanics of atoms and molecules. **Physical Review**, v. 28, n. 6, p. 1049–1070, 1926.
- 93 BORN, M.; OPPENHEIMER, R. Zur quantentheorie der molekeln. **Annalen der Physik**, v. 389, n. 20, p. 457–484, 1927.
- 94 HARTREE, D. R. The wave mechanics of an atom with a non-Coulomb central field. Part I. Theory and methods. **Mathematical Proceedings of the Cambridge Philosophical Society**, v. 24, n. 1, p. 89–110, 1928.
- 95 FOCK, V. „Selfconsistent field“ mit austausch für natrium. **Zeitschrift für Physik**, v. 62, n. 11-12, p. 795–805, 1930.
- 96 CAPELLE, K. A bird's-eye view of density-functional theory. **Brazilian Journal of Physics**, v. 36, n. 4a, p. 1318–1343, 2006.
- 97 KOHN, W.; BECKE, A. D.; PARR, R. G. Density functional theory of electronic structure. **The Journal of Physical Chemistry**, v. 100, n. 31, p. 12974–12980, 1996.
- 98 KATO, T. On the eigenfunctions of many-particle systems in quantum mechanics. **Communications on Pure and Applied Mathematics**, v. 10, n. 2, p. 151–177, 1957.
- 99 THOMAS, L. H. The calculation of atomic fields. **Mathematical Proceedings of the Cambridge Philosophical Society**, v. 23, n. 05, p. 542–548, 1927.
- 100 FERMI, E. Statistical method to determine some properties of atoms. **Rendiconti Lincei**, v. 6, p. 602–607, 1927.
- 101 HOHENBERG, P.; KOHN, W. Inhomogeneous electron gas. **Physical Review**, v. 136, n. 3B, p. B864–B871, 1964.
- 102 KOHN, W.; SHAM, L. J. Self-consistent equations including exchange and correlation effects. **Physical Review**, v. 140, n. 4A, p. A1133–A1138, 1965.
- 103 SLATER, J. C. A simplification of the hartree-fock method. **Physical Review**, v. 81, n. 3, p. 385–390, 1951.
- 104 GELL-MANN MURRAY; BRUECKNER, K. Correlation energy of an electron gas at high density. **Physical Review**, v. 106, n. 2, p. 364–368, 1957.
- 105 CEPERLEY, D. M. Ground state of the electron gas by a stochastic method. **Physical Review Letters**, v. 45, n. 7, p. 566–569, 1980.
- 106 PAINTER G. S.; AVERILL, F. W. Bonding in the first-row diatomic molecules within the local spin-density approximation. **Physical Review B**, v. 26, n. 4, p. 1781–1790, 1982.
- 107 PERDEW, J. P.; A., Z. Self-interaction correction to density-functional approximations for many-electron systems. **Physical Review B**, v. 23, n. 10, p. 5048–5079, 1981.
- 108 PERDEW, J. P.; BURKE, K.; ERNZERHOF, M. Generalized gradient approximation made simple. **Physical Review Letters**, v. 77, n. 18, p. 3865–3868, 1996.

- 109 BAO, J. L.; ZHANG, X.; XU, X.; TRUHLAR, D. G. Predicting bond dissociation energy and bond length for bimetallic diatomic molecules: a challenge for electronic structure theory. **Physical Chemistry Chemical Physics**, v. 19, n. 8, p. 5839–5854, 2017.
- 110 PERDEW JOHN P.; WANG, Y. Accurate and simple analytic representation of the electron-gas correlation energy. **Physical Review B**, v. 45, n. 23, p. 13244–13249, 1992.
- 111 PERDEW, J. P.; ERNZERHOF, M.; BURKE, K. Rationale for mixing exact exchange with density functional approximations. **The Journal of Chemical Physics**, v. 105, n. 22, p. 9982–9985, 1996.
- 112 PERDEW, J. P.; RUZSINSZKY, A.; TAO, J.; STAROVEROV, V. N.; SCUSERIA, G. E.; CSONKA, G. I. Prescription for the design and selection of density functional approximations: More constraint satisfaction with fewer fits. **The Journal of Chemical Physics**, v. 123, n. 6, p. 062201, 2005.
- 113 JANTHON, P.; LUO, S. A.; KOZLOV, S. M.; VIÑES, F.; LIMTRAKUL, J.; TRUHLAR, D. G.; ILLAS, F. Bulk properties of transition metals: A challenge for the design of universal density functionals. **Journal of Chemical Theory and Computation**, v. 10, n. 9, p. 3832–3839, 2014.
- 114 LEJAEGHERE, K.; BIHLMAYER, G.; BJORKMAN, T.; BLAHA, P.; BLUGEL, S.; BLUM, V.; CALISTE, D.; CASTELLI, I. E.; CLARK, S. J.; CORSO, A. D.; GIRONCOLI, S. de; DEUTSCH, T.; DEWHURST, J. K.; MARCO, I. D.; DRAXL, C.; AK, M. D.; ERIKSSON, O.; FLORES-LIVAS, J. A.; GARRITY, K. F.; GENOVESE, L.; GIANNOZZI, P.; GIANTOMASSI, M.; GOEDECKER, S.; GONZE, X.; GRANAS, O.; GROSS, E. K. U.; GULANS, A.; GYGI, F.; HAMANN, D. R.; HASNIP, P. J.; HOLZWARTH, N. A. W.; AN, D. I.; JOCHYM, D. B.; JOLLET, F.; JONES, D.; KRESSE, G.; KOEPERNIK, K.; KUCUKBENLI, E.; KVASHNIN, Y. O.; LOCHT, I. L. M.; LUBECK, S.; MARSMAN, M.; MARZARI, N.; NITZSCHE, U.; NORDSTROM, L.; OZAKI, T.; PAULATTO, L.; PICKARD, C. J.; POELMANS, W.; PROBERT, M. I. J.; REFSON, K.; RICHTER, M.; RIGNANESE, G.-M.; SAHA, S.; SCHEFFLER, M.; SCHLIPF, M.; SCHWARZ, K.; SHARMA, S.; TAVAZZA, F.; THUNSTROM, P.; TKATCHENKO, A.; TORRENT, M.; VANDERBILT, D.; SETTEN, M. J. van; SPEYBROECK, V. V.; WILLS, J. M.; YATES, J. R.; ZHANG, G.-X.; COTTENIER, S. Reproducibility in density functional theory calculations of solids. **Science**, v. 351, n. 6280, p. aad3000–aad3000, 2016.
- 115 LONDON, F. Zur theorie und systematik der molekularkräfte. **Zeitschrift für Physik**, v. 63, n. 3-4, p. 245–279, 1930.
- 116 LONDON, F. The general theory of molecular forces. **Transactions of the Faraday Society**, v. 33, p. 8b, 1937.
- 117 GRIMME, S. Density functional theory with London dispersion corrections. **WIREs Computational Molecular Science**, v. 1, n. 2, p. 211–228, 2011.
- 118 RECKIEN, W.; JANETZKO, F.; PEINTINGER, M. F.; BREDOW, T. Implementation of empirical dispersion corrections to density functional theory for periodic systems. **Journal of Computational Chemistry**, v. 33, n. 25, p. 2023–2031, 2012.

- 119 FREIRE, R. L. H.; GUEDES-SOBRINHO, D.; KIEJNA, A.; DA SILVA, J. L. F. Comparison of the performance of van der Waals dispersion functionals in the description of water and ethanol on transition metal surfaces. **The Journal of Physical Chemistry C**, v. 122, n. 3, p. 1577–1588, 2018.
- 120 KLIMEŠ, J.; MICHAELIDES, A. Perspective: Advances and challenges in treating van der Waals dispersion forces in density functional theory. **The Journal of Chemical Physics**, v. 137, n. 12, p. 120901, 2012.
- 121 GRIMME, S. Accurate description of van der Waals complexes by density functional theory including empirical corrections. **Journal of Computational Chemistry**, v. 25, n. 12, p. 1463–1473, 2004.
- 122 GRIMME, S. Semiempirical GGA-type density functional constructed with a long-range dispersion correction. **Journal of Computational Chemistry**, v. 27, n. 15, p. 1787–1799, 2006.
- 123 GRIMME, S.; ANTONY, J.; EHRLICH, S.; KRIEG, H. A consistent and accurate *ab initio* parametrization of density functional dispersion correction (DFT-D) for the 94 elements H-Pu. **The Journal of Chemical Physics**, v. 132, n. 15, p. 154104, 2010.
- 124 HUJO, W.; GRIMME, S. Performance of non-local and atom-pairwise dispersion corrections to DFT for structural parameters of molecules with noncovalent interactions. **Journal of Chemical Theory and Computation**, v. 9, n. 1, p. 308–315, 2012.
- 125 CASIMIR, H. B. G.; POLDER, D. The influence of retardation on the London-van der Waals forces. **Physical Review**, v. 73, n. 4, p. 360–372, 1948.
- 126 BLOCH, F. Über die quantenmechanik der elektronen in kristallgittern. **Zeitschrift für Physik**, v. 52, n. 7-8, p. 555–600, 1929.
- 127 SCHWERDTFEGGER, P. The pseudopotential approximation in electronic structure theory. **ChemPhysChem**, v. 12, n. 17, p. 3143–3155, 2011.
- 128 BLÖCHL, P. E. Projector augmented-wave method. **Physical Review B**, v. 50, n. 24, p. 17953–17979, 1994.
- 129 KRESSE, G.; JOUBERT, D. From ultrasoft pseudopotentials to the projector augmented-wave method. **Physical Review B**, v. 59, n. 3, p. 1758–1775, 1999.
- 130 SLATER, J. C. Wave functions in a periodic potential. **Physical Review**, v. 51, n. 10, p. 846–851, 1937.
- 131 KRESSE, G.; HAFNER, J. *Ab Initio* molecular dynamics for open-shell transition metals. **Physical Review B**, v. 48, n. 17, p. 13115–13118, 1993.
- 132 KRESSE, G.; FURTHMÜLLER, J. Efficient iterative schemes for *Ab Initio* total-energy calculations using a plane-wave basis set. **Physical Review B**, v. 54, n. 16, p. 11169–11186, 1996.
- 133 FREIRE, R. L. H. **Estudos de primeiros princípios da adsorção de água e de etanol sobre ligas de superfície de metais de transição sob efeitos de deformação expansiva e compressiva**. 2016. Tese (Doutorado) — Universidade de São Paulo, Instituto de Química de São Carlos, 2016.

- 134 FREIRE, R. L. H.; KIEJNA, A.; DA SILVA, J. L. F. Adsorption of water and ethanol on noble and transition-metal substrates: a density functional investigation within van der Waals corrections. **Physical Chemistry Chemical Physics**, v. 18, n. 42, p. 29526–29536, 2016.
- 135 CHAVES, A. S.; PIOTROWSKI, M. J.; DA SILVA, J. L. F. Evolution of the structural, energetic, and electronic properties of the $3d$, $4d$, and $5d$ transition-metal clusters (30 TM_n systems for $n = 2 - 15$): A density functional theory investigation. **Physical Chemistry Chemical Physics**, v. 19, n. 23, p. 15484–15502, 2017.
- 136 JUSTO, S. G. **Investigação *ab initio* dos mecanismos de formação de nanoligas *core-shell* com platina e metais de transição dos períodos 3d, 4d e 5d.** 2017. Dissertação (Mestrado) — Universidade de São Paulo, Instituto de Química de São Carlos, 2017.
- 137 AMARAL, R. C. **Estudo *ab initio* da adsorção de metanol, etanol e glicerol sobre superfícies de platina com defeitos e ligas de Pt_3Ni com tensões.** 2019. Tese (Doutorado) — Universidade de São Paulo, Instituto de Química de São Carlos, 2019.
- 138 NEUGEBAUER, J.; SCHEFFLER, M. Adsorbate-substrate and adsorbate-adsorbate interactions of Na and K adlayers on Al(111). **Physical Review B**, v. 46, n. 24, p. 16067–16080, 1992.
- 139 BADER, R. F. W. **Atoms in molecules: A quantum theory.** [S.l.: s.n.], 1994. (International Ser. of Monogr. on Chem). ISBN 9780198558651.
- 140 BADER, R. F. W. The zero-flux surface and the topological and quantum definitions of an atom in a molecule. **Theoretical Chemistry Accounts: Theory, Computation, and Modeling (Theoretica Chimica Acta)**, v. 105, n. 4-5, p. 276–283, 2001.
- 141 HENKELMAN, G.; ARNALDSSON, A.; JÓNSSON, H. A fast and robust algorithm for bader decomposition of charge density. **Computation Materials Science**, v. 36, n. 3, p. 354–360, 2006.
- 142 DA SILVA, J. L. F. All-electron first-principles calculations of clean surface properties of low-miller-index Al surfaces. **Physical Review B**, v. 71, n. 19, p. 195416, 2005.
- 143 DA SILVA, J. L. F.; STAMPFL, C.; SCHEFFLER, M. Converged properties of clean metal surfaces by all-electron first-principles calculations. **Surface Science**, v. 600, n. 3, p. 703–715, 2006.
- 144 BATISTA, K. E. A.; DA SILVA, J. L. F.; PIOTROWSKI, M. J. Adsorption of CO, NO, and H_2 on the Pd_nAu_{55-n} nanoclusters: A density functional theory investigation within the van der Waals D3 corrections. **The Journal of Physical Chemistry C**, v. 123, n. 12, p. 7431–7439, 2019.
- 145 MENDES, P. C. D.; OCAMPO-RESTREPO, V. K.; DA SILVA, J. L. F. *Ab Initio* investigation of quantum size effects on the adsorption of CO_2 , CO, H_2O , and H_2 on transition-metal particles. **Physical Chemistry Chemical Physics**, v. 22, n. 16, p. 8998–9008, 2020.

- 146 MENDES, P. C. D.; JUSTO, S. G.; MUCELINI, J.; SOARES, M. D.; BATISTA, K. E. A.; QUILES, M. G.; PIOTROWSKI, M. J.; DA SILVA, J. L. F. *Ab Initio* insights into the formation mechanisms of 55-atom Pt-based core-shell nanoalloys. **The Journal of Physical Chemistry C**, v. 124, n. 1, p. 1158–1164, 2019.
- 147 SANTORO, A.; MIGHELL, A. D. Determination of reduced cells. **Acta Crystallographica Section A**, v. 26, n. 1, p. 124–127, 1970.
- 148 WYCKOFF, R. W. G. **Crystal structures**. [S.l.: s.n.], 1963.
- 149 HUANG, J. Y.; WU, Y. K.; YE, H. Q. Phase transformation of cobalt induced by ball milling. **Applied Physics Letters**, v. 66, n. 3, p. 308–310, 1995.
- 150 STEINLE-NEUMANN, G.; STIXRUDE, L.; COHEN, R. E. Magnetism in dense hexagonal iron. **Proceedings of the National Academy of Sciences**, v. 101, n. 1, p. 33–36, 2003.
- 151 DA SILVA, J. L. F. Effective coordination concept applied for phase change $(\text{GeTe})_m(\text{Sb}_2\text{Te}_3)_n$ compounds. **Journal of Applied Physics**, v. 109, n. 2, p. 023502, 2011.
- 152 YOUNG, D. A. **Phase diagrams of the elements**. [S.l.: s.n.], 1991. p. 273. ISBN 0520074831.
- 153 JANTHON, P.; KOZLOV, S. M.; VIÑES, F.; LIMTRAKUL, J.; ILLAS, F. Establishing the accuracy of broadly used density functionals in describing bulk properties of transition metals. **Journal of Chemical Theory and Computation**, v. 9, n. 3, p. 1631–1640, 2013.
- 154 HAAS, P.; TRAN, F.; BLAHA, P. Calculation of the lattice constant of solids with semilocal functionals. **Physical Review B**, v. 79, n. 8, p. 085104, 2009.
- 155 PARTRIDGE, P. G. The crystallography and deformation modes of hexagonal close-packed metals. **Metallurgical Reviews**, v. 12, n. 1, p. 169–194, 1967.
- 156 KÖRLING, M.; HÄGLUND, J. Cohesive and electronic properties of transition metals: The generalized gradient approximation. **Physical Review B**, v. 45, n. 23, p. 13293–13297, 1992.
- 157 LEJAEGHERE, K.; SPEYBROECK, V. V.; OOST, G. V.; COTTENIER, S. Error estimates for solid-state density-functional theory predictions: An overview by means of the ground-state elemental crystals. **Critical Reviews in Solid State and Materials Sciences**, v. 39, n. 1, p. 1–24, 2013.
- 158 CHEN, H.; BRENER, N. E.; CALLAWAY, J. Electronic structure, optical and magnetic properties of fcc palladium. **Physical Review B**, v. 40, n. 3, p. 1443–1449, 1989.
- 159 MENDES, P. C. D.; COSTA-AMARAL, R.; GOMES, J. F.; DA SILVA, J. L. F. The influence of hydroxy groups on the adsorption of three-carbon alcohols on Ni(111), Pd(111) and Pt(111) surfaces: a density functional theory study within the D3 dispersion correction. **Physical Chemistry Chemical Physics**, v. 21, n. 16, p. 8434–8444, 2019.

- 160 METHFESSEL, M.; HENNIG, D.; SCHEFFLER, M. Trends of the surface relaxations, surface energies, and work functions of the 4d transition metals. **Physical Review B**, v. 46, n. 8, p. 4816–4829, 1992.
- 161 SPENCER, M. J.; HUNG, A.; SNOOK, I. K.; YAROVSKY, I. Density functional theory study of the relaxation and energy of iron surfaces. **Surface Science**, v. 513, n. 2, 2002.
- 162 SKRIVER, H. L.; ROSENGAARD, N. M. Surface energy and work function of elemental metals. **Physical Review B**, v. 46, n. 11, p. 7157–7168, 1992.
- 163 ALDÉN, M.; SKRIVER, H.; MIRBT, S.; JOHANSSON, B. Surface energy and magnetism of the 3d metals. **Surface Science**, v. 315, n. 1-2, p. 157–172, 1994.
- 164 BOER, F.; BOOM, R.; MATTENS, W. **Cohesion in metals: transition metal alloys**. [S.l.: s.n.], 1988. (Cohesion and structure). ISBN 9780444870988.
- 165 MICHAELSON, H. B. The work function of the elements and its periodicity. **Journal of Applied Physics**, v. 48, n. 11, p. 4729–4733, 1977.
- 166 SINGH-MILLER, N. E.; MARZARI, N. Surface energies, work functions, and surface relaxations of low-index metallic surfaces from first principles. **Physical Review B**, v. 80, n. 23, 2009.
- 167 ALONSO, J. A. Electronic and atomic structure, and magnetism of transition-metal clusters. **Chemical Reviews**, v. 100, n. 2, p. 637–678, 2000.
- 168 LIU, L.; CORMA, A. Metal catalysts for heterogeneous catalysis: From single atoms to nanoclusters and nanoparticles. **Chemical Reviews**, v. 118, n. 10, p. 4981–5079, 2018.
- 169 CHOI, Y. H.; JANG, Y. J.; PARK, H.; KIM, W. Y.; LEE, Y. H.; CHOI, S. H.; LEE, J. S. Carbon dioxide fischer-tropsch synthesis: A new path to carbon-neutral fuels. **Applied Catalysis B: Environmental**, v. 202, p. 605–610, 2017.
- 170 WANG, G.-C.; JIANG, L.; MORIKAWA, Y.; NAKAMURA, J.; CAI, Z.-S.; PAN, Y.-M.; ZHAO, X.-Z. Cluster and periodic DFT calculations of adsorption and activation of CO₂ on the Cu(*hkl*) surfaces. **Surface Science**, v. 570, n. 3, p. 205–217, 2004.
- 171 ZHANG, X.; LIU, J.-X.; ZIJLSTRA, B.; FILOT, I. A.; ZHOU, Z.; SUN, S.; HENSEN, E. J. Optimum Cu nanoparticle catalysts for CO₂ hydrogenation towards methanol. **Nano Energy**, v. 43, p. 200–209, 2018.
- 172 PADAMA, A. A. B.; OCON, J. D.; NAKANISHI, H.; KASAI, H. Interaction of CO, O, and CO₂ with Cu cluster supported on Cu(111): A density functional theory study. **Journal of Physics: Condensed Matter**, v. 31, n. 41, p. 415201, 2019.
- 173 IABLOKOV, V.; BEAUMONT, S. K.; ALAYOGLU, S.; PUSHKAREV, V. V.; SPECHT, C.; GAO, J.; ALIVISATOS, A. P.; KRUSE, N.; SOMORJAI, G. A. Size-controlled model Co nanoparticle catalysts for CO₂ hydrogenation: Synthesis, characterization, and catalytic reactions. **Nano Letters**, v. 12, n. 6, p. 3091–3096, 2012.
- 174 YANG, B.; LIU, C.; HALDER, A.; TYO, E. C.; MARTINSON, A. B. F.; SEIFERT, S.; ZAPOL, P.; CURTISS, L. A.; VAJDA, S. Copper cluster size effect in methanol synthesis from CO₂. **The Journal of Physical Chemistry C**, v. 121, n. 19, p. 10406–10412, 2017.

175 YU, H.; CAO, D.; FISHER, A.; JOHNSTON, R. L.; CHENG, D. Size effect on the adsorption and dissociation of CO₂ on Co nanoclusters. **Applied Surface Science**, v. 396, p. 539–546, 2017.

176 HALPERIN, W. P. Quantum size effects in metal particles. **Reviews of Modern Physics**, v. 58, n. 3, p. 533–606, 1986.

177 KOPAČ, D.; LIKOZAR, B.; HUŠ, M. Catalysis of material surface defects: Multiscale modeling of methanol synthesis by CO₂ reduction on copper. **Applied Surface Science**, v. 497, p. 143783, 2019.

178 HARMONY, M. D.; LAURIE, V. W.; KUCZKOWSKI, R. L.; SCHWENDEMAN, R. H.; RAMSAY, D. A.; LOVAS, F. J.; LAFFERTY, W. J.; MAKI, A. G. Molecular structures of gas-phase polyatomic molecules determined by spectroscopic methods. **Journal of Physical and Chemical Reference Data**, v. 8, p. 619–721, 1979.

179 PACCHIONI, G.; CHUNG, S.-C.; KRÜGER, S.; RÖSCH, N. On the evolution of cluster to bulk properties: a theoretical LCGTO-LDF study of free and coordinated Ni_n clusters ($n = 6 - 147$). **Chemical Physics**, v. 184, p. 125–137, 1994.

180 ZHANG, M. L.; LI, G. P. Energy and structure of copper clusters ($n = 2-70, 147, 500$) studied by the monte carlo method. **Solid State Phenomena**, v. 121-123, p. 607–610, 2007.

181 PIOTROWSKI, M. J.; PIQUINI, P.; DA SILVA, J. L. F. Density functional theory investigation of 3d, 4d, and 5d 13-atom metal clusters. **Physical Review B**, v. 81, p. 155446, 2010.

182 HAMMER, B.; NØRSKOV, J. Electronic factors determining the reactivity of metal surfaces. **Surface Science**, v. 343, n. 3, p. 211–220, 1995.

183 SINGH, R.; KROLL, P. Structural, electronic, and magnetic properties of 13-, 55-, and 147-atom clusters of Fe, Co, and Ni: A spin-polarized density functional study. **Physical Review B**, v. 78, p. 245404, 2008.

184 BORNEMANN, S.; ŠIPR, O.; MANKOVSKY, S.; POLESYA, S.; STAUNTON, J. B.; WURTH, W.; EBERT, H.; MINÁR, J. Trends in the magnetic properties of Fe, Co, and Ni clusters and monolayers on Ir(111), Pt(111), and Au(111). **Physical Review B**, v. 86, n. 10, p. 104436, 2012.

185 CHAVES, A. S.; PIOTROWSKI, M. J.; GUEDES-SOBRINHO, D.; DA SILVA, J. L. F. Theoretical investigation of the adsorption properties of CO, NO, and OH on monometallic and bimetallic 13-atom clusters: The example of Cu₁₃, Pt₇Cu₆, and Pt₁₃. **The Journal of Physical Chemistry A**, v. 119, n. 47, p. 11565–11573, 2015.

186 PARKS, E.; NIEMAN, G.; RILEY, S. Binding of deuterium to icosahedral nickel and cobalt clusters. **Surface Science**, v. 355, n. 1-3, p. 127–139, 1996.

187 ZHANG, R.; WANG, Y.; WANG, B.; LING, L. Probing into the effects of cluster size and Pd ensemble as active center on the activity of H₂ dissociation over the noble metal Pd-doped Cu bimetallic clusters. **Molecular Catalysis**, v. 475, p. 110457, 2019.

- 188 ZENG, Z.-H.; DA SILVA, J. L. F.; DENG, H.-Q.; LI, W.-X. Density functional theory study of the energetics, electronic structure, and core-level shifts of NO adsorption on the Pt(111) surface. **Physical Review B**, v. 79, n. 20, p. 205413, 2009.
- 189 FERNÁNDEZ, E. M.; ORDEJÓN, P.; BALBÁS, L. C. Theoretical study of O₂ and CO adsorption on Au_n clusters ($n = 5-10$). **Chemical Physics Letters**, v. 408, n. 4-6, p. 252-257, 2005.
- 190 JANTHON, P.; VIÑES, F.; SIRIJARAENSRE, J.; LIMTRAKUL, J.; ILLAS, F. Adding pieces to the CO/Pt(111) puzzle: The role of dispersion. **The Journal of Physical Chemistry C**, v. 121, n. 7, p. 3970-3977, 2017.
- 191 VAN HELDEN, P.; VAN DEN BERG, J.-A.; WESTSTRATE, C. J. Hydrogen adsorption on Co surfaces: A density functional theory and temperature programmed desorption study. **ACS Catalysis**, v. 2, n. 6, p. 1097-1107, 2012.
- 192 ZHI-JUN, Z.; WEI, H.; PEI-DE, H.; ZHI-HONG, L. CO and H₂ molecules adsorption on Cu(111) surface and solvent effects. **Acta Physico-Chimica Sinica**, v. 25, n. 12, p. 2507-2512, 2009.
- 193 WANG, S.-G.; LIAO, X.-Y.; CAO, D.-B.; HUO, C.-F.; LI, Y.-W.; WANG, J.; JIAO, H. Factors controlling the interaction of CO₂ with transition metal surfaces. **The Journal of Physical Chemistry C**, v. 111, n. 45, p. 16934-16940, 2007.
- 194 BURGHAUS, U. Surface chemistry of CO₂ – adsorption of carbon dioxide on clean surfaces at ultrahigh vacuum. **Progress in Surface Science**, v. 89, n. 2, p. 161-217, 2014.
- 195 RAMPRASAD, R.; VON ALLMEN, P.; FONSECA, L. R. C. Contributions to the work function: A density-functional study of adsorbates at graphene ribbon edges. **Physical Review B**, v. 60, n. 8, p. 6023-6027, 1999.
- 196 LEUNG, T. C.; KAO, C. L.; SU, W. S.; FENG, Y. J.; CHAN, C. T. Relationship between surface dipole, work function and charge transfer: Some exceptions to an established rule. **Physical Review B**, v. 68, p. 195408, 2003.
- 197 CHERNYSHOVA, I. V.; SOMASUNDARAN, P.; PONNURANGAM, S. On the origin of the elusive first intermediate of CO₂ electroreduction. **Proceedings of the National Academy of Sciences of the United States of America**, v. 115, n. 40, p. E9261-E9270, 2018.
- 198 AZIZ, M.; SETIABUDI, H.; TEH, L.; ANNUAR, N.; JALIL, A. A review of heterogeneous catalysts for syngas production via dry reforming. **Journal of the Taiwan Institute of Chemical Engineers**, v. 101, p. 139-158, 2019.
- 199 ÁLVAREZ, A.; BORGES, M.; CORRAL-PÉREZ, J. J.; OLCINA, J. G.; HU, L.; CORNU, D.; HUANG, R.; STOIAN, D.; URAKAWA, A. CO₂ activation over catalytic surfaces. **ChemPhysChem**, v. 18, n. 22, p. 3135-3141, 2017.
- 200 LEE, H.; HABAS, S. E.; KWESKIN, S.; BUTCHER, D.; SOMORJAI, G. A.; YANG, P. Morphological control of catalytically active platinum nanocrystals. **Angewandte Chemie International Edition**, v. 45, n. 46, p. 7824-7828, 2006.

- 201 HE, J.; JOHNSON, N. J. J.; HUANG, A.; BERLINGUETTE, C. P. Electrocatalytic alloys for CO₂ reduction. **ChemSusChem**, v. 11, n. 1, p. 48–57, 2017.
- 202 YU, W.; POROSOFF, M. D.; CHEN, J. G. Review of Pt-based bimetallic catalysis: From model surfaces to supported catalysts. **Chemical Reviews**, v. 112, n. 11, p. 5780–5817, 2012.
- 203 GARCÍA-DIÉGUEZ, M.; PIETA, I.; HERRERA, M.; LARRUBIA, M.; ALEMANY, L. Nanostructured Pt- and Ni-based catalysts for CO₂-reforming of methane. **Journal of Catalysis**, v. 270, n. 1, p. 136–145, 2010.
- 204 PAKHARE, D.; SPIVEY, J. A review of dry (CO₂) reforming of methane over noble metal catalysts. **Chemical Society Reviews**, v. 43, n. 22, p. 7813–7837, 2014.
- 205 NIU, J.; RAN, J.; OU, Z.; DU, X.; WANG, R.; QI, W.; ZHANG, P. CO₂ dissociation over Pt_xNi_{4-x} bimetallic clusters with and without hydrogen sources: A density functional theory study. **Journal of CO₂ Utilization**, v. 16, p. 431–441, 2016.
- 206 GÁLVEZ-GONZÁLEZ, L. E.; JUÁREZ-SÁNCHEZ, J. O.; PACHECO-CONTRERAS, R.; GARZÓN, I. L.; PAZ-BORBÓN, L. O.; POSADA-AMARILLAS, A. CO₂ adsorption on gas-phase Cu_{4-x}Pt_x ($x = 0-4$) clusters: a DFT study. **Physical Chemistry Chemical Physics**, v. 20, n. 25, p. 17071–17080, 2018.
- 207 ALVAREZ-GARCIA, A.; FLÓREZ, E.; MORENO, A.; JIMENEZ-OROZCO, C. CO₂ activation on small Cu-Ni and Cu-Pd bimetallic clusters. **Molecular Catalysis**, v. 484, p. 110733, 2020.
- 208 KHAN, M. U.; WANG, L.; LIU, Z.; GAO, Z.; WANG, S.; LI, H.; ZHANG, W.; WANG, M.; WANG, Z.; MA, C.; ZENG, J. Pt₃Co octapods as superior catalysts of CO₂ hydrogenation. **Angewandte Chemie International Edition**, v. 55, n. 33, p. 9548–9552, 2016.
- 209 ZENG, J.; ZHANG, W.; YANG, Y.; LI, D.; YU, X.; GAO, Q. Pd–Ag alloy electrocatalysts for CO₂ reduction: Composition tuning to break the scaling relationship. **ACS Applied Materials & Interfaces**, v. 11, n. 36, p. 33074–33081, 2019.
- 210 VASILEFF, A.; ZHI, X.; XU, C.; GE, L.; JIAO, Y.; ZHENG, Y.; QIAO, S.-Z. Selectivity control for electrochemical CO₂ reduction by charge redistribution on the surface of copper alloys. **ACS Catalysis**, v. 9, n. 10, p. 9411–9417, 2019.
- 211 HANSEN, H. A.; SHI, C.; LAUSCHE, A. C.; PETERSON, A. A.; NØRSKOV, J. K. Bifunctional alloys for the electroreduction of CO₂ and CO. **Physical Chemistry Chemical Physics**, v. 18, n. 13, p. 9194–9201, 2016.
- 212 GREELEY, J. Theoretical heterogeneous catalysis: Scaling relationships and computational catalyst design. **Annual Review of Chemical and Biomolecular Engineering**, v. 7, n. 1, p. 605–635, 2016.
- 213 LEE, C. W.; YANG, K. D.; NAM, D.-H.; JANG, J. H.; CHO, N. H.; IM, S. W.; NAM, K. T. Defining a materials database for the design of copper binary alloy catalysts for electrochemical CO₂ conversion. **Advanced Materials**, v. 30, n. 42, p. 1704717, 2018.

- 214 MUN, Y.; LEE, S.; CHO, A.; KIM, S.; HAN, J. W.; LEE, J. Cu-pd alloy nanoparticles as highly selective catalysts for efficient electrochemical reduction of CO₂ to CO. **Applied Catalysis B: Environmental**, v. 246, p. 82–88, 2019.
- 215 WU, N.; XIAO, L.; ZHUANG, L. Theoretical search for novel Au or Ag bimetallic alloys capable of transforming CO₂ into hydrocarbons. **Journal of Materials Chemistry A**, v. 7, n. 36, p. 20567–20573, 2019.
- 216 FENG, Y.; AN, W.; WANG, Z.; WANG, Y.; MEN, Y.; DU, Y. Electrochemical CO₂ reduction reaction on M@Cu(211) bimetallic single-atom surface alloys: Mechanism, kinetics, and catalyst screening. **ACS Sustainable Chemistry & Engineering**, v. 8, n. 1, p. 210–222, 2019.
- 217 BATISTA, K. E. A.; DA SILVA, J. L. F.; PIOTROWSKI, M. J. *Ab Initio* investigation of the role of atomic radius in the structural formation of Pt_nTM_{55-n} (TM = Y, Zr, Nb, Mo, and Tc) nanoclusters. **The Journal of Physical Chemistry C**, v. 122, n. 13, p. 7444–7454, 2018.
- 218 CHA, S.-H. Comprehensive survey on distance/similarity measures between probability density functions. **International Journal of Mathematical Models and Methods in Applied Sciences**, v. 1, n. 2, p. 300–307, 2007.
- 219 GEHRKE, R.; REUTER, K. Assessing the efficiency of first-principles basin-hopping sampling. **Physical Review B**, v. 79, n. 8, p. 085412, 2009.
- 220 COLL, D.; DELBECQ, F.; ARAY, Y.; SAUTET, P. Stability of intermediates in the glycerol hydrogenolysis on transition metal catalysts from first principles. **Physical Chemistry Chemical Physics**, v. 13, n. 4, p. 1448–1456, 2011.
- 221 EDAKE, M.; DALIL, M.; MAHBOUB, M. J. D.; DUBOIS, J.-L.; PATIENCE, G. S. Catalytic glycerol hydrogenolysis to 1,3-propanediol in a gas–solid fluidized bed. **RSC Advances**, v. 7, n. 7, p. 3853–3860, 2017.
- 222 CHARISIOU, N. D.; PAPAGERIDIS, K. N.; SIAKAVELAS, G.; TZOUNIS, L.; KOUSI, K.; BAKER, M. A.; HINDER, S. J.; SEBASTIAN, V.; POLYCHRONOPOULOU, K.; GOULA, M. A. Glycerol steam reforming for hydrogen production over nickel supported on alumina, zirconia and silica catalysts. **Topics in Catalysis**, v. 60, n. 15–16, p. 1226–1250, 2017.
- 223 LIU, B.; GREELEY, J. Decomposition pathways of glycerol via C–H, O–H, and C–C bond scission on Pt(111): A density functional theory study. **The Journal of Physical Chemistry C**, v. 115, n. 40, p. 19702–19709, 2011.
- 224 SEMINOVSKI, Y.; TERESHCHUK, P.; KIEJNA, A.; DA SILVA, J. L. F. The role of the cationic Pt sites in the adsorption properties of water and ethanol on the Pt₄/Pt(111) and Pt₄/CeO₂(111) substrates: A density functional theory investigation. **Journal of Chemical Physics**, v. 145, n. 12, p. 124709, 2016.
- 225 SEMINOVSKI, Y.; AMARAL, R. C.; TERESHCHUK, P.; DA SILVA, J. L. The role of the anionic and cationic Pt sites in the adsorption site preference of water and ethanol on defected Pt₄/Pt(111) substrates: A density functional theory investigation within the D3 van der Waals corrections. **Surface Science**, v. 667, p. 84–91, 2018.

226 AUNEAU, F.; MICHEL, C.; DELBECQ, F.; PINEL, C.; SAUTET, P. Unravelling the mechanism of glycerol hydrogenolysis over rhodium catalyst through combined experimental-theoretical investigations. **Chemistry – A European Journal**, v. 17, n. 50, p. 14288–14299, nov 2011.

227 CORTESE, R.; SCHIMMENTI, R.; ARMATA, N.; FERRANTE, F.; PRESTIANNI, A.; DUCA, D.; MURZIN, D. Y. Investigation of polyol adsorption on Ru, Pd, and Re using vdW density functionals. **The Journal of Physical Chemistry C**, v. 119, n. 30, p. 17182–17192, 2015.

228 SALCICCIOLI, M.; CHEN, Y.; VLACHOS, D. G. Density functional theory-derived group additivity and linear scaling methods for prediction of oxygenate stability on metal catalysts: Adsorption of open-ring alcohol and polyol dehydrogenation intermediates on Pt-based metals. **The Journal of Physical Chemistry C**, v. 114, n. 47, p. 20155–20166, 2010.

229 TAKKY, D.; BEDEN, B.; LEGER, J.-M.; LAMY, C. Evidence for the effect of molecular structure on the electrochemical reactivity of alcohols part ii. electrocatalytic oxidation of the butanol isomers on platinum in alkaline medium. **Journal of Electroanalytical Chemistry and Interfacial Electrochemistry**, v. 193, p. 159–173, 1985.

230 GOMES, J. F.; OLIVEIRA, V. L.; PRATTA, P. M. P.; TREMILIOSI-FILHO, G. Reactivity of alcohols with three-carbon atom chain on Pt in acidic medium. **Electrocatalysis**, v. 6, n. 1, p. 7–19, 2014.

231 ANGELUCCI, C. A.; VARELA, H.; TREMILIOSI-FILHO, G.; GOMES, J. F. The significance of non-covalent interactions on the electro-oxidation of alcohols on Pt and Au in alkaline media. **Electrochemistry Communications**, v. 33, p. 10–13, 2013.

232 KWON, Y.; LAI, S. C. S.; RODRIGUEZ, P.; KOPER, M. T. M. Electrocatalytic oxidation of alcohols on gold in alkaline media: Base or gold catalysis? **Journal of the American Chemical Society**, v. 133, n. 18, p. 6914–6917, 2011.

233 LOVAS, F.; PLUSQUELLIC, D.; PATE, B. H.; NEILL, J. L.; MUCKLE, M. T.; REMIJAN, A. J. Microwave spectrum of 1,2-propanediol. **Journal of Molecular Spectroscopy**, v. 257, n. 1, p. 82 – 93, 2009.

234 BULTINCK, P.; GOEMINNE, A.; VONDEL, D. V. de. *Ab Initio* conformational analysis of ethylene glycol and 1,3-propanediol. **Journal of Molecular Structure: THEOCHEM**, v. 357, n. 1, p. 19 – 32, 1995.

235 CALLAM, C. S.; SINGER, S. J.; LOWARY, T. L.; HADAD, C. M. Computational analysis of the potential energy surfaces of glycerol in the gas and aqueous phases: effects of level of theory, basis set, and solvation on strongly intramolecularly hydrogen-bonded systems. **Journal of the American Chemical Society**, v. 123, n. 47, p. 11743–11754, 2001.

236 PATTERSON, D.; SCHNELL, M.; DOYLE, J. M. Enantiomer-specific detection of chiral molecules via microwave spectroscopy. **Nature**, v. 497, n. 7450, p. 475–477, 2013.

-
- 237 IOTA, V.; KLEPEIS, J.-H. P.; YOO, C.-S.; LANG, J.; HASSEL, D.; SRAJER, G. Electronic structure and magnetism in compressed 3d transition metals. **Applied Physics Letters**, v. 90, n. 4, p. 042505, 2007.
- 238 KAUKASOINA, P.; LINDROOS, M.; DIEHL, R. D.; FISHER, D.; CHANDAVARKAR, S.; COLLINS, I. R. LEED determination of the structures of Ni(111) and the p(2*2) overlayer of potassium on Ni(111). **Journal of Physics: Condensed Matter**, v. 5, n. 18, p. 2875–2886, 1993.
- 239 OHTANI, H.; Van Hove, M.; SOMORJAI, G. Leed intensity analysis of the surface structures of Pd(111) and of CO adsorbed on Pd(111) in a $(\sqrt{3} \times \sqrt{3})R30^\circ$ arrangement. **Surface Science**, v. 187, n. 2-3, p. 372–386, 1987.
- 240 ADAMS, D. L.; NIELSEN, H. B.; Van Hove, M. A. Quantitative analysis of low-energy-electron diffraction: Application to Pt(111). **Physical Review B**, v. 20, p. 4789–4806, 1979.

Appendix

APPENDIX A – PERMISSIONS TO RE-USE MATERIALS PUBLISHED IN SCIENTIFIC ARTICLES TO ELABORATE THIS THESIS

This appendix shows permissions to re-use materials published in references number 145 and 159 for the thesis, concerning, respectively, in Chapters 4 and 6 of this thesis. The results discussed in Chapter 5 are currently being reviewed to be submitted for a future publication.

Figure A29 – Permission request process to re-use published material to elaborate Chapter 4. Permission is granted to the first author to use the complete material in this thesis and attribution was made appropriately.

Ab initio investigation of quantum size effects on the adsorption of CO₂, CO, H₂O, and H₂ on transition-metal particles

P. C. D. Mendes, V. K. Ocampo-Restrepo and J. L. F. Da Silva, *Phys. Chem. Chem. Phys.*, 2020, **22**, 8998
DOI: 10.1039/D0CP00880J

If you are not the author of this article and you wish to reproduce material from it in a third party non-RSC publication you must [formally request permission](#) using Copyright Clearance Center. Go to our [Instructions for using Copyright Clearance Center page](#) for details.

Authors contributing to RSC publications (journal articles, books or book chapters) do not need to formally request permission to reproduce material contained in this article provided that the correct acknowledgement is given with the reproduced material.

Reproduced material should be attributed as follows:

- For reproduction of material from NJC:
Reproduced from Ref. XX with permission from the Centre National de la Recherche Scientifique (CNRS) and The Royal Society of Chemistry.
- For reproduction of material from PCCP:
Reproduced from Ref. XX with permission from the PCCP Owner Societies.
- For reproduction of material from PPS:
Reproduced from Ref. XX with permission from the European Society for Photobiology, the European Photochemistry Association, and The Royal Society of Chemistry.
- For reproduction of material from all other RSC journals and books:
Reproduced from Ref. XX with permission from The Royal Society of Chemistry.

If the material has been adapted instead of reproduced from the original RSC publication "Reproduced from" can be substituted with "Adapted from".

In all cases the Ref. XX is the XXth reference in the list of references.

If you are the author of this article you do not need to formally request permission to reproduce figures, diagrams etc. contained in this article in third party publications or in a thesis or dissertation provided that the correct acknowledgement is given with the reproduced material.

Reproduced material should be attributed as follows:

correct acknowledgement is given with the reproduced material.

Reproduced material should be attributed as follows:

- For reproduction of material from NJC:
[Original citation] - Reproduced by permission of The Royal Society of Chemistry (RSC) on behalf of the Centre National de la Recherche Scientifique (CNRS) and the RSC
- For reproduction of material from PCCP:
[Original citation] - Reproduced by permission of the PCCP Owner Societies
- For reproduction of material from PPS:
[Original citation] - Reproduced by permission of The Royal Society of Chemistry (RSC) on behalf of the European Society for Photobiology, the European Photochemistry Association, and RSC
- For reproduction of material from all other RSC journals:
[Original citation] - Reproduced by permission of The Royal Society of Chemistry

If you are the author of this article you still need to obtain permission to reproduce the whole article in a third party publication with the exception of reproduction of the whole article in a thesis or dissertation.

Information about reproducing material from RSC articles with different licences is available on our [Permission Requests page](#).

Source: Content from the page

<<https://pubs.rsc.org/en/content/articlelanding/2020/cp/d0cp00880j#!divAbstract>> accessed on April (2020).

Figure A30 – Permission request process to re-use published material to elaborate Chapter 6. Permission is granted to the first author to use the complete material in this thesis and attribution was made in the respective chapter.

About Cited by Related

The influence of hydroxy groups on the adsorption of three-carbon alcohols on Ni(111), Pd(111) and Pt(111) surfaces: a density functional theory study within the D3 dispersion correction

P. C. D. Mendes, R. Costa-Amaral, J. F. Gomes and J. L. F. Da Silva, *Phys. Chem. Chem. Phys.*, 2019, **21**, 8434
DOI: 10.1039/C9CP00752K

If you are not the author of this article and you wish to reproduce material from it in a third party non-RSC publication you must [formally request permission](#) using Copyright Clearance Center. Go to our [Instructions for using Copyright Clearance Center page](#) for details.

Authors contributing to RSC publications (journal articles, books or book chapters) do not need to formally request permission to reproduce material contained in this article provided that the correct acknowledgement is given with the reproduced material.

Reproduced material should be attributed as follows:

- For reproduction of material from NJC:
Reproduced from Ref. XX with permission from the Centre National de la Recherche Scientifique (CNRS) and The Royal Society of Chemistry.
- For reproduction of material from PCCP:
Reproduced from Ref. XX with permission from the PCCP Owner Societies.
- For reproduction of material from PPS:
Reproduced from Ref. XX with permission from the European Society for Photobiology, the European Photochemistry Association, and The Royal Society of Chemistry.
- For reproduction of material from all other RSC journals and books:
Reproduced from Ref. XX with permission from The Royal Society of Chemistry.

If the material has been adapted instead of reproduced from the original RSC publication "Reproduced from" can be substituted with "Adapted from".

In all cases the Ref. XX is the XXth reference in the list of references.

If you are the author of this article you do not need to formally request permission to reproduce figures, diagrams etc. contained in this article in third party publications or in a thesis or dissertation provided that the correct acknowledgement is given with the reproduced material.

Reproduced material should be attributed as follows:

correct acknowledgement is given with the reproduced material.

Reproduced material should be attributed as follows:

- For reproduction of material from NJC:
[Original citation] - Reproduced by permission of The Royal Society of Chemistry (RSC) on behalf of the Centre National de la Recherche Scientifique (CNRS) and the RSC
- For reproduction of material from PCCP:
[Original citation] - Reproduced by permission of the PCCP Owner Societies
- For reproduction of material from PPS:
[Original citation] - Reproduced by permission of The Royal Society of Chemistry (RSC) on behalf of the European Society for Photobiology, the European Photochemistry Association, and RSC
- For reproduction of material from all other RSC journals:
[Original citation] - Reproduced by permission of The Royal Society of Chemistry

If you are the author of this article you still need to obtain permission to reproduce the whole article in a third party publication with the exception of reproduction of the whole article in a thesis or dissertation.

Information about reproducing material from RSC articles with different licences is available on our [Permission Requests page](#).

Source: Content from the page

<<https://pubs.rsc.org/en/content/articlelanding/2019/cp/c9cp00752k#!divAbstract>>
 accessed on April (2020).

Figure A31 – Explanation for re-use permission requests by the Royal Society of Chemistry showing the rules that apply to published material re-used in Chapters 4 and 6 of this thesis. Permission is granted to the first author to use the complete material in this thesis and attribution was made appropriately.

Re-use permission requests

Material published by the Royal Society of Chemistry and other publishers is subject to all applicable copyright, database protection, and other rights. Therefore, for any publication, whether printed or electronic, permission must be obtained to use material for which the author(s) does not already own the copyright. This material may be, for example, a figure, diagram, table, photo or some other image.

Author reusing their own work published by the Royal Society of Chemistry

You do not need to request permission to reuse your own figures, diagrams, etc, that were originally published in a Royal Society of Chemistry publication. However, permission should be requested for use of the whole article or chapter except if reusing it in a thesis. If you are including an article or book chapter published by us in your thesis please ensure that your co-authors are aware of this.

Reuse of material that was published originally by the Royal Society of Chemistry must be accompanied by the appropriate acknowledgement of the publication. The form of the acknowledgement is dependent on the journal in which it was published originally, as detailed in 'Acknowledgements'.

Material published by the Royal Society of Chemistry to be used in another of our publications

Authors contributing to our publications (journal articles, book or book chapters) do not need to formally request permission to reproduce material contained in another Royal Society of Chemistry publication. However, permission should be requested for use of a whole article or chapter. For all cases of reproduction the correct acknowledgement of the reproduced material should be given. The form of the acknowledgement is dependent on the journal in which it was published originally, as detailed in the 'Acknowledgements' section.

Acknowledgements —

Source: Content from the page <<https://www.rsc.org/journals-books-databases/journal-authors-reviewers/licences-copyright-permissions/#reuse-permission-requests>> accessed on April (2020).

Figure A32 – Continuation of the explanation for re-use permission requests by the Royal Society of Chemistry showing the rules that apply published material re-used in Chapters 4 and 6 of this thesis. This continuation shows how attribution must be done; both aforementioned chapters follow the rules highlighted for Physical Chemistry Chemical Physics. Permission is granted to the first author to use the complete material in this thesis and attribution was made appropriately.

Acknowledgements —

The Royal Society of Chemistry publishes some journals in partnership with, or on behalf of, other organisations; these journals require a specific wording of the acknowledgement when work is reproduced from them. The text for the acknowledgement for these journals, and the standard wording to be used by all other journals are given below.

Standard acknowledgement

Reproduced from Ref. XX with permission from the Royal Society of Chemistry.

Non-standard acknowledgements

Reproduction of material from NJC (New Journal of Chemistry)

Reproduced from Ref. XX with permission from the Centre National de la Recherche Scientifique (CNRS) and the Royal Society of Chemistry.

Reproduction of material from Photochemical & Photobiological Sciences (PPS)

Reproduced from Ref. XX with permission from the European Society for Photobiology, the European Photochemistry Association, and the Royal Society of Chemistry.

Reproduction of material from PCCP (Physical Chemistry Chemical Physics)

Reproduced from Ref. XX with permission from the PCCP Owner Societies.

Reproduction of material from Inorganic Chemistry Frontiers

Reproduced from Ref. XX with permission from the Chinese Chemical Society (CCS), Peking University (PKU), and the Royal Society of Chemistry.

Reproduction of material from Organic Chemistry Frontiers

Reproduced from Ref. XX with permission from the Chinese Chemical Society (CCS), Shanghai Institute of Organic Chemistry (SIOC), and the Royal Society of Chemistry.

Reproduction of material from articles in the Journal Archive from Geochemical Transactions

Reproduced from Ref. XX with permission from the American Chemical Society, Division of Geochemistry and the Royal Society of Chemistry.

Source: Content from the page <<https://www.rsc.org/journals-books-databases/journal-authors-reviewers/licences-copyright-permissions/#reuse-permission-requests>> accessed on April (2020).

APPENDIX B – DEMONSTRATION FOR SPIN-POLARIZED AND NON SPIN-POLARIZED CALCULATIONS

The total energy was calculated in a collinear standard spin-polarized approach for all systems of the thesis; this means that the spin quantum number was included for the electronic states considering *up* and *down* spin densities. However, certain well-known structures yield the same results regardless of spin polarization, as will be shown here. To demonstrate this, the total energy was calculated for the following bulk phases: body-centered cubic Fe, hexagonal close-packed Co, face-centered cubic Ag and face-centered cubic Cu using ISPIN = 2 (with spin polarization) and ISPIN = 1 (without spin polarization); all other computational parameters were treated equivalently. The results are shown in Table A15.

Table A15 – Total energy, E_{tot} , and total time required to run the calculation, CPU time, for stable crystals obtained for spin-polarized (ISPIN = 2) and non spin-polarized (ISPIN = 1) calculations.

	bcc Fe	hcp Co	fcc Ag	fcc Cu
$E_{tot}^{ISPIN=1}$ (eV)	-7.67118035	-6.79006307	-2.71413634	-3.74722296
$E_{tot}^{ISPIN=2}$ (eV)	-8.25475299	-7.04521675	-2.71413614	-3.74722322
$E_{tot}^{ISPIN=1} - E_{tot}^{ISPIN=2}$ (eV)	0.58357264	0.25515368	-0.00000020	0.00000026
CPU time ISPIN=1 (s)	38.902	161.250	37.830	60.304
CPU time ISPIN=2 (s)	230.850	260.132	101.594	164.446

Source: Own study.

The metals Fe, Co, Ag e Cu were chosen to demonstrate the effect of spin polarization, because this set includes two structures that have a high magnetic moment, Fe e Co, and two structures with total magnetic moment equal to zero, Ag e Cu. The difference $E_{tot}^{ISPIN=1} - E_{tot}^{ISPIN=2}$, shown in Table A15, is an indication of the effect of spin polarization on the total energy. As expected, neglecting spin polarization causes a significant change for the energy of Fe e Co, of 0.58 and 0.25, respectively. In contrast, for Ag e Cu the total energy does not depend on ISPIN. Notably, the energies of bcc Fe and hcp Co are lower for the spin-polarized calculation. In fact, ISPIN = 2 is realistic and necessary for materials with non-zero magnetic moments, which leads to a better approximation for the ground-state electron density. Alternatively, non-collinear spin polarization can be employed to allow the spin to point towards multiple directions and provide more details about the electronic structure, however, this approach was not explored in this thesis. Although important, the spin-polarized approach is computationally costly, as observed by

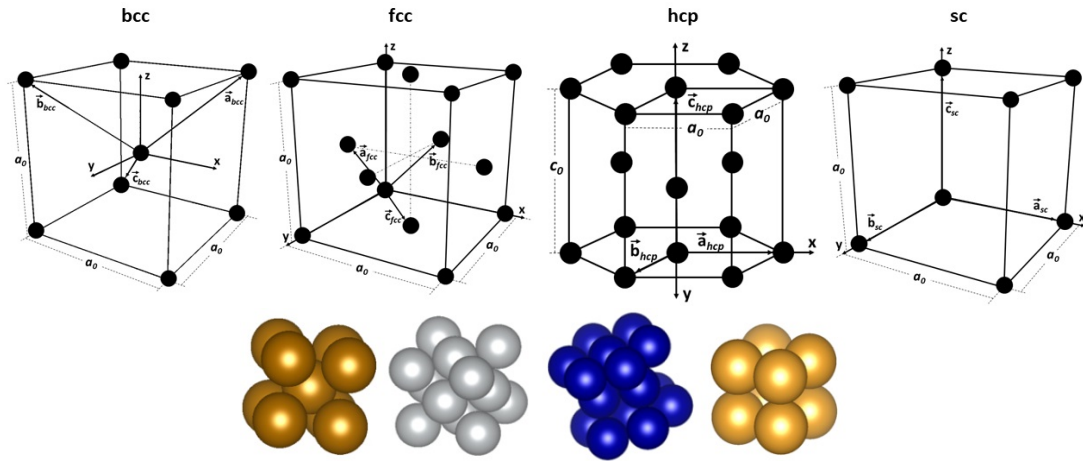
the CPU time shown in Table A15; all spin-polarized calculations, except for hcp Co, more than double the CPU time compared to $\text{ISPIN} = 1$. The tests support the following ideas:

1. $\text{ISPIN} = 2$ should be used always if the system is affected by spin polarization, due to total or local magnetic moments different than zero. Then, it is important to determine the magnetic moment before defining ISPIN ;
2. If the system has total and local magnetic moments equal to zero, using $\text{ISPIN} = 1$ or $\text{ISPIN} = 2$ does not affect significantly the total energy;
3. The use of $\text{ISPIN} = 2$ substantially increases the computational cost; then, the user can choose $\text{ISPIN} = 1$ in cases where the spin polarized calculation is not necessary, which should be identified based on a previous study of the total and local magnetic moments. Identifying this requires careful considerations, because it is possible for a system to have total magnetic moment equal to zero, but non-zero local magnetic moments, moreover, geometric changes can affect the magnetic moments;
4. For this thesis, the adsorbed systems were treated with spin-polarization, because the structural distortions after adsorption can change the magnetic properties of the substrate. However, we observed only small effects for systems such as Pt(111) and Cu(111) after adsorption.

APPENDIX C – ADDITIONAL DETAILS ON MODELING TRANSITION-METAL SOLIDS

This part presents fundamental concepts to understand how to model the solid state; these concepts are presented in great detail elsewhere.⁸⁷ Figure A33 presents the conventional unit cells for the crystal structures studied here indicating the lattice parameters and the translation vectors that define the smallest possible cells.

Figure A33 – Crystal structures. From the left: body-centered cubic (bcc), face-centered cubic (fcc), hexagonal close-packed (hcp) and simple cubic (sc). \mathbf{a}_i , \mathbf{b}_i and \mathbf{c}_i , with $i = \text{fcc, bcc, hcp}$ and sc , indicate the translation vectors for the crystal that define the smallest unit cells.



Source: Own study.

The translation vectors that define the smallest possible cells for the fcc, bcc, hcp and sc crystals are shown in Figure A33 and expressed in Table A16 in terms of the lattice parameter. Here, the notation \mathbf{a}_i , \mathbf{b}_i and \mathbf{c}_i represent the translation vectors for the crystal i , with $i = \text{fcc, bcc, hcp}$ and sc ; $\hat{\mathbf{i}}$, $\hat{\mathbf{j}}$ and $\hat{\mathbf{k}}$ are the unit vectors in the directions x , y and z ; a_0 and c_0 are the lattice parameters. The smallest cells define a volume in space, $V = |\mathbf{a}_i \cdot (\mathbf{b}_i \times \mathbf{c}_i)|$, in which only one atom centered in the origin is sufficient to represent the basis for fcc, bcc and sc bulks; for hcp, one atom centered in the origin and one additional atom, in coordinates $(0.66, 0.33, 0.5)$ relative to the lattice translation vectors, are sufficient.

As examples, some POSCAR files are shown ahead with the optimized structures of Ru crystals for all four phases studied. Following the format of the POSCAR files, line 1 is a comment, line 2 is an optional scaling constant for the lattice vectors, lines 3, 4 and 5 express the lattice translation vectors that define the unit cell (Table A16), lines 6 and 7 indicate the type of atom and the quantity of each respective atom in the structure,

Table A16 – Mathematical representation of the lattice translation vectors that define the smallest possible cells to construct POSCAR files for the transition-metal bulks.

	a	b	c
fcc	$\left(\frac{1}{2}\hat{\mathbf{j}} + \frac{1}{2}\hat{\mathbf{k}}\right) a_0$	$\left(\frac{1}{2}\hat{\mathbf{i}} + \frac{1}{2}\hat{\mathbf{k}}\right) a_0$	$\left(\frac{1}{2}\hat{\mathbf{i}} + \frac{1}{2}\hat{\mathbf{j}}\right) a_0$
bcc	$\left(\frac{1}{2}\hat{\mathbf{i}} - \frac{1}{2}\hat{\mathbf{j}} + \frac{1}{2}\hat{\mathbf{k}}\right) a_0$	$\left(-\frac{1}{2}\hat{\mathbf{i}} + \frac{1}{2}\hat{\mathbf{j}} + \frac{1}{2}\hat{\mathbf{k}}\right) a_0$	$\left(-\frac{1}{2}\hat{\mathbf{i}} - \frac{1}{2}\hat{\mathbf{j}} - \frac{1}{2}\hat{\mathbf{k}}\right) a_0$
hcp	$\hat{\mathbf{i}}a_0$	$\left(-\sin(30^\circ)\hat{\mathbf{i}} + \cos(30^\circ)\hat{\mathbf{j}}\right) a_0$	$\hat{\mathbf{k}}c_0$
sc	$\hat{\mathbf{i}}a_0$	$\hat{\mathbf{j}}a_0$	$\hat{\mathbf{k}}a_0$

Source: Own study.

respectively. Line 8 allows relaxing only some desired atomic coordinates that can be specified by controlling the marks T T T that can be observed in the next lines; if marked with F instead of T, the positions are fixed during the optimization. This resource can be useful for the adsorption studies, in which the bottom layers of the slab can be frozen in relaxed surface positions to reduce the computational cost without impairing the accuracy. Finally, the last lines of the file indicate the coordinates of each atom, in the same order that they appear in the aforementioned lines, preceded by a line indicating the type of coordinates (direct or cartesian). The POSCAR files for the surfaces, nanoparticles and adsorbed systems follow the same file format to represent the geometry of each system.

```

POSCAR Ru fcc
1.0000000000000000
0.0000000000000000  1.9004950893714896  1.9004950893714896
1.9004950893714896  0.0000000000000000  1.9004950893714896
1.9004950893714896  1.9004950893714896  0.0000000000000000

Ru
1

Selective dynamics
Direct
0.0000000000000000  0.0000000000000000  0.0000000000000000  T  T  T

POSCAR Ru bcc
1.0000000000000000

```

```
  1.5225727010000001  -1.5225727010000001  1.5225727010000001
-1.5225727010000001  1.5225727010000001  1.5225727010000001
-1.5225727010000001  -1.5225727010000001  -1.5225727010000001

Ru
1
Selective dynamics
Direct
0.0000000000000000  0.0000000000000000  0.0000000000000000  T T T

POSCAR Ru hcp
1.0000000000000000
  2.7148237216347031  0.0000000000000000  0.0000000000000000
-1.3574118608173515  2.3511063094750710  0.0000000000000000
  0.0000000000000000  0.0000000000000000  4.2808275652624825

Ru
2
Selective dynamics
Direct
0.0000000000000000  0.0000000000000000  0.0000000000000000  T T T
0.6666666666666643  0.3333333333333357  0.5000000000000000  T T T

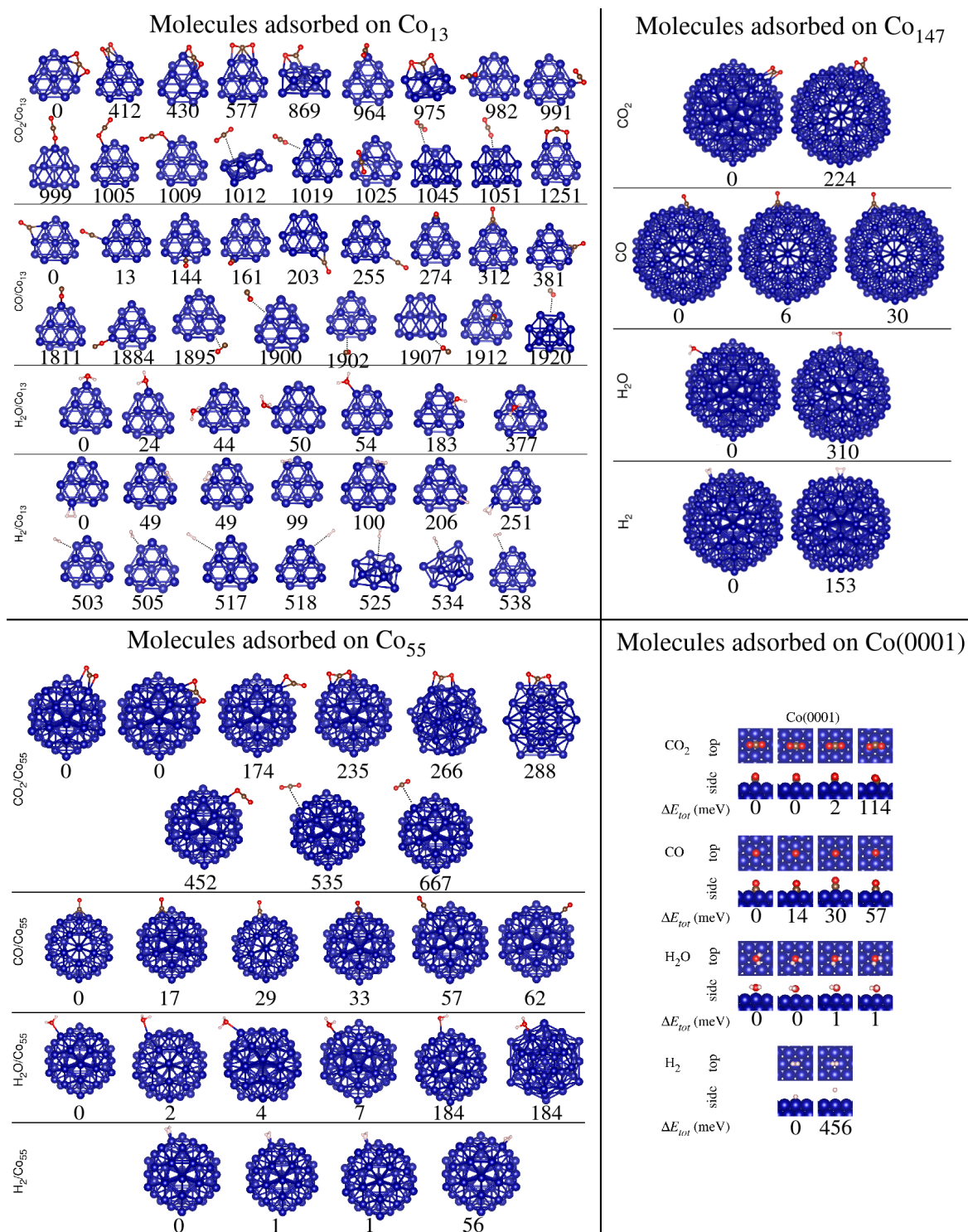
POSCAR Ru sc
1.0000000000000000
  2.5017663410172069  0.0000000000000000  0.0000000000000000
  0.0000000000000000  2.5017663410172069  0.0000000000000000
  0.0000000000000000  0.0000000000000000  2.5017663410172069

Ru
1
Selective dynamics
Direct
0.0000000000000000  0.0000000000000000  0.0000000000000000  T T T
```


APPENDIX D – COMPLETE SET OF CONFIGURATIONS TO STUDY QUANTUM SIZE EFFECTS ON THE ADSORPTION OF CO₂, CO, H₂ AND H₂O ON TRANSITION-METAL SUBSTRATES

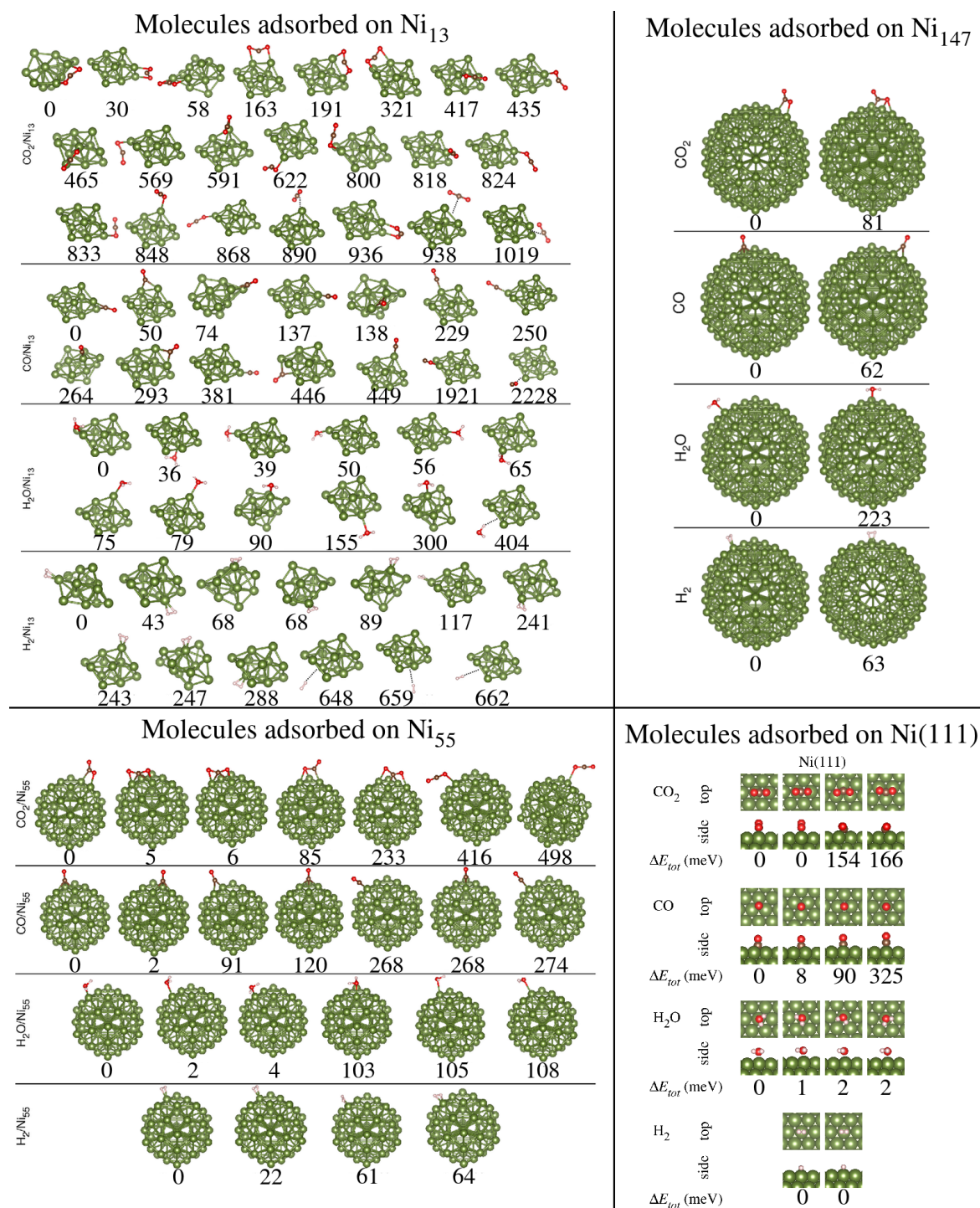
Here, we show a pictorial representation, in Figures A34, A35 and A36, of the complete set of adsorption configurations employed for the study discussed in Chapter 4 of the thesis. For more resources, such as atomic coordinates, we direct the reader to: Paulo C. D. Mendes, Vivianne K. Ocampo-Restrepo, Juarez L. F. Da Silva, *Ab Initio* Investigation of Quantum Size Effects on the Adsorption of CO₂, CO, H₂O, and H₂ on Transition-metal Particles. *Physical Chemistry Chemical Physics*, v. 22, n. 16, p. 8998-9008 (2020) <<https://doi.org/10.1039/D0CP00880J>>. ¹⁴⁵ Reproduced by permission of the PCCP Owner Societies.

Figure A34 – Pictorial representation of all optimized adsorption structures of CO₂, CO, H₂O or H₂ adsorbed on Co₁₃, Co₅₅, Co₁₄₇ or Co(0001) substrates. For each set, the structures are ordered by the energy relative to the most stable configuration, ΔE_{tot} , in meV.



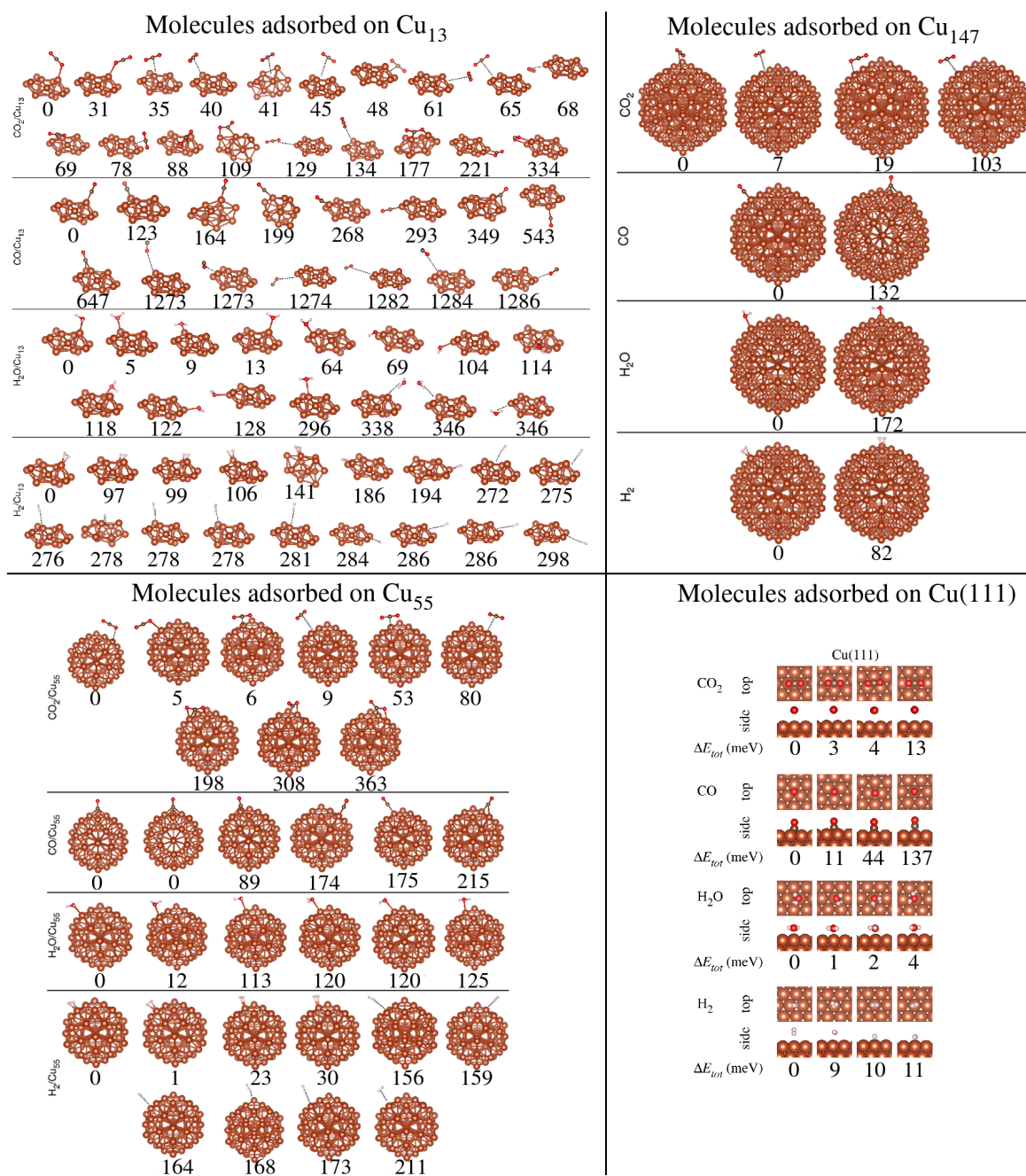
Source: Own study reproduced with permission for the thesis.¹⁴⁵ Reproduced from Ref. 145 with permission from the PCCP Owner Societies.

Figure A35 – Pictorial representation of all optimized adsorption structures of CO₂, CO, H₂O or H₂ adsorbed on Ni₁₃, Ni₅₅, Ni₁₄₇ or Ni(111) substrates. For each set, the structures are ordered by the energy relative to the most stable configuration, ΔE_{tot} , in meV.



Source: Own study reproduced with permission for the thesis.¹⁴⁵ Reproduced from Ref. 145 with permission from the PCCP Owner Societies.

Figure A36 – Pictorial representation of all optimized adsorption structures of CO₂, CO, H₂O or H₂ adsorbed on Cu₁₃, Cu₅₅, Cu₁₄₇ or Cu(111) substrates. For each set, the structures are ordered by the energy relative to the most stable configuration, ΔE_{tot} , in meV.



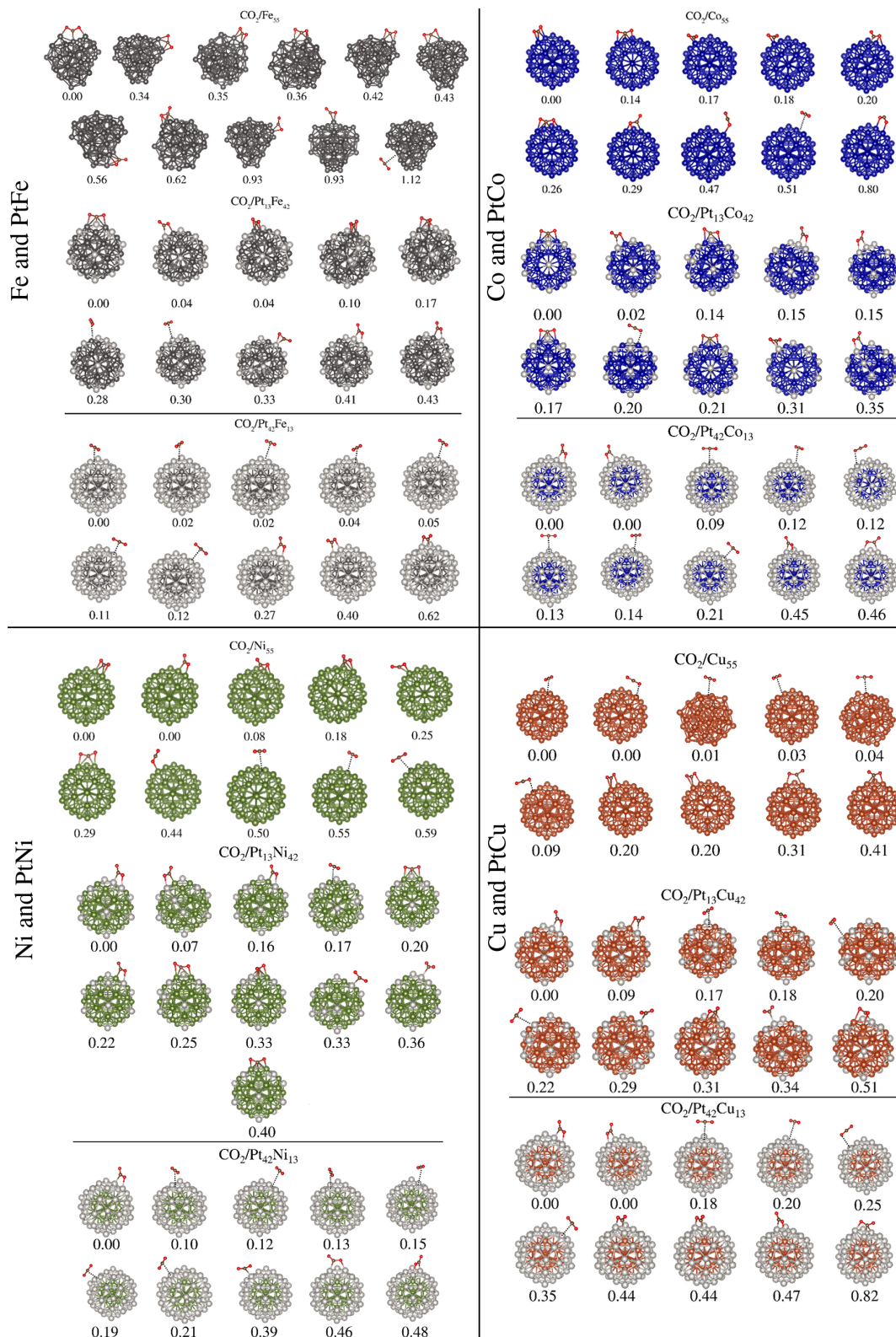
Source: Own study reproduced with permission for the thesis.¹⁴⁵ Reproduced from Ref. 145 with permission from the PCCP Owner Societies.

APPENDIX E – COMPLETE SET OF CONFIGURATIONS TO STUDY THE ALLOYING EFFECTS ON THE ADSORPTION OF CO₂ ON Pt-BASED BIMETALLIC NANOALLOYS

Here, we show a pictorial representation, in Figures [A37](#), [A38](#), [A39](#) and [A40](#), of the complete set of adsorption configurations employed for the study discussed in Chapter 5 of the thesis. Currently, around the time of writing this thesis, these results are being reviewed, further analyses are in progress and will be published in the near future. For more resources, we direct the reader to this future publication expected for the year 2020. The authors that contributed to the study, up to the present moment, are: Paulo C. D. Mendes, Lucas G. Verga, Juarez L. F. Da Silva. Permissions to re-use and adapt the material for the thesis will be requested and are normally granted for the purpose of the thesis.

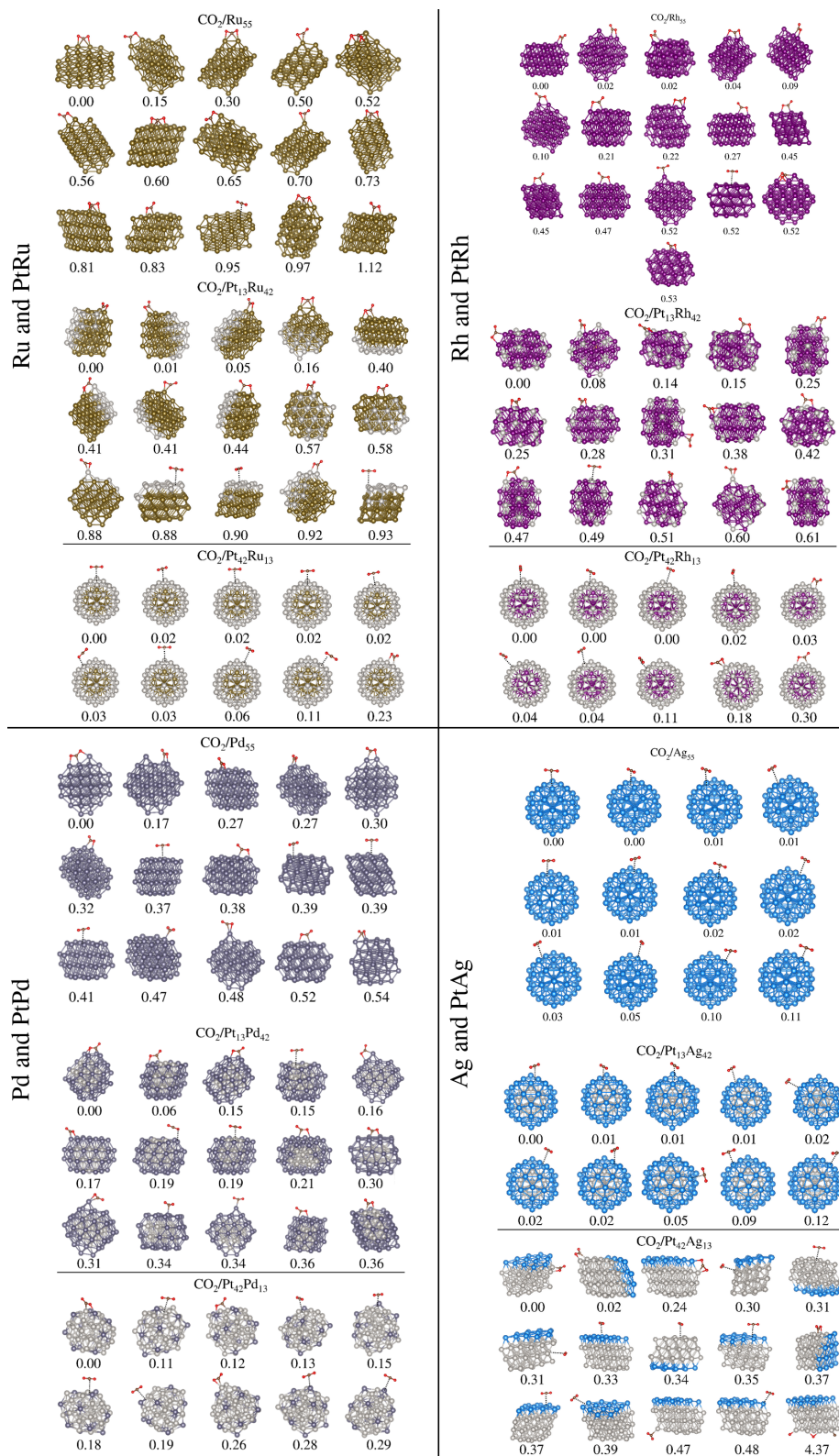
Paulo C. D. Mendes, Lucas G. Verga, Juarez L. F. Da Silva (expected for the year 2020).

Figure A37 – Pictorial representation of the optimized configurations of $\text{CO}_2/\text{TM}_{55}$ and CO_2/PtTM for the $3d$ transition period. For each set, the structures are ordered by the energy relative to the most stable configuration, in eV.



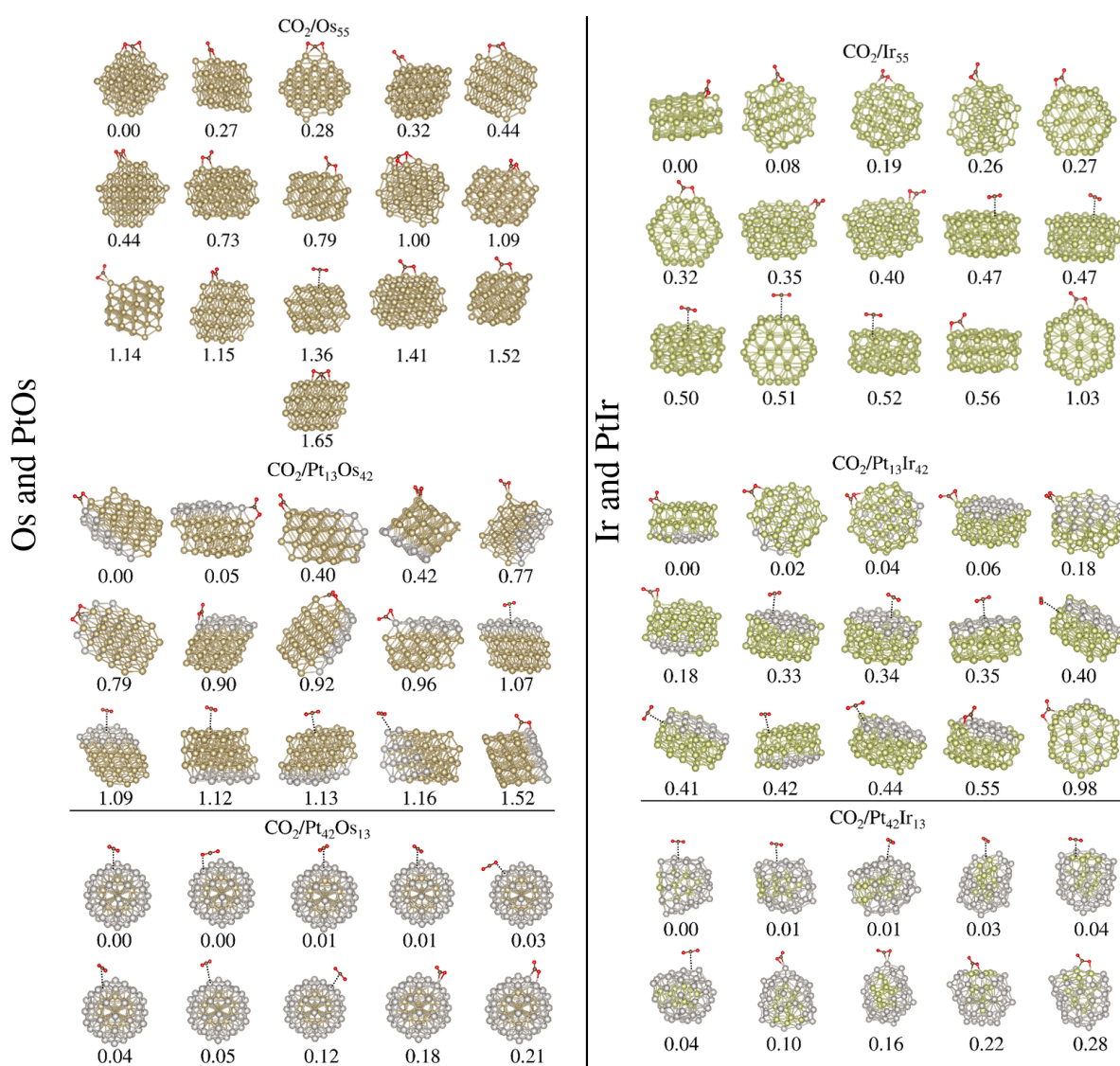
Source: Own study in preparation to be submitted for publication. Permission to use will be requested.

Figure A38 – Pictorial representation of the optimized configurations of $\text{CO}_2/\text{TM}_{55}$ and CO_2/PtTM for the 4d transition period. For each set, the structures are ordered by the energy relative to the most stable configuration, in eV.



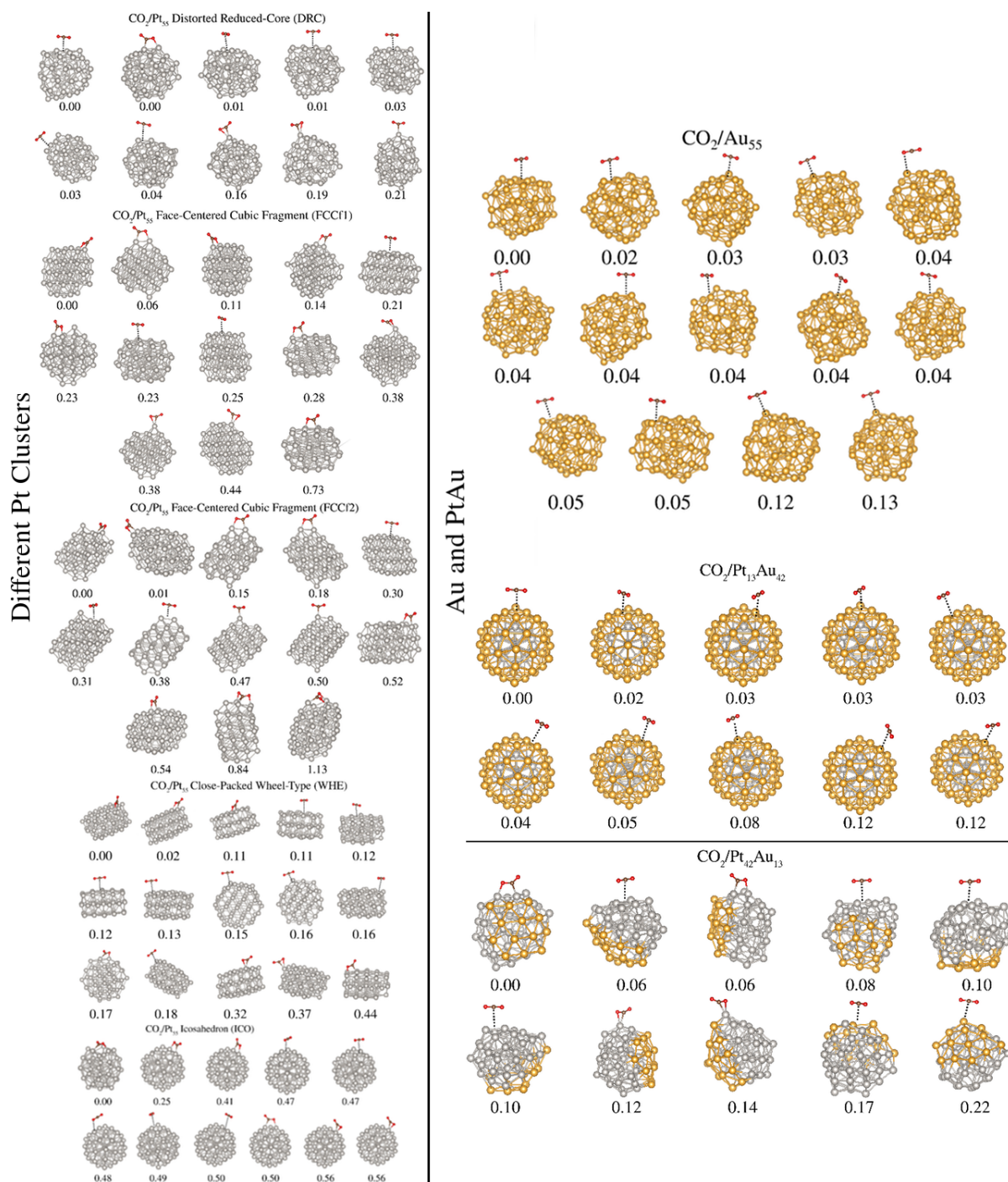
Source: Own study in preparation to be submitted for publication. Permission to use will be requested.

Figure A39 – Pictorial representation of the optimized configurations of $\text{CO}_2/\text{TM}_{55}$ and CO_2/PtTM for the $5d$ transition period, Os and Ir systems. For each set, the structures are ordered by the energy relative to the most stable configuration, in eV.



Source: Own study in preparation to be submitted for publication. Permission to use will be requested.

Figure A40 – Pictorial representation of the optimized configurations of $\text{CO}_2/\text{TM}_{55}$ and CO_2/PtTM for the 5d transition period, Pt and Au systems. For each set, the structures are ordered by the energy relative to the most stable configuration, in eV.

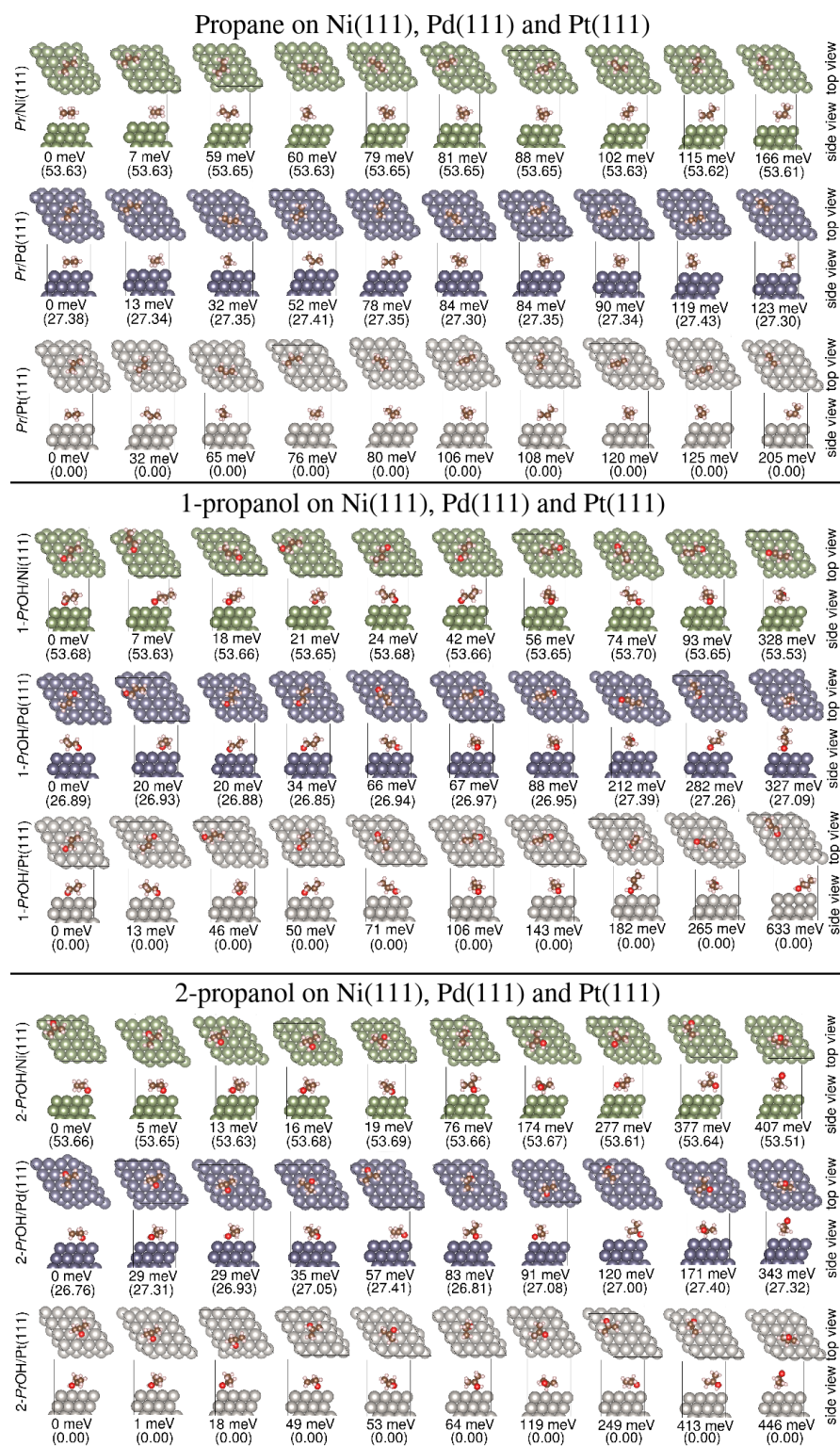


Source: Own study in preparation to be submitted for publication. Permission to use will be requested.

APPENDIX F – COMPLETE SET OF CONFIGURATIONS TO STUDY THE EFFECTS OF HYDROXY GROUPS IN THE ADSORPTION THREE-CARBON ALCOHOLS ON TRANSITION-METAL SURFACES

Here, we show a pictorial representation, in Figures A41 and A42, of the complete set of adsorption configurations employed for the study discussed in Chapter 6 of the thesis. For more resources, such as atomic coordinates, we direct the reader to: Paulo C. D. Mendes, Rafael Costa-Amaral, Janaina F. Gomes, Juarez L. F. Da Silva, The Influence of Hydroxy groups on the Adsorption of Three-carbon Alcohols on Ni(111), Pd(111) and Pt(111) Surfaces: a Density Functional Theory Study within the D3 Dispersion Correction. *Physical Chemistry Chemical Physics*, v. 21, n. 16, p. 8434-8444 (2019) <<https://doi.org/10.1039/C9CP00752K>>. ¹⁵⁹ Reproduced by permission of the PCCP Owner Societies.

Figure A41 – Pictorial representation of the optimized adsorption structures of propane, 1-propanol and 2-propanol on Ni(111), Pd(111) and Pt(111). For each set, the structures are ordered by the energy relative to the most stable configuration. The total magnetic moment, in μ_B , is indicated between parentheses.



Source: Own study reproduced with permission for the thesis.¹⁵⁹ Reproduced from Ref. 159 with permission from the PCCP Owner Societies.

Figure A42 – Pictorial representation of the optimized adsorption structures of 1,2-propanediol, 1,3-propanediol and glycerol on Ni(111), Pd(111) and Pt(111). For each set, the structures are ordered by the energy relative to the most stable configuration. The total magnetic moment, in μ_B , is indicated between parentheses.



Source: Own study reproduced with permission for the thesis.¹⁵⁹ Reproduced from Ref. 159 with permission from the PCCP Owner Societies.